

Electronic Theses and Dissertations, 2004-2019

2019

Computational Fluid Dynamics Investigation of A Novel Hybrid Comprehensive Stage II Operation For Single Ventricle Palliation

Marwan Hameed
University of Central Florida

 Part of the [Biomechanical Engineering Commons](#)
Find similar works at: <https://stars.library.ucf.edu/etd>
University of Central Florida Libraries <http://library.ucf.edu>

This Doctoral Dissertation (Open Access) is brought to you for free and open access by STARS. It has been accepted for inclusion in Electronic Theses and Dissertations, 2004-2019 by an authorized administrator of STARS. For more information, please contact STARS@ucf.edu.

STARS Citation

Hameed, Marwan, "Computational Fluid Dynamics Investigation of A Novel Hybrid Comprehensive Stage II Operation For Single Ventricle Palliation" (2019). *Electronic Theses and Dissertations, 2004-2019*. 6787. <https://stars.library.ucf.edu/etd/6787>

COMPUTATIONAL FLUID DYNAMICS INVESTIGATION OF A NOVEL HYBRID
COMPREHENSIVE STAGE II OPERATION FOR SINGLE VENTRICLE
PALLIATION

by

MARWAN SALAH HAMEED

B.S. University of Anbar, Iraq, 2011
M.S. Embry-Riddle Aeronautical University, USA, 2016

A dissertation submitted in partial fulfillment of the requirements
for the degree of Doctor of Philosophy
in the Department of Mechanical and Aerospace Engineering
in the College of Engineering and Computer Science
at the University of Central Florida
Orlando, Florida

Fall Term
2019

Major Professor: Alain Kassab

© 2019 Marwan Salah Hameed

ABSTRACT

Hypoplastic left heart syndrome (HLHS) is a type of heart defect where the left ventricle is underdeveloped or not developed, resulting in only a single functioning right ventricle. Approximately 7.5% of patients with congenital heart disease are born with a single ventricle (SV) which is accompanied by a spectrum of other malformations such as atrophied ascending aorta, atrial septal defects, and ventricular septal defects (VSD).

The existing three-hybrid staged surgical approach serving as a palliative treatment for this anomaly entails multiple complications and achieves a survival rate of only 50%. To reduce the trauma associated with the second stage of the hybrid procedure the hybrid comprehensive stage 2 (HCSII) operation can be a novel palliation alternative for a select subset of SV patients with adequate antegrade aortic flow. The procedure reduces surgical trauma in newborns by introducing a stented intrapulmonary baffle to avoid dissection of the pulmonary arteries and reconstruction of the aortic arch while obviating the dissection of the ductal continuation and distal arch.

It is the purpose of this dissertation to undertake a computational investigation to elucidate the complex hemodynamics of patients who have undergone HCS II. This was accomplished in a multiscale manner coupling a 0D lumped parameter model (LPM) of the peripheral circulation with 3D pulsatile Computational Fluid Dynamics (CFD) model providing the details and enabling investigation of the HCS II complex hemodynamics. The use of CFD allows modeling of blood flow, the study of the effect of different surgical procedures, suggestion of potential improvements from investigation of areas of concern which are: the pressure drop across the baffle, the loading of the baffle itself, shear stress and shear rates that might lead to thrombus formation, as well as oxygen transport and particle residence time.

A 3D anatomical model representative of a patient having undergone the HCSII was rendered utilizing the solid modeling software Solidworks based on anatomical landmarks from

CT scans, and a 0D LPM was tuned to produce flowrates and waveforms that matched catheter data. The pulsatile CFD computations were carried out using the commercial STARCCM+ solver. Several cases of baffle strictures relevant to surgical implementations were considered and results showed that the largest pressure drop across the baffle reported was about 3 mmHg while for the same narrowing size and accounting for the distal arch kink, a four-fold increase is observed yielding a 12.15 mmHg drop. Moreover, the analysis showed that for averaged blood flow velocity of 0.5 m/s, no vortex shedding from the baffle was observed in the computational model due to the short distance from the baffle to the aortic arch apex.

The velocity and pressure-flow fields were examined at different points throughout the cardiac cycle: late diastole, early systole, peak systole, and early diastole. Reverse flow was observed towards late diastolic phase due to the presence of an adverse pressure gradient, and a stagnant flow in the aortic arch apex was also noticed. For the pulmonary circulation and due to the low flow velocity and low pulsatility, the T-junction shape of the SVC presented no risk of recirculation or swirling that may promote thrombogenesis.

The wall shear stress on the baffle surface was also reported in pulsatile flow. It was observed that the flow detaches in systole and subsequently reattaches to the baffle surface. Moreover, the baffle surface experiences high wall shear stress magnitudes during systole and uneven distribution of WSS during diastole.

The variation in the baffle related narrowing had a little impact on the flow hemodynamics, as shown by the nearly constant oxygen transport across the models. The geometrical modification applied to the models had little effect on the oxygen delivery for up to a 15% change between a 4 mm increment of MPA minimum diameter. The results showed consistency with the published data of Glenn patients. Particle residence time was also reported to identify any blood recirculation or flow stagnation that may lead to platelet activation leading to clot formation rate. On average

particles take about 0.5(s) to exit the fluid domain. This time span is equal to the time of one cardiac cycle. Finally, the energy loss and energy efficiency were calculated as a function of split ratio and baffle related narrowing. Across all models, the efficiency was shown to be high.

To my mother, my father, my siblings, and friends.

ACKNOWLEDGMENTS

I would like to express my deepest appreciation to my advisor, Professor **Alain Kassab**, for his guidance, encouragement, and patience rendered throughout my years of study at the University of Central Florida (UCF). I'm extremely indebted for his suggestions and daily discussions; he continually and convincingly conveyed a spirit of adventure regarding both basic research level and industrial applications. Without his guidance and persistent help, this dissertation would not have been possible.

I would like to thank my Ph.D. committee members, Professor **William DeCampli**, Professor **Hansen Mansy**, Professor **Louis Chow** and Professor **Eduardo Divo**, for their suggestions and continuous instruction regarding my research. . I am extending my thanks for Dr. **Ray Prather**, for his never-ending generous advice and efforts to make this dissertation more meaningful. Furthermore, I would like to express my appreciation to my friends in the lab for their limitless help and support.

I am grateful for this opportunity to acknowledge all of my family members – especially my parents, my brothers, and my sisters – for their appreciation, encouragement, and prayers.

TABLE OF CONTENTS

LIST OF FIGURES	xi
LIST OF TABLES	xiv
NOMENCLATURE	xvi
CHAPTER ONE: INTRODUCTION.....	1
1.1 Normal Heart Anatomy	1
1.2 Hypoplastic Left Heart Syndrome (HLHS)	3
1.2.1 Surgical Stage 1	5
1.2.2 Surgical Stage 2.....	6
1.2.3 Surgical Stage 3.....	7
1.3 General Introduction	14
CHAPTER TWO: LITERATURE REVIEW.....	19
CHAPTER THREE: MATERIALS AND METHODS	29
3.1 The Model	29
3.2 Patient-Specific Model.....	32
3.3 Boundary Conditions.....	34
3.4 Lumped Parameter Model.....	36
Ventricular Septal Defect.....	44
3.5 Coupling.....	46
3.6 Discretization	48
3.7 Computational Fluid Dynamics (CFD).....	52

3.8	Oxygen Transport Model	56
3.9	Hemodynamic Parameters.....	60
CHAPTER FOUR: RESULTS AND DISCUSSION		65
4.1	Mesh Independence Study	65
4.2	Lumped Parameter Model (LPM).....	65
4.3	Multi-Scale Model Convergence	70
4.4	Systemic pressure drop.....	72
4.5	Vortex Formation	75
4.6	Flow Field	76
4.7	Baffle Loading and Wall shear Stresses.....	82
4.8	Energy Loss.....	85
4.9	Particle Residence Time.....	88
4.10	Oxygen Transport.....	91
4.10.1	Effect of Ascending Aorta Diameter.....	91
4.10.2	Effect of Area over the Baffle	92
4.10.3	Effect of the Split Ratio.....	94
CHAPTER FIVE: CONCLUSION.....		96
5.1	Conclusion.....	96
5.2	Limitations	98
5.3	List of Current Publication.....	99
APPENDIX A: FULL LPM equations		100

APPENDIX B: AORTA SIZE STUDY CFD SCENES.....	105
APPENDIX C: AREA OVER THE BAFFLE STUDY CFD SCENES.....	130
LIST OF REFERENCES.....	147

LIST OF FIGURES

Figure 1 Human Circulatory System[1].....	2
Figure 2 Anatomy of Normal Human Heart (Left) versus Hypoplastic Left Heart Syndrome Heart (Right)[16]	4
Figure 3 Norwood Procedure (Left) the procedure with a systemic pulmonary artery shunt (Blalock-Taussig), (Right) a shunt between the right ventricle–pulmonary artery[17].....	5
Figure 4 Stage 2 Bidirectional Glenn procedure[23].....	7
Figure 5 Extracardiac Fenestrated Fontan Operation [25].....	8
Figure 6 Hybrid Stage 1 Procedure[63].....	11
Figure 7 Comprehensive stage 2 procedure[65].....	12
Figure 8 Hybrid Comprehensive Stage II Operation[76]	16
Figure 9 Schematic of the Hybrid Comprehensive Stage II Procedure	17
Figure 10 Dimensions of the synthetic model (in millimeters)	29
Figure 11 H represents the minimum distance between the surface of the systemic baffle surface and the outside surface of the pulmonary trunk.....	30
Figure 12 Locations where the pressure was measured to calculate the pressure drop.....	31
Figure 13 Synthetic model configurations :(Top Left) Nominal, (top Right) -15%,.....	31
Figure 14 Different ascending aorta configurations	32
Figure 15 Three Dimensional Patient-Specific Model of a Post-Operative Hybrid Comprehensive Stage II Segmented from MRI Scan.....	34
Figure 16 RLC representation for atrial and venous beds.	37
Figure 17 Hydraulic Analogy	38
Figure 18 Elastance function waveform	39
Figure 19 Heart Chambers Electrical Bed	39

Figure 20 Schematic relate equations 4 and 5 to calculate y	40
Figure 21 Multiscale model of the HCS II circulation, three-dimensional CFD model, coupled with the lumped parameter model.....	42
Figure 22 Detailed LPM schematic.	43
Figure 23 Coupling scheme	48
Figure 24 (Left) Meshed geometry, (Right) meshed ascending aorta inlet	51
Figure 25 Three separate fluid regions, Systemic flow (left) and Pulmonary flow (middle).....	52
Figure 26 Relationship between hematocrit and viscosity [166].....	53
Figure 27 Fluid domain locations to calculate flow rate and pressure	56
Figure 28 Oxygen transport model for HCS II	58
Figure 29 Oxygen transport model without flow split.....	60
Figure 30 MPA: main pulmonary artery injection grid	64
Figure 31 Pressure waveforms.....	66
Figure 32 Sample BC waveforms for all inlets and outlets (AORTA=Aortic Root, SVC=Superior Vena Cava, DA=Descending Aorta, RPA=Right Pulmonary Artery, LPA=Left Pulmonary Artery, LcorA=Left Coronary Artery, RcorA=Right Coronary Artery, LCA=Left Carotid Artery, RCA=R	68
Figure 33 BCs waveforms (top) De-identified main pulmonary artery (bottom) tuned LPM MPA pressure	69
Figure 34 Tuned Aorta pressure (Left) De-identified data from APH,(Right) tuned LPM pressure	70
Figure 35 MPA cross-section.....	71
Figure 36 MPA averaged flowrate per iteration	71
Figure 37 Location of the MPA lumen defining MPA narrowing characteristic height (H).....	72

Figure 38 Time-averaged peak and surface averaged pressure drop across the baffle (top), and time-averaged peak and surface averaged pressure drop from baffle to distal arch (bottom) with respect to obstruction size.....	73
Figure 39 Velocity field representation using streamlines for a second heart cycle.	78
Figure 40 Pulmonary trunk axial cross-sectional cut with velocity field contour plot.	79
Figure 41 Pulmonary trunk axial cross-sectional cut with pressure field contour plot.	81
Figure 42 Comparison of velocity vs. wall shear stress during early systole (top) and early diastole (bottom), with pressure measurement locations the same as in Figure 29.	82
Figure 44 Wall shear stress contour plot on the baffle surface in the systemic region (pressure measurements locations the same as in Figure 34)	84
Figure 45 Energy loss versus area over the baffle	87
Figure 46 Energy loss versus split ratio.....	87
Figure 47 Particle Residence Time at different point of the cardiac cycle(Early systole,Peak systole,Early diastole and Late diastole	89
Figure 48 Particle Residence Time (s) plot.....	90
Figure 49 offers full detailed information about systemic saturation with different pulmonary venous saturation as a function of aorta size	92
Figure 50 Full detailed information about systemic saturation with different pulmonary venous saturation as a function of the area over the baffle	93
Figure 51 full detailed information about systemic saturation with different pulmonary venous saturation as a function of the blood flow split ratio	95

LIST OF TABLES

Table 1 some of the catheterization data provided by Arnold Palmer Hospital.	35
Table 2 Boundary conditions imposed in this study	36
Table 3 Mesh independent study	49
Table 4 Mesh independent study	50
Table 5 (Left) number of cells for models as the area over the baffle increases, (Right) as the aorta size increases.....	50
Table 6 Tabulated value for Carreau-Yasuda model constants	54
Table 7 - Surface averaged, and peak pressures drop for incremental pulmonary trunk narrowing sizes.....	75
Table 8 - Energy Loss and Energy Efficiency (E efficiency) as a function of the area over the baffle	85
Table 9 - Energy Loss (EL) and Energy Efficiency (E efficiency) as a function of split ratio ..	86
Table 10 Results for the Ascending aorta and area over the baffle studies (TotalSys: Cardiac Output, DA: Descending Aorta)	91
Table 11 Total systemic flow rate in (Liter per minutes) as a function of Ascending Aorta size and flow percentage of each boundary (TOTSYS: Total Cardiac Output,DA: Descending Aorta, LcorA=Left Coronary Artery, RcorA=Right Coronary Artery, LCA=Left Caro.....	92
Table 12 Total Systemic Flow Rate (Liter per minutes) as a Function of Area over the Baffle and The Flow Percentage of Each Boundary (TOTSYS: Total Cardiac Output, DA: Descending Aorta, LcorA=Left Coronary Artery, RcorA=Right Coronary Artery, LCA=Left Carotid Artery, LSA=Left Subclavian Artery, RCA=Right Carotid Artery, RSA=Right Subclavian Artery).....	93

Table 13 Oxygen transport and oxygen saturation comparison between 60-40 and 50-50 split ratio for the nominal Case (TOTSYS: Total Cardiac Output, DA: Descending Aorta, PVO2: Pulmonary Venous Flow Oxygen Saturation)..... 94

Table 14 Total systemic flow rate (Liter per minutes) as a function split ratio and the flow percentage of each boundary (TOTSYS: Total Cardiac Output, DA: Descending Aorta, LcorA=Left Coronary Artery, RcorA=Right Coronary Artery, LCA=Left Carotid Artery, LSA=Left Subclavian Artery, RCA=Right Carotid Artery, RSA=Right Subclavian Artery)..... 95

NOMENCLATURE

Acronyms

AO	Ascending Aorta
ASD	Atrial Septal Defect
APH	Arnold Palmer Hospital
BDG	Bidirectional Glenn
BSA	Body surface Area
CO	Cardiac Output
CHD	Congenital Heart Disease
CFD	Computational Fluid Dynamics
CT	Computer Tomography
DA	Descending Aorta
Damus-Kaye-Stanzl	DKS
EL	Energy Loss
$E(t)$	Time-Varying Elastance
HLHS	Hypoplastic Left Heart Syndrome
HCS II	Hybrid Comprehensive Stage 2
HR	Heart Rate
IVC	Inferior Vena Cava
HFP	Hemi-Fontan Procedure
LPM	Lumped Parameter Method
LCA	Left Carotid Artery
LCORA	Left Coronary

LSA	Left Subclavian Artery
LPA	Left Pulmonary Artery
MPA	Main Pulmonary Artery
MRI	Magnetic Resonance Images
MBTS	Modified Blalock Taussig Shunt
ODEs	Ordinary Differential Equations
O ₂	Oxygen
PDA	Patent Ductus Arteriosus
PVR	Pulmonary Vascular Resistance
PPAB	Branch Pulmonary Artery Banding
PRT	Particle Residence Time
P _s	Static Pressure
Q	Flow rate
RPA	Right Pulmonary Artery
RCA	Right Carotid Artery
RSA	Left Subclavian Artery
RCORA	Right Coronary
Re	Reynold Number
RVS	Right Ventricle Shunt
St	Strouhal Number
SVC	Superior Vena Cava
SV	Single Ventricle
TCPC	Total Cavo-Pulmonary Connection
VSD	Ventricular Septal Defect

WSS Wall Shear Stress

Roman Symbols

C Compliance

E Elastance

I Inertia

P Pressure

Q Flow rate

R Resistance

T Period

t Time

V Volume

Units

Hz Frequency

Kg kilogram

pa Pascal

l/min Liter per minute

mmHg Millimeters of Mercury

ml Milliliter

mm Millimeter

min Minute

s Second

CHAPTER ONE: INTRODUCTION

1.1 Normal Heart Anatomy

Humans have a very complicated cardiovascular system that consists of the heart and a closed system of vessels (arteries, veins, and capillaries). The heart consists of two parts left and right, four chambers and four valves. The atrial and ventricular septum separates the left and right parts of the heart, and both consist of upper and lower chambers. The upper two chambers are the left and right atriums, and the lower two chambers are the left and right ventricles. The right atrium receives the deoxygenated blood from the upper circulation through the superior vena cava and from the lower body circulation through the inferior vena cava. Then the poor-oxygen blood flows down to the right ventricle through the tricuspid valve.

A healthy human has two blood circulations: the systemic circulation and the pulmonary circulation. The systemic is responsible for supplying the blood and nutrients to the organs and all the vessels and the capillaries where the exchange happens. The pulmonary circulation vessels carry the deoxygenated blood from the right ventricle to the lungs to be oxygenated. Then, the pulmonary veins transport the oxygen-rich blood back to the left atrium as shown in Figure 1.

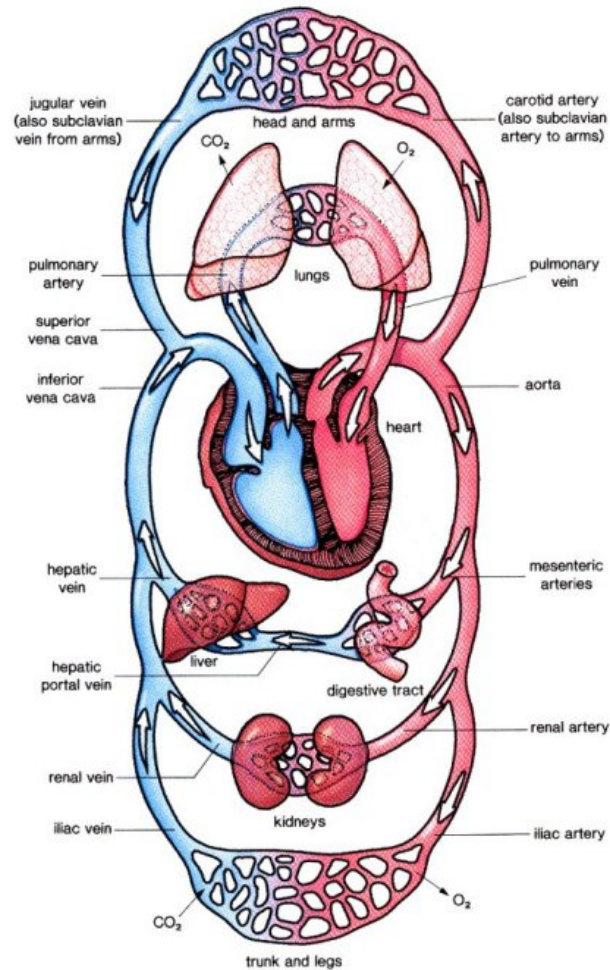


Figure 1 Human Circulatory System[1]

The pulmonary circulation starts when the pulmonary valve, which controls the blood flow between the right ventricle and the lungs, opens and the right ventricle walls contract to pump the depleted blood to the left and right lungs through the pulmonary arteries. The lungs job is to pass oxygen into the blood and get rid of any waste like carbon dioxide. The oxygenated blood, then, flows back to the heart, specifically to the left atrium, and through the mitral valve, the blood passes into the left ventricle. The left ventricle walls are thicker and more developed than the right ventricles to allow the ventricle to pump high-pressure blood to the systemic circulation through the aortic valve. The heart muscles are provided with blood through small vessels named the

coronaries. The coronaries receive blood from the ascending aorta root and consist of two branches right and left coronary arteries.

1.2 Hypoplastic Left Heart Syndrome (HLHS)

Hypoplastic left heart syndrome (HLHS) is a congenital heart defect where patients are born with underdeveloped or not developed left ventricle resulting in only a single functioning right ventricle. Approximately 2-9% of patients with congenital heart disease are born with a single ventricle (SV), and it accounts for 23% of cardiac death that occurs in the early days after birth[2]. Moreover, yearly, about 640 to 1440 neonates are born with a single ventricle in the United States[3]. Furthermore, HLHS occurs mainly in men (55% to 70 %)[4]. The inherited genes might be the reason for this disease, but researchers have not yet fully understood the genetic causes. Turner syndrome, Holt-Oram syndrome, Smith-Lemli-Opitz syndrome, Noonan syndrome, trisomy 13, etc. are examples of genetic disorders associated with this defect [4-7]. HLHS is usually accompanied by a spectrum of other malformations such as the atrophied ascending aorta, atrial septal defects (ASD), and atresia of the mitral and aortic valves and that means no ejection from the left ventricle to the systemic circulation. A surgical intervention is required to restore the heart function by making the right ventricle the main pump for both the systemic and the pulmonary circulation in order to save the lives of these patients. Usually, the patent ductus arteriosus (PDA) is open after birth for patients with a single ventricle. The PDA is a hole that allows the blood to bypass the lungs and flow directly to the body since the blood is oxygenated at the placenta, and it closes during the first few days of life, and that will lead to death in patients with single ventricle. The Atrial septal defect (ASD) is a hole in the wall that separates the two upper chambers of the heart. This opening allows the blood to flow from the lungs to the heart. Now, both the oxygenated and the deoxygenated blood are mixed up in the right atrium, and the

right ventricle is responsible for pumping blood to both the systemic circulation and the pulmonary circulation. The survival rate was about 5% during the first month of life before 1980 [8-10]. There are two options to treat patients with a single ventricle: heart transplant or staged surgical procedures. The heart transplant is limited due to the lack of donors, and many infants die waiting for a donor [8, 11, 12]. One study found that the waiting time for the right donor ranges between zero to 100 days. Moreover, the management during the waiting period could be challenging[9]. The survival rate was reported to be 48% after two years and 47% after three years and the major cause of death is a rejection of the transplant [13-15]. The second option is more common, and it consists of a three staged operations. The main goal of the palliative open-heart surgeries is to achieve a functional serial circulation driven by the single functioning right ventricle.

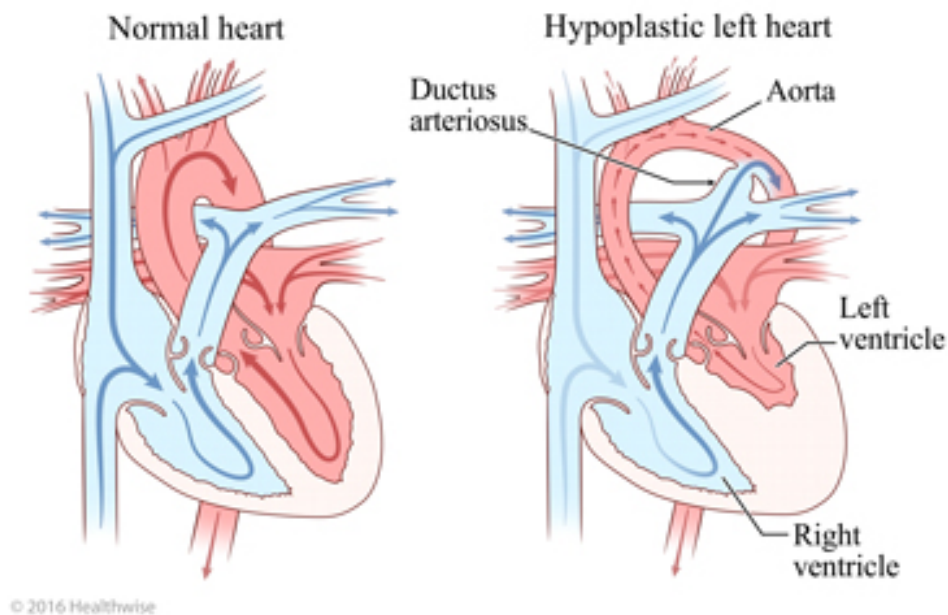


Figure 2 Anatomy of Normal Human Heart (Left) versus Hypoplastic Left Heart Syndrome Heart (Right)[16]

1.2.1 Surgical Stage 1

Stage 1 (Norwood procedure) was named after William Norwood, who developed this surgery in 1979 at Boston children's Hospital. This procedure takes place right after birth, and the main goal of the Norwood procedure is to make the right ventricle the main pump. This surgical procedure consists of: (1) dissect the pulmonary arteries (PAs) of the pulmonary trunk and patched, (2) connect the right ventricle and the aorta and that can be done by reconstructing the aorta using the main pulmonary artery to generate a new aorta, (3) place a shunt between the innominate artery and the PAs to provide blood flow to the lungs, (4) enlarge the atrial septum to allow oxygenated blood to return to the right atrium. After the operation, the right ventricle is now pumping the mixed blood through the constructed aorta to the systemic circulation, and part of the flow will be flowing to the lungs through the shunt. Furthermore, the heart now is carrying a higher load than usual because it must pump more blood than usual, and the arterial oxygen saturation ranges between 75-85%[\[2\]](#) due to the mixing in blood between the poor and rich oxygen in the atrium.

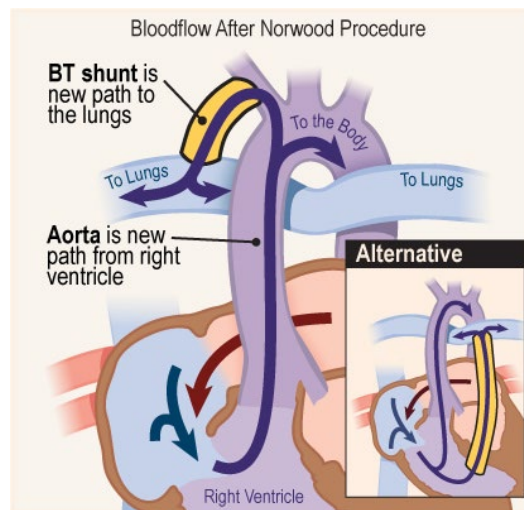


Figure 3 Norwood Procedure (Left) the procedure with a systemic pulmonary artery shunt (Blalock-Taussig), (Right) a shunt between the right ventricle–pulmonary artery[\[17\]](#)

The first shunt was used by Blalock and Taussig in 1945 and named Blalock Taussig (BT) shunt[18]. The BT shunt is a connection between the transected subclavian artery or the innominate artery and the pulmonary artery. The BT shunt has a long operation time, and it required the sacrifices of an artery(subclavian artery or the innominate)[19]. A synthetic shunt named, a modified BT shunt (MBTs) was introduced to between the innominate artery and pulmonary arteries. The shunt diameter is 3.5 or 4.0 mm, depending on the patient's size [2]. Sano shunt is considered an alternative to the MBTs where a shunt is placed between the right ventricle and a pulmonary artery, and it works as the source for the pulmonary flow[20].

1.2.2 Surgical Stage 2

The second stage is known as Bidirectional Glenn, and it takes place around 6-8 months of age when the pulmonary vascular resistance has dropped. The main goal of this transitional procedure is to reduce the load on the right ventricle and provide stabled low-pressure pulmonary flow. Glenn procedure consists of (1) removing the MBTs shunt, (2) dissection of the superior vena cava from the right atrium and anastomosed to the right pulmonary artery to provide venous return to the lungs and to prevent any mix in the atrium between the deoxygenated blood coming from the upper body and the oxygen-rich blood coming from the lungs.

Surgeons have two options to establish a source of pulmonary flow - the bidirectional Glenn (BDG) and the Hemi-Fontan procedure (HFP). The BDG is a straightforward operation where the SVC is detached from the right atrium and connected directly to the pulmonary arteries. The HFP does not require extensive dissection around the SVC, which may lead to phrenic nerve injury, it provides better hemodynamics performance than the BDG and less mortality and morbidity, but it is more complicated than the BDG and may lead to arrhythmias [21, 22]. In this

operation, a patch is placed at the end of the superior vena cava to prevent the depleted blood from entering the right atrium. Moreover, two incisions are made by a surgeon: the first one is at the top of the right atrium, and the second incision takes place at the pulmonary arteries posterior to the SVC. The two openings are sewn together, directing the blood flow to the lungs.

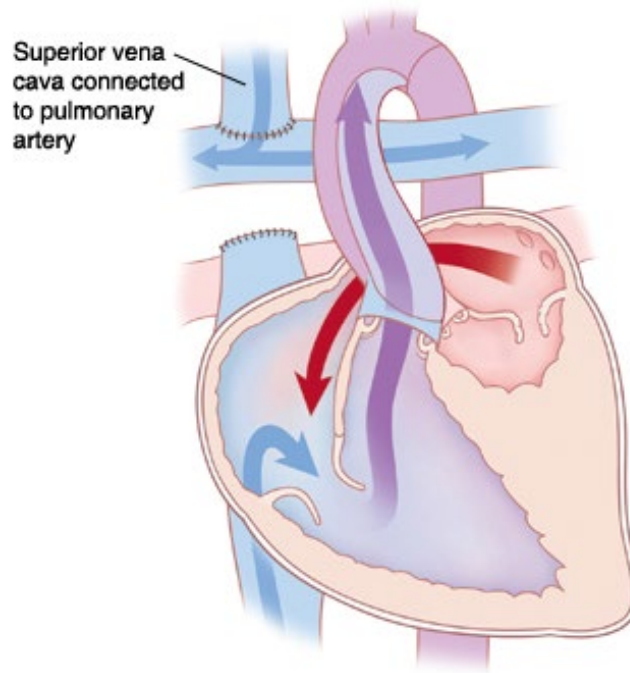


Figure 4 Stage 2 Bidirectional Glenn procedure[23]

1.2.3 Surgical Stage 3

The third stage is named Fontan after Francis Fontan, a French surgeon, who introduced this operation in 1970 and since then became the final palliation stage for HLHS patients[24]. The Fontan operation performed when patients are 18 to 36 months old. During this operation, the inferior vena cava is dissected off the right atrium and anastomosed to the pulmonary arteries using Goretex (Fontan) conduit establishing a total cavopulmonary connection (TCPC).

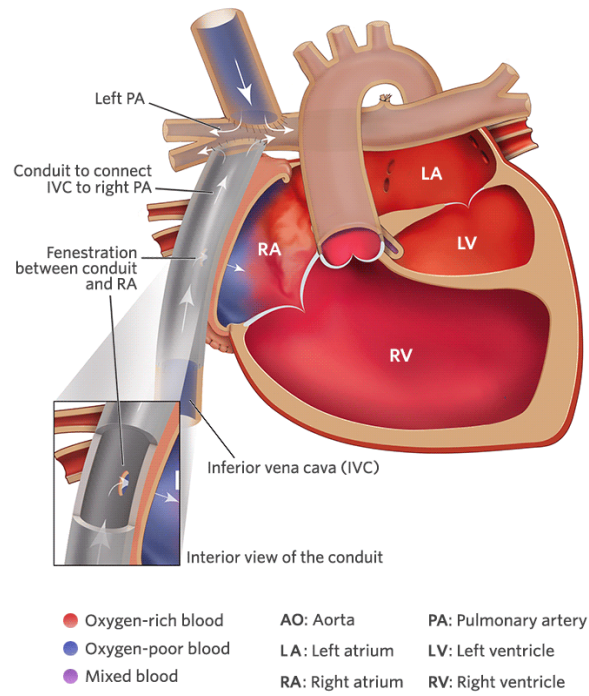


Figure 5 Extracardiac Fenestrated Fontan Operation [25]

For most Fontan patients, a fenestration in the conduit is created, which could be helpful, especially when high pulmonary vascular pressure presents. A study by Bridges [26] found lower mortality and shorter hospitalization for Fontan patients with fenestration[26]. After this operation, the right ventricle now pumps oxygen-rich blood only to the systemic circulation, and oxygen-poor blood returns passively to the lungs. However, Fontan physiology has some complications such as plastic bronchitis, protein-losing, renal and liver failure, and more complications that affect the patient's quality of living negatively[27, 28].

Although this staged operation has been widely adopted and optimized for years, studies reported that the survival rate at the age of five ranges between 58-72% [29-31]. Recently, a center reported that the surviving rate is only 40% for patients undergone the three surgical operations by the age of 10 years old [32]. The heart failures can be due to ventricular dysfunction, elevated pulmonary vascular resistance (PVR), and high inferior vena cava (IVC) pressure, which lead to

death. Over the years, many improvements have been suggested to the Fontan; some suggested using a mechanical pump to push the blood to the pulmonary circulation. However, pumps have issues like causing recirculation and obstruction, and cannot be shut off [33-36]. Others proposed using different diameters and locations for inferior cavopulmonary connection (ICPS) or use Y-shaped ICPS [37-41]. Gewillig M. et al. [42-44] in their work explained in detail the Fontan complications such as low flow pulsatility, high pulmonary vascular resistance, and underdeveloped pulmonary vasculature. Moreover, a fenestration at the inferior vena cava was proposed to reduce the IVC pressure and improve the cardiac output by returning some of the IVC flow back to the right atrium. However, that can decrease the oxygen saturation and causes cyanosis if the returned IVC flow was high.

The current survival rate is about 70% after the Norwood procedure. However, high mortality was reported for a subset of patients after the Norwood operation [45]. Moreover, with the current three staged procedures still only 63-80% of infants survive at one year of age [22, 46-48] and the need for less invasive palliative treatment that mitigate the risk factors such as low birth weight and aortic atresia, several variants (hybrid) staged surgeries have been proposed in an effort to improve success of the HLHS palliative treatment by delaying the more invasive operation until patients become more mature[49-51]. Although the Norwood procedure has become for a long time the standard option to treat patients with a single ventricle, it is still not a viable option for many patients because of its complexity that requires patients to be clinically stable before undergoing the procedure. Moreover, in some cases, surgeons cannot perform the Norwood procedure if the patient is prematurely born or has a serious illness that needs to be treated immediately like neonatal sepsis.

In 1993, Gibbs et al. introduced a less invasive approach without the use of cardiopulmonary bypass, which can cause bleeding, platelet dysfunction, inflammatory, and coagulation, etc.[[52](#), [53](#)]. The hybrid Norwood procedure consists of three steps: (1) a band is placed on both branches of the pulmonary artery to balance the blood flow between the systemic and the pulmonary circulations and to control the pulmonary flow, (2) stenting the patent ductus arteriosus (PDA) to prevent it from closing to allow blood circulation from the right ventricle into the systemic circulation, (3) a balloon atrial septostomy is performed to provide an opening between the left and right atria to allow blood flow from the lungs to the right, atrium[[49](#), [51](#), [52](#), [54](#)]. Both, the classic and the hybrid procedures attain the same physiological goals but the hybrid is less invasive and, in both procedures, the systemic and the pulmonary circulations are fed by the main pulmonary artery and have the same oxygen content. The hybrid procedure was reported to be adopted in many centers around the world, in Japan [[55](#)], Brazil [[56](#)] and Germany [[57](#)] with low mortality compared to the classic Norwood [[50](#), [58](#)]. However, the hybrid approach can cause complications such as retrograde aortic arch obstruction (RAAO), which is an obstruction that occurs in patients who underwent the hybrid Norwood. The RAAO was reported to occur in 10-24 % of patients, and it can increase the number of deaths between infants with this issue[[59](#), [60](#)]. The degree of stenosis varies between patients before undergoing the second stage [[59](#), [60](#)]. Another complication for post-operative patients is the migration of stent and PAs band, this can happen due to incorrect placement. A review study reported 100% (3 out of 3) mortality of patients with low birth weight and aortic atresia who underwent initial branch pulmonary artery banding (bPAB) and also reported a high mortality risk among premature patients after bPAB [[61](#)]. Another study found that the hybrid procedure is a safe alternative for high-risk patients who have organ

dysfunction after reviewing data of 10 patients from one center with ductal-dependent systemic outflow obstruction [62].

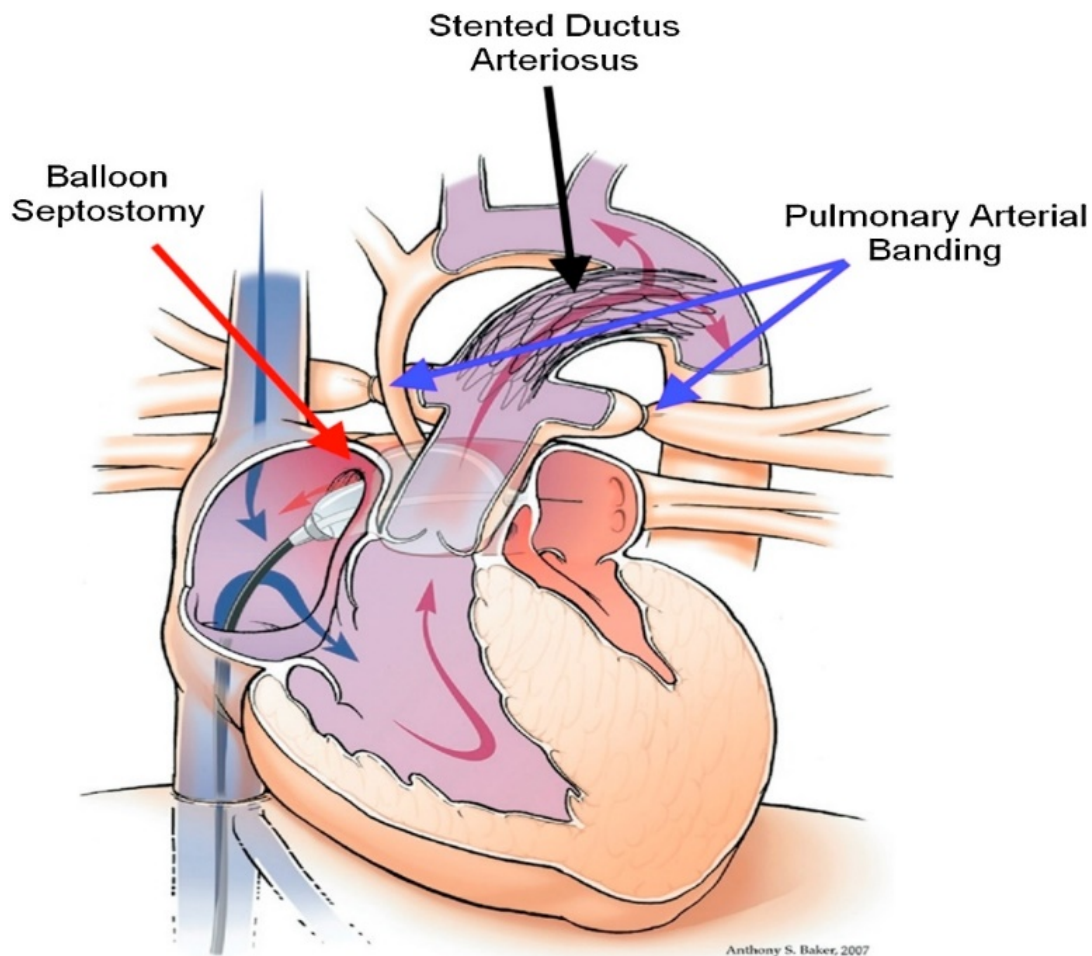


Figure 6 Hybrid Stage 1 Procedure[63]

The Comprehensive Stage II procedure, which follows the Hybrid Norwood, was performed for the first time by Hakan Akintuerk in 1998 [64]. The Comprehensive Stage II procedure, which takes place at 4-6 months of age, involves: (1) PDA stent removal, (2) pulmonary arteries band removal, (3) reconstruction of the aortic arch, (4) atrial septectomy, and (5) Bidirectional cavopulmonary anastomosis creation. The comprehensive stage II establishes the same physiology as the Glenn procedure.

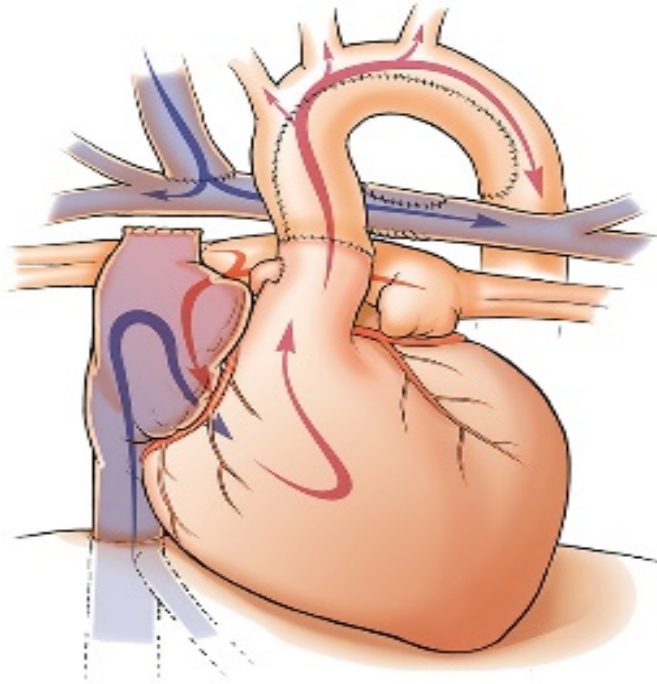


Figure 7 Comprehensive stage 2 procedure[65]

Only few centers reported the outcomes of the comprehensive stage II procedure. A center in Germany reported that 81 (91% survival) patients survived after comprehensive stage II (8 died out of 89 patients)[58] and another center in Canada, reported (6% mortality) two deaths out of 32 patients [66]. The comprehensive stage II procedure is more complex and requires aortic arch and pulmonary artery reconstruction. Moreover, a study found that there was no difference in survival rate between the Norwood and hybrid I patients up to 3 years after the second stage procedure. The study reviewed 43 Norwood patients and 32 hybrid patients who underwent the first procedure. The survival rate at one year was 83.8% for Norwood and 85.6% for the hybrid group and 80.4% versus 85.6% after three years[66]. A higher PA intervention, 20 interventions in hybrid (31 %) versus 5 in Norwood (11%) after few months, and less developed PA in hybrid patients was reported by the same study [66]. At three years, 43.3% of the hybrid group needed intervention versus 11.9% for the Norwood group [66]. A study by Venugopal [67] of 21 patients undergone the hybrid stage I and II showed higher mortality than the standard Norwood operation.

The mortality rate was 42 % (9 died out of 21 patients). The same study reported higher necrotizing enterocolitis (NEC), which is an infection that affects the intestine, incidents in hybrid patients (23.8% versus 18% for Norwood patients) [67]. A study carried out by Naguib [68] to review and evaluate the pain management after comprehensive stage II and compare the results with Glenn patients. A total of 57 patients' data was reviewed, 36 patients underwent the comprehensive stage II, and 21 underwent the Glenn procedure. The study reported not only a higher pain scores after the comprehensive stage II but also a greater amount of fentanyl, which is the initial opioid prescribed for most patients in this study. The higher requirements of opioids were due to the fact that the comprehensive stage II requires reconstruction of the aorta, longer time operation and bypass usage, and longer mechanical ventilation for the majority of patients [67, 68]. A similar interstage mortality and morbidity rate between two groups of patients (14 hybrid and 19 Norwood) who underwent the second stage palliation was reported [51]. A study reported the outcomes of 41 patients undergone the hybrid procedure between 2005 and 2013, where 17 of them had a low body weight (average 2.6 kg). There were 13 inpatients, and interstage deaths were reported after the hybrid procedure. Furthermore, 28 survivals, 13 underwent the comprehensive stage II, 4 underwent biventricular repair, and 11 underwent the Norwood procedure. The study found that the survival rate after the comprehensive stage II compared with the Norwood procedure as a second procedure was inferior. Four deaths were reported in the same study of patients undergone the comprehensive stage II, while no death was reported of patients who underwent the Norwood procedure [54]. Similar median and long term survival of patients undergone stage I Norwood or the comprehensive stage II following branch pulmonary artery banding (bPAB), similar transplant-free survival was reported by Davies [61]. The same study found that there were no benefits of delaying the comprehensive stage II to mitigate the risk factors like low birth weight

[61]. One study reported excellent outcomes of patients undergone the comprehensive stage II following the hybrid stage I. The mortality was reported to be 4% (2 out of 55) patients after the comprehensive stage II [69].

1.3 General Introduction

This project aims to study the Hybrid Comprehensive Stage II, which is a new surgical palliative procedure for single-ventricle disease by using multiscale modeling with CFD. Congenital heart disease (CHD) is the main cause of death for children with congenital disabilities and affects 1% of the newborns in the U.S, according to the Center of Disease Control and Prevention [70]. Infants born with one working ventricle make up 25 % of patients with CHD, and about 30-40 % of them die at the age of five and rises to about 50% by the age of 20 years [59, 71, 72]. Moreover, surgical palliative treatment of CHD could cost up to 1 million per patient in the first five years [73, 74]. Infants with a single ventricle need to undergo staged surgical procedures to reroute the blood flow and restore the heart function. The Norwood procedure is considered the major stage where the cardiopulmonary bypass is performed, and it was reported that the Norwood procedure has the highest risks of mortality [70].

Approximately 30% of patients do not survive after the initial Norwood operation, and this percentage is higher for a subset of newborns, especially patients who weigh less than 2.5 kg [59]. Consequently, in order to increase the number of survivals, three chained hybrid operations were proposed as an alternative to avoid the cardiopulmonary bypass and the circulatory arrest [59]. In the first operation called the Hybrid Norwood, the left and right pulmonary arteries flows are restricted with a band to balance the flow between the to the lungs and the rest of the body. Moreover, a stent is placed in the patent ductus arteriosus in the pulmonary trunk to allow blood

circulation from the right ventricle into the systemic circulation [75]. However, the first stage is followed by a more complex procedure called the comprehensive stage II, consisting of cardiopulmonary bypass, hypothermia, ductal stent debridement, aortic arch reconstruction, Damus-Kaye-Stanzl (DKS) connection, cavopulmonary anastomosis, and atrial septectomy [65]. In some centers, the morbidity and mortality rates of the comprehensive stage II are greater than that of the traditional stage II operation [59, 66]. Therefore, there remains concerns that the “hybrid” strategy, as currently conducted, may not confer a net morbidity or survival advantage to the patient.

The hybrid comprehensive stage II was recently proposed at Arnold Palmer Hospital to further reduce the trauma of the comprehensive stage II [76]. The HCS II is applicable to the subset (30-50%) of single ventricle patients that have sufficient antegrade aortic flow to sustain upper body perfusion. Such patients may include an unbalanced atrioventricular canal, double inlet left ventricle, tricuspid atresia with ventriculo-arterial discordance, mitral atresia with large ventricular septal defect (VSD), and some cases of hypoplastic left heart syndrome with mitral and aortic stenosis. The technique avoids the creation of a DKS connection and surgical arch reconstruction entirely and, with further technical development, may be achieved without hypothermia, cardiac, and circulatory arrest[76]

The procedure is designed to follow the hybrid stage 1 approach to single ventricle repair. It requires a limited incision into the main pulmonary artery (MPA) and avoids dissection of the branch pulmonary arteries. A stent is placed to reinforce a baffle that bridges the Ostia of the branch pulmonary arteries, helping to support the compressive load from hemodynamics of the neo-aorta. In addition, to avoid stent migration, given the strong stresses exerted by the systemic circulation, the stent is sutured onto the orifice of each branch pulmonary artery[76]. The MPA

is then patched, and the stented ductus is re-stented with a bare-metal stent to maintain patency. The stented ductus may lead to distal arch obstruction, as it does in the Hybrid Norwood, and in the extreme case of total arch obstruction, the upper-body systemic flow is separated from the lower-body systemic flow.

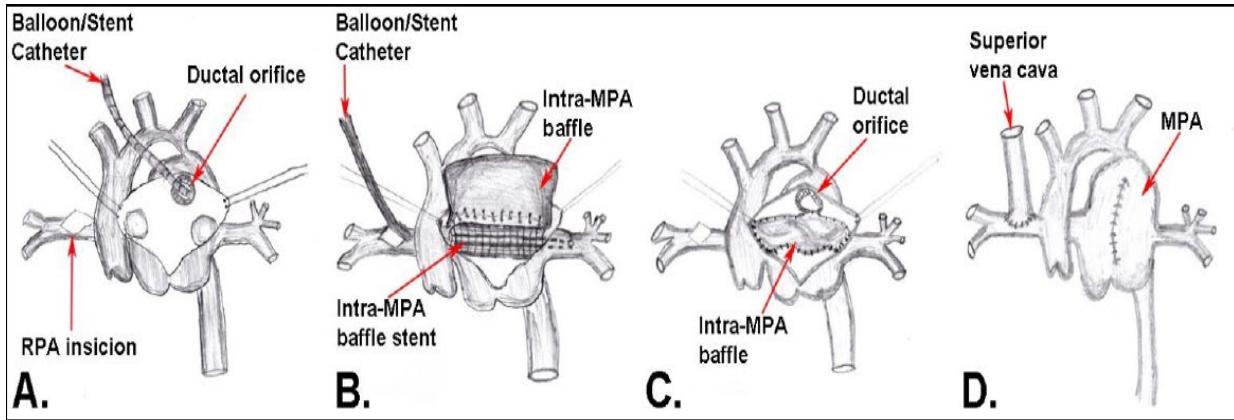


Figure 8 Hybrid Comprehensive Stage II Operation[76]

Short-time operation, as well as shorter hypothermia, are among the potential advantages of HCS II[76]. But like other procedures, the HCS II has some potential disadvantages, and that includes left pulmonary artery and ductal arch stenosis and thrombosis formation in areas where low shear stress or circulation occurs. Moreover, due to the presence of two different forces acting on the stent, one of which with high pressure flowing externally and the other force with low pressure, stent distortion may occur. Finally, the most important condition for patients to undergo this surgery is the adequate size of the ascending aorta as mentioned earlier. For some patients, the ascending aorta development might take longer than others, and that can lead to insufficient upper body blood flow[76].

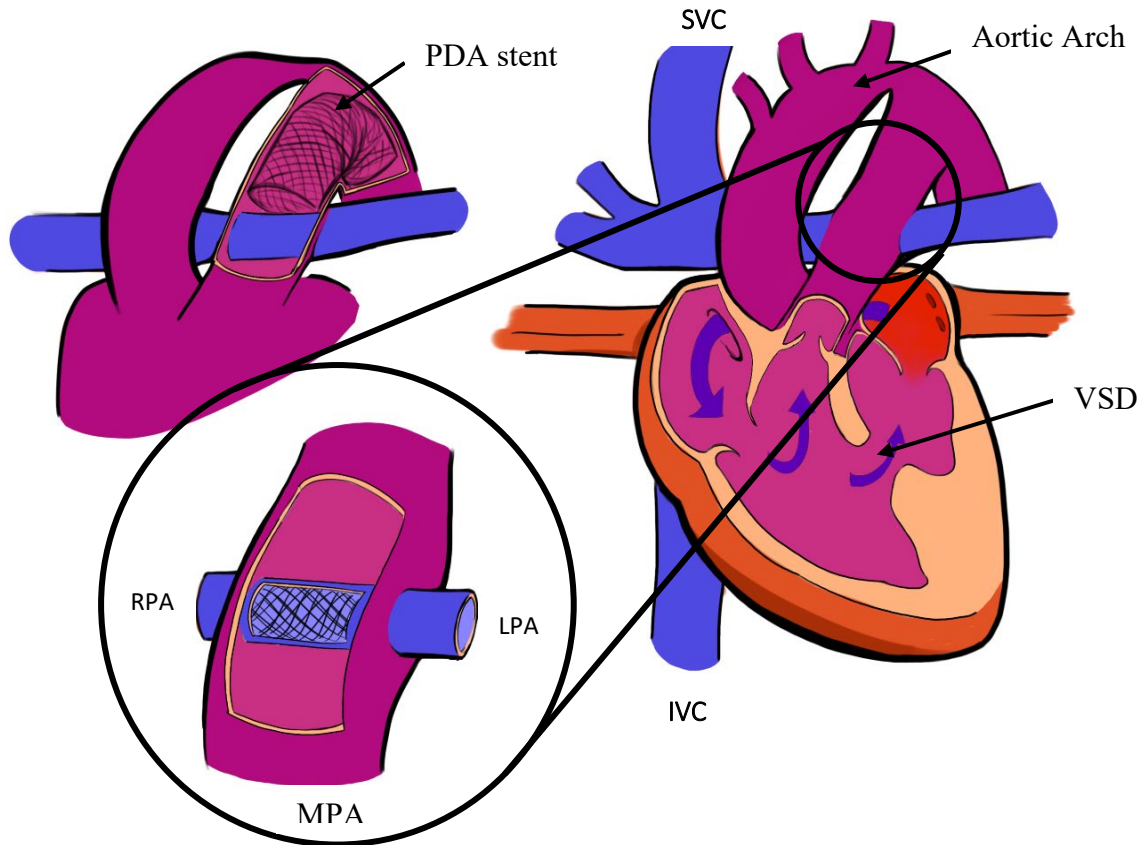


Figure 9 Schematic of the Hybrid Comprehensive Stage II Procedure

Given the novelty and complexity of the resultant circulation, we developed a multiscale computational fluid dynamics model to explore the overall HCSII hemodynamics. The specific aims of this dissertation are:

Aim 1: Obtain de-identified angiographic images for a patient who underwent the HCS II operation recently to extract a patient-specific geometry as well as waveforms for validation. Generate a synthetic representative model of the HCS II and generate the CFD mesh model. Finally, tune the 0D LPM circuit to generate the boundary waveforms needed for the CFD.

Aim 2: Utilize the developed multiscale CFD model to obtain: (a) the flow profile through the stented baffle and to investigate the pressure drop across the baffle and the tendency of forming

blood clots. (b) The flow near the aortic isthmus to see if there is any indication of thrombosis formation.

Aim 3: Determine the lower limits of aortic root/ascending aortic diameter that assure adequate cerebral blood flow. This will be accomplished in our computational model by: (1) synthetically narrowing the ascending aorta of the patient-specific solid model using the Software Solidworks (*Dassault Systemes*, Concord, MA) and (2) running the multi-scale CFD simulation holding the LPM parameters constant and that will aid in predicting suitable patients (i.e., magnitude of antegrade aortic flow) for the HCS2 operation.

Aim 4: Calculate stresses on the outer surface of the inter-pulmonary baffle and estimated resulting deformation of the stent over short time scales.

Aim 5: Calculate the energy losses in the flow from the main pulmonary artery to the descending aorta.

Aim 6: Construct an oxygen transport model and calculate the oxygen delivery as a function of aortic root size and flow split ratio.

Aim 7: Calculate the particle residence time PRT, which can help identify the area of circulation and stagnation.

CHAPTER TWO: LITERATURE REVIEW

Computational fluid dynamics (CFD) using coupled multiscale modeling has been used widely to obtain physiologic information and compare different surgical approaches. In particular, the CFD tool has been used to predict the hemodynamic changes in single-ventricle patients [29, 39, 40, 77-84]. The use of CFD in such cases was due to a lack of animal models and the difficulty of conducting clinical measurement [41]. CFD modeling was first used in aerospace and automotive engineering and then became a crucial tool in biomedical research to develop and improve medical devices, cardiovascular research, and surgical planning [85].

The hybrid Norwood procedure was modeled by Ceballos [73] when he investigated the effect of different reverse-Blalock-Taussig shunt diameter (RBTS) on the hemodynamics and found out that the 3.5 mm had lower thrombus formation risks and lower shear rates than the other two cases (3.0 mm and 4.0 mm). He also modeled the hybrid Norwood procedure with distal aortic arch obstruction and an RBTS. Four synthetic models were analyzed in this study, with and without 90 % stenosis and with and without RBTS 4.0 mm. Using loosely coupled schemes showed that 4.0 mm RBTS completely compensate for the 90 % obstruction restoring the pressure to the nominal levels [74].

Corsini [86] studied the influence on cardiac output and oxygen delivery as the branched pulmonary arteries (BPA) banding, and ductal stent diameter varied. In this study, he found the 2 mm BPA to be optimal and that the cardiac output is more sensitive to changes in BPA than the changes in ductal diameter.

Hsia [87] developed 3D models of the hybrid stage 1, the Norwood procedure with MBTS, and the Norwood with right ventricle to pulmonary shunt to investigate the difference in oxygen

delivery and blood flow to the head and the rest of the body. Multi-scales models were utilized in this study by coupling the 3D models to the 0D LPM model of each procedure. The results showed a reduction in the systemic oxygen delivery in the hybrid case, 475 mL/min/m² compare to RVS, 640, and MBTS 475 mL/min/m². Moreover, the coronary perfusion pressure was found to be higher in the MBTS and RVS than the hybrid procedure.

Prather[[88](#)] carried out a loosely coupled multi-scale CFD analysis to study the relationship between the reverse Blalock –Taussig shunt size and placement influence on embolism formation. Moreover, a non-Newtonian blood model, patient-specific geometry, was implemented in this study. He used a Lagrangian phase model to track individual particles in order to investigate the pattern of embolization. The study showed that the stroke decreases by about 20 % when there is a distal arch obstruction, and the shunt size has a small effect when no stenosis present. However, when 90% of stenosis introduced, the stroke is sensitive to the shunt size. Moreover, the 3 mm RBTS could help to reduce the cerebral and coronary thromboembolic but no effect on the pulmonary.

Bove [[29](#)], in this study, compared the effect of the right ventricle artery shunt and the RBTS in standard Norwood. The results showed that in the case of right ventricle shunts, a better oxygen delivery was displayed. On the other hand, the RBTS had more negative effects on the hemodynamics.

Migliavacca [[89](#)] developed 3-synthetic models of Norwood procedure with different shunt placement locations : (1) Blalock-Taussig shunt connecting the innominate artery to the pulmonary artery, (2) Central shunt (CS) connects the aorta to the pulmonary artery(3) right ventricle to pulmonary artery shunt, known as San operation(SO). The multiscale approach was utilized to couple the 3D CFD model with the 0D LPM model of each geometry and different

shunt sizes were investigated (3, 3.5, and 4 mm). The results showed that the SO shunt produces minimal backflow, lower pulmonary to systemic flow ratio, and higher coronary pressure. Laganà [90] carried out a multiscale CFD model to compare the changes in pulmonary and the coronary blood flow dynamic of Norwood patients between using the Blalock-Taussig shunt (MBTS) and the central shunt (CS). Different shunt sizes (3, 3.5, 4 mm) were investigated. The CFD results showed: (1) The cardiac output was higher with the CS, (2) The pulmonary flow increases as the shunt size increases in both models, (3) Unbalanced right and left pulmonary flow.

Satoshi [91] developed the chimney reconstruction, which consists of a longitudinal extension and horizontal plication with the absence of path supplementation to prevent turbulent blood flow, neo-aortic root dilation, as well as enabling low energy loss. Satoshi and his team utilized computational fluid dynamics (CFD) analysis to investigate the ideal configuration of the reconstructed aortic arch using patient-specific models. The results showed laminar flow in the reconstructed aortic arch, specifically, in the isthmus at systole. Vortex flow in the neo-aortic trunk was also observed at diastole. In reality, the patients showed low wall shear stress in the isthmus, along with low energy levels. Meanwhile, the CFD results showed a moderately high oscillatory shear index with low wall shear stress in the small portion of the neo-aortic trunk.

Migliavacca [92] proposed a procedure of calculating the blood flow in a systematic to pulmonary artery shunt using CFD models based on the finite element method to calculate the velocity profiles in the shunt. With a varying shunt size from 3-5 mm, velocity profiles were evaluated at the distal and proximal positions, and correlations were drawn between the mean and maximum spatial velocities. The CFD results showed that the distal shunt Doppler velocities were always less than the proximal ones. The CFD models showed a $\frac{V_{mean}}{V_{max}}$ ratio of 0.579 at the distal junction and a ratio of 0.48 at the proximal one.

Studies have found that the Sano shunt provides a more stable hemodynamics state and low mortality compared to MBTs [93]. Moreover, a study found that using a conduit between the right ventricle and the pulmonary artery produces a better systemic and pulmonary flow distribution compared to the systemic to pulmonary conduit after reviewing the hemodynamics data of 24 patients, 10 with systemic to pulmonary artery conduit and 14 with right ventricle to pulmonary artery shunt [94]. The current survival rate is reported to be about 70 % after the Norwood procedure [47]. However, high mortality was reported for a subset of patients after the Norwood operation [45]. Risk factors like low birth weight, intact atrial septum, genetic syndromes, and small ascending aorta have a negative impact on survival for patients after the Norwood procedure [58, 95-100]. Moreover, It was reported that the death rate of patients who underwent Norwood operation was 40 % and 46 % at the age of 1 and 5 years, respectively[101].

The shunt design in stage 1 palliation has been the focus of numerous studies due to the fact that it controls the flow split between the pulmonary and the systemic and controls the pressure in both circulations. Many studies have been conducted on vessels with branches or bends, which can cause diseases such as arteriosclerosis (fat built up in arteries) and thrombus [102, 103]. For those reasons, several researchers have been investigating the design parameters of the shunt like diameter and angle of insertion.

Song [104] developed three synthetic models of a Norwood procedure with Blalock Taussig shunts and used CFD as a tool to study the blood flow of three different diameter shunts (3 mm, 4mm, and 5 mm). The study showed that the shear stress was higher when using 3 mm and 4 mm shunt sizes but higher energy losses were observed compared with the 5 mm model. A study by Sant'Anna was conducted to find the effect of Blalock Taussig shunt diameter and the angle of anastomosis on the blood hemodynamics. The models used in this study were built based on

average patient data, and the blood was modeled as a Newtonian fluid. The study showed that the angles between 60 to 90 deliver higher pulmonary flow, and the shunt diameter is the main factor in regulating the amount of blood flow[105]. Waniewski [106] utilized CFD tools along with in vitro simulation to estimate the hemodynamics of the Norwood procedure with Blalock Taussig shunt. Another study by Migliavacca [107] investigated, by using a mathematical multiscale CFD model, how the shunt diameters (3,3.5,4,4.5 and 5 mm), systemic and pulmonary vascular resistances and the heart rate affect the blood flow distribution and oxygen transport. This model showed that the 5- mm shunt increased the Q_p/Q_s but dropped O₂ delivery. Moreover, the effect of heart rate on O₂ delivery was minimal. Finally, $Q_p/Q_s = 1$ was optimal for O₂ delivery.

Moghadam et al., in their simulation, coupled the lumped parameter network of a Norwood anatomy to a 3D finite element solver. This study aimed to obtain the optimal shunt diameter, angle and patching location that provide the best systemic and coronary oxygenation. The simulation found that small distal shunt increases the systemic flow, while a more proximal shunt increases the coronary oxygen deliveries[108]. In 1995, Kitagawa and his group published a paper that aimed to find the optimal shunt diameter that provides the best flow to the lungs for Norwood patients. The study suggested using a shunt diameter that ranges between 3.0 mm and 3.5 mm to obtain suitable pulmonary flow [109].

Pennati and his group studied in vitro the effect of anastomotic dispensability, and suture restriction affects the pressure-flow relationship as a follow up of another numerical study carried out by the group (Migliavacca 2000). Two Gore-Tex shunts (3 mm and 4 mm) were used in this steady flow study, and the results showed that the pulmonary artery pressure has an impact on the pressure-flow relationship but presents no influence on the total pressure drop across the shunt[110].

Other studies have focused on determining the optimal Qp/Qs for Norwood circulation since this ratio affects the oxygen delivery of the system. A study by Barnea ,where a mathematical model was used, found that (i) the systemic oxygen increases as the Qp/Qs increases and then starts dropping ,(ii)the optimal ratio was found to be less than or equal to 1,(iii) the Qp/Qs ratio drops as the cardiac output increases[108].

Moreover, there have been plenty of studies regarding the Glenn procedure. One of which reported the major cause of death for standard Glenn patients was due to insufficient pulmonary flow after collecting data of more than 500 patients [111].

Shiavazzi [112] studied how different left pulmonary artery stenosis affects the hemodynamics for Glenn patients by using multiscale CFD analysis. Data from 6 patients were used in this study to produce the 3-dimensional model, and by using mesh morphing, he was able to vary the LPA stenosis level. The study showed a minor effect on the hemodynamics of the superior cavopulmonary connection when the stenosis is less than 65 %, but it is recommended to use LPA arterioplasty when the stenosis above 65 %.

Esmaily-Moghadam [113] analyzed an assisted bidirectional Glenn (ABG) using CFD. A shunt was placed to connect the right innominate and the superior vena cava. He also used a clip in one of the three models used in this study to constrict the flow near the SVC to create a Venturi effect. The study showed that ABG provided higher oxygen delivery and pulmonary blood flow than modified Baloch-Taussig shunt but higher SVC.

Zhou and his group [114] used an in vitro model to validate the simulation results carried by [115 259]. The results showed a mean pressure difference of 1.2 mmHg and that the ABG

increase the systemic oxygenation by about 30 %. However, they also found an increase in SVC pressure.

Another alternative to the bidirectional Glenn procedure is the Hemi Fontan, where the right atrium is constructed by using a baffle to direct the SVC flow to the lungs. Bove [116], in his study, used computational fluid dynamic techniques to compare the hemodynamics between the Hemi-Fontan and the bidirectional Glenn as well as Fontan procedure with different models. The models (the Hemi-Fontan procedure (HFP) and the bidirectional Glenn anastomosis (BDG) after the Norwood procedure and the lateral tunnel (LT), total cavopulmonary connection (TCPC), and extracardiac conduit (ECC)) were constructed based on average clinical data). The study found that the Bidirectional Glenn and the Hemi-Fontan produce similar blood distribution and energy losses while the lateral tunnel energy loss was less compared to the other Fontan models (TCPC and ECC).

Kung [41] constructed two patients specific models from magnetic resonance imaging and a total of four simulations carried out with resting and active conditions for both models. The study demonstrated big differences in power losses between the two cases and different hemodynamic properties due to physiological differences.

The shear stress on the arterial walls was also investigated by Strony [117], who analyzed the effect of a high wall shear stress on thrombus formation.

Holme [118] found in his experimental study that aimed to find the relationship between shear rate and thrombus formation, that thrombus formation started at shear rate of 10500 1/s. Also, Baumgartner [119] and Sakariassen [120] both investigated the effect of shear rate and shear

stress on the thrombus formation. These studies showed that as the shear rate increases the risk of thrombus formation increases as well.

Troianowski [121] developed 5-patients specific geometries from MRA data and imposed pulsatile boundary conditions from their clinical data. The aim was to examine the hemodynamics of each model. The CFD results showed that the power loss was low and linearly proportional to the cardiac index in all models and low wall shear stress. Moreover, this study results showed some differences in results between the models, which emphasize the importance of patient-specific simulation.

Kung and his colleagues developed two patients' specific geometries of stage 2 with Hemi-Fontan based on magnetic resonance imaging. The 3D- geometrical model was then coupled to 0D lumped parameter models to describe the entire circulation. The CFD results showed swirling in the Hemi-Fontan in both models, and the power loss was similar, less than 13% in the pulmonary circulation. However, the swirl and stagnation levels were higher in one model than the other, and that shows the importance of stimulation of patient-specific models [122].

Pekkan et al.[123] studied, using CFD tools, two-second stage models (Glenn and Hemi-Fontan). Both geometries were constructed based on clinical data. The Glenn models showed better hemodynamic and flow performance compared with the Hemi-Fontan model. Moreover, by comparing the power loss of the second stage models (Glenn and Hemi-Fontan) with the total cavopulmonary connection model (TCPC), it was noticed that the power loss of the TCPC model was higher. The mortality rate after the second stage ranges from 0 % to 8 %, which is better than the first stage mortality by far [111, 124].

Moreover, the third stage of single ventricle palliation procedures called Fontan, which was named after Frances Fontan who completed the first Fontan ever in 1968 by repairing tricuspid atresia in the right ventricle. Since then, the procedure was performed on several numbers of patients. However, ventricle dysfunction and an increase in the pulmonary vascular resistance could lead to death in some cases. In other cases, a Fontan failure can be due to Inferior vena cava pressure rise, which can damage the liver [43, 125]. Moreover, researchers have been using the CFD tools to quantify the hemodynamics of Fontan and to help optimize the procedure [126-129]. One of the studies by Alexi-Meskishvili [130] aimed to determine the right size of the Gore-Tex. Moreover, 20 patients participated in this study and the results showed that using a conduit with a diameter that doesn't exceed 20 % of the IVC diameter is recommended to lower the risks of thrombus formation, and it is optimal to perform the extracardiac Fontan operation at 2-4 years of age at a bodyweight of 12-15 kg.

Itatani [40] also investigated the optimal size of the extracardiac Fontan operation. The size of the conduit varied between 14 mm and 22 mm. Moreover, a synthetic model was built based on data from 17 patients. This study showed that the conduit sizes between 16 mm and 18 mm displayed less energy loss and reduced flow stagnation while the larger conduit size displayed backflow.

Ni [131] investigated a self- powered Fontan circulation that injects energy into the right and left pulmonary artery to in order to drop the inferior vena cava pressure by 3-5 mmHg. A tightly coupled scheme at the time step level with the 3D CFD model was used in this study. A synthetic model of Fontan patients and two patients -specific geometries 10 and 24 years old were investigated with different IJS nozzle diameter and IJS placement along the Pulmonary artery. The study showed a drop in the IVC pressure and pressure and flow increase in the pulmonary system.

Pulsatile and continuous mechanical pump devices have been proposed and studied by many researchers to mainly increase the pulmonary arteries flow pressure. Delorme et al.[132] proposed a viscous impeller pump (VIP) inserted in the center of the TCPC connection. The large-eddy numerical simulation used in the study showed that the VIP: (i) does not obstruct the flow, (ii) reduces the instability and the turbulence, (iii) the VIP at high rpm (100-2000 rpm) decreased the IVC pressure.

Pekkan et al.[34] modeled three pump configurations : (i) upstream TCPC baffle (ii) downstream TCPS baffle, (iii) at the TCPC using computational fluid dynamics. The results showed the upstream pediatric ventricular device (VAD) caused a higher pressure in the IVC while the downstream VAD led to graft collapse. Moreover, the VAD in the TCPS intersection was preferred because of its simplicity and ease of use.

Shimizu et al.[133] used CFD as a tool to analyze the performance of placing a rotational pump between the IVC and the PA. The multi-scale approach results showed that the PA pressure increased while the IVC and SVC pressure decreased. However, the SVC flow was decreased.

Mackling et al.[134] reported successful implantation of a Berlin Heart EXCOR Pediatric VAD for patients who had Glenn procedure.

Rodefeled and Tsuda [135, 136] reported low IVC pressure after continuous pump implantation in sheep models mimicking the Fontan procedure.

Even though the Pediatric ventricular devices (VADs) have shown promising results, they can lead to more complications for Fontan patients: (1) increase the infection risk,(2) increase the thrombosis risk [137],(3) increase of bleeding risk because of using anticoagulation therapy [138],(4) suction and blood cavitation that can cause collapse [139, 140]

CHAPTER THREE: MATERIALS AND METHODS

3.1 The Model

There will be two models employed in this study: (a) a synthetic model representative of the HCS II, and (b) a patient-derived model obtained from de-identified MRI scan. SolidWorks (Dassault Systemes) was used to build a synthetic 3D model for a patient with dimensions gathered from X-Ray angiography images provided by the Arnold Palmer Hospital of a patient who recently underwent the procedure. The geometry includes the main pulmonary artery (MPA), branched pulmonary arteries (left=LPA, right=RPA), the descending aorta (DA), the ascending aorta (AA), right and left coronary arteries (RcorA, LcorA), right and left carotid arteries (RCA, LCA) and right and left subclavian arteries (RSA, LSA) as shown in Figure 10. Future models will be patient-specific models, and the 3D geometry is gathered through CT scans by using the medical segmentation software MIMICS as indicated in aim 3.

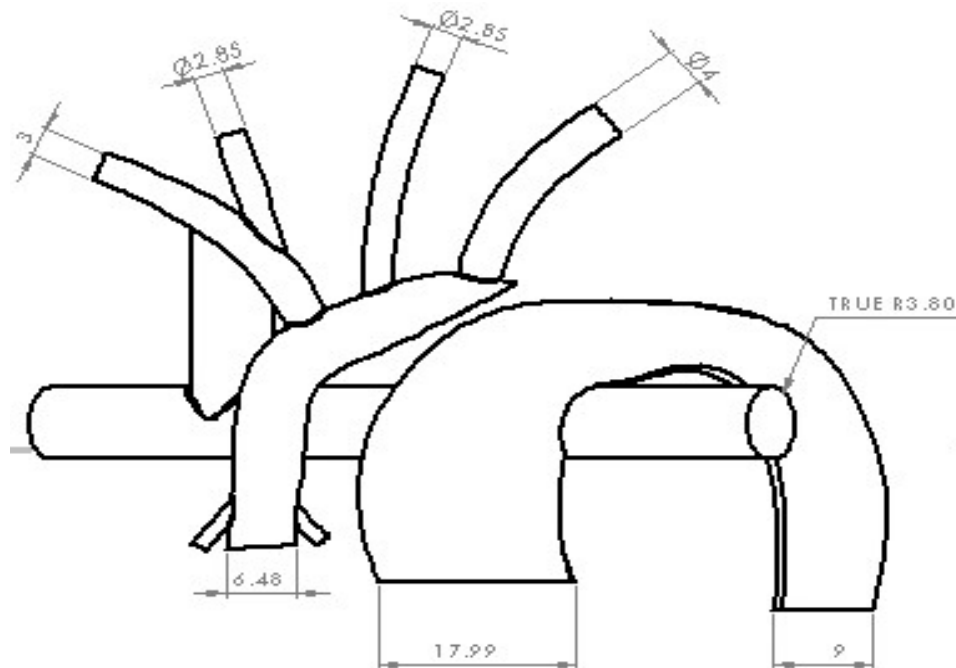


Figure 10 Dimensions of the synthetic model (in millimeters)

This 3D model will be the basis for the investigation of the detailed hemodynamics of the HCS II. However, the pulsatile boundary conditions that drive this CFD model must be provided and must be representative of the peripheral circulation. Consequently, it is common practice in a multiscale CFD analysis to utilize a reduced 0D lumped parameter model of the peripheral circulation that is either loosely or strongly coupled to the 3D CFD model for this purpose [88, 141, 142].

In order to carry out the study in aim 2, section 1.1, that targets to elucidate the relationship between the baffle narrowing and the pressure drop in the main pulmonary artery as a function of the area over the baffle as shown in Figure 11. The synthetic geometry was modified, and 5- synthetic geometries were constructed with a different area over the baffle sizes. Table 8 shows all the various narrowing measurements used in this study. Figure 12 shows the locations where the pressure was measured in this study to determine the pressure drop; more details can be found in section 4.4.

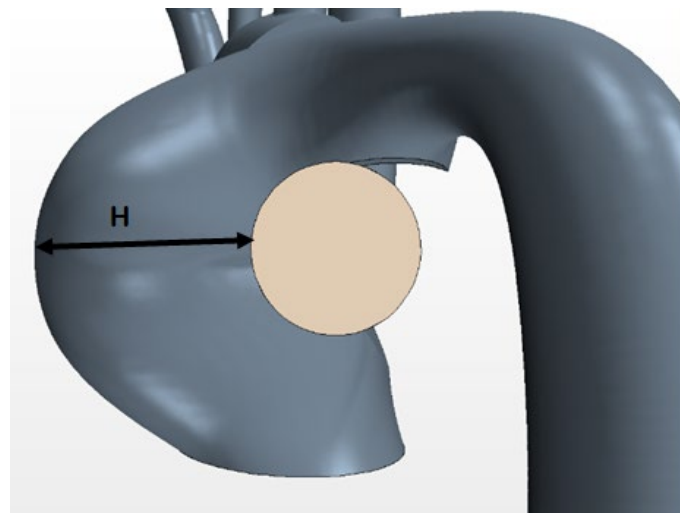


Figure 11 H represents the minimum distance between the surface of the systemic baffle surface and the outside surface of the pulmonary trunk

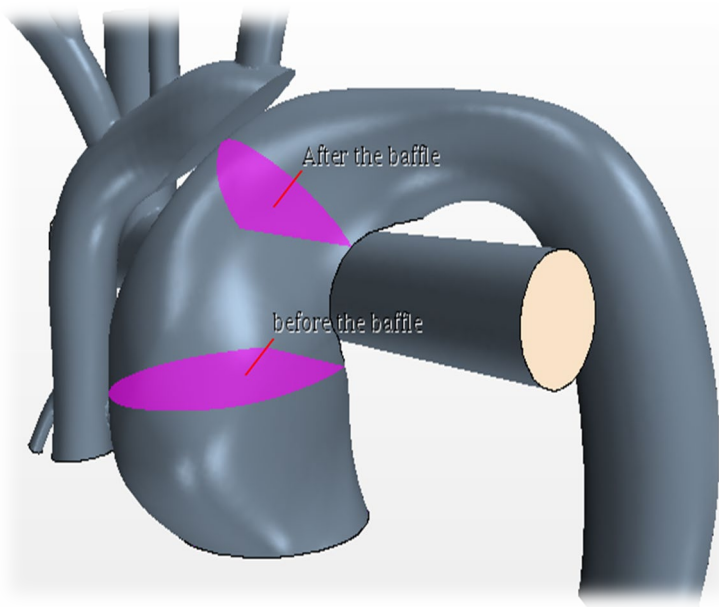


Figure 12 Locations where the pressure was measured to calculate the pressure drop.

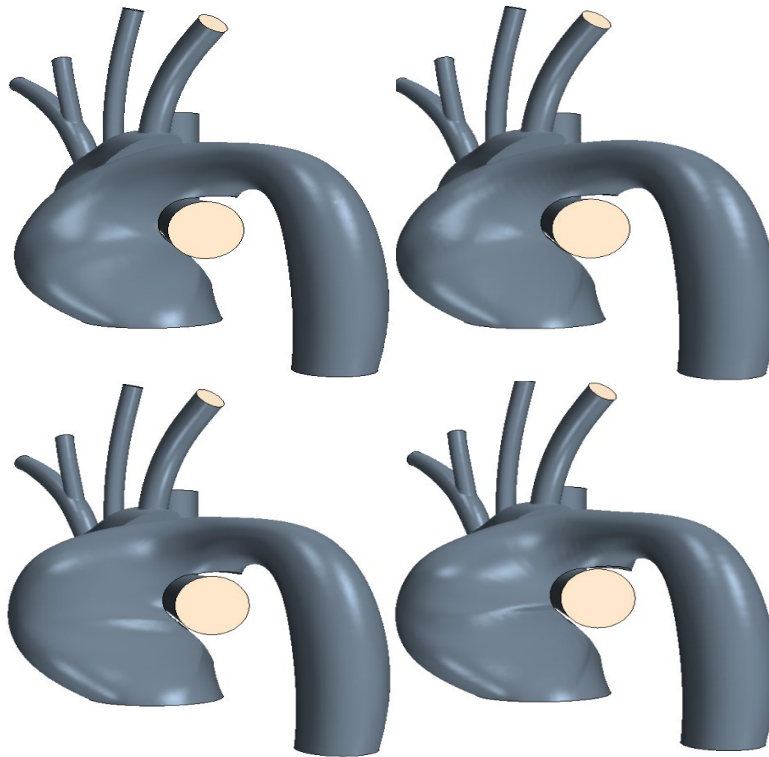


Figure 13 Synthetic model configurations : (Top Left) Nominal, (top Right) -15%,
(Bottom Left) +10%,(Bottom Right) +15%

Furthermore, one of the main goals of this dissertation is to determine the lower limits of aortic root/ascending aortic diameter that assure adequate cerebral blood flow. Therefore, different aortic root configurations were built using SolidWorks (Dassault Systemes), as shown in Figure 14, the AO diameter was manipulated with $\pm 15\%$. In this study, the oxygen delivery was calculated as a function of the aortic root size and also how the aortic diameter would affect the flow field.

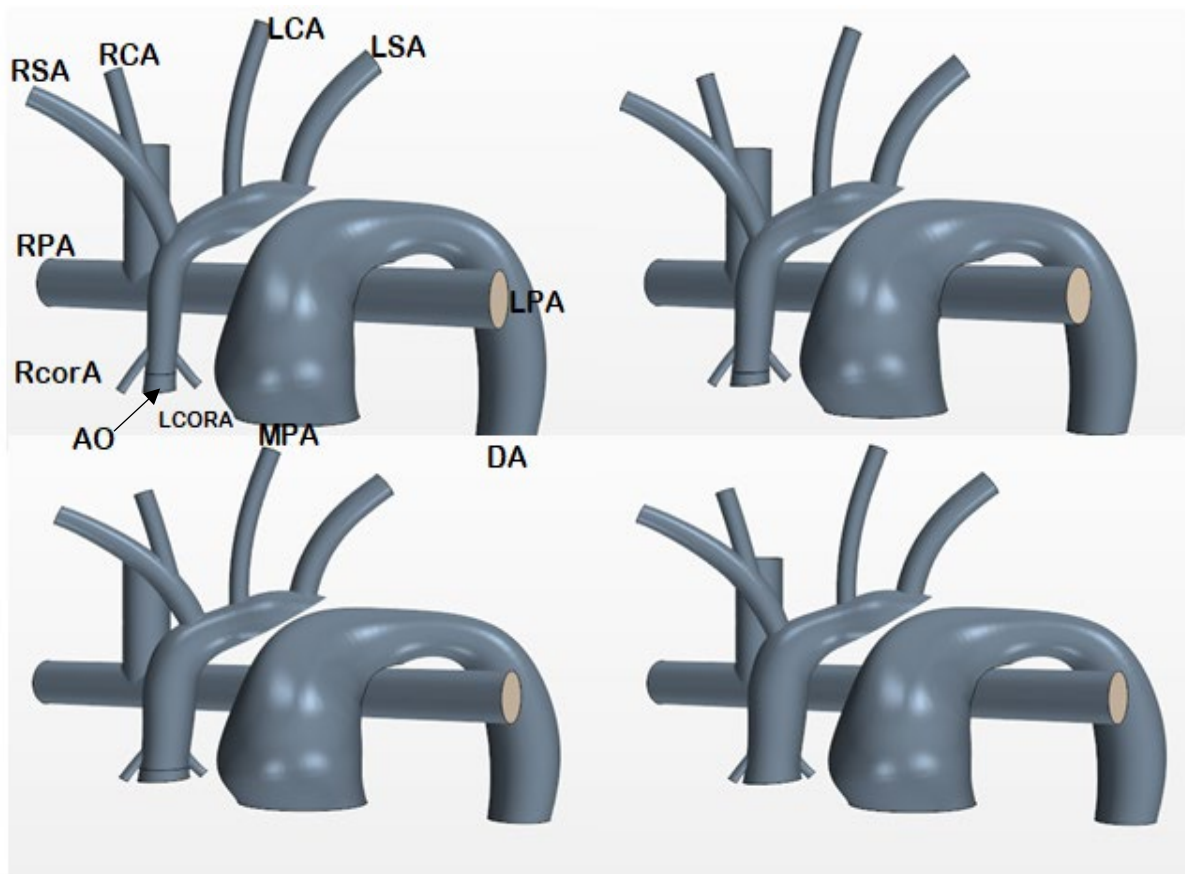


Figure 14 Different ascending aorta configurations

3.2 Patient-Specific Model

Advanced medical imaging and image processing have been developed and utilized since 1990 to stimulate blood flow [143-145]. Constructing patient-specific geometries can be done using in vivo non-invasive imaging technologies such as X-ray, ultrasound, computed tomography

(CT), and magnetic resonance imaging [146, 147]. The next step after data acquisition is to construct the area of interest using 2D or 3D segmentation. The anatomical model surface can be represented or defined using discrete techniques that approximate the model surface by triangulating it or using functions that analytically describe the geometry; an example of that method is b-spline.

Moreover, the 2D segmentation demands a high user interaction but can deal with low-quality images. On the other hand, the 3D segmentation is easier to utilize especially with high data quality[148]. Arnold Palmer Hospital provided the 2D images for a specific patient by using a Computerized Tomography (CT) scan. The 2D images were then converted to a 3D geometrical model by using the combination of two commercial software, the Materialize Interactive Medical Image Control System (MIMICS) (Materialize, Leuven, Belgium),software, which is an image processing software that was used to convert the 2D images into 3D model, and 3-Matic. The latter is built-in advanced CAD software that comes with IMICS and can be used by users to perform different operations such as remeshing, fixing and making design changes, etc. to develop the final 3D model. The final 3D model was then imported to STARCCM+ to stimulate the fluid domain in the area of interest. The patient-specific model consists of the following vessels: the main pulmonary artery, the ascending aorta, the descending aorta, the right and left coronaries, and the left and right subclavian and carotids. MIMICS did not reconstruct the ductal stent area because of the poor resolution and the contrast of the CT images. As such, a synthetic loft was created using 3-Matic to connect the main pulmonary artery and the descending aorta, as shown in Figure 15. Also, the left and right coronaries were synthetically modeled in the patient-derived geometry by using Solidworks (Dassault Systemes, Waltham, MA) for the same reasons mentioned above.

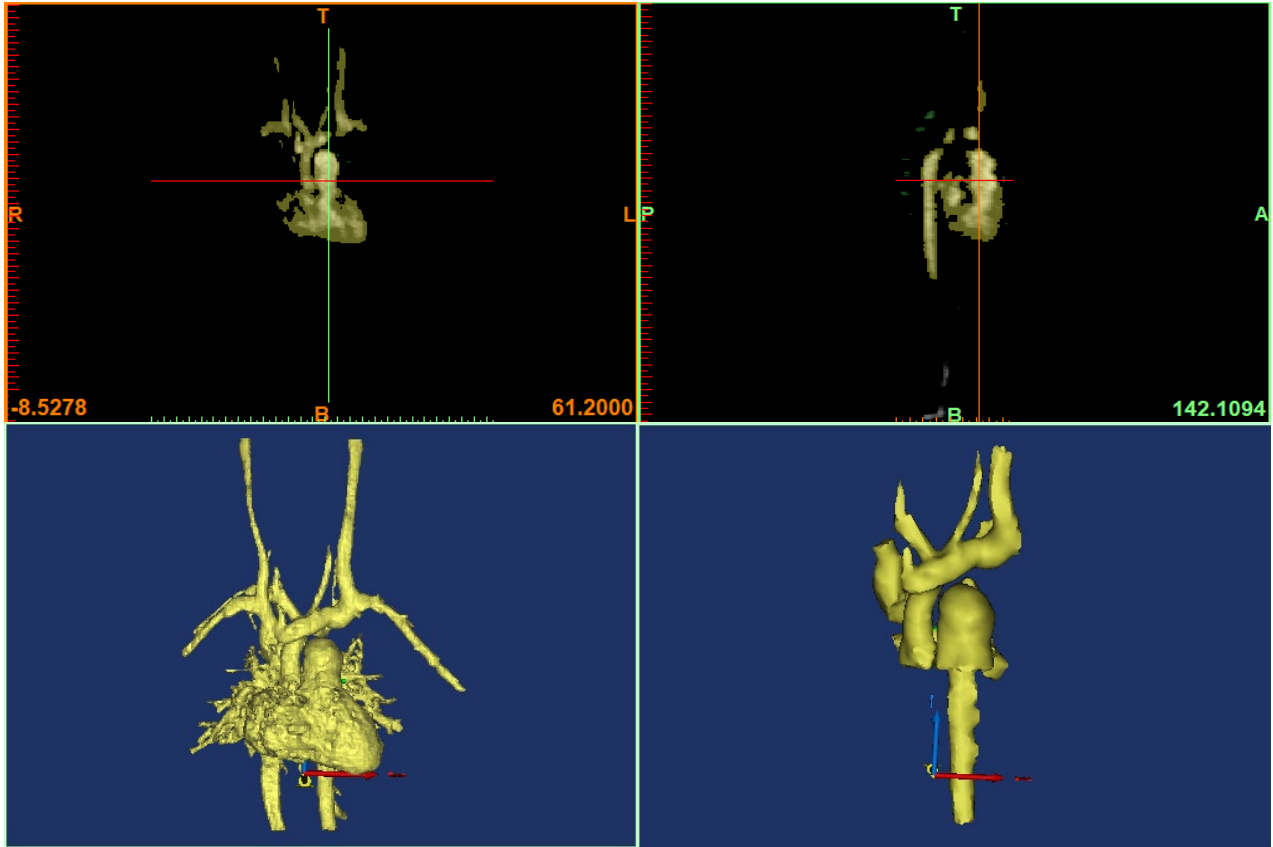


Figure 15 Three Dimensional Patient-Specific Model of a Post-Operative Hybrid Comprehensive Stage II Segmented from MRI Scan

3.3 Boundary Conditions

Boundary conditions accuracy is very important since they have a vital role in determining the dynamic results of the multi-scale simulations. Furthermore, boundary conditions type have also a big impact on the system dynamic [149, 150]. Currently, PC-MRI, ultrasound, and catheterization have made it possible to obtain very sophisticated boundary conditions such as pressure and velocity of patients specific and incorporate the clinical data in computer simulations. Moreover, numerous studies have used Lumped Parameter Models introduced by Fry and Greenfield [151] to couple the flow rate and pressure of the CFD to the LPM. The Navier-Stokes equations used to study blood flow require boundary conditions prescribed at the boundaries of

any model to be able to represent the three-dimensional motion of the flow. It is worth to mention, that it is not possible with the current technologies to model the whole human circulatory system for two reasons: (1) current imaging techniques can not characterize small vessels, which can be as small as 3.7 microns in the capillaries[149, 152, 153], (2) current hardware and software cannot computationally handle such a long circulatory system which can range between 60,000 miles and 100,000 for children and adults, respectively. Thus, only the area of interest is modeled in the 3D CFD simulation. In this study, the boundary conditions were defined at each face of CFD geometry. STARCCM+ users have the option to specify the desired boundary condition type (pressure outlet, stagnation inlet, etc.) at each inlet and outlet. In this study, the boundary conditions imposed: a stagnation inlet at the pulmonary artery (PA) and mass flow rates inlet and an outlet for the rest (SVC, RPA, LPA, RCORA, LCORA, RCA, RSA, LCA, and LSA). Arnold Palmer Hospital in Orlando provided clinical data of a patient who underwent the HCS II procedure. A sample of the catheterization data provided is shown in the table below.

Table 1 some of the catheterization data provided by Arnold Palmer Hospital.

<i>Boundaries</i>	Type	Physics Quantity
<i>Main pulmonary artery (MPA)</i>	Stagnation inlet	Pressure
<i>Ascending aorta (AO)</i>	Stagnation inlet	Pressure
<i>Descending Aorta (DA)</i>	Mass flow outlet	Mass flow
<i>Right coronary (R_Cor)</i>	Mass flow outlet	Mass flow
<i>Left coronary (L_Cor)</i>	Mass flow outlet	Mass flow
<i>Right subclavian (RSA)</i>	Mass flow outlet	Mass flow
<i>Left subclavian (LSA)</i>	Mass flow outlet	Mass flow
<i>Right carotid (RCA)</i>	Mass flow outlet	Mass flow
<i>Left carotid (LCA)</i>	Mass flow outlet	Mass flow

Table 2 Boundary conditions imposed in this study

<i>Part</i>	<i>Value</i>
HR	120 bpm
CO	2.99 l/min
Qp/Qs	0.6
R/L pulmonary flow	0.42
PA average pressure	65 mmHg
AO ascending average pressure	65 mmHg
AO descending average pressure	54 mmHg
SVC average pressure	9 mmHg
Right pulmonary artery average pressure	8 mmHg

3.4 Lumped Parameter Model

The LPM is a simplified model that has been widely used to model the part of the circulatory system outside the 3D region by many studies [29, 87, 90, 154, 155]. The Windkessel was first described by Otto Frank to represent the heart and arterial system back in 1899 [156]. The LPM can be tailored to represent any patient’s anatomy or clinical data. The HCS II circulation can be modeled using a multi-degree of freedom Windkessel, which is used to describe the heart pumping load through the systemic or pulmonary flow and the relation between the blood pressure and flow. The LPM is an electrical analog of the circulatory system [87] that models viscous drag as a resistor (R), vessel compliance as a capacitor (C), flow inertia as an inductor (L), and valves as diodes. The HCS II circulation is divided into multi coupled beds for simplicity, and these beds are known

as a multi-degree of freedom Windkessel models. Each bed consists of resistors capacitors and inductors, which can be time-dependent [40]. The HCSII model consists of 5 subsystems: the right ventricle, the upper circulation, the lower circulation, the coronaries, and the pulmonary circulation. The systemic circulation consists of 7 arterial compartments, the pulmonary circulation has four compartments, and the coronary circulation is divided into 4 compartments. The lumped parameter model (LPM) is used to produce the waveforms for the boundary conditions and to determine the cardiovascular output of the system as well as the pressures and flow rates at every node in the circuit.

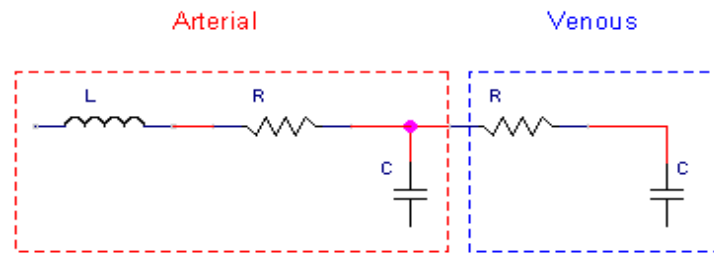


Figure 16 RLC representation for atrial and venous beds.

As shown in Figure 16, the resistance, R [mmHg-s/ml], stimulates the resistance the blood encounter as it flows through the blood vessels, and it depends on the length and the cross-section area. The capacitor, C [ml/mmHg], accounts for the dynamic vascular compliance (expanding and contracting), and the inductor, L [mmHg s^2 /ml] to account for the inertial effect of the flow. Finally, a diode is utilized to model the heart valves to ensure unidirectional flow from the heart. In some parts of the circulatory system where small capillaries and vessels present, capacitors or inductors can be ignored because other forces have a stronger influence. That would simplify the calculations and reduce the computation cost. On the other hand, the resistors cannot be neglected for small vessels as it depends on the vessel geometry and the friction losses. Figure 14 shows the hydraulic analogy.

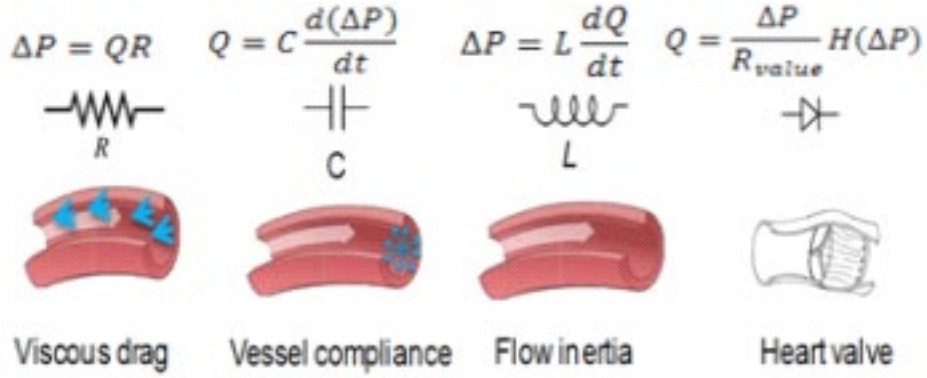


Figure 17 Hydraulic Analogy

To mimic the heart function, a time-varying capacitor that acts as a pumping heart is introduced to provide a pulsatile cardiac output, as shown in Figure 15. The elastance function $E_n(t_n)$, which relates the pressure and volume of the cardiac cycle, is the inverse of the capacitance. Based on previous studies [157, 158], the “double hill” elastance function is

$$E(t) = (E_{max} - E_{min})E_n(t_n) + E_{min} \quad (1)$$

$$E_n(t_n) = \left[\frac{\left(\frac{t_n}{0.303}\right)^{1.32}}{1 + \left(\frac{t_n}{0.303}\right)^{1.32}} \right] \left[\frac{1}{1 + \left(\frac{t_n}{0.508}\right)^{121.9}} \right] \quad (2)$$

$$t_n = \frac{t}{t_c} \dots t_c = \frac{60}{HR} \dots HR = \text{Heart Rate} \quad (3)$$

Where (E_{max}) and (E_{min}) represent the end-systolic pressure-volume relationship and the end-diastolic pressure-volume relationship, respectively. t_n is the normalized time by a time constant t_c .

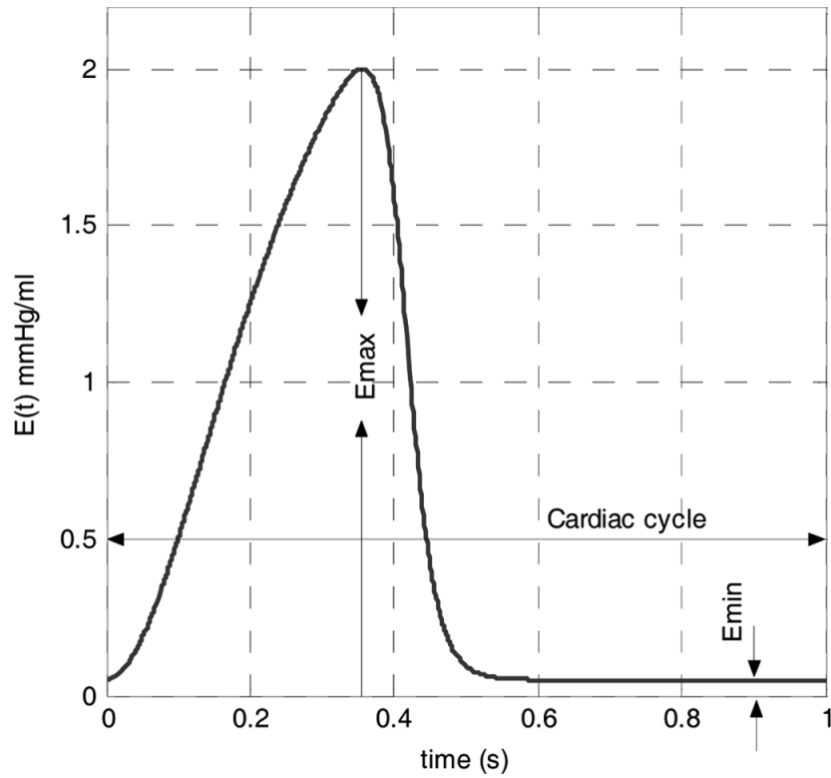


Figure 18 Elastance function waveform

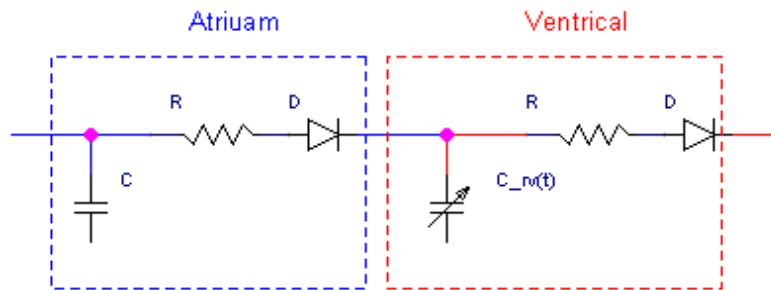


Figure 19 Heart Chambers Electrical Bed

The LPM is a closed system, which means all beds interact with each other, and to obtain the differential equations of the HCS II circulatory system, Kirchhoff node and loop laws (Equations 4, 5) were used along with the hydraulic analogies. Kirchhoff laws state that the current entering a junction or a node is equal to the current exit it, and the sum of voltages in a closed-loop has to be zero.

$$y_{i-1} = C \frac{dy_i}{dt} + y_{i+1} \rightarrow \frac{dy_i}{dt} = \frac{1}{C} [y_{i-1} - y_{i+1}] \quad (4)$$

$$y_i = y_{i+2} + R y_{i+1} + L \frac{dy_{i+1}}{dt} \rightarrow \frac{dy_{i+1}}{dt} = \frac{1}{L} [y_i - R y_{i+1} - y_{i+2}] \quad (5)$$

Both the voltage (pressure) and the current (mass flowrate) were labeled ‘y’ for consistency. Equations 4 and 5 can be applied to obtain the rest of the ODEs equations that represent the circulatory system.

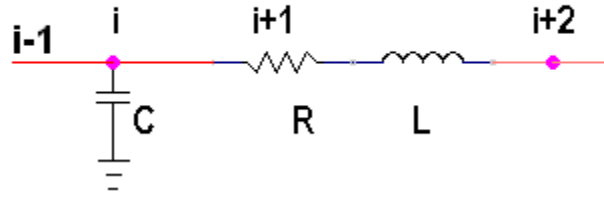


Figure 20 Schematic relate equations 4 and 5 to calculate y

Based on Figure 20, the current flows in from the left side and charges the capacitor first. Then the current will experience a drop in voltage at the resistor and at the inductor due to current change. The pressure drop is given by $\Delta P = l \frac{dQ}{dt} + RQ$ and the flow rate across compliance is $Q = C \frac{dP}{dt}$ and by applying Kirchhoff loop and node laws for the heart, the systemic system, the pulmonary system, and the coronary system, we were able to represent the circuit as a set of ODE.

$$\Delta p = L \frac{dQ}{dt} + RQ \quad (6)$$

$$Q = C \frac{d(\Delta p)}{dt} \quad (7)$$

$$C = \frac{dV}{dp} \quad (8)$$

Where Q is the flow-rate, Δp is the pressure difference, and V is the volume. The result of performing this equilibrium equation at each node a system of coupled 34 ordinary differential equations that are solved using 4th order adaptive Runge-Kutta methods. The solver requires besides the ODEs, initial conditions for each pressure and flow rate equation, error tolerance, and the number of time steps to produce the desired number of heart cycles that can be used as BCs for the CFD solver. Mathcad (2015 PTC Inc.MA, USA) was used first to tune and validate the model, and then the C++ programming language was utilized since it executes computations considerably faster. The baseline values of R, L, and C are tuned to obtain the desired waveforms. Bed resistance values usually are tuned first as it the primary control of the total flow in any vessel. Then compliance and inductance values were tuned to obtain the desired waveforms [87, 112, 113]. In total, 12 BCs were generated from the C++ code, and then as mentioned earlier, the waveforms obtained are compared with the waveforms we received from Arnold Palmer hospital for the post-operative patient for validation. In summary, the 3-D problem of modeling the whole circulation system of HCS II patient was reduced to a 34 degree of freedom (DOF) 0-D problem that can be used to represent any patient underwent HCS II.

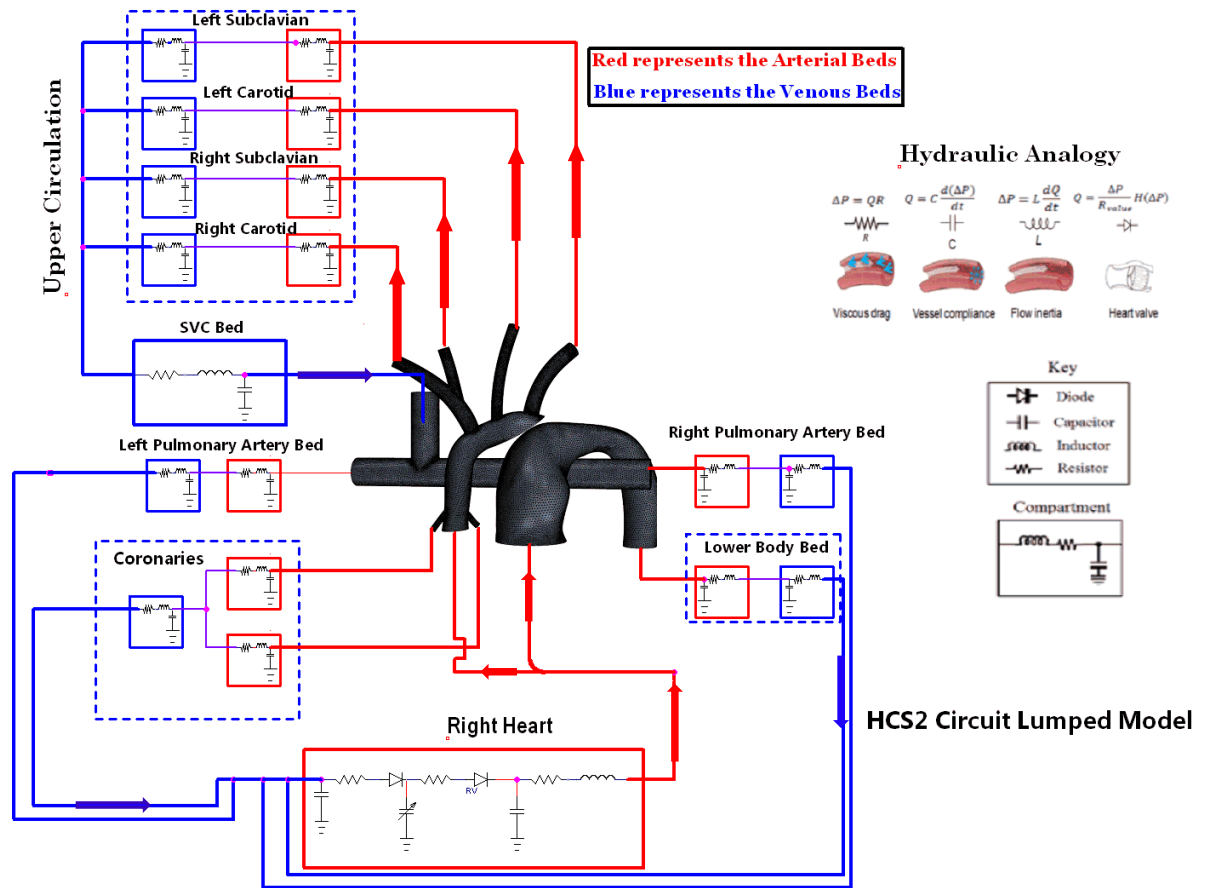


Figure 21 Multiscale model of the HCS II circulation, three-dimensional CFD model, coupled with the lumped parameter model

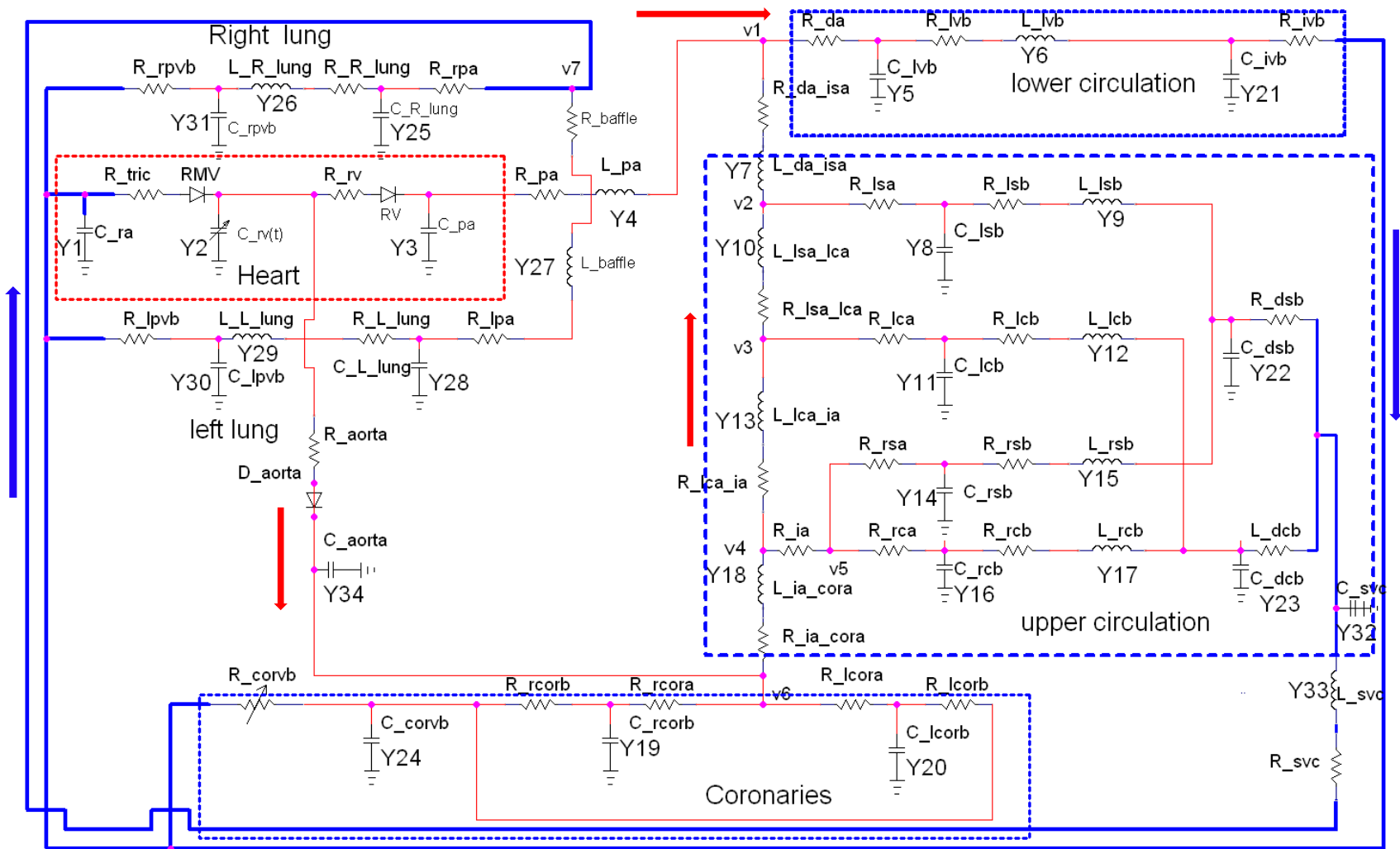


Figure 22 Detailed LPM schematic.

The target for the cardiac output is 2.99 L/min, 60% of which goes to the lower body through the pulmonary trunk, and 40 % flows through the ascending aorta to provide blood to the upper body. The average target pressure for the right ventricle, aortic root, descending aorta, superior vena cava, and left and right pulmonary artery were 65, 65, 54, 9, and 8 mmHg, respectively.

In the LPM, two non-linear resistance models are now discussed. The first is the coronary bed resistance model adapted from [74, 88]. The coronaries supply the myocardium with oxygen-rich blood, and then the cardiac veins return the deoxygenated blood to the right atrium. The coronaries experience high pressure from the ventricle when contracting (systole). As a result, most of the blood perfusion through the coronaries takes place during diastole. The coronaries can be modeled based on the elastance function in the LPM to capture the flow during diastole.

$$R_{cora}(t) = \left[1.75 * \left(\frac{E_{lv}(t)}{E_{lv}(0)} \right)^2 + 6.796 \right] * R_{fact_cor} \quad (9)$$

Where R_{fact_cor} can be used to tune the model.

3.4.1 Ventricular Septal Defect

The second resistance modeled in this problem is the non-linear resistance across the ventricular septal defect (VSD) that appears in the circuit Figure 22 between the inlet to the pulmonary trunk and the inlet to the ascending aorta. The VSD doesn't appear in the CFD domain, but it is represented in the LPM, where R_{aorta} expresses a flow-dependent non-linear resistance, typical of an orifice.

From the Bernoulli equation, it is simple to obtain a relationship for the mass flow rate across the orifice as

$$\dot{m} = \frac{\dot{K} A_{VSD}}{\sqrt{1 - \beta^4}} \sqrt{2\rho \Delta P_{VSD}} \quad (10)$$

where β is the diameter ratio of the orifice and the right ventricle diameter, and κ is a loss coefficient, A_{VSD} and ΔP_{VSD} are the area of the orifice and the pressure difference across the defect [159]

$$K = 0.5959 + 0.0312\beta^{1.2} - 0.184\beta^8 + \frac{91.71\beta^{2.5}}{Re_{DV}^{0.75}} \quad (11)$$

with Re_{D_1} The Reynold number based on the right ventricle nominal diameter. Moreover, by observing a magnitude β to be less than one, K equation can be simplified to $\kappa=0.5959$.

The pressure drop across the circulatory circuit segment containing the septal defect can be represented by $\Delta P(t) = C\dot{Q}(t)^2$ which leads to a nonlinear resistance in terms of volumetric flow rate $R(\dot{Q}) = C\dot{Q}(t)$ [29, 110, 160-162]. Equation 10 can be rewritten to determine an expression for resistance to be included in the LPM equations as

$$R_{VSD}(\dot{Q}) = \frac{\dot{Q}\rho}{266.64(1000^2 K A_{VSD})^2} \quad (12)$$

The flow rate equation (12) can be more simplified. In addition to this resistance, we add a linear resistor to represent a portion of the aortic root in conjunction with the atrophied left ventricle traversed by the flow.

$$R_{aorta}(Q) = R_{VSD} + \frac{Q}{266.64 (1000^2 k A_{VSD})^2} \quad (13)$$

Where, R_{VSD} is a linear resistor that can be tuned to obtain the right flow and pressure.

3.5 Coupling

The principle behind the coupling scheme between the 0D lumped parameter model and the 3D computational fluid dynamics (CFD) model is to take the whole circulatory system into account when evaluating a hemodynamic of a specific region. CFD coupled with Lumped Parameter Models (LPM) has been utilized to tackle numerous hemodynamic circulations. Quarteroni [163, 164] derived a method to solve these multi-scale models using a mathematical model. This model followed an iterative structure which had the lumped parameter model leading the CFD in time. Moreover, Quarteroni and his team focused on the Neumann boundary condition setup, in which the calculated pressures are transferred over to the CFD on all outlets and inlets.

Esmaily-Moghadam [165] goes even further by incorporating more coupling boundary conditions such as the Dirichlet, Neumann, and mixed. In the Dirichlet approach, mass flows are applied to all the outlets and inlets in the CFD model. Whereas the mixed approach applies pressure as well as mass flows to the outlets and inlets. As a result of the assumptions made to the velocity profile, the Dirichlet approach loses information. However, it is the least computationally costly of the two. By modeling the LPM to receive pressures at inductors and flows at capacitors, they were able to achieve interface stability.

Different coupling boundary condition schemes (Dirichlet, Neumann, and mixed) can be implemented, as mentioned earlier, between the 3D CFD and the 0D LPM to achieve convergence. The Neumann approach feeds pressure to the LPM while the Dirichlet transfer mass flows to all the CFD boundaries. The mixed approach refers to feeding pressure and flows to the LPM for the same model [165]. The interaction (coupling) in this study between the CFD and the LPM was at the heart cycle level “Loose coupling,” which was utilized in previous studies [73, 74]. The process starts by first constructing and then tuning the nominal LPM to obtain the clinical waveforms of

pressure and flow provided by Arnold Palmer Hospital. A converged solution using the loose coupling can be achieved by (1) tuning the HCS II circuit to obtain the desired boundary conditions waveforms for an HCS II patients, (2) impose stagnation pressure for the inlet boundaries and flow rate for the outlets (SVC,RPA,LPA,RCORA,LCORA,LAS,LCA,RCA,RSA and DA) using the initial tuned data from the LPM, (3) run the CFD for a complete 3-heart cycles to obtain flow solution, (4) update the CFD resistance for the area of interest within the LPM (5) Impose the new boundary conditions values after running the LPM, (6) keep iterating until a converged solution is obtained . Updating the resistance for the area of interest can be done by measuring pressure and mass flow rate at each section of the geometry in corresponding to the 0D circuit nodes and segments. The surface averaged mass flow and pressure are then time-averaged over the cycle. Furthermore, the obtained results are used to update the resistance based on Ohm's law. Finally, the new flow and pressure boundaries are imposed on the CFD solver after the LPM converges. The user carries on this process, which usually takes about 15-20 runs to achieve convergence. The coupling steps can be automated by using a java macro that handles feeding the BCs to the CFD solver and returns the new updated resistance values to the RK solver. The convergence criteria are set so that the change in the flow in all branches is less than 10^{-3} or resistor values no longer change across when iterate. Usually, the CFD is run for three more cycles after convergence achieves a sustained periodic solution and then post-processing starts.

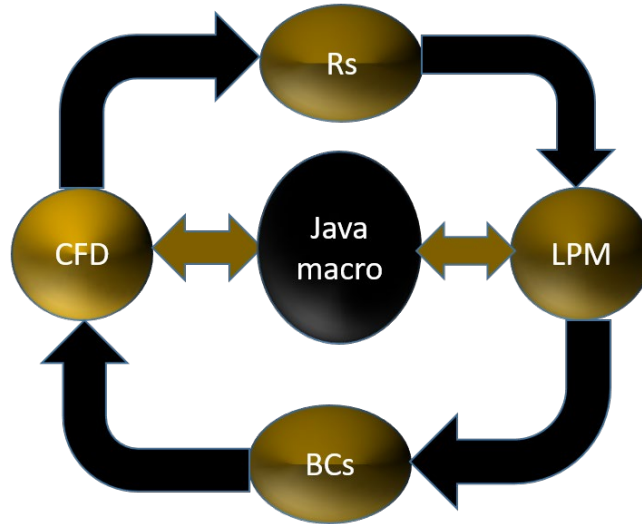


Figure 23 Coupling scheme

3.6 Discretization

The next step, after importing the geometry to the CFD solver, is to divide the computational domain into small finite elements or cells, i.e., mesh. Discretization in most CFD software is automated, but manual refinement is needed for complicated geometries.

Moreover, different mesh methods are available: finite volume method, finite element method, finite difference method, and meshless method and the mesh technique used in any study depends on the CFD software. A high-quality mesh was generated using tetrahedral elements, which is considered more practical for complex geometries[166], with a base size of 0.3 mm along with 3-prism layers near walls to capture the boundary layer flow. STAR-CCM+ (Siemens), which is a commercial computational fluid dynamic solver was used in this study, allows users to control prism layer can be by: (1) layer total thickness, (2) number of prism layers, (3) layer stretching. Customization and refinement of the mesh were used in this study because the model has a different range of diameters as well as non-uniform vessels, specifically the area over the baffle. The customized tool allows users, for example, to control the number of are generated in a

specified area or change the base size. The number of cells varied between 1.5 and 2.3 million depending on the anatomy, as shown in Table 5.

Mesh independence study was carried out to find the required mesh density for the solution to converge by measuring the changes in the computational results of the fine and the finer grids. That was done by running the simulation in a steady-state and monitor the pressure at the inlets and the flow rate at the outlets. In this study, 3-different levels of refinement carried out, and percentage errors were evaluated. The mass flow rate and the pressure were calculated at different locations (RPA root, SVC, RPA, DA, AO, and LPA). Table 3 and Table 4 show the flow rate and pressure at a different location with different mesh refinement. The +20% model percentage errors were ranging between 0.0 -0.15 % for the majority of the quantities evaluated.

Table 3 Mesh independent study

Cell count	Case 1 (Baseline)	Fine (+20%)	Coarse (- 20%)	Percentage change	
	1344341	1604514	1079184	Fine	Coarse
PA root flowrate [Kg/s]	0.0226	0.0226	0.0226	0.0	0.0
SVC flowrate [Kg/s]	0.01566	0.01566	0.01566	0.0	0.0
RPA flowrate [Kg/s]	0.00716	0.00715	0.00715	0.14	0.14
DA flowrate [Kg/s]	0.0144	0.0144	0.0144	0.0	0.0
LCA flowrate [Kg/s]	0.00407	0.0407	0.0406	0.0	0.25
Aorta flowrate [Kg/s]	0.009119	0.00911	0.009114	0.099	0.055
LPA flowrate [Kg/s]	0.0085	0.0085	0.00851	0.0	0.12

Table 4 Mesh independent study

Cell count	Case 1 (Baseline)	Fine (+20%)	Coarse (- 20%)	Percentage change	
	1344341	1604514	1079184	Fine	Coarse
PA root pressure [Pa]	9368	9368	9368	0.0	0.0
SVC pressure [Pa]	25	26	16	4.0	36.0
RPA pressure [Pa]	14	14	5	0.0	64.29
DA pressure [Pa]	8571	8558	8575	0.15	0.047
LCA pressure [Pa]	5253	5001	5455	4.80	3.85
Aorta pressure [Pa]	5950	5708	6150	4.07	3.36
LPA pressure [Pa]	-22	-22	-30	0.0	36.36

As can be seen in the table above, the flow and pressure analysis for the baseline case and the +20%, which has a finer mesh, are consistent.

One of this study's aims was to investigate the pressure drop across the baffle by varying the area over the baffle. Another aim was to determine the limits of the aorta diameters that assure adequate cerebral blood flow. Table 5 shows the number of cells of three different geometries used in this study as the area over the baffle increases, and as the aortic root diameter increases.

Table 5 (Left) number of cells for models as the area over the baffle increases, (Right) as the aorta size increases

Model	Cells Count (million)		Model	Cells Count (million)
Case1	2.1		Case1	2.3
Case2	2.3		Case2	2.7
Case3	2.5		Case3	2.8

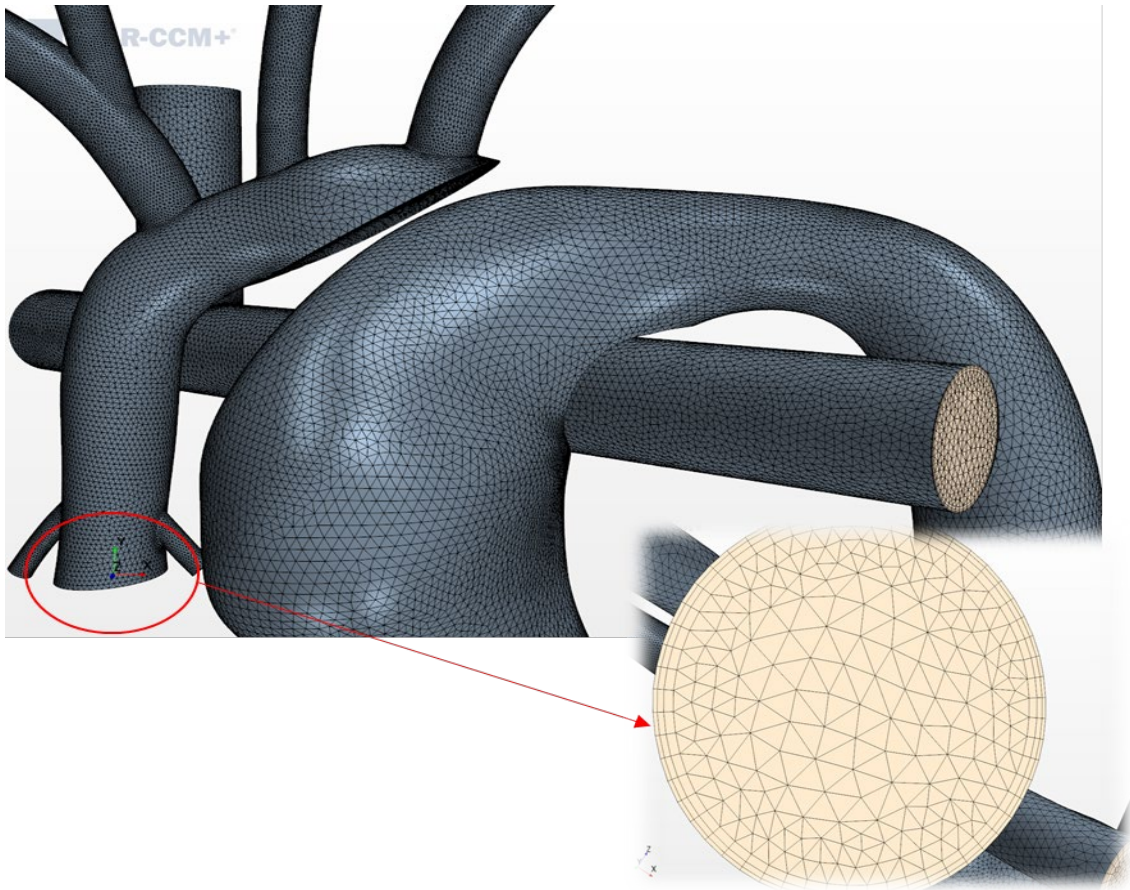


Figure 24 (Left) Meshed geometry, (Right) meshed ascending aorta inlet

3.7 Computational Fluid Dynamics (CFD)

The patient-specific model constructed from CT scan image and the synthetic models built in SolidWorks is imported into StarCCM+, which is a commercial finite volume multi-scale computational fluid dynamics solver developed by SIEMENS. StarCCM+ is used to solve numerically the continuity equation and Navier-Stokes equations, which describes the blood motion in the three spatial dimensions.

$$\nabla \cdot \vec{V} = 0 \quad (15)$$

$$\rho \frac{\partial \vec{V}}{\partial t} + \rho (\vec{V} \cdot \nabla) \vec{V} = -\nabla p + \nabla \cdot \underline{\underline{\sigma}} \quad (14)$$

Where, \vec{V} is the velocity, $\underline{\underline{\sigma}}$ is the viscous stress tensor, and p is the pressure.

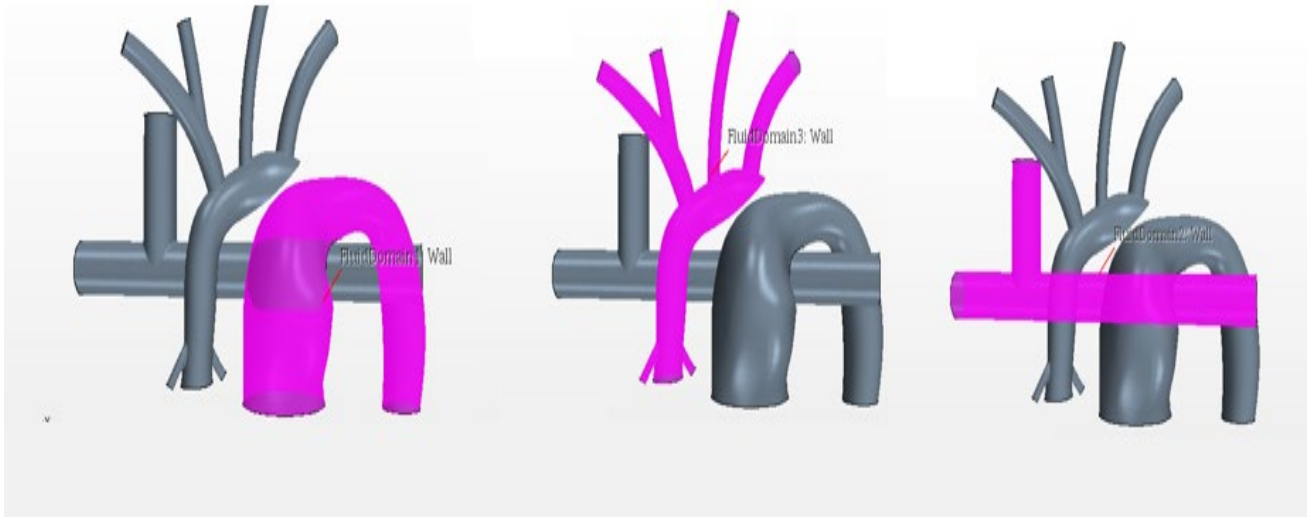


Figure 25 Three separate fluid regions, Systemic flow (left) and Pulmonary flow (middle) and Aortic flow (right) with 100% stenosis

This study assumes:

1. The space is three dimensional.
2. Laminar flow
3. Incompressible fluid
4. Rigid walls
5. Non-Newtonian
6. For completeness, the gravity force is considered.

The blood was considered as a non-Newtonian shear-thinning fluid, where the viscosity is inversely proportional to the shear rates. Hematocrit, which is the ratio of red blood cells to the total volume of the blood, controls the blood viscosity, as shown in Figure 26.

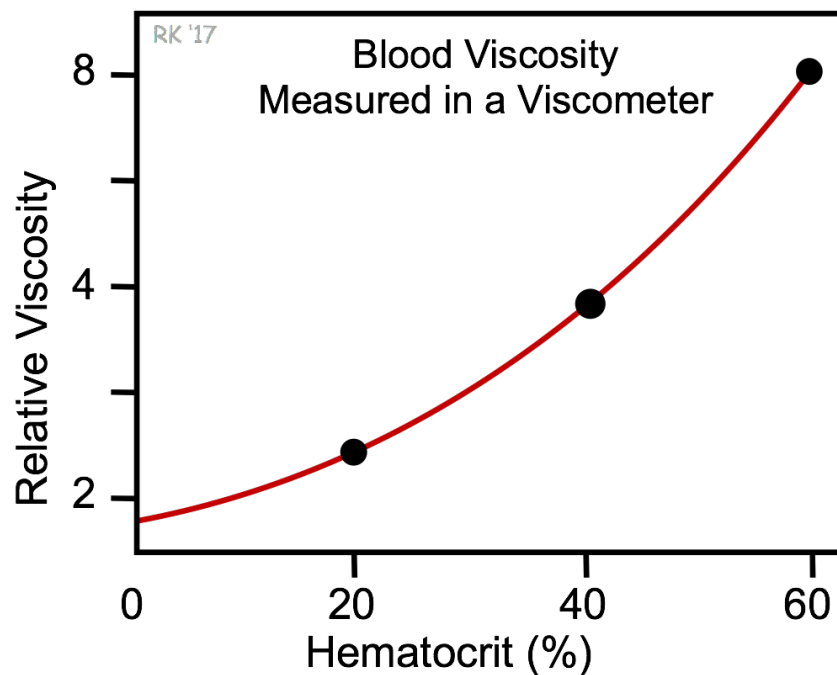


Figure 26 Relationship between hematocrit and viscosity [167]

The Carreau-Yasuda model was used in this numerical study to specify the non-Newtonian behavior of the blood.

$$\mu(\dot{\gamma}) = \mu_{\infty} + (\mu_o - \mu_{\infty}) \frac{1}{[1 + (\lambda\dot{\gamma})^2]^{\frac{1}{3}}} \quad (16)$$

Where μ_o is the zero-shear viscosity, μ_{∞} is the infinite-shear viscosity, λ is the relaxation time constant and $\dot{\gamma}$ is the shear rate. Using this model, the viscous stress tensor is expressed as

$$\underline{\underline{\sigma}} = \mu(\dot{\gamma}) [\nabla\vec{V} + \nabla\vec{V}^T] \quad (17)$$

Table 6 shows model constants for different hematocrit levels (20%, 40%, and 60%) which were obtained by curve fitting clinical data [168]

Table 6 Tabulated value for Carreau-Yasuda model constants

Hematocrit [%]	μ_{∞} [cP]	μ_o [cP]	λ [s]
20	2.7459	3.5832	-2.783
40	4.3989	8.4248	0.3103
60	7.0151	19.8035	0.2646

The governing equations were solved in StarCCM+ using the unsteady implicit solver with a second-order time discretization and second-order upwinding of the convective derivatives. The boundary conditions imposed: a stagnation inlet at the pulmonary artery (PA) and mass flow rates inlet and an outlet for the rest (SVC, RPA, LPA, RCORA, LCORA, RCA, RSA, LCA, and LSA). All the boundary conditions are calculated using the 0D lumped parameter model. The wall was modeled as a rigid and non-permeable wall for simplicity and computation cost reduction. Moreover, the segregated solver was chosen in this study to solve the mass equation and the

momentum equations subsequently, and as mentioned earlier, the second-order upwinding scheme was used to discretize the momentum convection terms. Furthermore, the time step used in this simulation is 0.005 seconds based on calculating the Courant number, which should be about one to obtain time-accurate solutions. The Courant number was calculated from equation (18).

$$Courant\ Number = \frac{u\Delta t}{\Delta x} \quad (18)$$

Where $u = velocity$, $\Delta t = time\ step$ and $\Delta x = mesh\ size$.

Based on the volumetric flow rate, we calculated the flow velocity. Then by back-calculation, the time step based on mesh size used to discretize the geometry. All the computations were performed using Caesar, Newton, and Stokes computer clusters at the University of Central Florida.

After imposing the initial BCs from the LPM, the CFD solver will run until reaching the physical time set by the user (1.5 seconds in this case). Then, the mass flow rate and pressure are calculated and time-averaged to determine the new resistance by

$$R = \frac{P_i - P_{i+1}}{\dot{m}_i} \quad (19)$$

The above equation is applied to all the cross-sections shown in Figure 27, which each represents a node in the 0D lumped parameter model. The coupling scheme as explained in section 3.5, will be carried out using the newly calculated resistance to run the LPM and update the CFD BCs until a converged solution obtained.

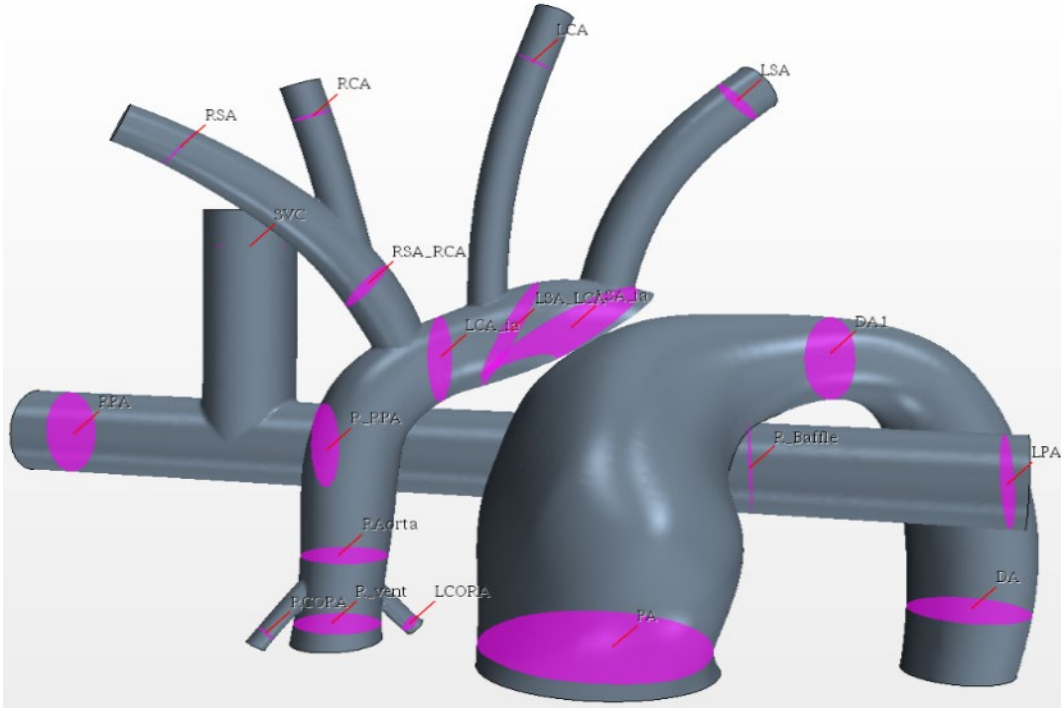


Figure 27 Fluid domain locations to calculate flow rate and pressure

3.8 Oxygen Transport Model

Based on the oxygen consumption in the systemic circulation, the oxygen uptake in the pulmonary circulation, and conservation equations, the oxygen model equations were derived for the HCS II procedure. The major parameter that affects the oxygen content is the flow split between the systemic and the pulmonary flow. In the HCS II model, the right ventricle flow is distributed to the lower body circulation and the upper body circulation. The venous blood from the lower circulation flows back through the inferior vena cava (IVC) to the right atrium while the upper body deoxygenated blood flows back to the pulmonary arteries through the superior vena cava (SVC) and that leads to two parallel flows as shown in Figure 28.

With reference to Figure 28 that shows the circulation model of HCS II, the oxygen transport equations were derived as follows

$$C\dot{V}_{O_2} = x C\dot{V}_{O_2} + (1 - x)C\dot{V}_{O_2} \quad (20)$$

The upper and lower body splits the oxygen consumed in every cardiac cycle, and x represents the oxygen portion the upper body consumes ($x C\dot{V}_{O_2}$) as shown in equation (20)

$$C_{SO_2} * Q_U - x C\dot{V}_{O_2} + S\dot{V}_{O_2} = C_{SV_{O_2}} * Q_U \quad (21)$$

Equation (21) states that the upper circulation venous oxygen flow rate ($C_{SV_{O_2}} * Q_U$) returning to the heart from the lungs is equal to the oxygen flow rate into the upper systemic circulation ($C_{SO_2} * Q_U$) plus the oxygen uptake in the lungs reduced by the oxygen consumed by the upper body ($x C\dot{V}_{O_2}$).

$$C_{SO_2} * Q_L - (1 - x)C\dot{V}_{O_2} = C_{SV_{O_2}} * Q_L \quad (22)$$

For the lower body circulation, equation (22) states that the product of subtracting the oxygen consumed by the lower body ($(1 - x)C\dot{V}_{O_2}$) from the systemic oxygen flow rate into the lower body ($C_{SO_2} * Q_L$) is equal to the oxygen flow rate returning to the heart from the lower circulation ($C_{SV_{O_2}} * Q_L$).

The relation between the upper and lower circulation to the cardiac output of the systems is shown in equation (23)

$$Q_U + Q_L = CO \quad (23)$$

Equation (23) states that according to the mass conservation law, the oxygen uptake in the lungs is equal to the oxygen consumed by the body.

$$S\dot{V}_{O_2} = x C\dot{V}_{O_2} + (1 - x) C\dot{V}_{O_2} \quad (24)$$

From equation (22)

$$C_{S_{O_2}} = \frac{C_{S_{V_{O_2}}} * Q_L + (1 - x) C\dot{V}_{O_2}}{Q_L} \quad (25)$$

and by replacing $C_{S_{O_2}}$ in (21) we obtain

$$C_{S_{V_{O_2}}} = \frac{C_{P_{V_{O_2}}} * Q_U - \frac{Q_U}{Q_L} (1 - x) C\dot{V}_{O_2} + x C\dot{V}_{O_2} - S\dot{V}_{O_2}}{Q_U} \quad (26)$$

From (23) and (24) and (26)

$$C_{S_{O_2}} * CO = C_{P_{V_{O_2}}} * CO + \left(\frac{Q_L}{Q_U} + 1\right)x C\dot{V}_{O_2} - \left(\frac{Q_L}{Q_U} + 1\right)S\dot{V}_{O_2} \quad (27)$$

$$C_{S_{O_2}} * CO = C_{P_{V_{O_2}}} * CO - \left(\frac{Q_L}{Q_U} + 1\right)(1 - x)C\dot{V}_{O_2} \quad (28)$$

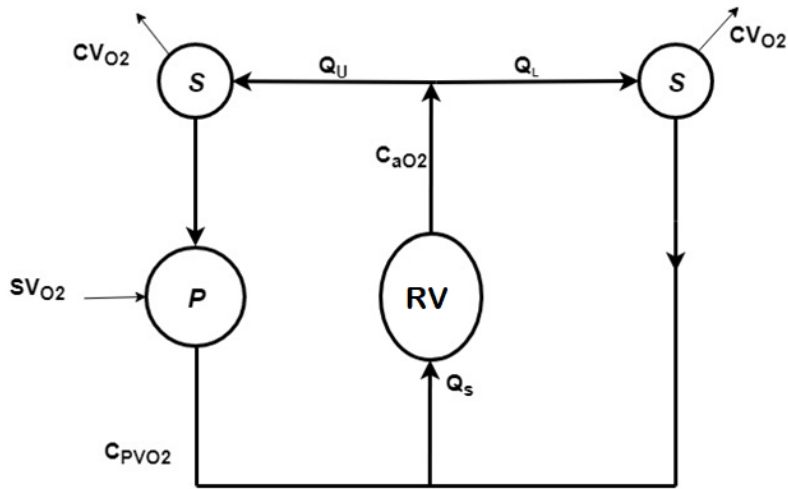


Figure 28 Oxygen transport model for HCS II

Another oxygen model was constructed for the HCS II, but in this case, the split ratio between the upper and lower circulation was ignored.

In this case, the same analysis used with the first model was utilized to derive the oxygen model equations as follows

$$C_{SO_2} * CO - C\dot{V}_{O_2} = C_{SV_{O_2}} * Q_U + C_{SV_{O_2}} * Q_L \quad (29)$$

Equation (29) states that the systemic oxygen flow into the body ($C_{SO_2} * CO$) is reduced by the whole body consumption ($C\dot{V}_{O_2}$) leaving the returned oxygen flow to the heart.

$$C_{SV_{O_2}} * Q_U + S\dot{V}_{O_2} = C_{PV_{O_2}} * Q_U \quad (30)$$

Equation (30) states that the sum of the oxygen uptake in the lungs ($S\dot{V}_{O_2}$) $S\dot{V}_{O_2}$ for our model and the oxygen flow rate into the pulmonary circulation ($C_{PV_{O_2}} * Q_U$) gives the oxygen flow rate into the pulmonary veins.

$$S\dot{V}_{O_2} = C\dot{V}_{O_2} \quad (31)$$

$$Q_U + Q_L = CO \quad (32)$$

From equation (30)

$$C_{SV_{O_2}} = \frac{C_{PV_{O_2}} * Q_U - S\dot{V}_{O_2}}{Q_U} \quad (33)$$

By substitute $C_{SV_{O_2}}$ in equation (29) and using equation (30) and (31)

$$C_{SO_2} * CO = CO * C_{PV_{O_2}} - \frac{1}{\frac{Q_U}{Q_L}} C\dot{V}_{O_2} \quad (34)$$

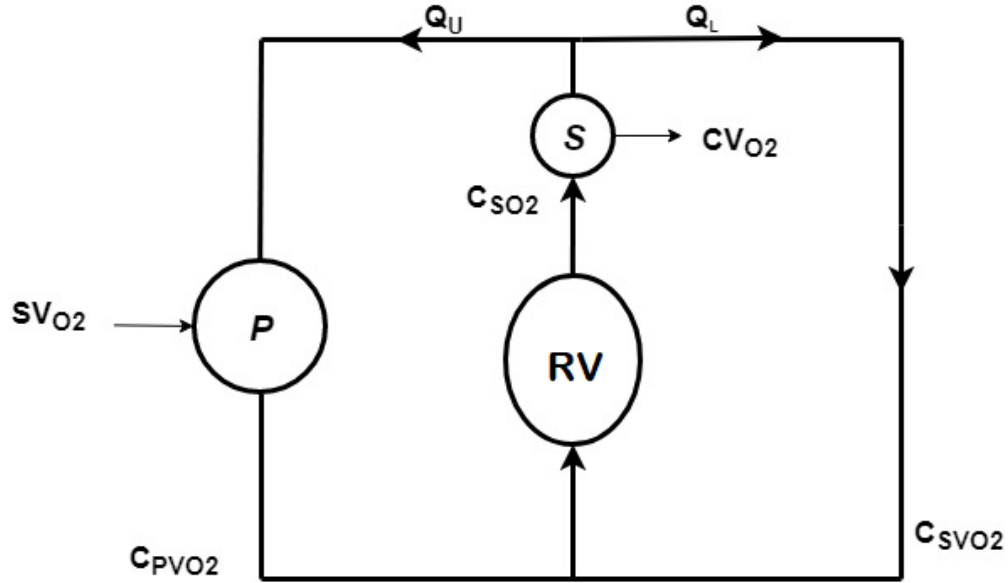


Figure 29 Oxygen transport model without flow split

3.9 Hemodynamic Parameters

After obtaining satisfactory solutions (flow and pressure), more quantities are examined in this study including, the energy loss (EL) of the flow, the wall shear stress (WSS), and the velocity vectors.

The energy loss can be calculated in two methods: the dissipation function method, which attributes all the energy loss to viscous force (friction) for laminar flow, and the control volume approach, which is used in this study.

$$EL = E_{inlet} - E_{outlet} \quad (35)$$

$$EL = \sum_{i=1}^{\text{number of inlets}} \left(\frac{1}{2} \rho |\vec{v}|^2 + P_{static} \right) Q - \sum_{i=1}^{\text{number of outlets}} \left(\frac{1}{2} \rho |\vec{v}|^2 + P_{static} \right) Q \quad (36)$$

The energy loss used in this study was justified by [39, 40, 169-171], where Q represents the blood flow rate, A is the area at an inlet or an outlet. P_{total} was computed using Bernoulli's theorem.

$$Q = \overline{v}A \quad (37)$$

$$\frac{1}{2}\rho v^2 + P_{static} = P_{total} \quad (39)$$

The inlet is the pulmonary artery (PA) and the outlet is the descending aorta (DA). The energy efficiency is calculated for each case and it is defined as the ratio between the fluid energy exiting the model and the energy going into the model.

$$Energy\ Efficiency = \frac{E_{Outlet}}{E_{inlet}} \quad (38)$$

The EL was calculated as a function of split ratio and as a function of the area over the baffle. In the first study, the coupled multi-scale CFD was run with various flow split ratio between the lower and the upper body circulations. The nominal 60/40 lower body/upper body split and three more different split ratios (50/50,55/45,65/35) simulations carried out until a converged solution was obtained.

The second study requires a geometric manipulation to create 5- synthetic geometries with various MPA narrowing sizes, measured as the minimum distance between the systemic baffle surface and the distal pulmonary trunk surface the stricture size was manipulated to build various surgical baffle as shown in Figure 11 &13 to determine the effect of the baffle size on the energy loss. Both studies results are reported and plotted in the results section.

$$WSS = \left| \frac{1}{T} \int_0^T \overline{\tau_w} dt \right| \quad (40)$$

WSS magnitude calculated in equation 40 is the time-averaged value of the WSS magnitude. $\overline{\tau_w}$ is the wall shear stress tensor. WSS was found to cause platelet activation, red blood cell damage, and it increases the thrombus risks, as mentioned in the literature section [172-175].

Particle residence time (PRT) was also calculated in this study by randomly releasing particles and then calculate the residence time of each particle. PRT can help identify regions of recirculation that can increase the risk of thrombus formation. Higher residence time in a specific region may cause platelets to accumulate shear stress and become activated [172, 176]. Furthermore, PRT can be calculated by injecting a high number of particles at the inlet or inside of the region of interest and then tracing the particle locations over time [177-179]. Reininger et al. [176] calculated residence time to determine the effect of shear stress and residence time on fibrin clot formation in a laminar and turbulent flow. A simple T-branching model was used in this study to test the clotting time, quantify the flow separation and calculate the residence time. The study found that residence time and convergent flow are more critical for clot formation than the shear rates. Suh et al. [178] used CFD as a tool to calculate the particle residence time (PRT) and particle residence index of different patient specific model with aortic aneurysm. About 100,000 particles were injected during the first cardiac cycle, and the PRT and PRI were monitored over ten cycles. The results showed the importance of using a patient's specific models since none of the models showed similar results to the balloon-shaped aneurysm. Moreover, PRT and PRI calculations were different between patients, and this study demonstrated the importance of PRT and PRI to identify the recirculation and stagnation zones. Kunov et al. [177] introduced and

calculated particle volumetric residence time (VRT) which takes into account the accumulating regions and the time each particle spends. The model was a simple artery (one inlet and one outlet) with 45% stenosis. The areas with high shear stress and low velocity showed a high PRT. Moreover, in this study, a concept “platelet activation” was introduced when particles are exposed to shear stress higher than the critical value. In similar studies PRT calculations were different between patients and demonstrated the importance of PRT to identify the recirculation and stagnation zones.

In this study, a Lagrangian scheme was implemented to track the released particles. The Lagrangian model can also be used to visualize the area of circulation and stagnation and to count the number of particles (thrombi) that passes through each outlet in the fluid domain, which can induce clot formation. After obtaining a converged flow field, the Lagrangian tracking scheme was activated, and particles are injected. The Maxey-Riley particle equation is given by

$$m_p \frac{d\vec{v}_p}{dt} = m_f \frac{D^* \vec{U}_f}{Dt} + (m_p - m_f) \vec{g} + 6\pi a \mu \left(\vec{U}_f - \vec{v}_p + \frac{a^2}{6} \Delta \vec{U}_f \right) + \frac{m_f}{2} \left(\frac{d\vec{v}_p}{dt} - \frac{D}{Dt} \left(\vec{U}_f + \frac{a^2}{10} \Delta \vec{U}_f \right) \right)$$

Where a is the particle radius; μ fluid viscosity, $m_f = \rho_f V$, $m_p = \rho_{fp} V$, V is particle volume, ρ_f is fluid density, ρ_p is particle density and g is gravity. The right side terms represent the fluid pressure gradient, the gravity, the drag force and the added mass, respectively.

In order to prevent particles from affecting the converged flow field, zero mass particles were injected at the MPA inlet. Spherical particles were injected for several cardiac cycles using injection grids at the MPA inlet, as shown in Figure 30. This study aims to investigate the area

where the pulmonary arteries stent placed. The high-pressure blood from the ventricle flow over a half-cylindrical shaped vessel that may lead to flow circulation due to pressure drop.

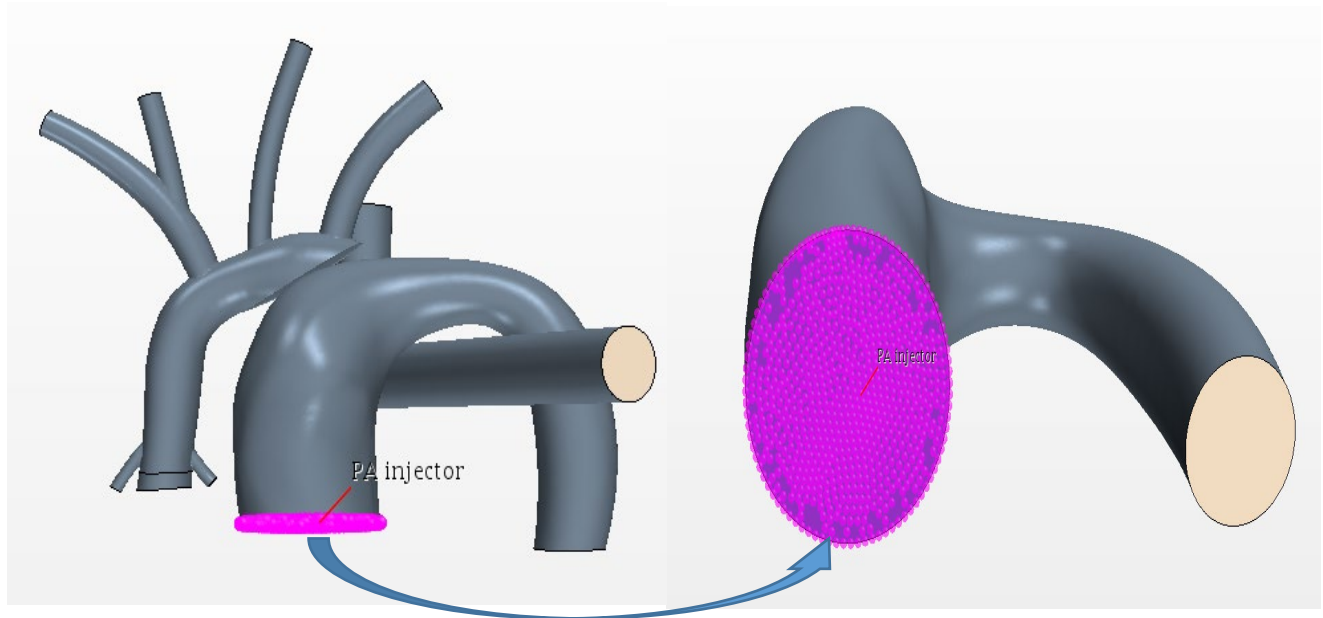


Figure 30 MPA: main pulmonary artery injection grid

A high number of particles were released at each run to obtain a spatial distribution, with the initial velocity set to be zero. Moreover, the release of particles from each node of the grid was controlled by point inclusion probability function built-in STARCCM+. Excel was used to generate a table bounded by 0 and 1 to randomize the particle release time. The simulation was set to continuously release particles over time for several runs because PRT depends on the release time. Also, a particle tracking counter was set at each boundary in the fluid domain to calculate how many particles leaving from each outlet.

CHAPTER FOUR: RESULTS AND DISCUSSION

4.1 Mesh Independence Study

The post-processing and the data visualization was carried out after obtaining a sustained flow and pressure solutions. The CFD results must be independent of the mesh used in the study. Thus, a mesh independence study was carried out with different meshes while monitoring the flow and pressure at the inlets and the outlets of the boundaries. The results of this study are shown in Table 3 and Table 4 for 3-different mesh refinements and the percentage error.

4.2 Lumped Parameter Model (LPM)

The LPM for HCS II consists of 5 subsystems (the heart, the upper circulation, the lower circulation, the coronaries, and the pulmonary circulation), and each consists of multiple compartments (arterial and venous). The LPM was tuned to produce the desired waveforms as boundary conditions to the CFD. In this case, a 6-months old patient with a cardiac output of about 3 (L/min) with a cardiac cycle of 0.5(s). Traditionally HLHS has atrophied aortic root where no or little flow output through the left part of the heart. But that is not the case for applicable HCS II patients who have a ventricular septal defect allowing a sufficient amount of blood flow through the aortic root. The LPM was tuned to a 60/40 inflow split and 70/30 split between the MPA supplying the lower circulation and the AA feeding the upper circulation and the left and the right coronary arteries, respectively. The converged boundary conditions plots from the LPM are shown in Figure 32. Also, to validate the LPM results after tuning, the waveforms obtained from the LPM of the heart pressure were compared to the catheter plots provided by Arnold Palme Hospital. For example, a similar magnitude and features are noticed when comparing the MPA pressure plot and the catheter pressure waveform for the MPA as shown in Figure 33.

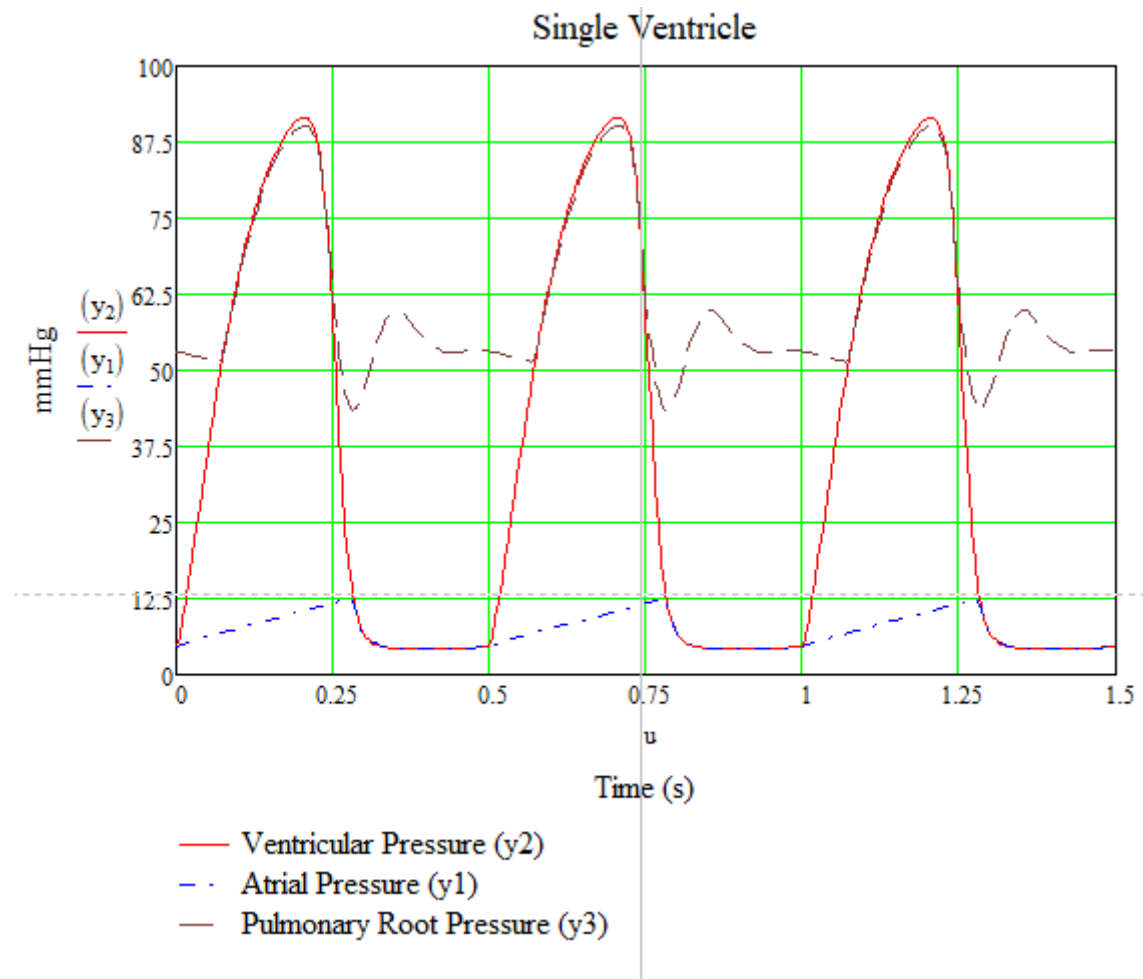
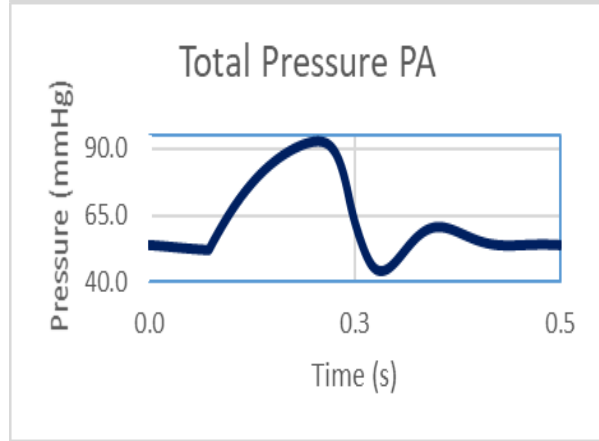
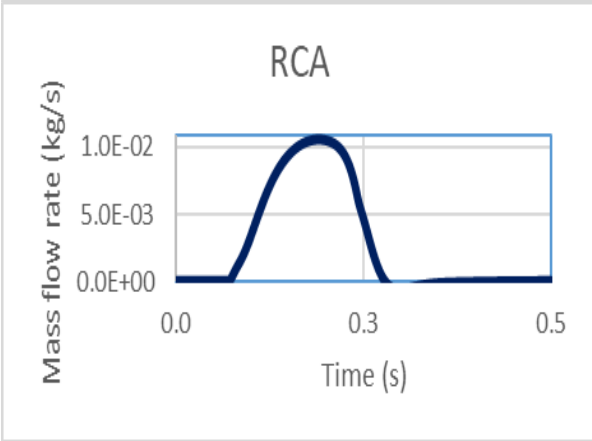
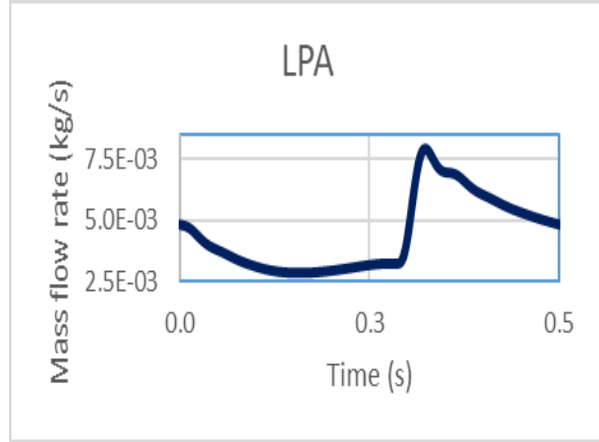
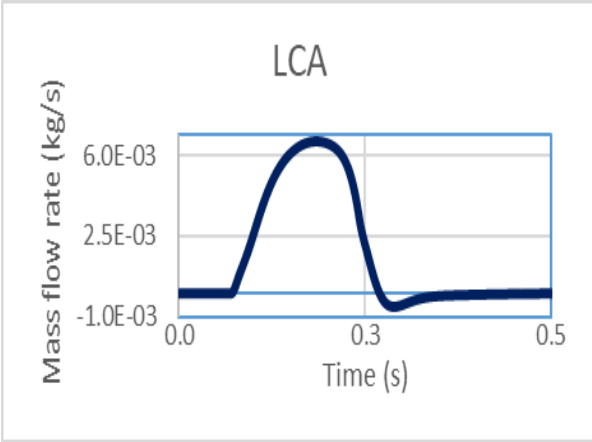
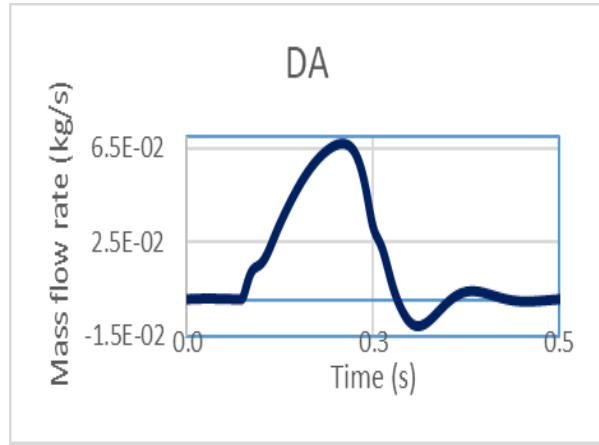
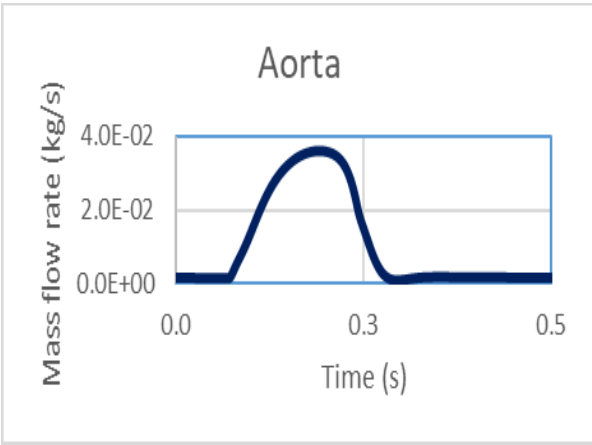


Figure 31 Pressure waveforms



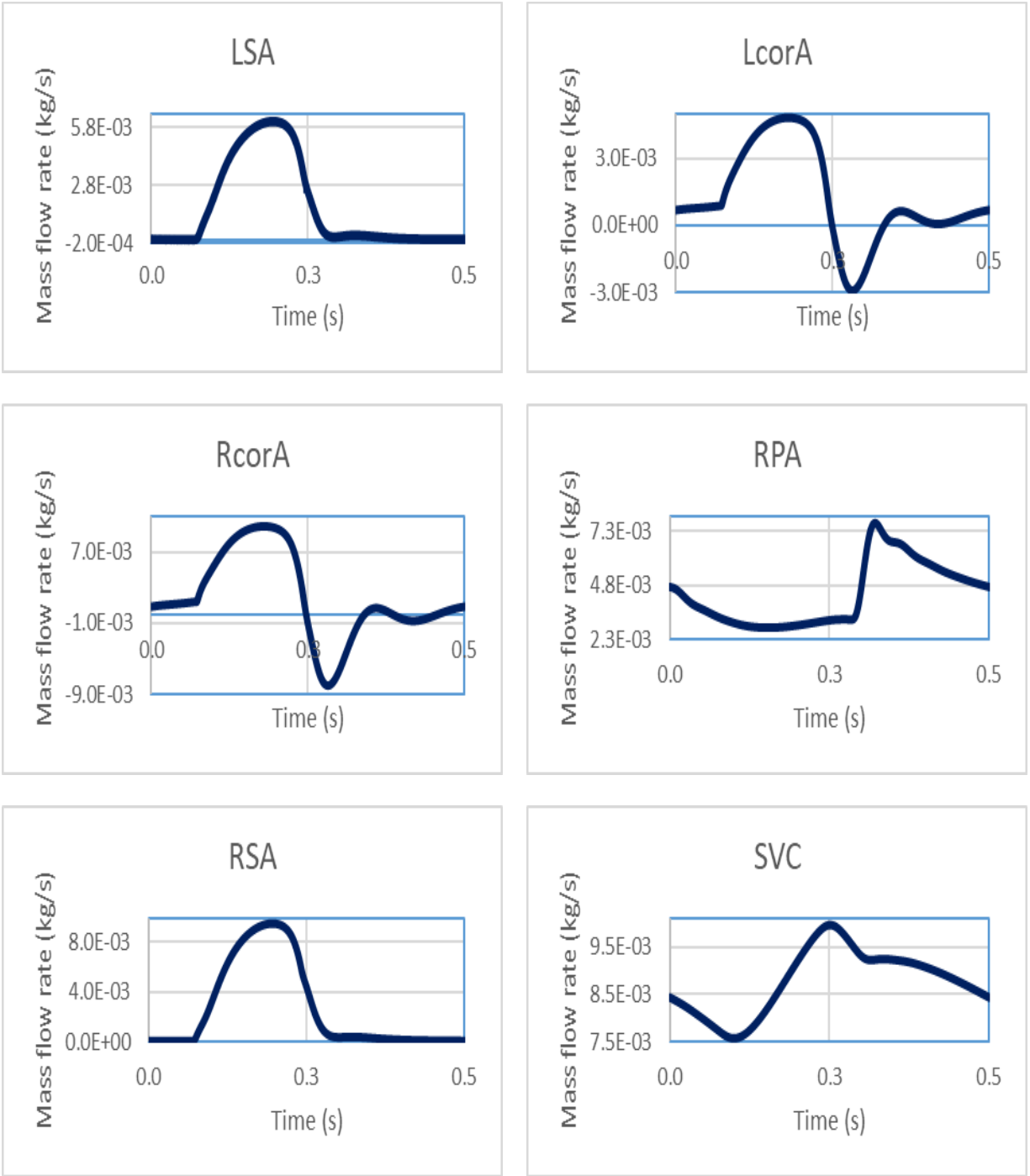


Figure 32 Sample BC waveforms for all inlets and outlets (AORTA=Aortic Root, SVC=Superior Vena Cava, DA=Descending Aorta, RPA=Right Pulmonary Artery, LPA=Left Pulmonary Artery, LcorA=Left Coronary Artery, RcorA=Right Coronary Artery, LCA=Left Carotid Artery, RCA=R

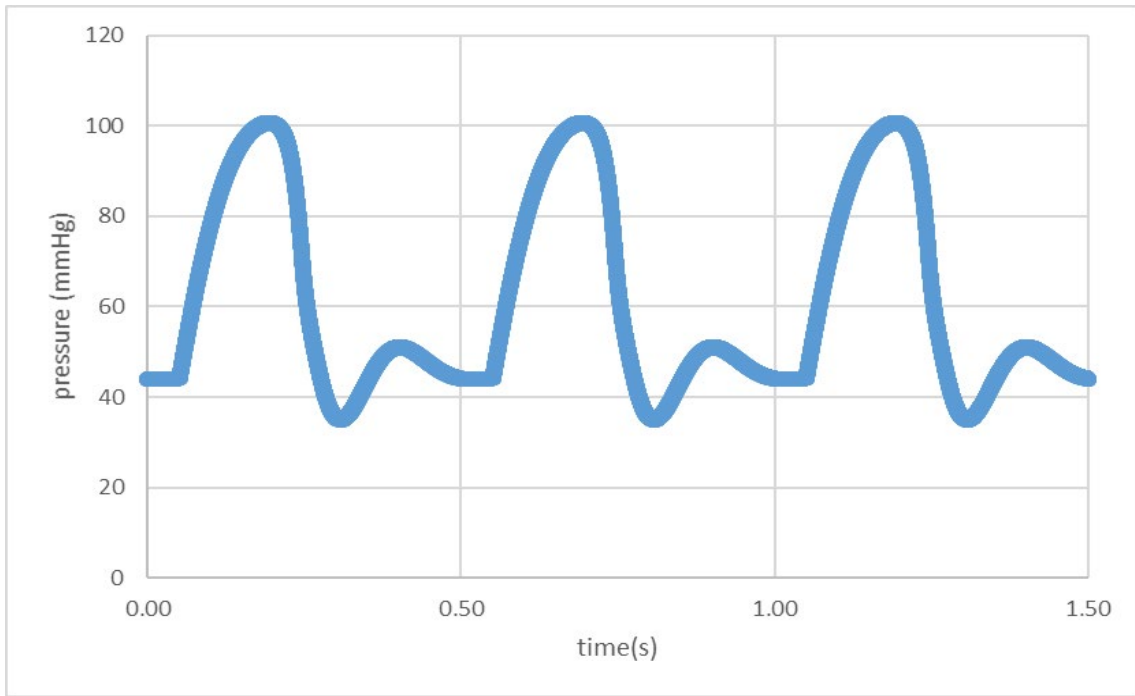
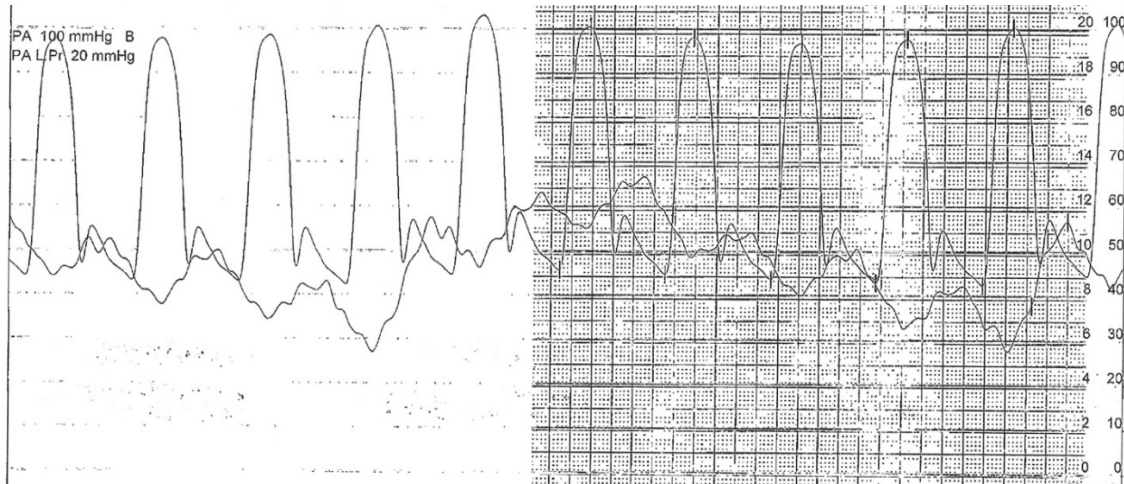


Figure 33 BCs waveforms (top) De-identified main pulmonary artery (bottom) tuned LPM MPA pressure

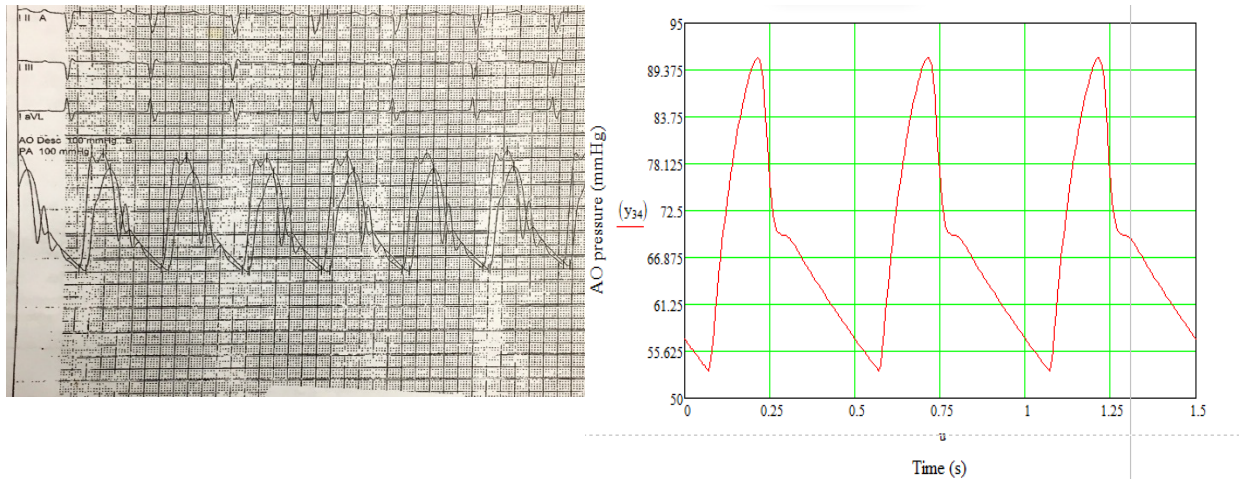


Figure 34 Tuned Aorta pressure (Left) De-identified data from APH,(Right) tuned LPM pressure

4.3 Multi-Scale Model Convergence

A stable solution was successfully obtained for all the different CFD models. The coupling procedure, as mentioned in section 3.5, was run until a converged solution was reached. The number of iteration required was ranging between 15-25 iterations based on the geometry and the flow fields. Figure 36 displays the flow rate measured at the main pulmonary artery cross-section at each iteration (as an example). This procedure was conducted for each cross-section showed in Figure 24 to check for convergence, which can be achieved by reaching a sustained flow field.

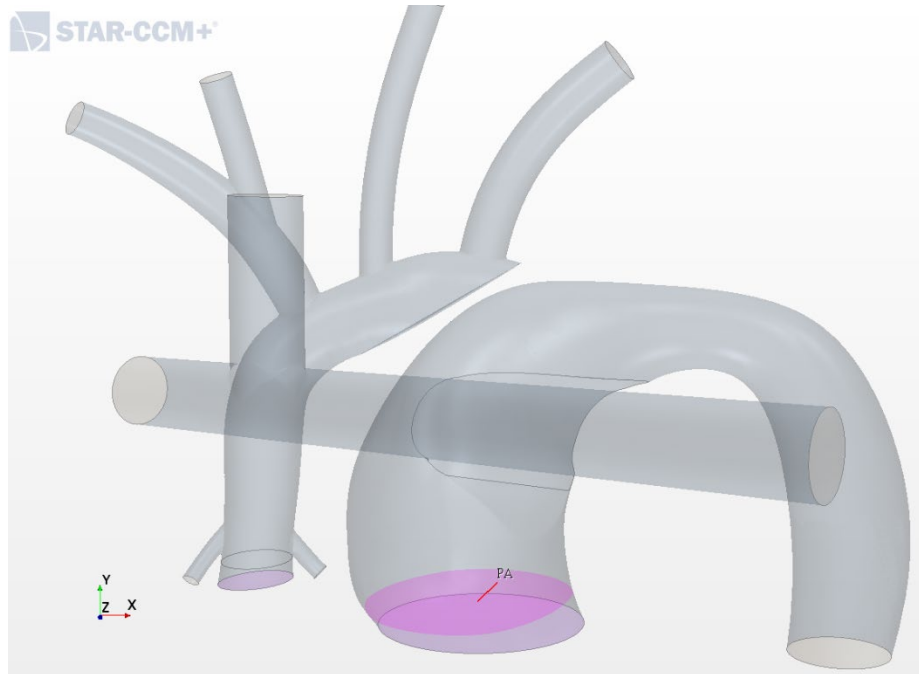


Figure 35 MPA cross-section

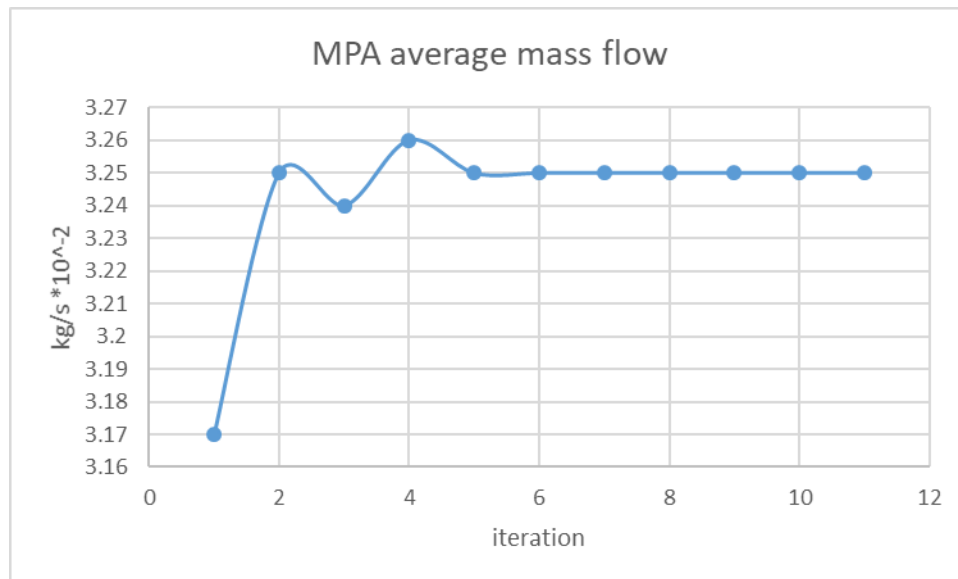


Figure 36 MPA averaged flowrate per iteration

Figure 36 shows the flow rate at each iteration with about 1.5 million mesh cells, where 3-heart cycles take about 20 hours, employing 32 CPUs. The figure shows a negligible change in the flow field starting at the 6th iteration.

4.4 Systemic pressure drop

The presence of the baffle in the pulmonary trunk mandates further elucidation of the relationship between the baffle-related narrowing and the pressure drop across the main pulmonary artery. This requires two examinations: first, we want to isolate how the protruding baffle affects the flow field. Second, it is of interest to quantify the combined effect of the pulmonary trunk restriction and subsequent distal arch “kink.” The geometry shown in Figure 10 can easily be manipulated to investigate various MPA narrowing sizes, measured as the minimum distance between the systemic baffle surface and the distal pulmonary trunk surface (Figure 37). Table 7 offers an overview of all the measurements carried out for the various narrowing increments. Average values are computed as surface-averaged pressures over the sampling surface, which are then time-averaged, while peak values are the maximum values observed across the sampling surface throughout a single heart cycle.

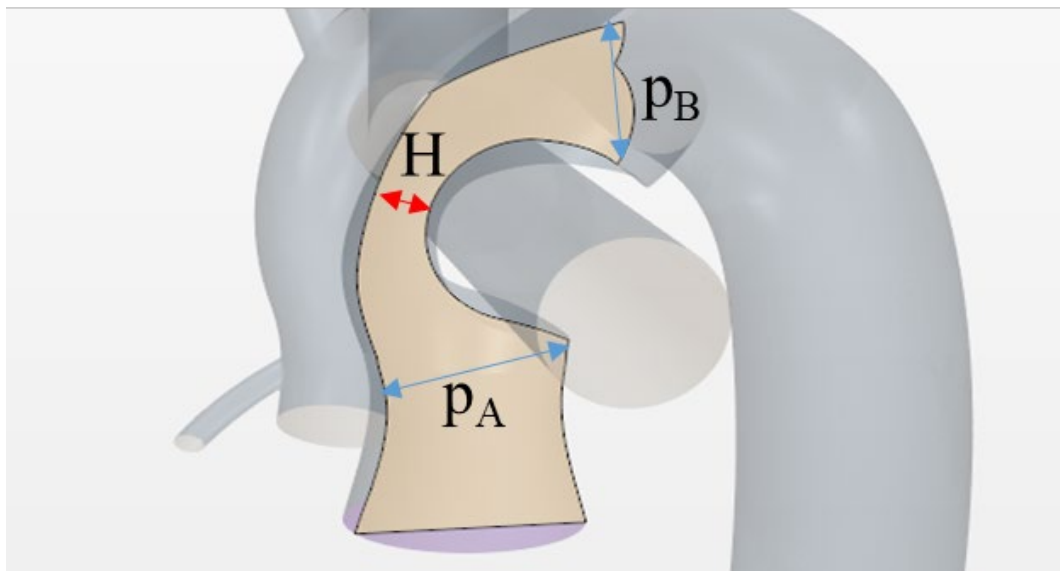


Figure 37 Location of the MPA lumen defining MPA narrowing characteristic height (H)

As shown in Figure 38, we sampled pressure data relative to stricture before, P_A , and after the baffle, P_B , for various obstruction levels. A similar approach was applied to monitor the

pressure in the distal arch. The purpose of these pressure measurements was to ensure that any level of obstruction considered in this and future studies would not exceed a clinically accepted pressure drop of 10 mmHg. In addition, we were able to visualize a wider array of hemodynamics and observe how strongly the baffle affects the downstream flow regime. Figure 38 (presented as the absolute pressure difference between pressure proximal and distal to the baffle, ($\Delta p = P_A - P_B$) shows how the peak Δp is strongly affected by the incrementally large obstruction of the flow, while the surface averaged Δp experience little change.

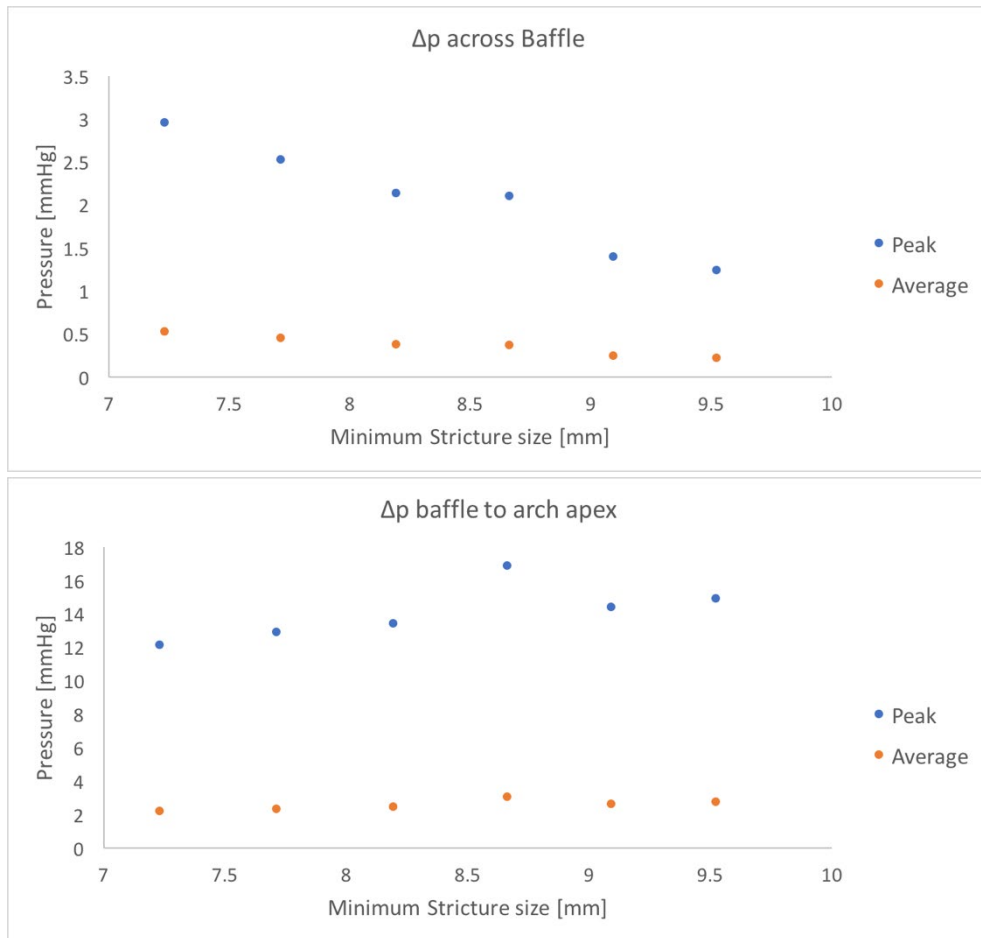


Figure 38 Time-averaged peak and surface averaged pressure drop across the baffle (top), and time-averaged peak and surface averaged pressure drop from baffle to distal arch (bottom) with respect to obstruction size.

Similar observations are made for the pressure difference between proximal to the baffle and the distal arch. The peak pressures clearly display a change, while the average pressure does not undergo significant variation. Of great relevance, however, is the magnitude change of the pressure drop for the peak pressures between the first and second plots. Across the baffle, the largest pressure drop was 2.96 mmHg, while for the same narrowing size and accounting for the distal arch kink, a four-fold increase is observed yielding a 12.15 mmHg drop. The largest pressure drop measured is 14.95 mmHg, which, interestingly, did not occur at the narrowest obstruction size. While the trend observed when isolating the baffle effect was expected, the trend displayed in the pressure drop to the distal arch could be counterintuitive. When accounting for the distal arch contribution, the peak pressure difference shows a mild upward slope, indicating that for increasing MPA narrowing an increased pressure drop is observed. This can be explained by how the geometry in the pulmonary trunk is implemented and modified. As the diameter of the narrowing is incrementally increased, then the pulmonary trunk is geometrically inflated, corresponding to a larger patch of the MPA. This means that proximal to the baffle, the right ventricular flow will see an incremental increase volume. For a rigid wall model, this additional volume creates a region that acts similarly to a reservoir, causing a mild build up in pressure. In order to meet physiological flow rates, an increased pressure drop is required.

Despite the increased peak pressure drop observed, our model predicts that the current geometrical implementations fall within the predetermined clinical thresholds.

Table 7 - Surface averaged, and peak pressures drop for incremental pulmonary trunk narrowing sizes.

PA trunk size		Pressure drop across baffle		Pressure drop from baffle to apex	
δ_{min} [mm]	δ_{max} [mm]	$\overline{\Delta p}$ [mmHg]	Δp_{max} [mmHg]	$\overline{\Delta p}$ [mmHg]	Δp_{max} [mmHg]
7.23	14.40	0.53	2.96	2.20	12.15
7.71	15.48	0.46	2.53	2.36	12.92
8.19	16.70	0.38	2.14	2.48	13.44
8.66	18.80	0.37	2.11	3.09	16.91
9.09	19.00	0.25	1.40	2.66	14.41
9.52	19.60	0.22	1.25	2.78	14.95

4.5 Vortex Formation

In the systemic circulation, the baffle can be thought of as a half-cylinder in cross-flow. A prime feature of such flow is the von Kármán vortex street caused by an unsteady flow separation around the cylinder. Vortices downstream from the baffle would be undesirable flow features; hence it should be determined if vortices may indeed form due to this particular geometry. Around the area of interest, the free-stream (at the centerline of the conduit) Reynolds number (Re) was computed to be about 1807 (laminar flow, pipe flow transitions at $Re \cong 2300$). The empirical relation in Equation 41 valid for Re range $250 < Re < 2 \cdot 10^5$ is used to calculate the Strouhal number ($St = \frac{fD}{U}$), which is a dimensionless number expressing the ratio of the rate of vortex

shedding frequency (f) to the main fluid velocity (U) for a given hydraulic diameter (D) characterizing the oscillatory nature of the flow,

$$St = 0.198 \left(1 - \frac{19.7}{Re}\right) \quad (41)$$

For the computed Reynolds number of around $Re = 1807$, the Strouhal number was found to be $St = 0.1958$. This corresponds to a shedding frequency of $f = 6.53 \text{ Hz}$. Inverting the frequency, we obtain a period of 0.15 s . Given the shedding period and the flow velocity, it is possible to determine the distance required to form and sustain vortices. For an average fluid velocity of $0.5 \frac{m}{s}$, a transport distance is calculated at $\sim 75 \text{ mm}$ which is far larger than the distance from the baffle to the aortic arch apex. This indicates a low probability of significant vortex propagation, as there would not be enough space for a vortex to form fully, even though when drawing a parallel between the vortex period to the heart cycle ($0.15\text{s} < 0.5\text{s}$), about three vortices per heart cycle would be generated. Indeed, no vortex shedding from the baffle is observed in the computational model. This suggests that vortex shedding for the HCS II baffle should not be of great concern.

4.6 Flow Field

In this model, we are studying three separate circulatory regions: two high-pressure systems driven by the right ventricle and a low-pressure system heading to the pulmonary arteries. Figure 12 displays the unsteady velocity field the model predicts at four points during the heart cycle: late diastole, early systole, peak systole, and early diastole.

In the upper-body systemic circulation, left ventricular (LV) output can be readily observed in systole, characteristic of the HCS II. In diastole, the upper-body circulation experiences very

mild retrograde flow due to severely weakened pulsatility. Stagnant flow is observed in the aortic arch apex as well. Coronary flow can be seen at its peak in early/mid diastole (bottom of Figure 39), presenting the characteristic out-of-phase waveform. As expected, the pulmonary flow presents weak pulsatility compared to the systemic flow. Due to the 90° T-junction shape of the SVC anastomosis to the pulmonary arteries, flow originating from the SVC impinges on the distal junction wall. However, due to low flow velocities and lack of pulsatility in the pulmonary circulation, the branching flow does not present large recirculation or swirling, which could be seen at higher inflow speeds. Though localized, a combination of rotational flow and impingement can pose many different issues ranging from intimal hyperplasia to thrombogenesis. As such, shaping the SVC anastomosis, as is effectively done in the Y-Fontan graft [180], would reduce such pathologies in the flow. In the pulmonary trunk leading to the distal arch section, the model can be thought of as a half-cylinder in cross-flow. Figure 40 offers better insight into the flow acceleration in the geometrical restriction due to the baffle over the cardiac cycle. Since the fluid is assumed incompressible, a lumen area reduction would promote flow acceleration. Both figures 39-40 display this phenomenon. In addition, as the systolic phase picks up, the flow detaches from the baffle surface. In diastole, as the ventricular pressure gradient dissipates, the flow re-attaches to the surface nearly all the way to the baffle suture to the inner aortic arch wall.

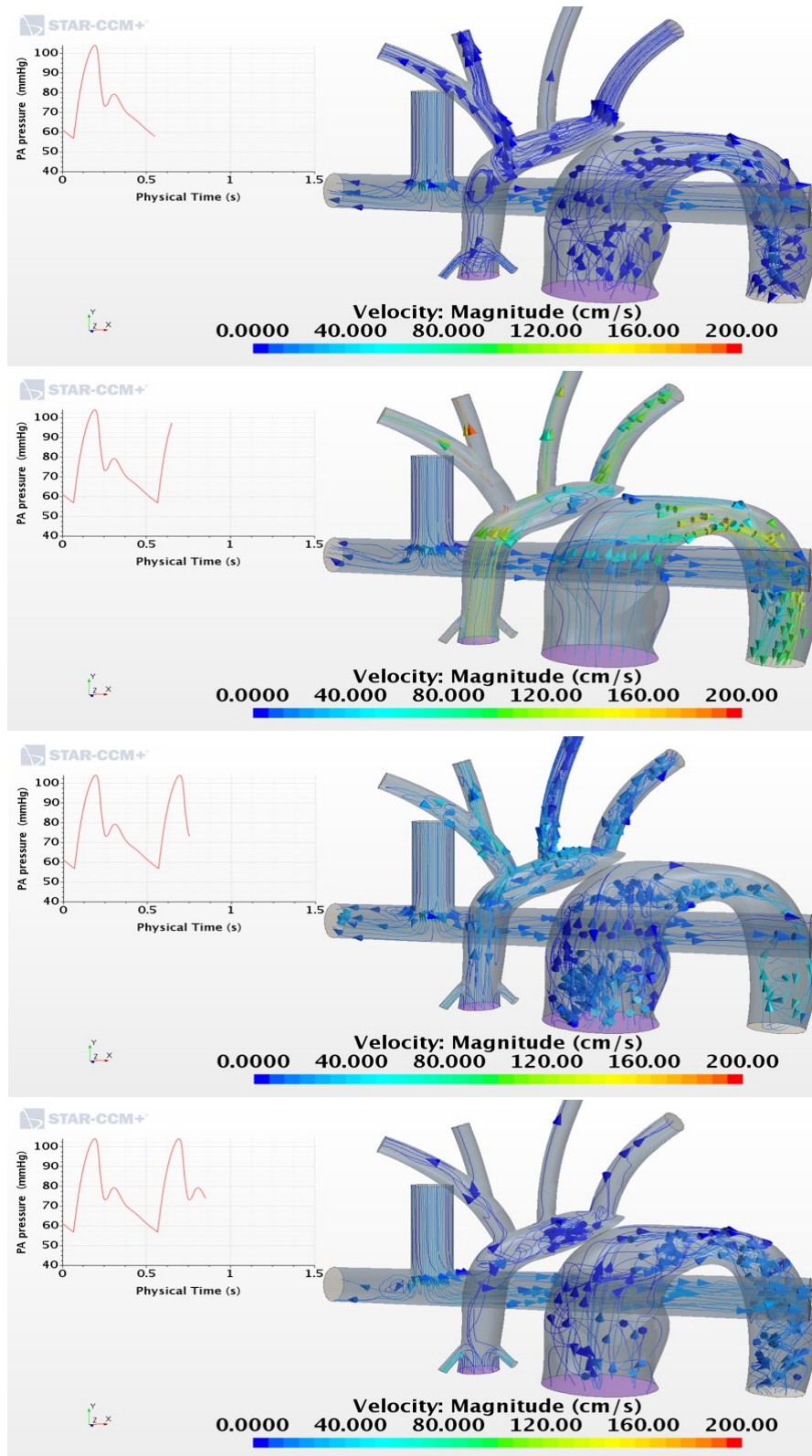


Figure 39 Velocity field representation using streamlines for a second heart cycle.

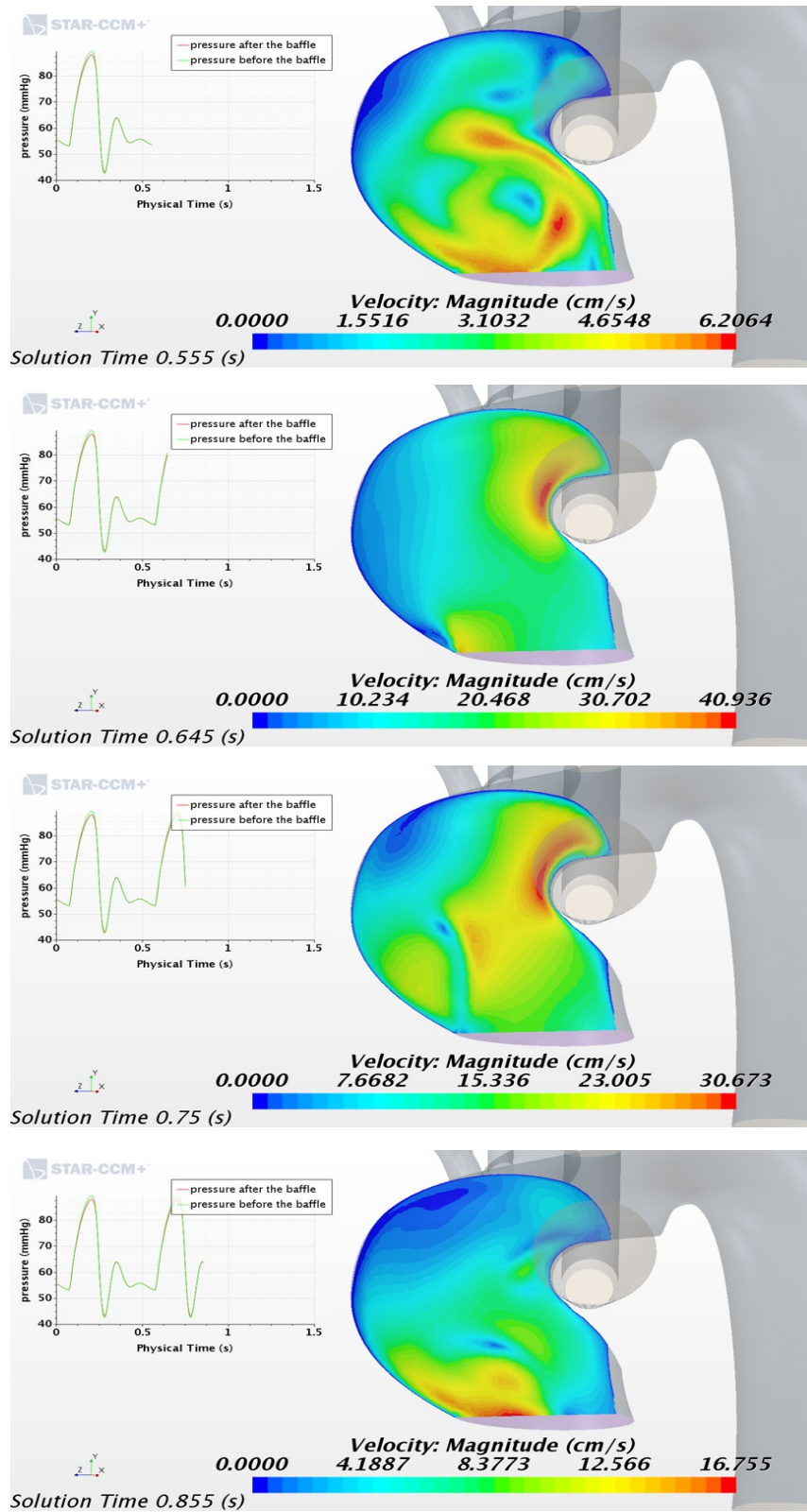
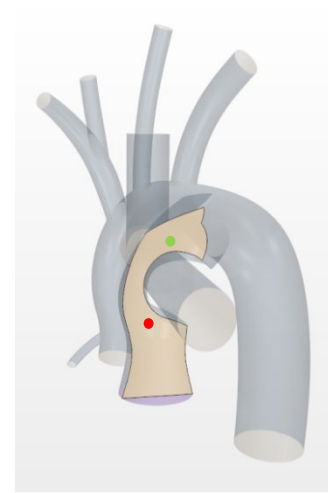
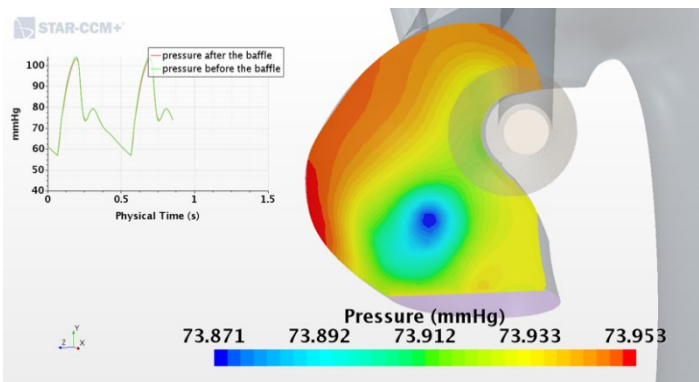
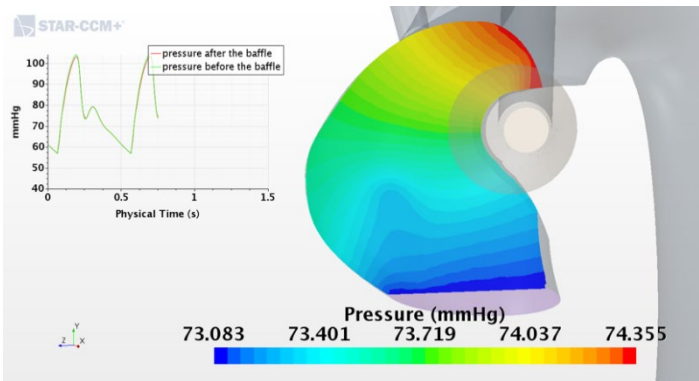
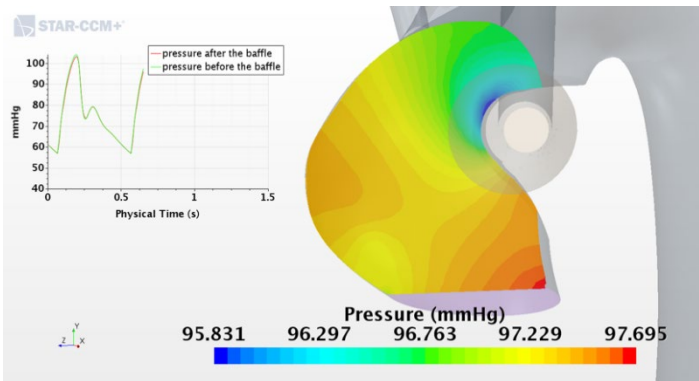
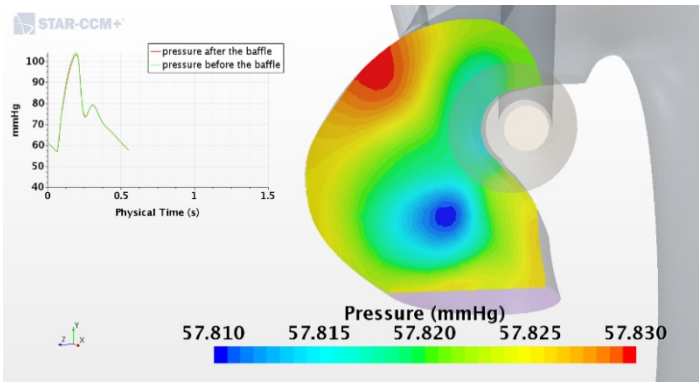


Figure 40 Pulmonary truck axial cross-sectional cut with velocity field contour plot.

Figure 41 displays the pressure field on the same cut plane, as in Figure 40. This image clearly shows the pressure gradient across the baffle (upstream and downstream). The plot accompanying the pressure contour plot displays the pressure at point probes placed before (in green) and after (in red) the baffle. In particular, during systole, the adverse pressure gradient causes the flow to detach from the baffle. In diastole, due to the absence of right ventricle output and the anatomical enlargement of the conduit, the pulmonary root region experiences a large region of recirculation. In addition, this figure highlights the pressure loads experienced by the underlying stent during systole. The stent, placed beneath the baffle in the pulmonary circulation, undergoes normal and shear loads throughout the cardiac cycle. It must be emphasized that the stent perceives a combination of cyclic systemic and pulmonary loading, which could ultimately lead to mechanical failure. Identifying structural response induced by cyclic fatigue is important to assess potential issues with stent integrity under these conditions, and is under current investigation within our group.

The localized pressure increase in the upper section of the contour is caused by the converging-diverging nozzle (CDN) effect induced by the restriction in the MPA, which becomes more evident during diastole. These pressure fields can be partially responsible for the flow reattaching to the baffle surface.



Pressure measurements locations

Figure 41 Pulmonary trunk axial cross-sectional cut with pressure field contour plot.

4.7 Baffle Loading and Wall shear Stresses

The main feature of HCS II is the presence of a baffle separating the systemic flow from the pulmonary flow; therefore, close inspection of the effects of the high-pressure flow on the baffle surface is important. Figure 42 provides a good insight on wall shear stress (WSS) distribution on the baffle. In addition, it allows us to observe the location of flow detachment and re-attachment from the baffle surface. It can be observed that in systole, as expected, shear stresses are high on the surface directly facing the right ventricle outlet and, due to mild detachment, wall shear stresses on the far side drop to notably low values. Uneven contour distribution is due to the bent present in the aortic arch, which strongly affects the velocity profile across the lumen. The secondary wall shear stress peak observed in Figure 42, downstream of the baffle, is due to the recirculation of the flow around the whole baffle surface.

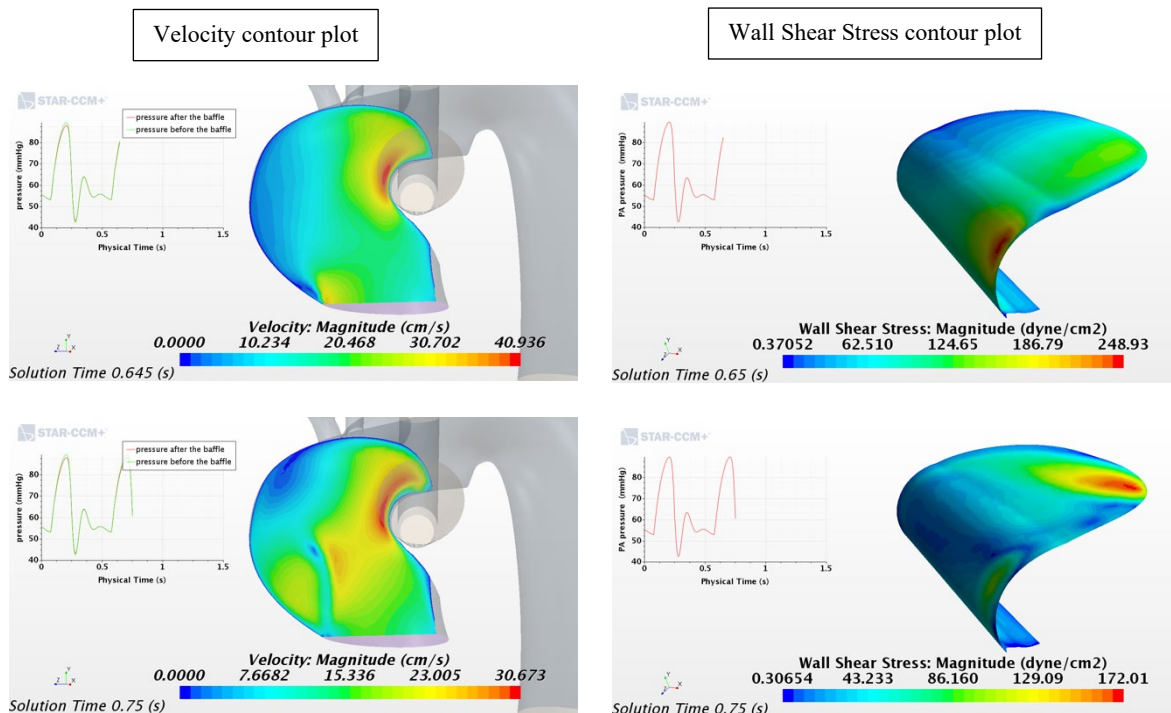


Figure 42 Comparison of velocity vs. wall shear stress during early systole (top) and early diastole (bottom), with pressure measurement locations the same as in Figure 29.

Figure 42 shows a comparison between wall shear stress and velocity to understand better where and how a diastolic wall shear stress peak occurs posteriorly to the baffle. The peak can be seen to match the locations where the flow reattaches to the surface, causing a localized rise in wall shear stress. In magnitude, this peak is markedly smaller than the peaks observed in systole; nevertheless, this cyclic peak may induce some fatigue stress on the underlying tissue, which should not be ignored. To be noted once again is the uneven distribution of the wall shear stress during diastole that can be attributed to the geometric irregularities present in this model. Uneven stress distribution may have strong repercussions on how the epithelial tissue regenerates and heals following the procedure.

Figure 44 focuses on the WSS distribution on the baffle surface on the systemic circulation side across one heart cycle. As previously observed, the uneven distribution is ever-present. In addition, the WSS peaks appear to periodically migrate, which leads to varying shear loads on the baffle.

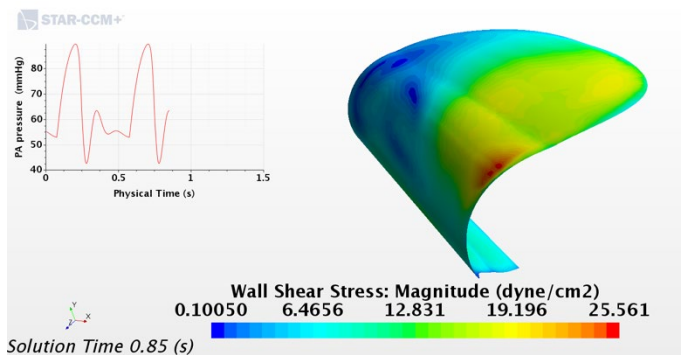
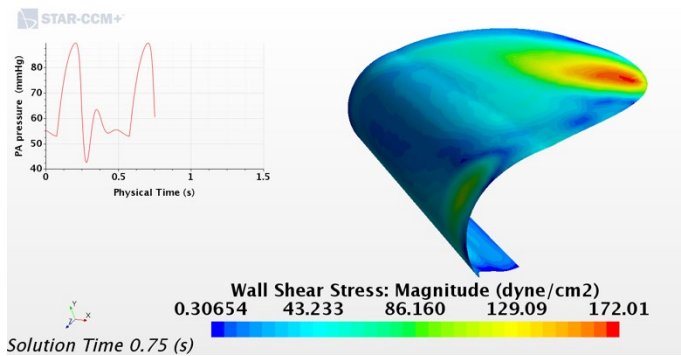
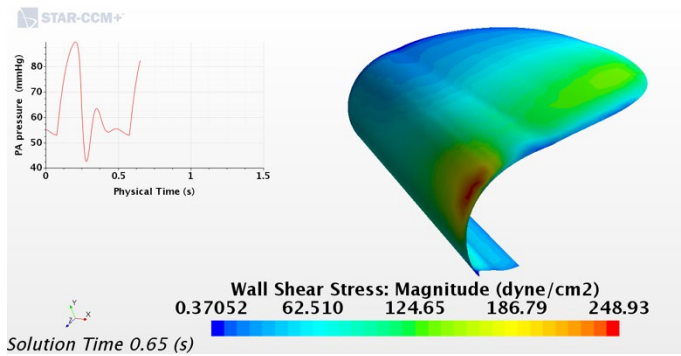
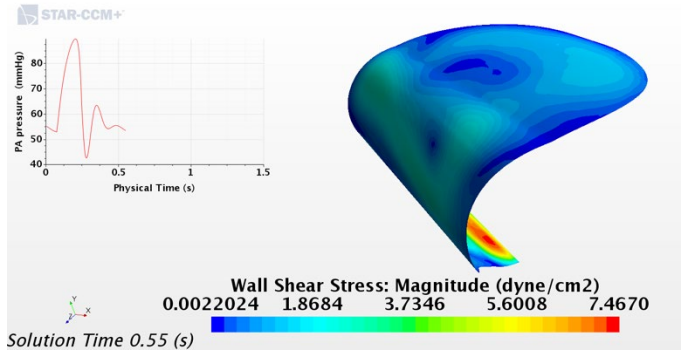


Figure 43 Wall shear stress contour plot on the baffle surface in the systemic region (pressure measurements locations the same as in Figure 34)

4.8 Energy Loss

Energy loss and energy efficiency were calculated and plotted first with respect to the flow split ratio between the upper body and the lower body circulation and second with respect to the area over the baffle. The nominal split ratio in this study was set to be 60/40 lower body / upper body circulation based on the clinical data provided by Arnold Palmer Hospital. Moreover, energy loss as a function of split ratio and area over the baffle were calculated, as shown in section 3.9.

The average energy loss due to the pressure drop and the viscous losses was found to be 12.53 ± 1.39 mW for the split ratio study, and the average efficiency was found to be 0.91. For the area over the baffle study, the average energy loss and the efficacy were found to be 12.47 ± 0.18 mW and 0.91, respectively.

Table 8 - Energy Loss and Energy Efficiency (E efficiency) as a function of the area over the baffle

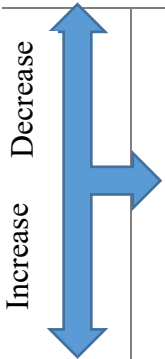
	<i>Case</i>	<i>PA energy</i>	<i>DA energy</i>	<i>EL (mW)</i>	<i>E Efficiency</i>
	1	0.418	0.381	12.33	0.91
	2	0.417	0.379	12.66	0.9
	3	0.413	0.375	12.66	0.9
	4	0.411	0.374	12.33	0.9
	5	0.407	0.37	12.33	0.91

Table 8 offers a closer look at the effect of the baffle related narrowing on the energy loss, where case 3 represents the nominal model.

Table 9 - Energy Loss (EL) and Energy Efficiency (E efficiency) as a function of split ratio

<i>case</i>	<i>PA energy</i>	<i>DA energy</i>	<i>EL (mW)</i>	<i>E Efficiency</i>
50/50	0.338	0.307	10.33	0.9
55/45	0.428	0.386	14	0.9
60/40	0.414	0.376	12.66	0.9
65/35	0.42	0.38	13.33	0.91

The energy loss as shown in Table 8, increased by about 3% (from 12.33 to 12.66) as the descending aorta increases from case 1 to case 2 . However, no changes were examined in EL between case 2 and case 3 (nominal). Moreover, the EL loss dropped in case 4 as the ascending aorta increases and did not change in case 5, where the ascending aorta diameter was larger than the nominal.

Furthermore, the energy loss for the 50/50 case exhibits the lowest energy loss value 10.3 mW, and then EL increased to 14 mW for the 55/45 split ratio as seen in Table 10 . Then starts dropping as more blood flows to the lower body, 12.66 mW for the nominal 60/40 split ratio, and 13.33 mW for the 65/35 ratio.

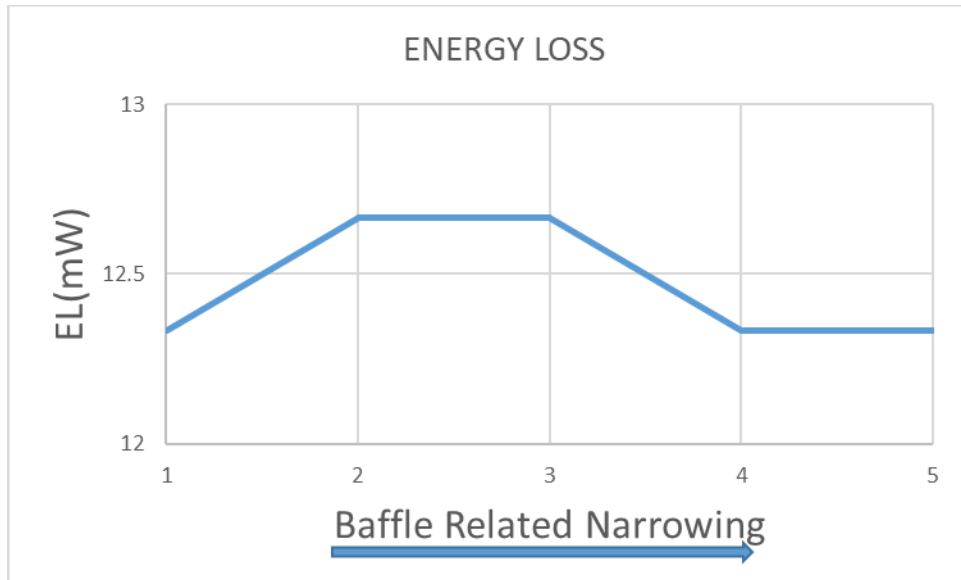


Figure 44 Energy loss versus area over the baffle

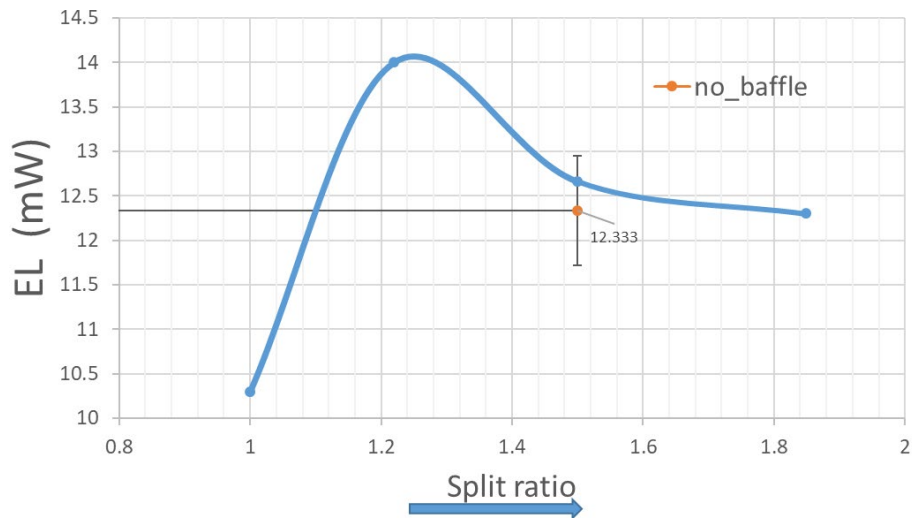


Figure 45 Energy loss versus split ratio

4.9 Particle Residence Time

Particle residence time (PRT) represents the time required for a particle in the flow field to exit any boundary. Areas with recirculation and flow stagnation can lead to a longer PRT, and that indicates an increased risk of blood clotting. The coupled scheme was carried out first until a converged solution was obtained and then the Lagrangian model was introduced by injecting spherical particles randomly in space and time. We computed the PRT with different particle diameters (2mm, 4mm, and 5mm) to quantify how long the particles take to exit the flow field and flow circulation. A continuous release of particles throughout the cardiac cycle was set, and particles were trace to calculate the average time plot was created to calculate the average time particles take to travel from the injection point (MPA inlet) to the exit DA. Massless and material particles were injected separately in this case. The massless particles follow the velocity vectors, while the material particles might have some effects on the flow field. For the material particles, the particle mass, gravity, buoyancy, drag, Saffman, and pressure gradient forces were considered with 1116.73 (kg/m³) density. We carried out each simulation for several runs to measure the PRT and to obtain a consistent solution. The results showed that, on average, particles take about less than 0.5 (s) to exit the fluid domain. However, it also shows that some particles take longer to exit (≥ 3 s). Moreover, as can be seen in Figure 47 contour, the peak PRT starts decreasing from 3.34 s at the early systole then starts decreasing as the flow starts accelerating but then starts increasing again at the late diastole. That could be due to the fact that some particles were stuck and then were flushed by the high-pressure flow since we have a continuous particle injection, which could be the reason for PRT increase at the end of diastole.

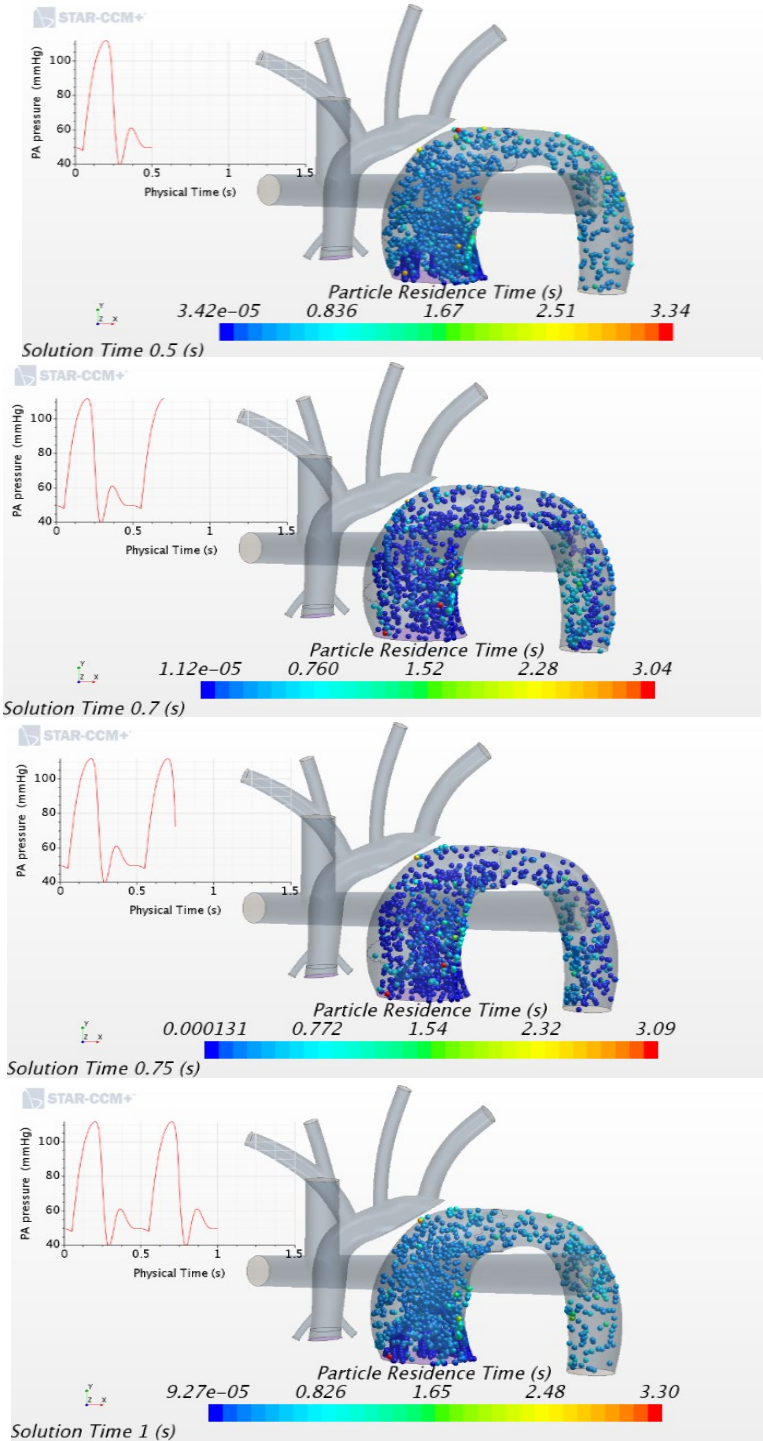


Figure 46 Particle Residence Time at different point of the cardiac cycle (Early systole, Peak systole, Early diastole and Late diastole)

In Figure 47, we plotted the maximum, the minimum, and average PRT the particles take to exit the flow field. The blue line represents the minimum PRT, which is almost (0 s), and then we have the maximum time plot in green, which goes to (≥ 3 s). The take away from this plot is that on average the particles clear the flow field in about (≥ 0.5 s).

For the material particles (2mm, 4 mm, and 5mm) models, we did not observe big differences in the PRT calculations. The no change in PRT calculation could be because of two reasons: (1) The short distance from the injection location to the exit and the fact the there is only one exit for the particles, (2) we are calculating the average time of a higher number of particles and even if some particles get stuck that would not affect the average PRT.

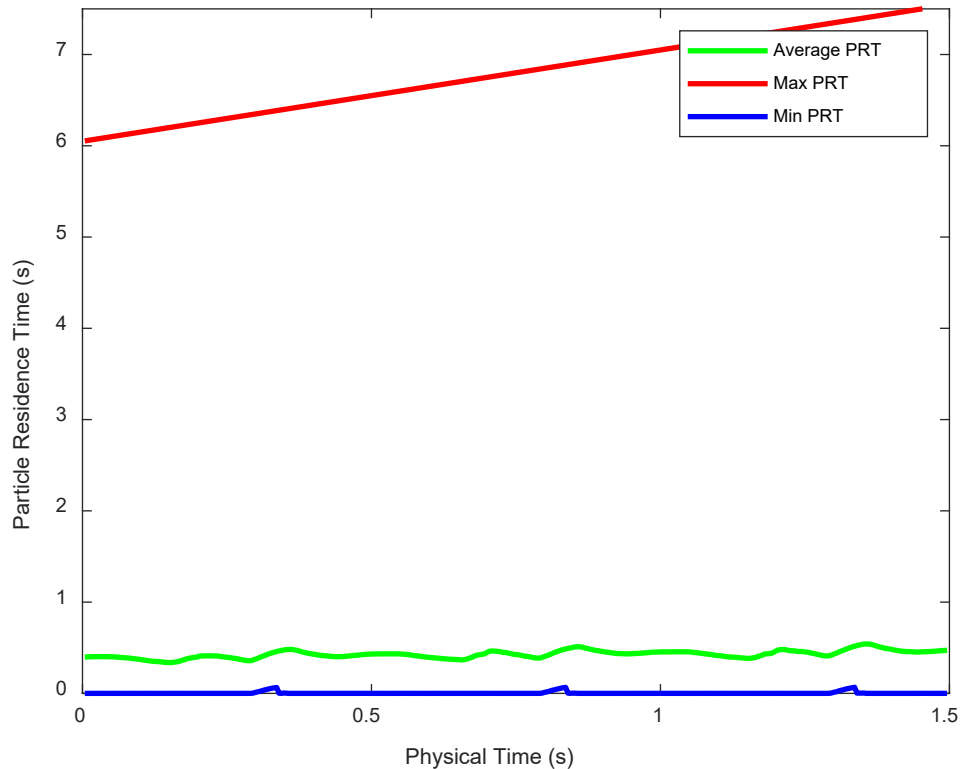


Figure 47 Particle Residence Time (s) plot

4.10 Oxygen Transport

The oxygen transport was reported as a function of the aortic root size, the area over the baffle, and the flow split ratio between the upper body circulation and the lower body circulation. The oxygen delivery and saturation were reported with different pulmonary vein saturation values (100%, 95%, 90%, 85%, 80 %) depending on how healthy the pulmonary system of a patient

Table 10 Results for the Ascending aorta and area over the baffle studies (TotalSys: Cardiac Output, DA: Descending Aorta)

	Ascending Aorta Size Study						The Area Over The Baffle Study				
case#	1	2	3	4	5	6	1	2	3	4	5
TotalSys(L/min)	2.93	2.96	2.93	2.92	2.93	2.91	2.93	2.91	2.93	2.91	2.88
DA%	63.07	62.5	62.63	63.04	62.7	62.36	63.07	63.99	62.76	62.68	62.72
O2 delivery	548.8	557.8	549.3	546.3	548.4	544.4	548.8	543.2	548.4	543.5	539.6
Saturation	84.99	85.52	85.1	84.96	85.07	84.82	84.99	84.69	85.07	84.98	85.0

4.10.1 Effect of Ascending Aorta Diameter

The total cardiac output for the AO study was 2.93 ± 0.02 (L/min) with a 60/40 split ratio between the lower body and upper body circulation, as shown in Table 10. Moreover, it can be seen that the changes in the AO diameter did not greatly affect the oxygen delivery compared to the nominal model (case 4), where the standard deviation of the total systemic oxygenation s was about ± 4.2 (average $549.17 \text{ l}\cdot\text{min}^{-1}\cdot\text{m}^{-2}$). Table 10 offers a closer look at the effects of the AO diameter on oxygen delivery and oxygen saturation, where 6 different aortic root configuration were used. For full detailed results, see the appendix.

Table 11 Total systemic flow rate in (Liter per minutes) as a function of Ascending Aorta size and flow percentage of each boundary (TOTSYS: Total Cardiac Output, DA: Descending Aorta, LcorA=Left Coronary Artery, RcorA=Right Coronary Artery, LCA=Left Caro

	TOTSYS(l/min)	DA[%]	LCA[%]	LSA[%]	LcorA[%]	RCA[%]	RSA[%]	RcorA[%]
1	2.94	63.08	7.53	11.22	1.65	8.70	5.18	2.64
2	2.97	61.51	4.44	8.53	1.66	12.91	8.47	2.49
3	2.93	62.63	6.98	10.29	1.65	9.49	6.40	2.57
4	2.92	63.04	7.54	11.08	1.67	8.56	5.41	2.68
5	2.93	62.77	7.27	11.31	1.66	9.12	5.22	2.66
6	2.92	63.36	7.46	10.83	1.66	8.58	5.45	2.67

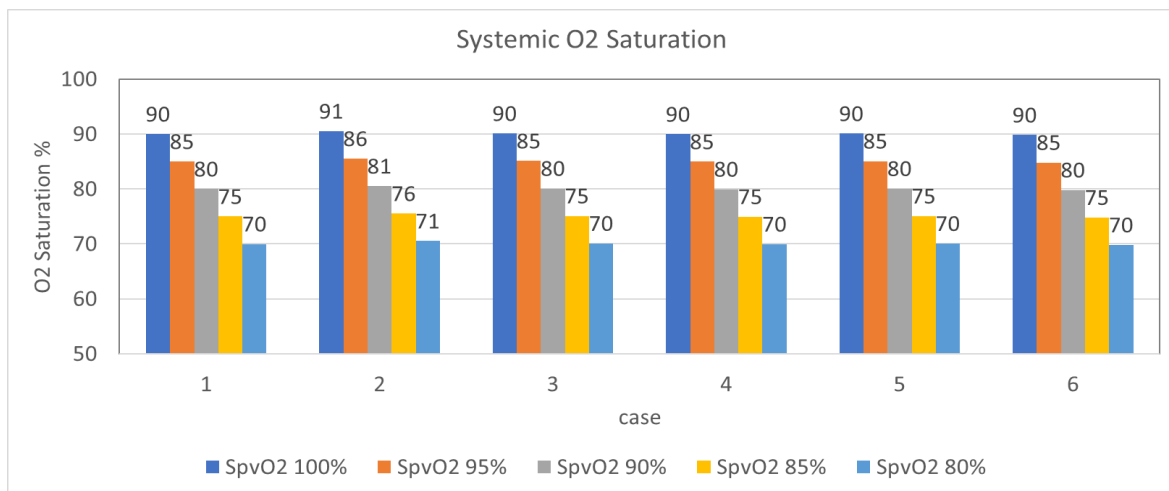


Figure 48 offers full detailed information about systemic saturation with different pulmonary venous saturation as a function of aorta size

4.10.2 Effect of Area over the Baffle

As illustrated in section 3.1 and 4.4, different geometries were created by varying the MPA narrowing sizes, measured as the minimum distance between the systemic baffle surface and the distal pulmonary trunk surface. In section 4.4, we reported that all the MPA narrowing sizes in that study did not cause pressure drops across the baffle above the clinically suggested threshold, and all our geometries fell well within the acceptable range. In this study, we looked into the

oxygen transport for the same synthetic geometries used in section 4.4 to quantify the effects the MPA narrowing may impose on the oxygen delivery. In Table 13, we reported the cardiac output and individual flow rates as a percentage of cardiac output with a 60/40 split ratio as a function of the area over the baffle. The average oxygen delivery was $(544.7 \pm 3.5 \text{ ml.min}^{-1} .\text{m}^{-2})$ and the saturation about 84.95 as shown in Table 10.

Table 12 Total Systemic Flow Rate (Liter per minutes) as a Function of Area over the Baffle and The Flow Percentage of Each Boundary (TOTSYS: Total Cardiac Output, DA: Descending Aorta, LcorA=Left Coronary Artery, RcorA=Right Coronary Artery, LCA=Left Carotid Artery, LSA=Left Subclavian Artery, RCA=Right Carotid Artery, RSA=Right Subclavian Artery)

	TOTSYS (L/min)	DA[%]	LCA[%]	LSA[%]	LcorA[%]	RCA[%]	RSA[%]	RcorA[%]
1	2.94	63.08	7.5	11.22	1.65	8.70	5.18	2.64
2	2.92	63.99	7.36	11.17	1.65	8.38	4.74	2.71
3	2.93	62.77	7.27	11.31	1.66	9.12	5.22	2.66
4	2.91	62.69	7.52	11.29	1.67	8.81	5.34	2.69
5	2.89	62.72	7.58	11.18	1.71	8.86	5.16	2.80

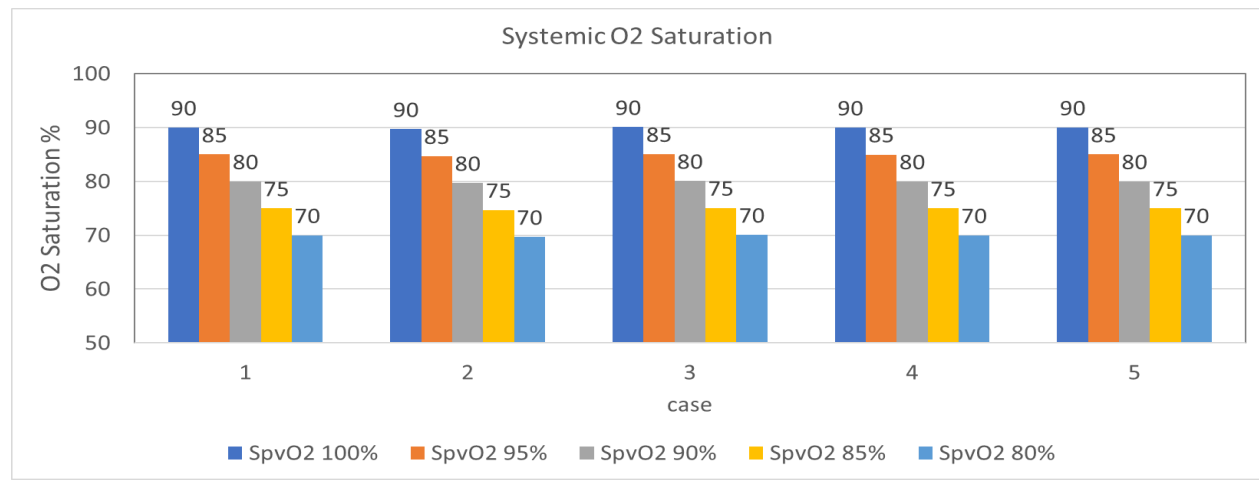


Figure 49 Full detailed information about systemic saturation with different pulmonary venous saturation as a function of the area over the baffle

4.10.3 Effect of the Split Ratio

In this study, we compare the systemic oxygen transport between the 60-40 and 50-50 split ratio of the nominal MPA size and $\pm 15\%$. The 50-50 did not hold the flow split after the solution convergence, as can be seen in Table 15; it is more like 55-45.

Table 13 Oxygen transport and oxygen saturation comparison between 60-40 and 50-50 split ratio for the nominal Case (TOTSYS: Total Cardiac Output, DA: Descending Aorta, PVO2: Pulmonary Venous Flow Oxygen Saturation)

<i>PULMONARY VENOUS SATURATION</i>	<i>OXYGEN RESULTS</i>		
	<i>Split ratio</i>	<i>TOTSYS(ml.min⁻¹)</i>	<i>Systemic Saturation</i>
100	50-50	578.64	91.3
	60-40	580.58	90.07
95	50-50	546.95	86.3
	60-40	548.35	85.1
90	50-50	515.27	81.3
	60-40	516.12	80.1
85	50-50	483.58	76.3
	60-40	483.89	75.07
80	50-50	451.9	71.3
	60-40	451.66	70.07

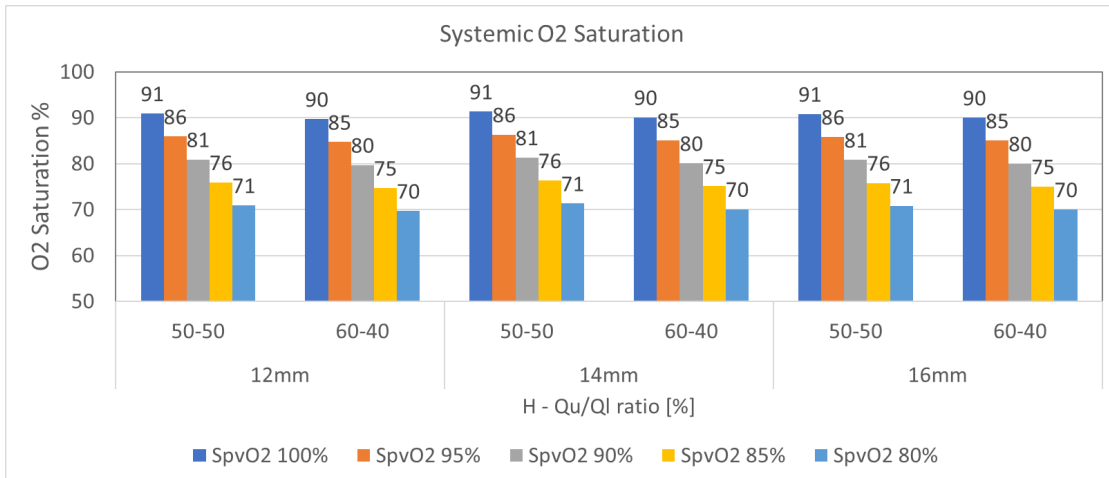


Figure 50 full detailed information about systemic saturation with different pulmonary venous saturation as a function of the blood flow split ratio

Table 14 Total systemic flow rate (Liter per minutes) as a function split ratio and the flow percentage of each boundary (TOTSYS: Total Cardiac Output, DA: Descending Aorta, LcorA=Left Coronary Artery, RcorA=Right Coronary Artery, LCA=Left Carotid Artery, LSA=Left Subclavian Artery, RCA=Right Carotid Artery, RSA=Right Subclavian Artery)

	TOTSYS	DA%	LCA%	LSA%	LcorA%	RCA%	RSA%	RcorA%
50-50	2.88	58.45	6.93	12.93	1.58	11.85	5.70	2.58
60-40	2.92	63.99	7.36	11.2	1.65	8.38	4.74	2.71
65-35	2.91	66.85	6.14	9.78	1.72	8.129	4.54	2.59

CHAPTER FIVE: CONCLUSION

5.1 Conclusion

In this study, we have demonstrated a preliminary numerical analysis of a novel surgical procedure for select newborns with single ventricle congenital heart disease. Using CFD techniques, we investigated the flow in the systemic and pulmonary circulations in particular near the baffle at the distal arch stenosis and near the T-junction of the SVC to the pulmonary arteries. We display a viable model to investigate the HCS2 procedure critically.

In the first part of the analysis, we ensure that the mesh used for the unsteady calculation would provide repeatable results. Similarly, under steady-state condition, we analyzed vortex shedding from the baffle and determined that due to inadequate distances, vortices would be dissipated at an early stage. Then we focused on geometrical features such as converging-diverging nozzles that produce flow accelerations, hence large localized wall shear stress loads. This was observed near the baffle. Large shear loads on the local tissue may cause damage. In both circulations, there are two instances of flow impingement at the T-junction in the pulmonary circulation and at the foreface of the baffle. Flow impinging on the surface generates high local load concentrations, which, on a pulmonary artery, may cause vessel damage or even rupture and on the baffle, may induce fatigue failure in the underlying stent. We will investigate these loading conditions to ensure that over a prolonged period, the stent does not buckle as this would compromise the pulmonary circulation. We will report the results of this study in the near future.

We isolated the baffle surface to further observe wall shear stress loads in relation to the oscillatory nature of the unsteady flow. We have shown that throughout a cardiac cycle, the flow detaches in systole and subsequently reattaches to the baffle surface. This induces very distinct

wall shear distributions on the surface. In systole, wall shear stress magnitudes are rather elevated, and in diastole, we observe uneven wall shear stress distribution, which can alter the mechanical and chemical properties of the local tissue. It must be noted that due to the complex topology, irregular flow patterns such as recirculation regions and strong secondary flows are generated. Given the current model, there is an opportunity to computationally explore, via shape optimization, topological improvement of the HCS2. Moreover, loading conditions on the stent obtained from these computations can serve as input to the mechanical analysis of the stented baffle.

The effect of incremental flow obstruction due to the baffle was also investigated to ensure that the model did not include MPA narrowing sizes that caused pressure drops across the baffle above the clinically suggested threshold. We concluded that our geometries fell well within the acceptable range.

The average particle residence time was about 0.5 (s) which is equal to the same period each heart cycle takes. The peak time was also reported and the results show that some particles might take up to (3 s) to exit the fluid domain. Finally, the energy loss and energy efficiency were calculated as a function of split ratio and baffle related narrowing. Across all models, the efficiency was shown to be high.

The systemic oxygen transport model was derived based on conservation of mass and oxygen uptake and consumption. Three geometric parameters were modified while calculating oxygen saturation: (1) The aortic root size, (2) The baffle related narrowing and (3) the flow split ratio. The saturation results showed consistency with published Glenn procedure data and the change in the ascending aorta size did not have a great impact on the oxygen transport.

5.2 Limitations

The first limitation of this study is the rigid vessel wall assumption for all the models in this study. However, a study by [181] found a little effect of implementing fluid-structure interaction (FSI) on pressure and energy efficiency. For the particle residence time study, we assumed massless particles that passively convected by the converged fluid domain. The adhesion between the particles and the walls were neglected. We also did not look at how long particles spend at certain location since we are looking for the total accumulative time. The discrete method used in this study to measure PRT is mesh independency which means that the calculated time highly dependent on the orientation of the cells.

5.3 List of Current Publication

Journal:

- Marwan Hameed MS, Ray Prather PhD, Eduardo Divo, Alain Kassab PhD, David Nykanen MD, Michael Farias MD MS MBA and William DeCampli MD, PhD “A Computational Fluid Dynamics Investigation of a Novel Hybrid Comprehensive Stage II Operation” *Journal of Thoracic Cardiovascular Technology* (in submission)
- Marwan Hameed MS, Ray Prather PhD, Eduardo Divo PhD2, Alain Kassab PhD, David Nykanen MD, Michael Farias MD MS MBA and William DeCampli MD, PhD “Multi-Scale Modeling of the Hybrid Comprehensive Stage II Circulation: Effects of Descending Aorta, Area over the Baffle and Split Ratio” , *BMES Journal of Cardiovascular Technology* (in preparation).

Conference:

- Marwan Hameed, Ray Prather, Eduardo Divo, Alain Kassab, David Nykanen, Michael Farias And William Decampli ”Multi-Scale Computational Fluid Dynamics Analysis Of A Novel Hybrid Comprehensive Stage II Surgery For Single Ventricle Circulation” at the 6th International Conference on Clinical and Engineering Frontiers in Pediatric and Congenital Heart Disease Conference , MAY 9-11, 2019 PHILADELPHIA ,PA (Abstract and Poster Presentation).
- Marwan Hameed, Arka Das, Ray Prather, Eduardo Divo, Alain Kassab, David Nykanen, Michael Farias And William Decampli “Overview Of An In-Vitro And In-Silico Analysis Of A Novel Hybrid Comprehensive Stage II Surgery For Single Ventricle Circulation” At The 2019 Bmes Annual Meeting, October 16-19, 2019 Philadelphia ,Pa (Abstract And Poster Presentation)
- Marwan Hameed, Ray Prather, Eduardo Divo, Alain Kassab, David Nykanen, Michael Farias And William Decampli A Multi-Scale Computational Fluid Dynamics Investigation of a Novel Hybrid Comprehensive Stage II Operation for Single Ventricle Circulation” at the VIII International Conference on Coupled Problems in Science and Engineering,, June 3-5 2019 , Barcelona, Spain (Abstract and Oral Presentation)

APPENDIX A: FULL LPM EQUATIONS

Current Auxiliary Equations

$$i_1 = \frac{y_1 - y_2}{R_{tri}} * hev(y_1, y_2)$$

$$i_2 = \frac{y_2 - y_3}{R_{rv}} * hev(y_2, y_3)$$

$$i_1 = \frac{y_3 - y_{34}}{R_{aorta}} * hev(y_3, y_{34})$$

$$I_{in}(y) = \frac{y_{21} - y_1}{R_{ivb}} + \frac{y_{24} - y_1}{R_{corvb}} + \frac{y_{30} - y_1}{R_{lpvb}} + \frac{y_{31} - y_1}{R_{rpvb}}$$

where $hev(x1, x2) = \begin{cases} 1 & \text{if } x1 - x2 > 0 \\ 0 & \text{if } x1 - x2 \leq 0 \end{cases}$ is a heaviside step function

Voltage Auxiliary Equations

$$v_1(y) = R_{da}(y_4 - y_7) + y_5$$

$$v_2(y) = R_{lsa}(y_7 + y_{10}) + y_8$$

$$v_3(y) = R_{lca}(y_{13} - y_{10}) + y_{11}$$

$$v_5(y) = \frac{y_{18} - y_{13} + \left(\frac{y_{14}}{R_{rsa}} + \frac{y_{16}}{R_{lca}} \right)}{\frac{1}{R_{rsa}} + \frac{1}{R_{rca}}}$$

$$v_4(y) = R_{ia}(y_{18} - y_{13}) + v_5(y)$$

$$v_6(y) = \frac{y_{18} + \left(\frac{y_{19}}{R_{rcora}} + \frac{y_{20}}{R_{lcora}} + \frac{y_3}{R_{aorta}} \right)}{\frac{1}{R_{rcora}} + \frac{1}{R_{lcora}} + \frac{1}{R_{aorta}}}$$

$$y(1) = \frac{1}{C_{ra}} (I_{in}(y) - i_1(y))$$

$$y(2) = \frac{1}{C_{rv(t)}} (i_1(y) - i_2(y) * dc_{rv(t)}(y) - i_3(y))$$

$$y(3) = \frac{1}{C_{pa}} (i_2(y) - y_4)$$

$$y(4) = \frac{1}{L_{pa}} (y_3 - y_4 * R_{pa} - v1(y))$$

$$y(5) = \frac{1}{C_{IVb}} \left(\frac{v1(y) - y_5}{R_{da}} - y_6 \right)$$

$$y(6) = \frac{1}{L_{Ivb}} (y_5 - y_6 * R_{Ivb} - y_{21})$$

$$y(7) = \frac{1}{L_{I_{da_lsa}}} (v1(y) - y_7 * R_{da_lsa} - v2(y))$$

$$y(8) = \frac{1}{C_{Isb}} \left(\frac{v2(y) - y_8}{R_{lsa}} - y_9 \right)$$

$$y(9) = \frac{1}{L_{Isb}} (y_8 - y_9 * R_{Isb} - y_{22})$$

$$y(10) = \frac{1}{L_{I_{sa_ica}}} (v3(y) - y_{10} * R_{I_{sa_ica}} - v2(y))$$

$$y(11) = \frac{1}{C_{Icb}} \left(\frac{v3(y) - y_{11}}{R_{ica}} - y_{12} \right)$$

$$y(12) = \frac{1}{L_{Icb}} (y_{11} - y_{12} * R_{Icb} - y_{23})$$

$$y(13) = \frac{1}{L_{lcaia}} (v4(y) - y_{13} * R_{lcaia} - v3(y))$$

$$y(14) = \frac{1}{C_{rsb}} \left(\frac{v5(y) - y_{14}}{R_{rsa}} - y_{15} \right)$$

$$y(15) = \frac{1}{L_{rsb}} (y_{14} - y_{15} * R_{rsb} - y_{22})$$

$$y(16) = \frac{1}{C_{rcb}} \left(\frac{v5(y) - y_{16}}{R_{rca}} - y_{17} \right)$$

$$y(17) = \frac{1}{L_{rcb}} (y_{16} - y_{17} * R_{rcb} - y_{23})$$

$$y(18) = \frac{1}{L_{iacora}} (y_{34} - y_{18} * R_{iacora} - v4(y))$$

$$y(19) = \frac{1}{C_{rcorab}} \left(\frac{y_{34} - y_{19}}{R_{rcora}} - \frac{y_{19} - y_{24}}{R_{rcorab}} \right)$$

$$y(20) = \frac{1}{C_{lcorab}} \left(\frac{y_{34} - y_{20}}{R_{lcora}} - \frac{y_{20} - y_{24}}{R_{lcorab}} \right)$$

$$y(21) = \frac{1}{C_{ivb}} \left(y_6 - \frac{y_{21} - y_1}{R_{ivb}} \right)$$

$$y(22) = \frac{1}{C_{dsb}} \left(y_{15} + y_9 - \frac{y_{22} - y_{32}}{R_{dsb}} \right)$$

$$y(23) = \frac{1}{C_{dcb}} \left(y_{12} + y_{17} - \frac{y_{23} - y_{32}}{R_{dcb}} \right)$$

$$y(24) = \frac{1}{C_{corvb}} \left(\frac{y_{19} - y_{24}}{R_{rcorab}} + \frac{y_{20} - y_{24}}{R_{lcorab}} - \frac{y_{24} - y_1}{R_{corvb}} \right)$$

$$y(25) = \frac{1}{C_{rlung}} \left(\frac{v7(y) - y_{25}}{R_{rpa}} - y_{26} \right)$$

$$y(26) = \frac{1}{L_{rlung}} (y_{25} - y_{26} * R_{rlung} - y_{31})$$

$$y(27) = \frac{1}{L_{baffle}} (v7(y) - y_{27} * R_{baffle} - y_{28})$$

$$y(28) = \frac{1}{C_{Llung}} (y_{27} - y_{29})$$

$$y(29) = \frac{1}{L_{Llung}} (y_{28} - y_{29} * R_{Llung} - y_{30})$$

$$y(30) = \frac{1}{C_{lpvb}} \left(y_{29} - \frac{y_{30} - y_1}{R_{lpvb}} \right)$$

$$y(31) = \frac{1}{C_{rpvb}} \left(y_{26} - \frac{y_{31} - y_1}{R_{rpvb}} \right)$$

$$y(32) = \frac{1}{C_{svc}} \left(\frac{y_{22} - y_{32}}{R_{dsb}} + \frac{y_{23} - y_{32}}{R_{dcb}} - y_{33} \right)$$

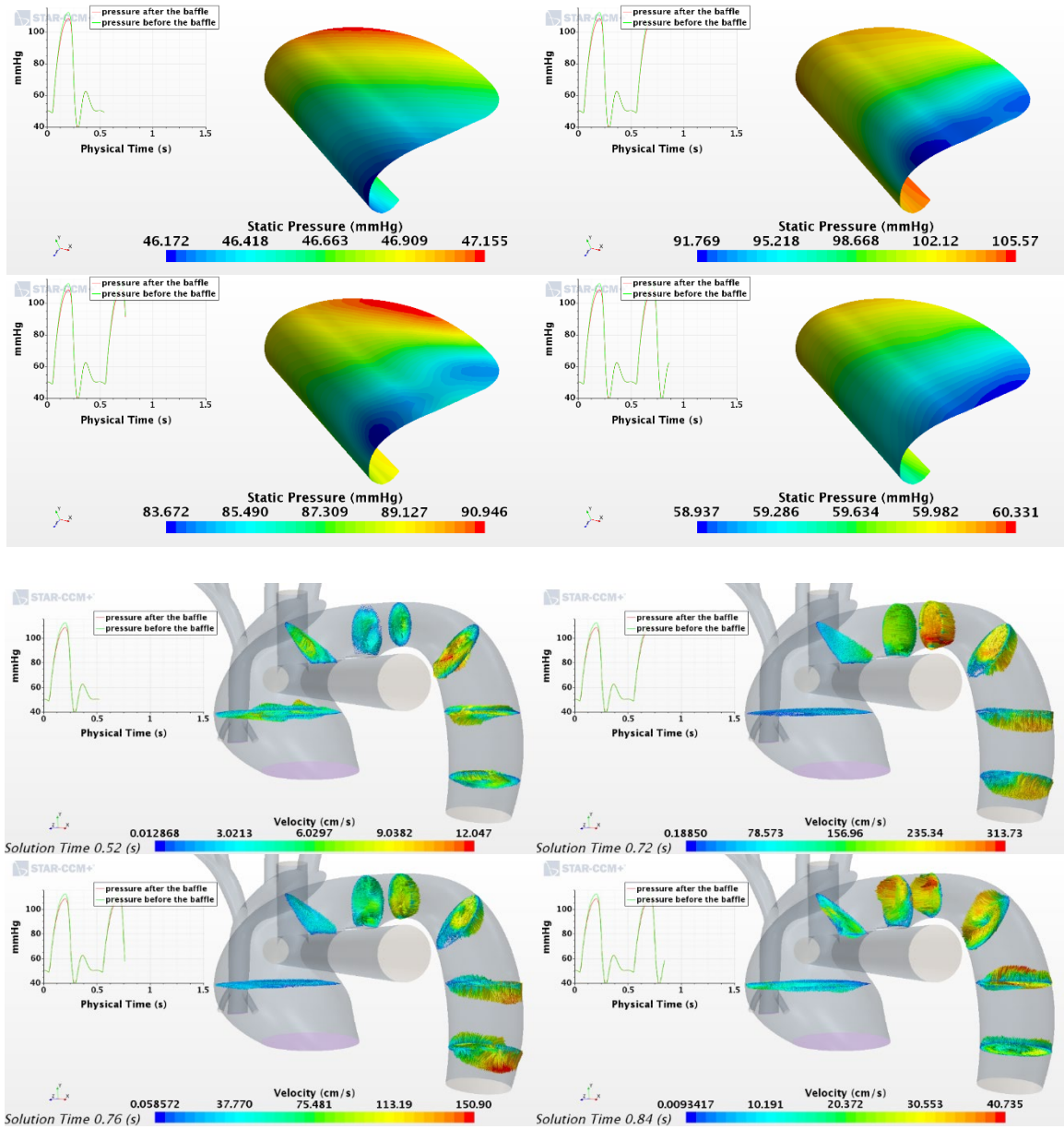
$$y(33) = \frac{1}{L_{svc}} (y_{32} - y_{33} * R_{svc} - v7(y))$$

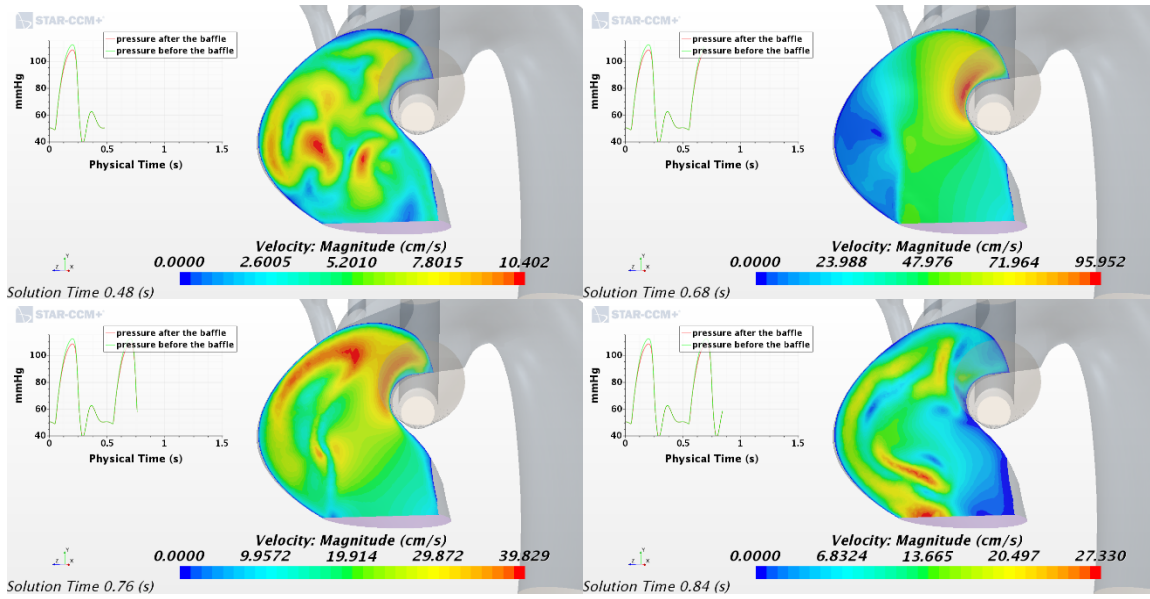
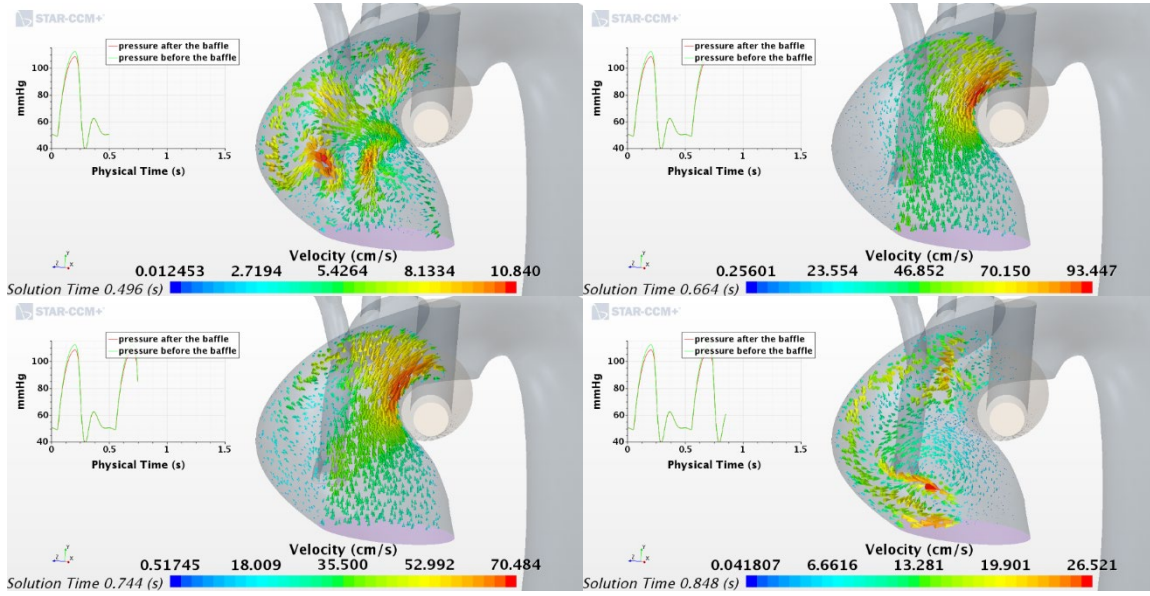
$$y(34) = \frac{1}{C_{aorta}} \left(i_3(y) - y_{18} - \frac{y_{34} - y_{20}}{R_{lcora}} - \frac{y_{34} - y_{19}}{R_{rcora}} \right)$$

where $dC(t) = \frac{C(t + \Delta t) - C(t)}{\Delta t}$ and $\Delta t = 10^{-6}$

APPENDIX B: AORTA SIZE STUDY CFD SCENES

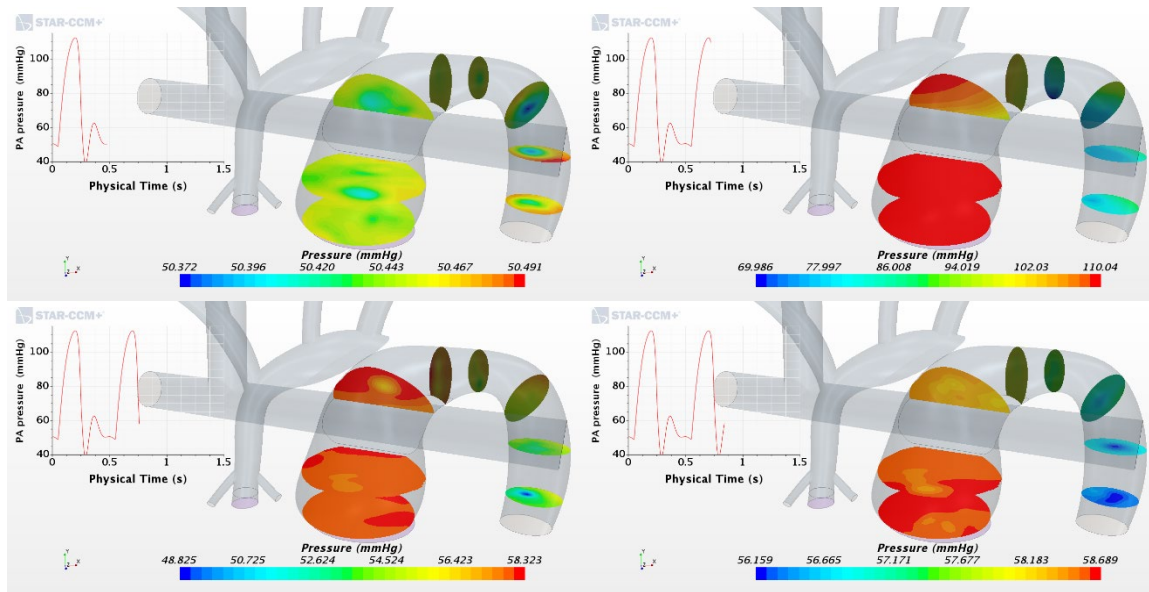
Case1



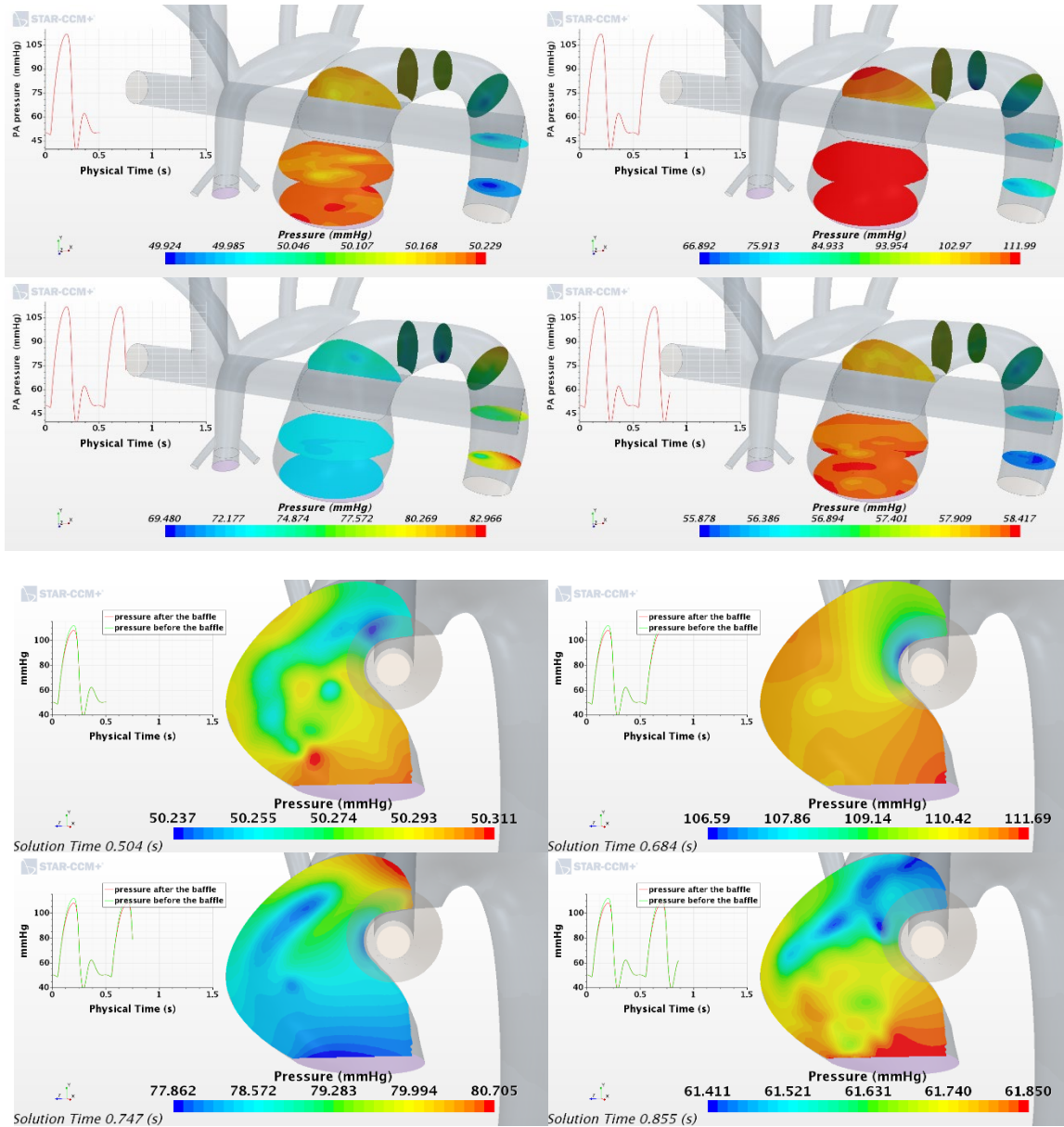


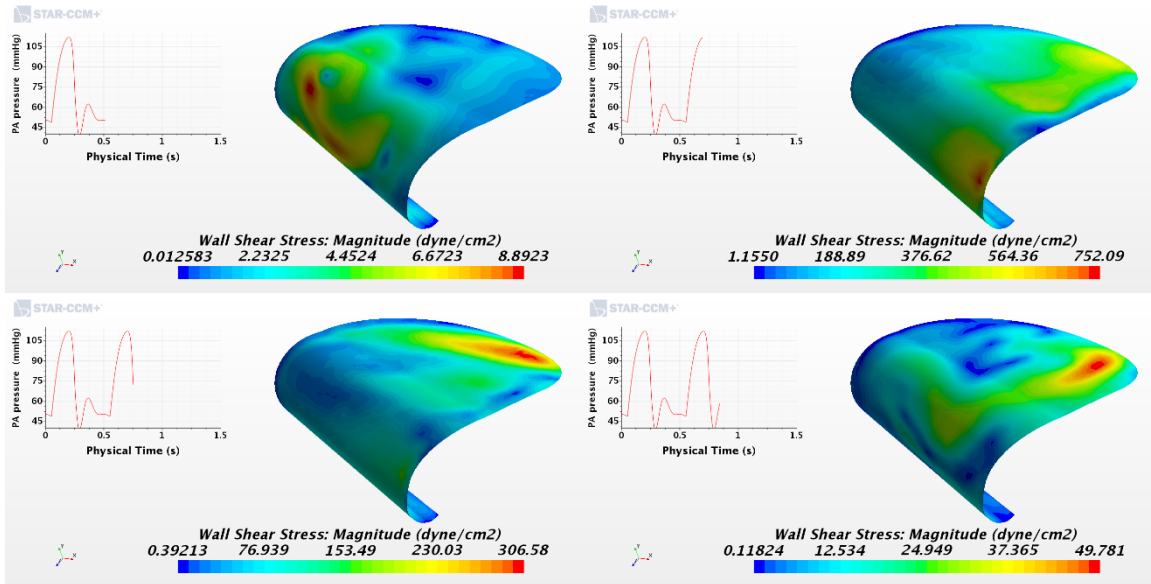
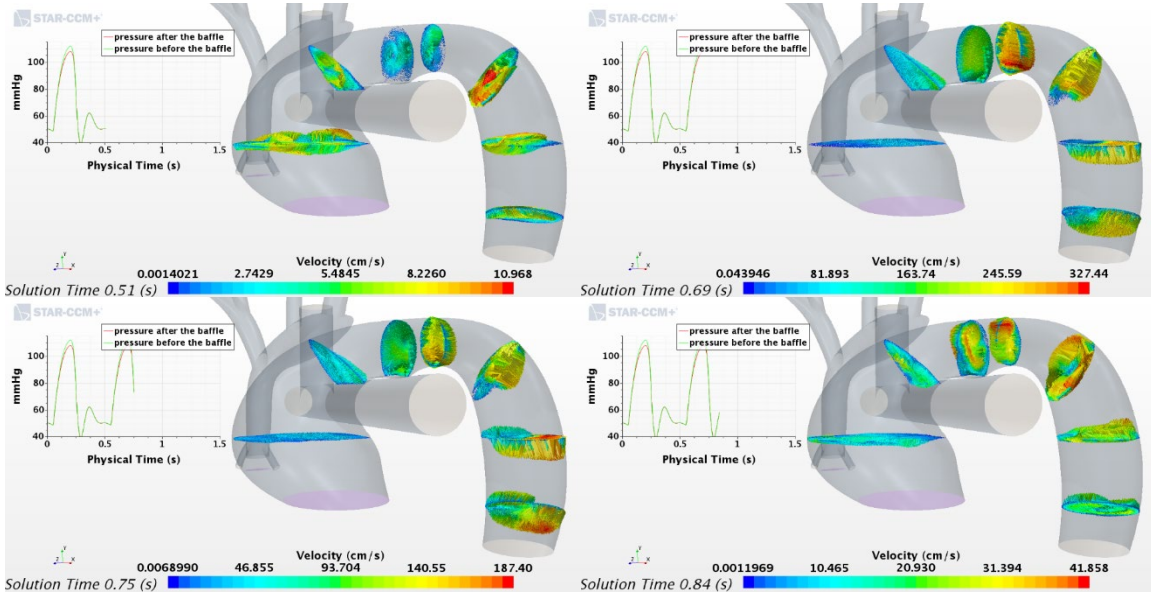
Case1

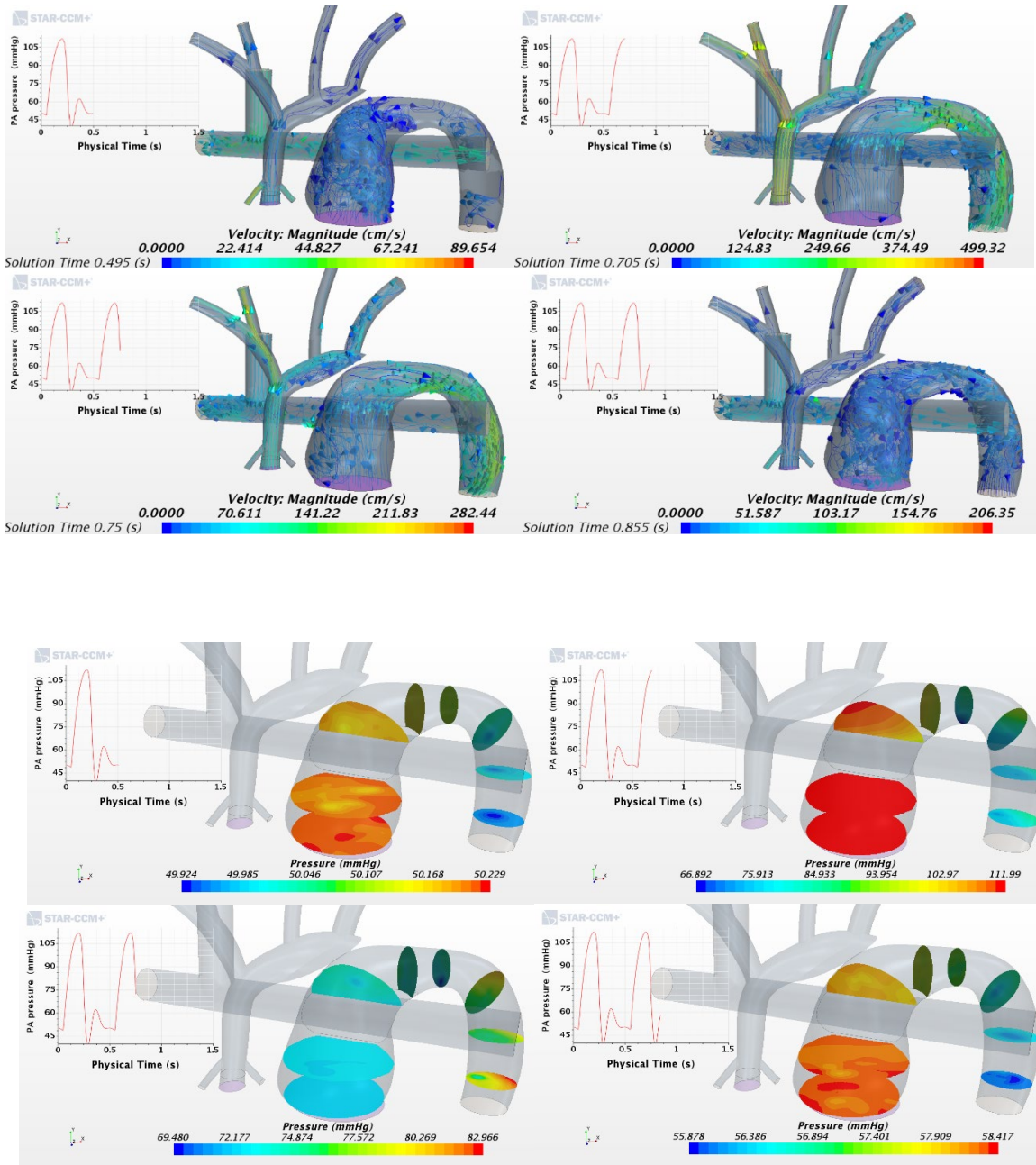
CASE3

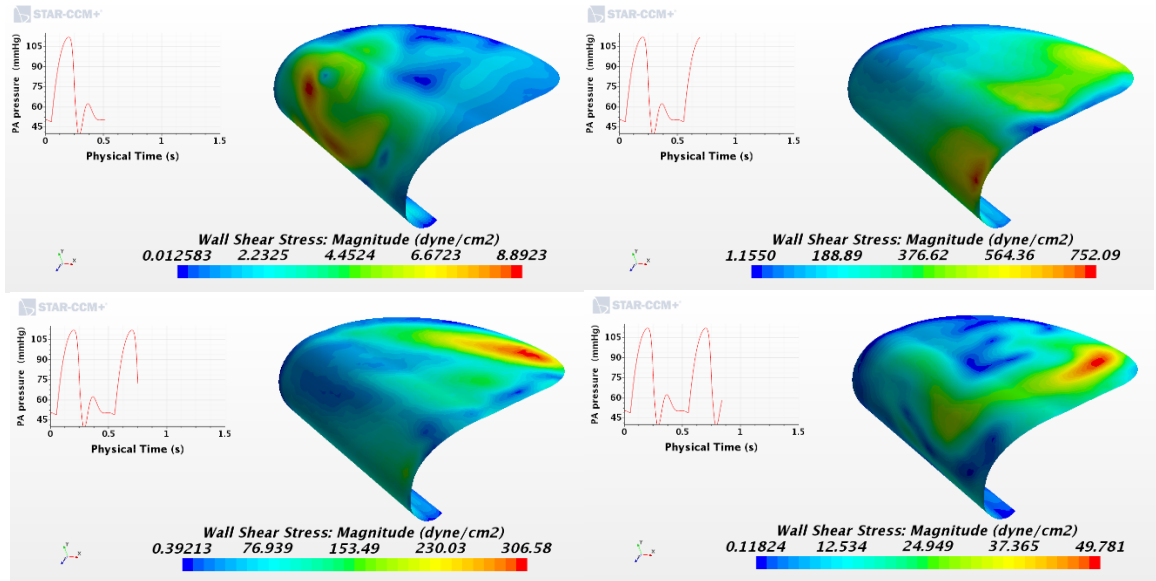
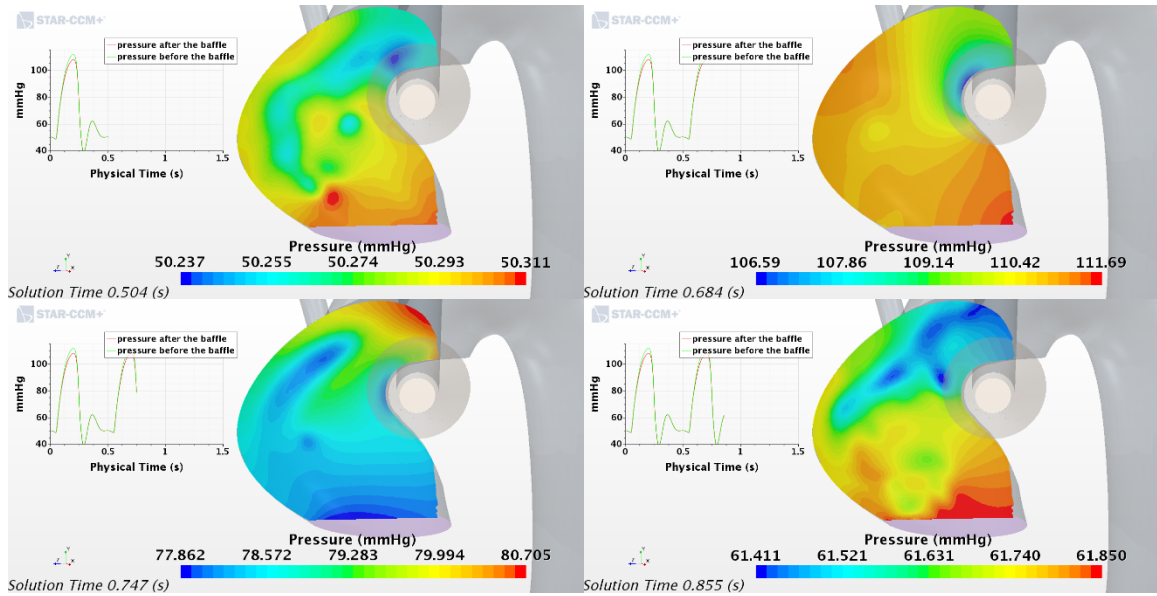


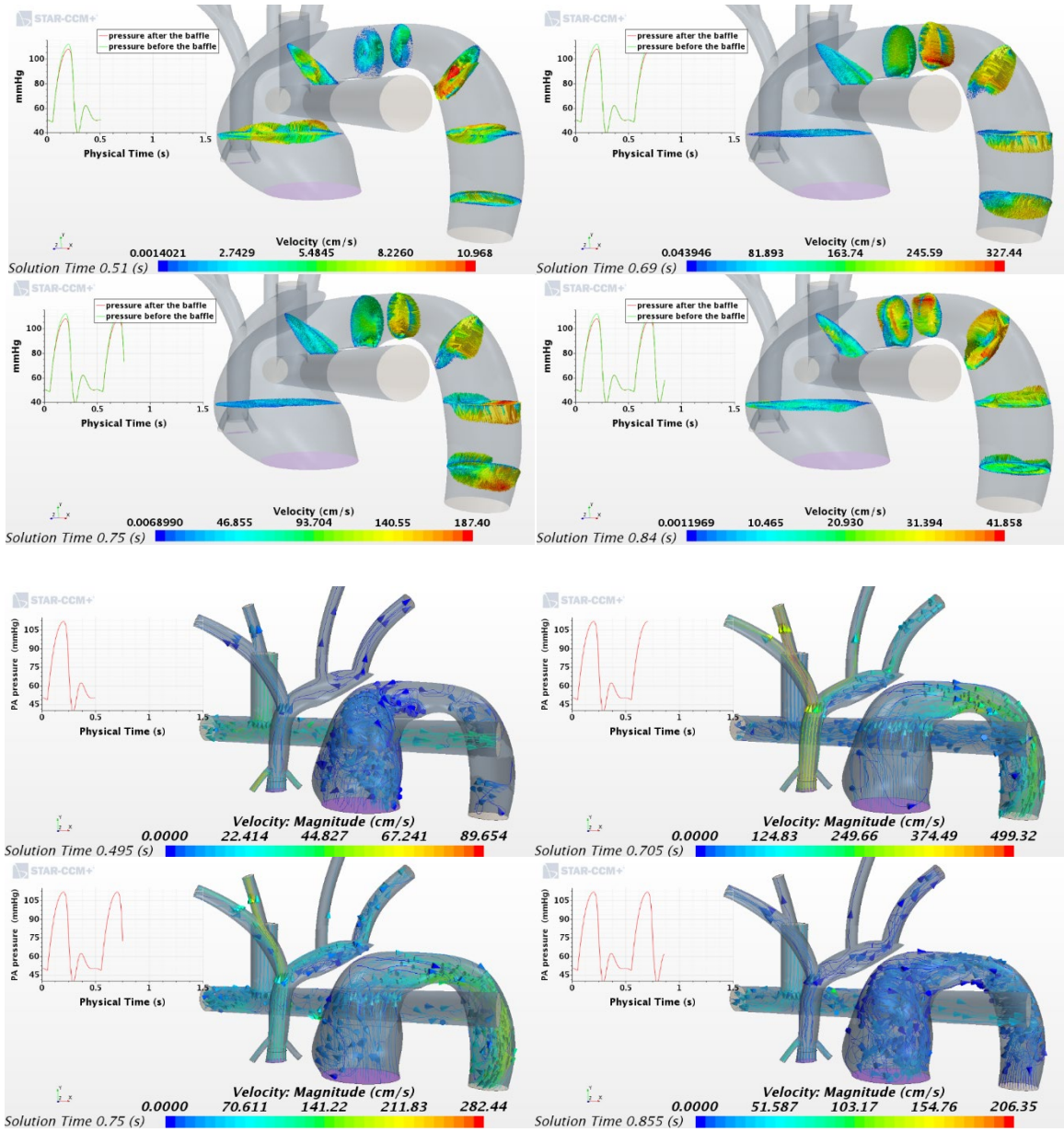
Case2



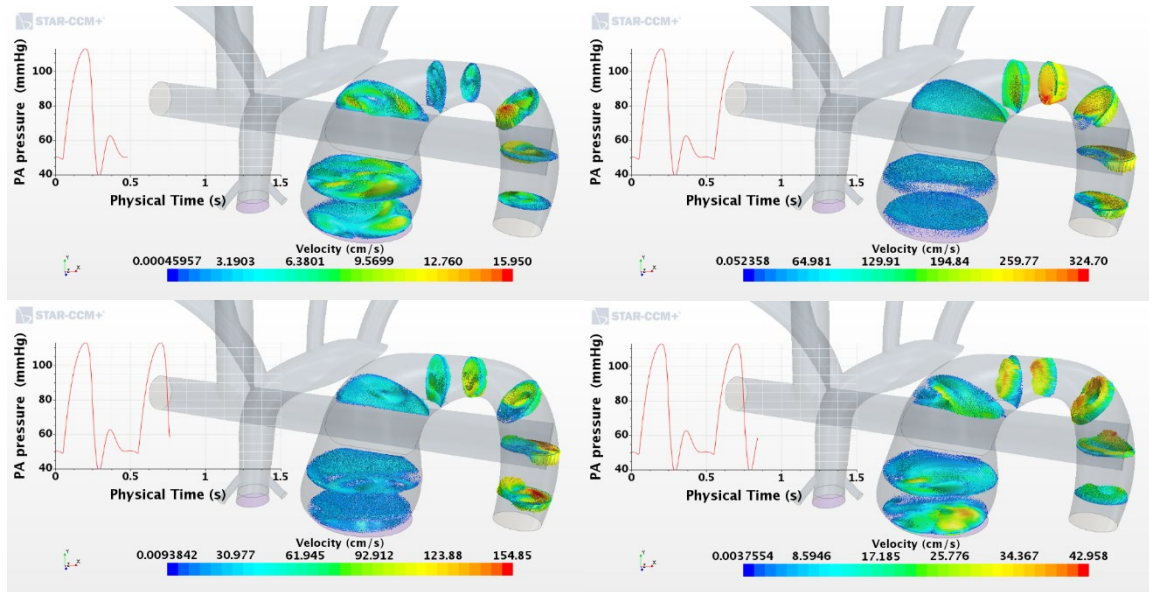
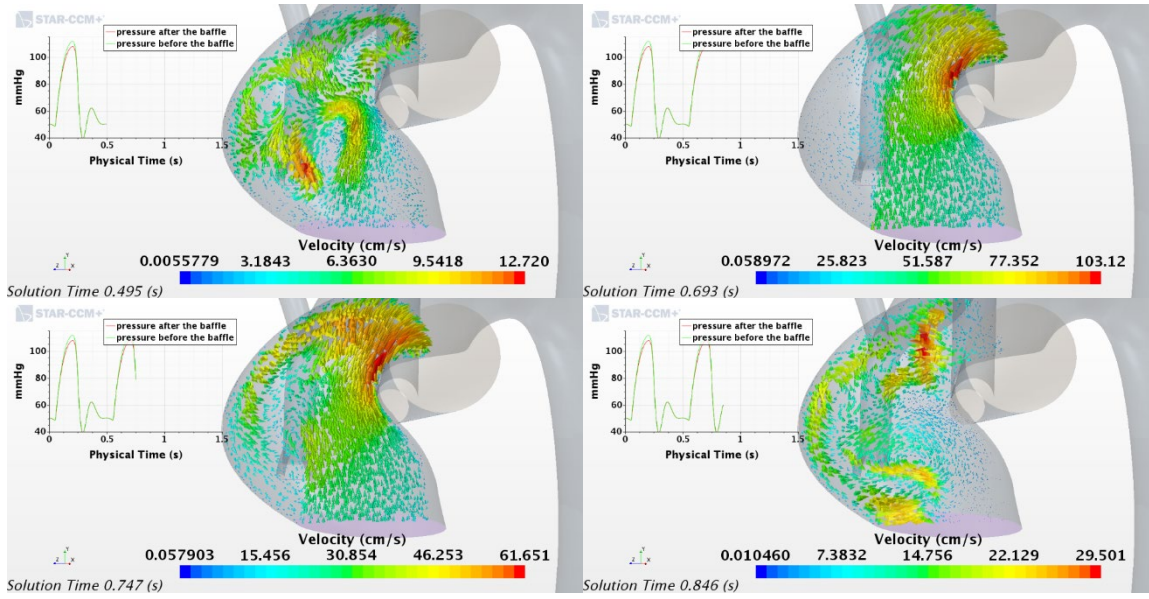




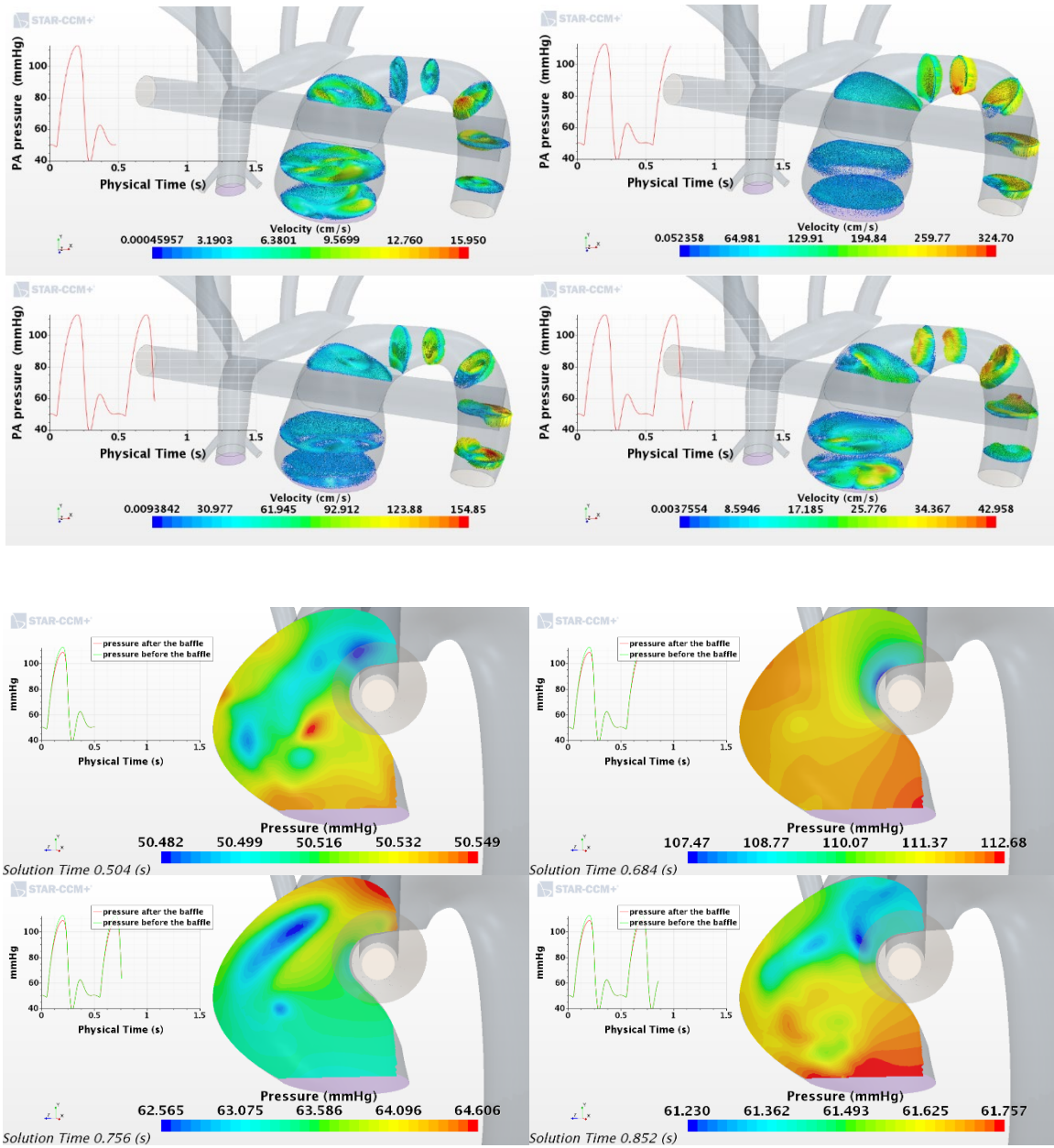




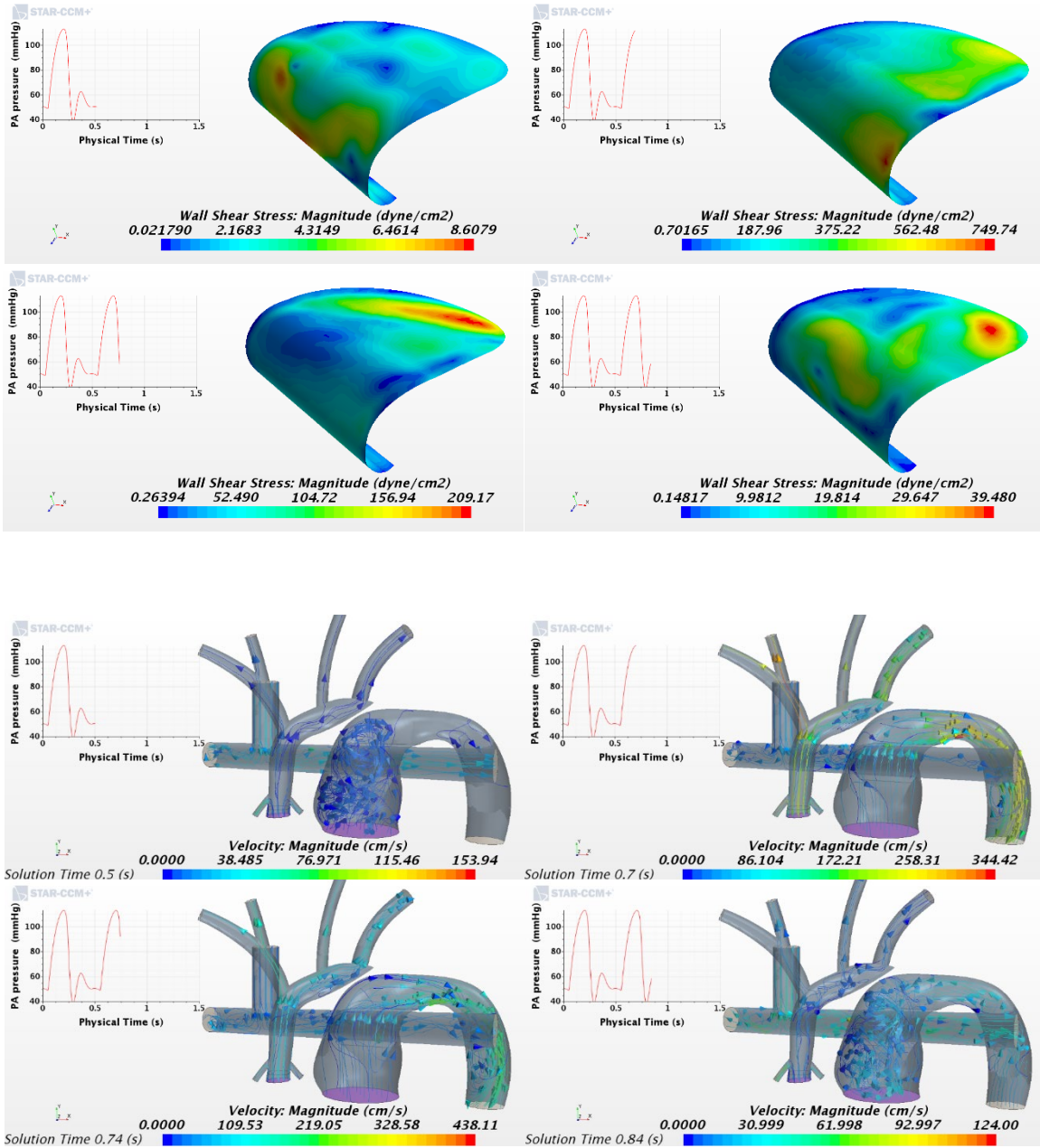
Case3

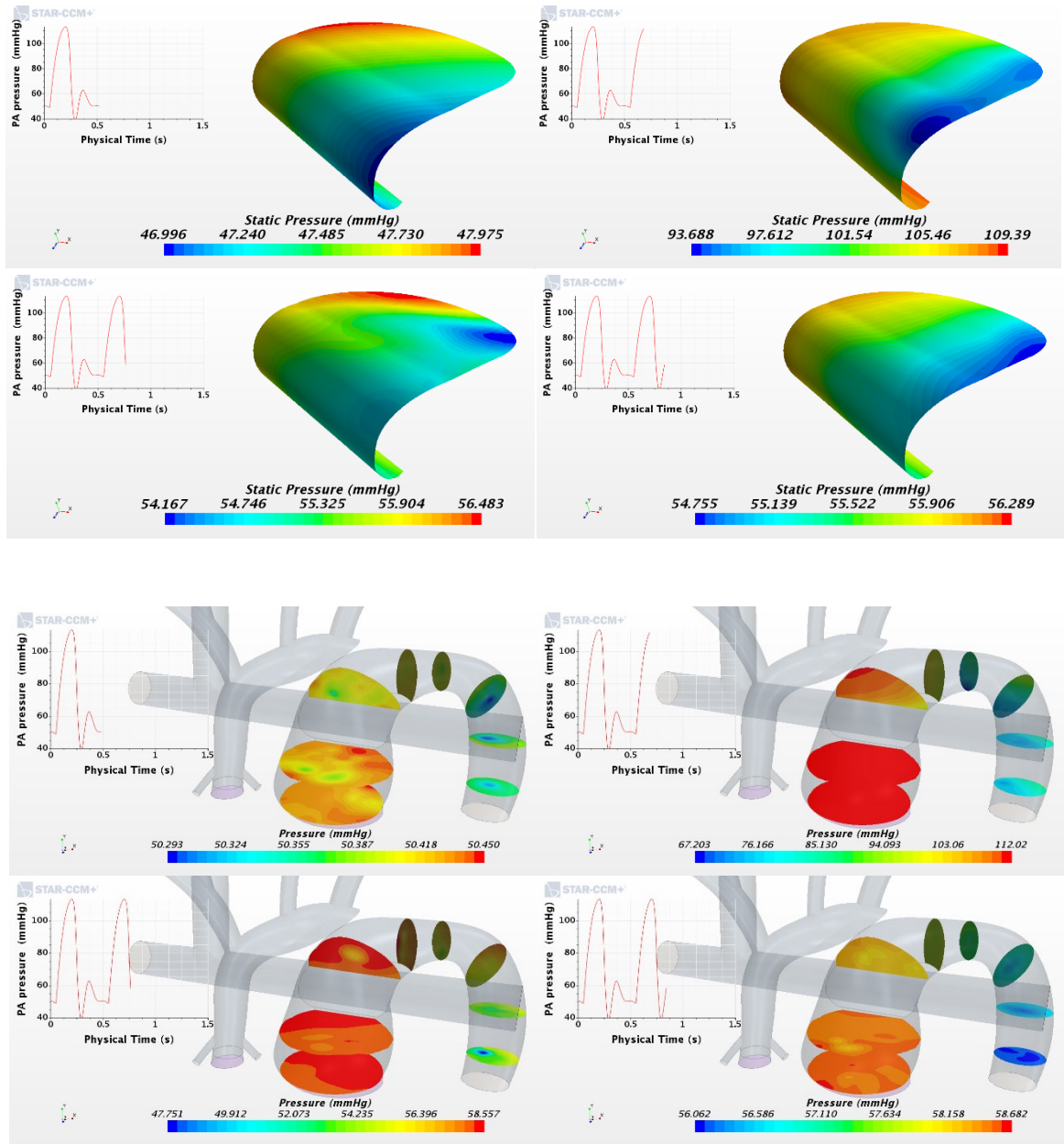


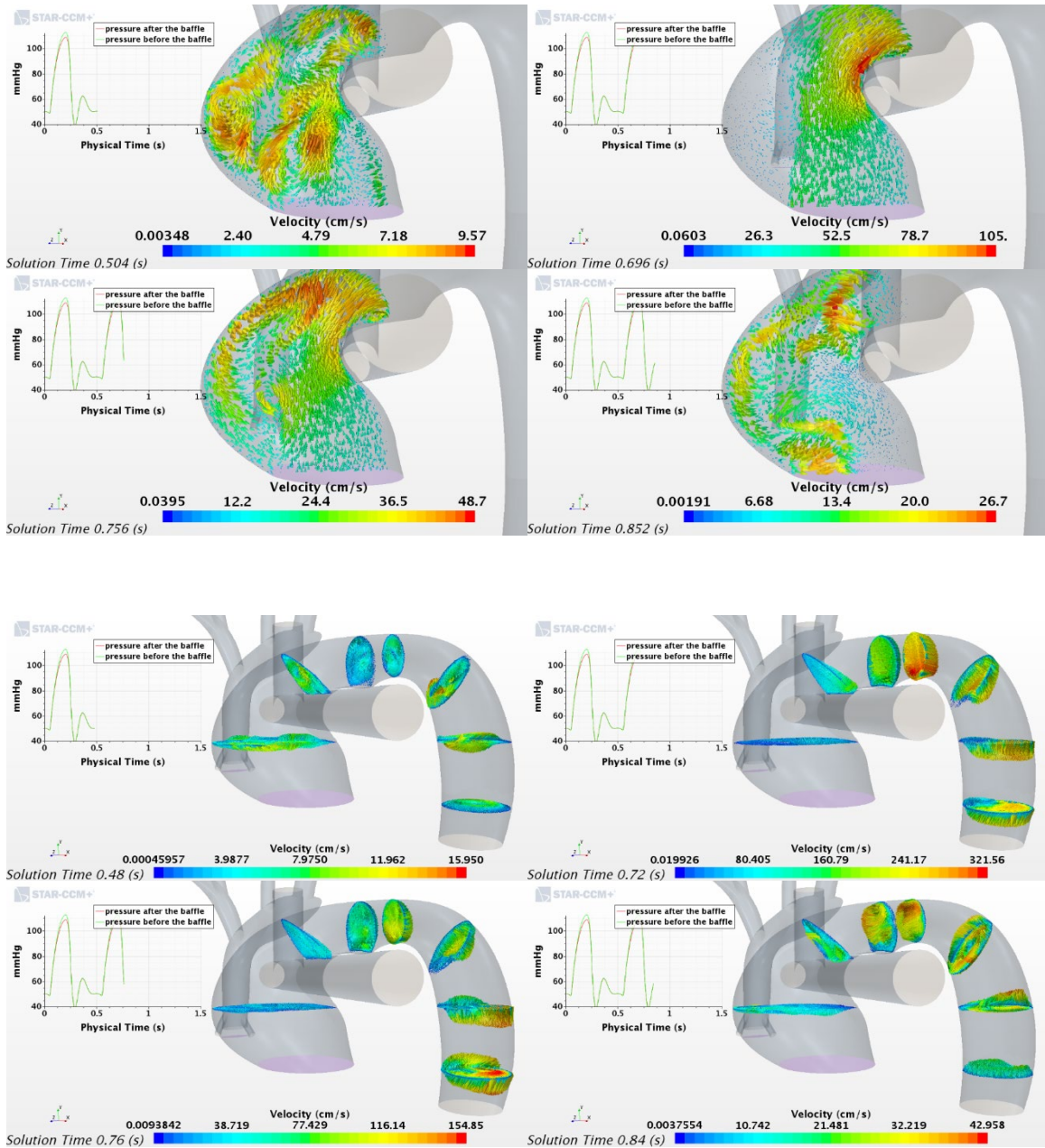
Case5



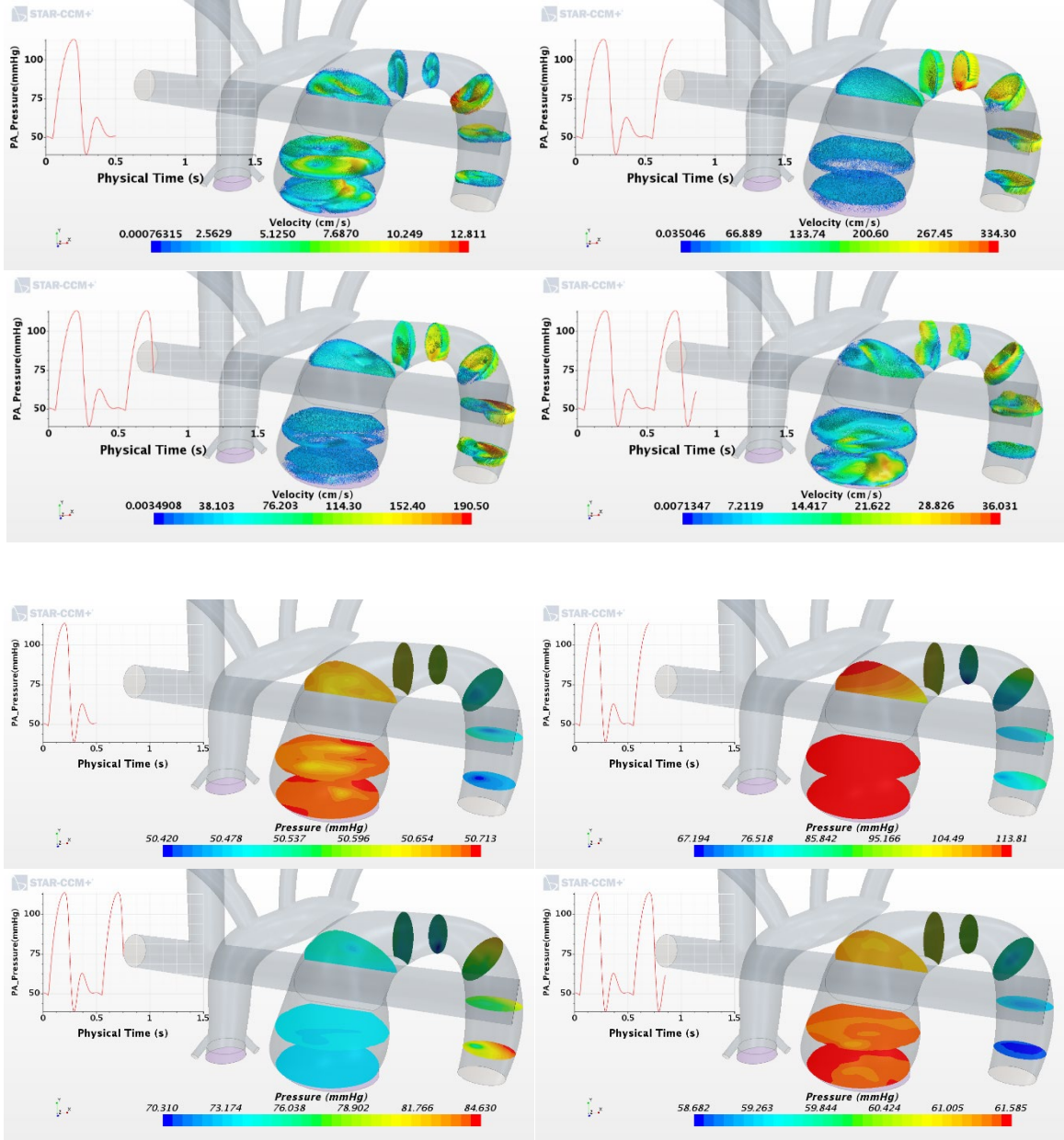
Case5

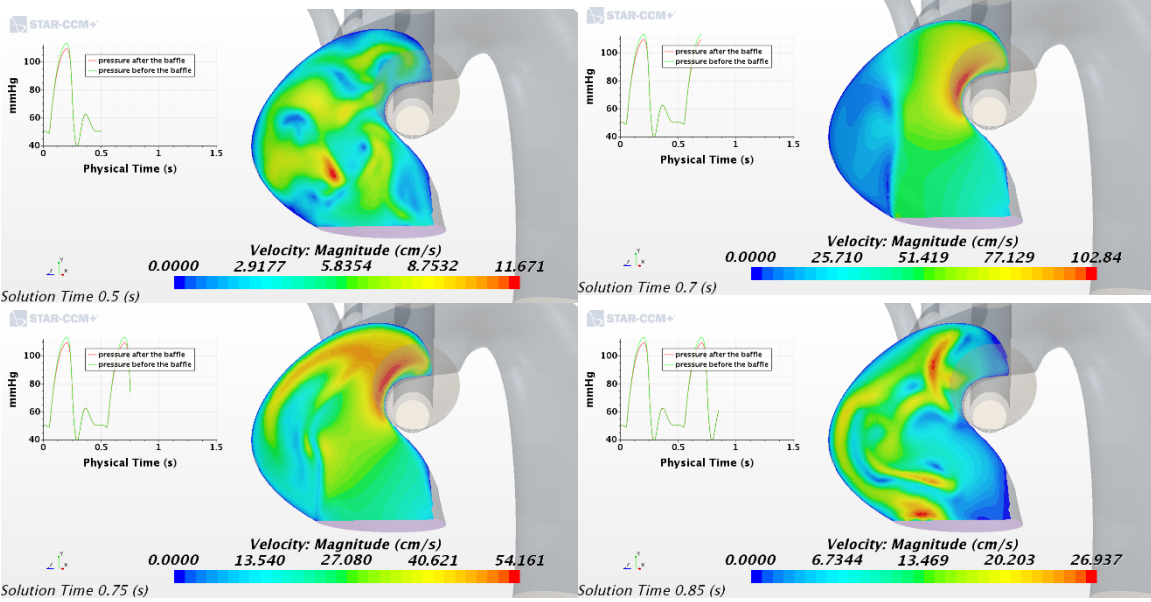
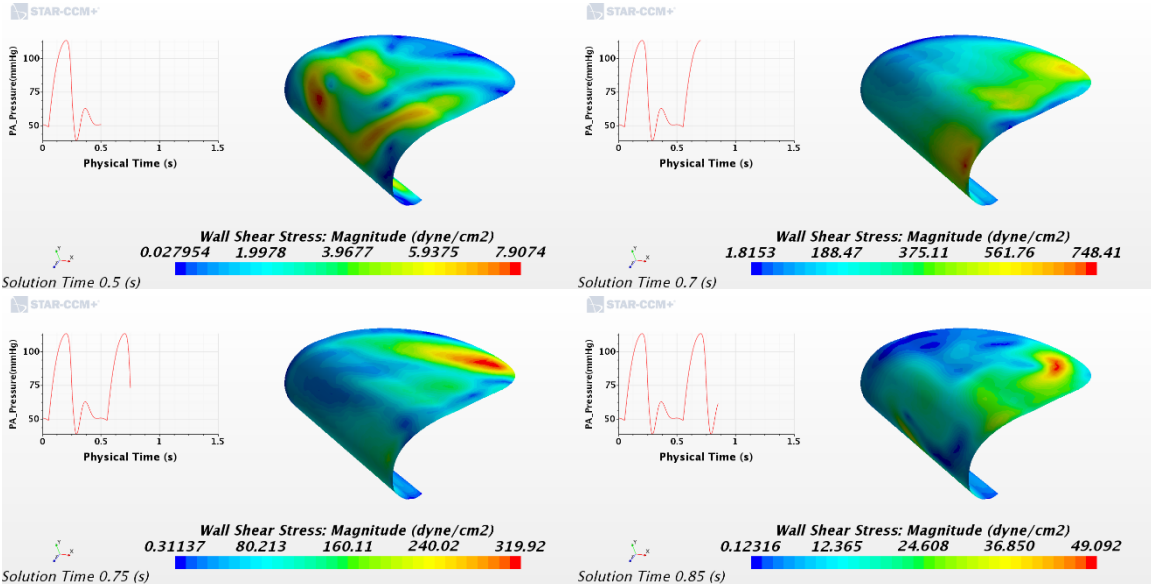


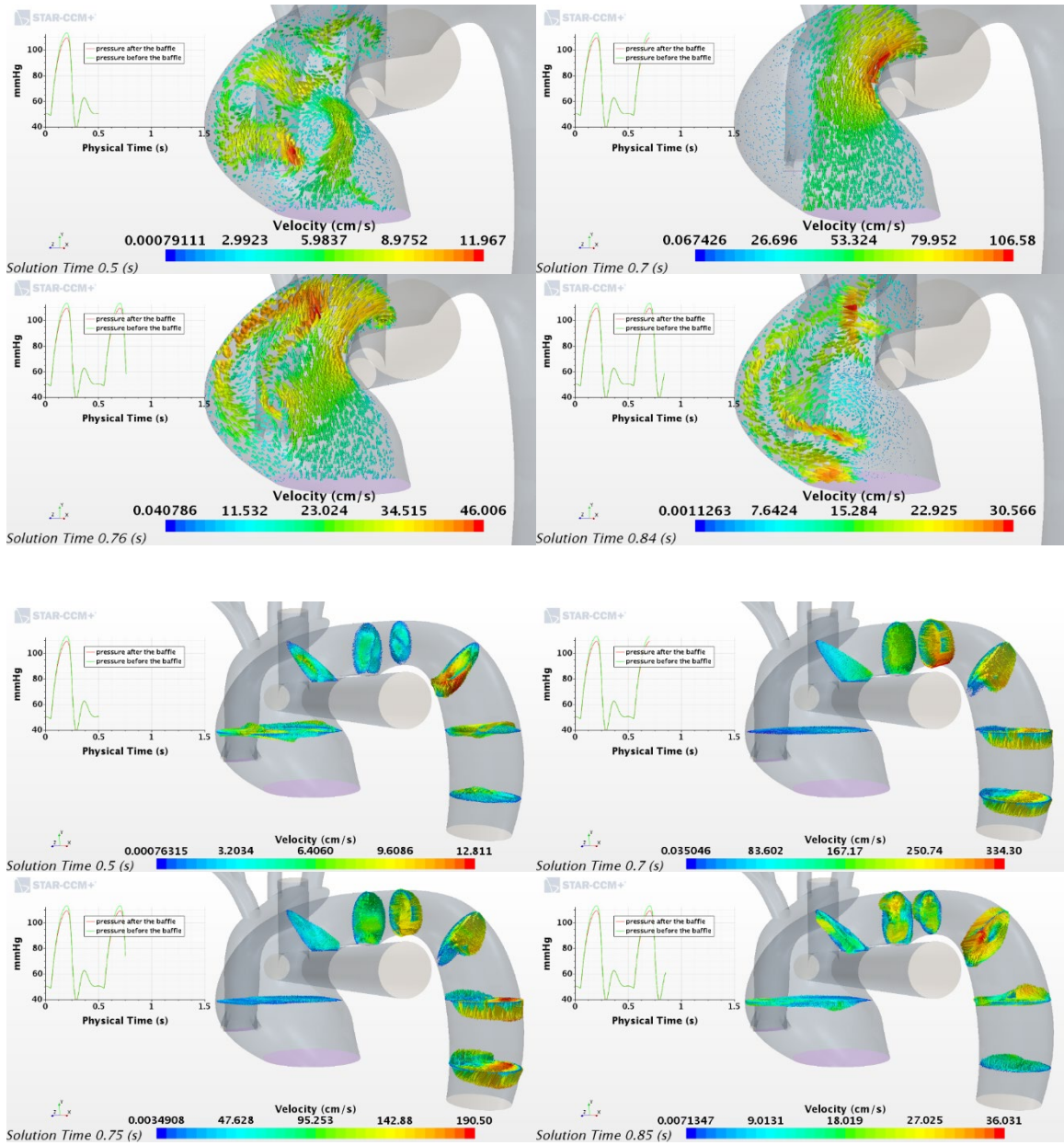


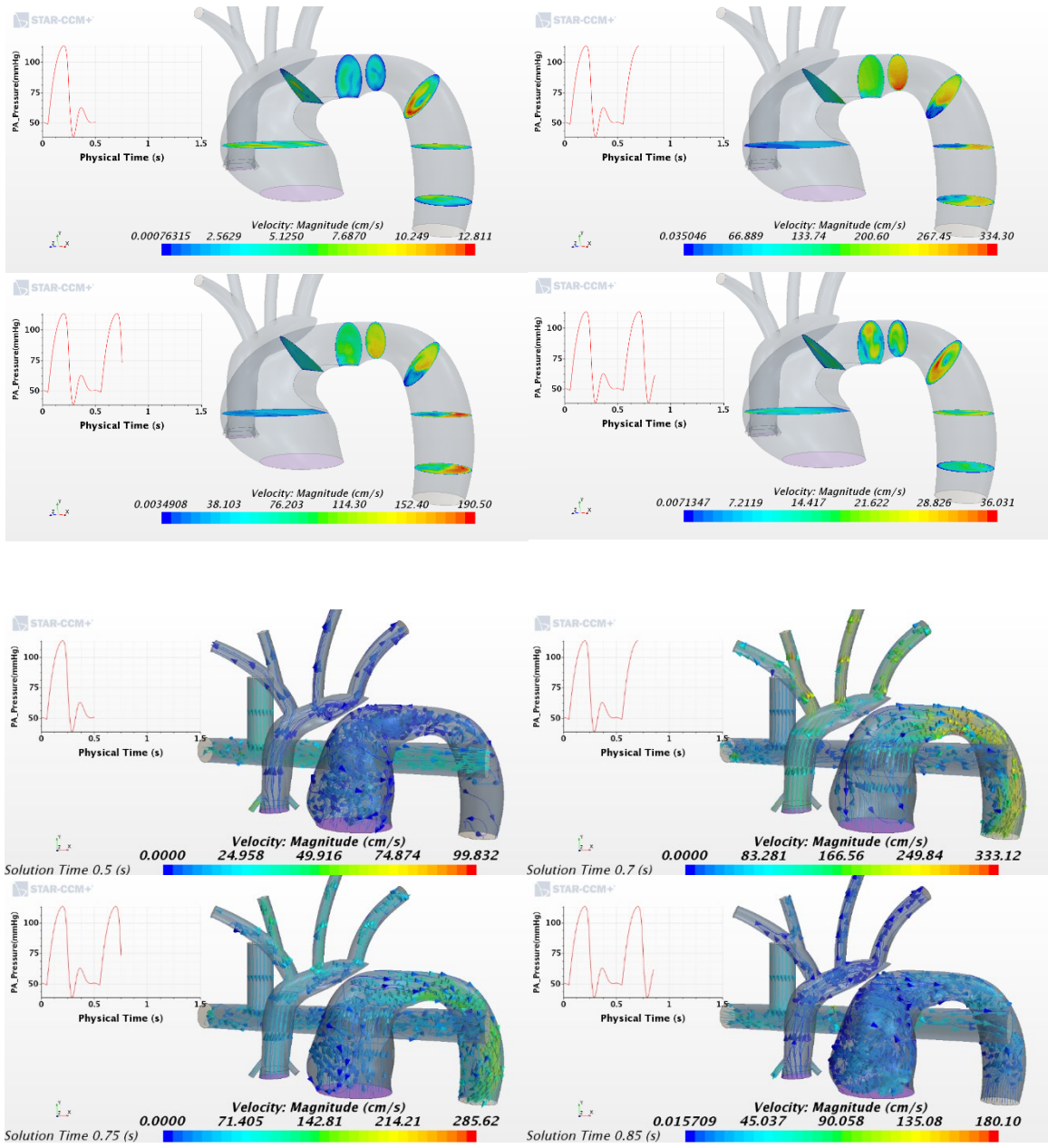


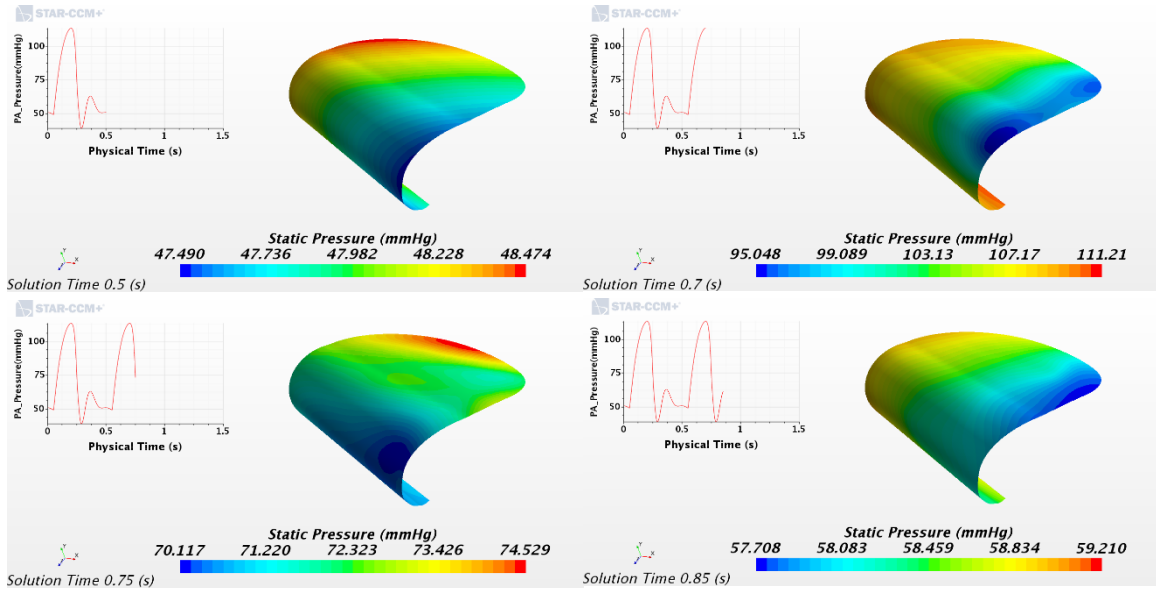
Case4



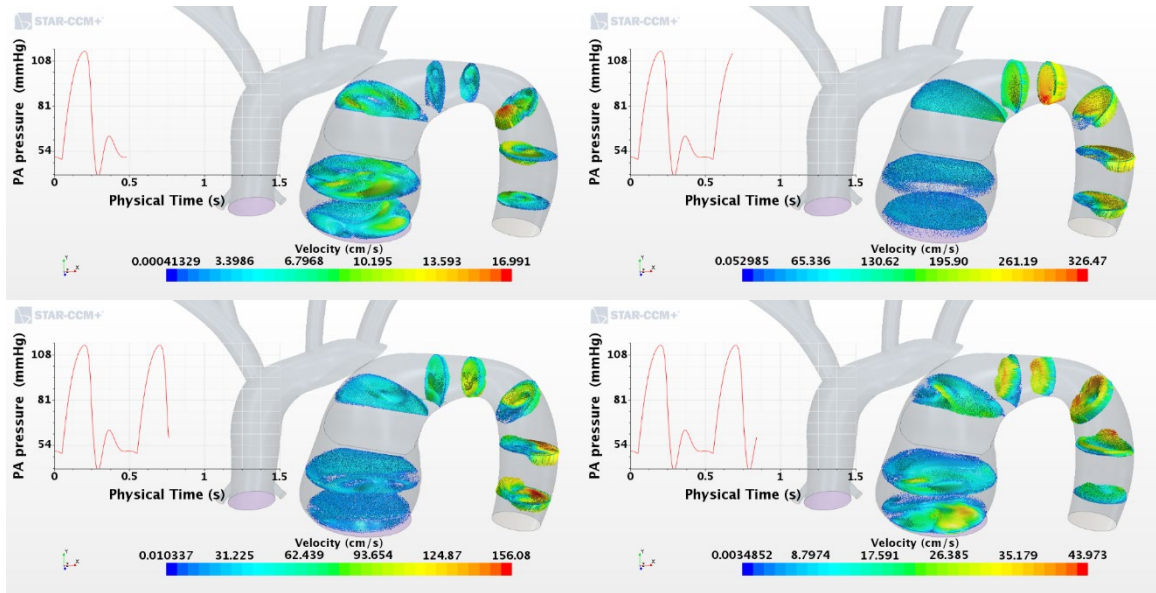


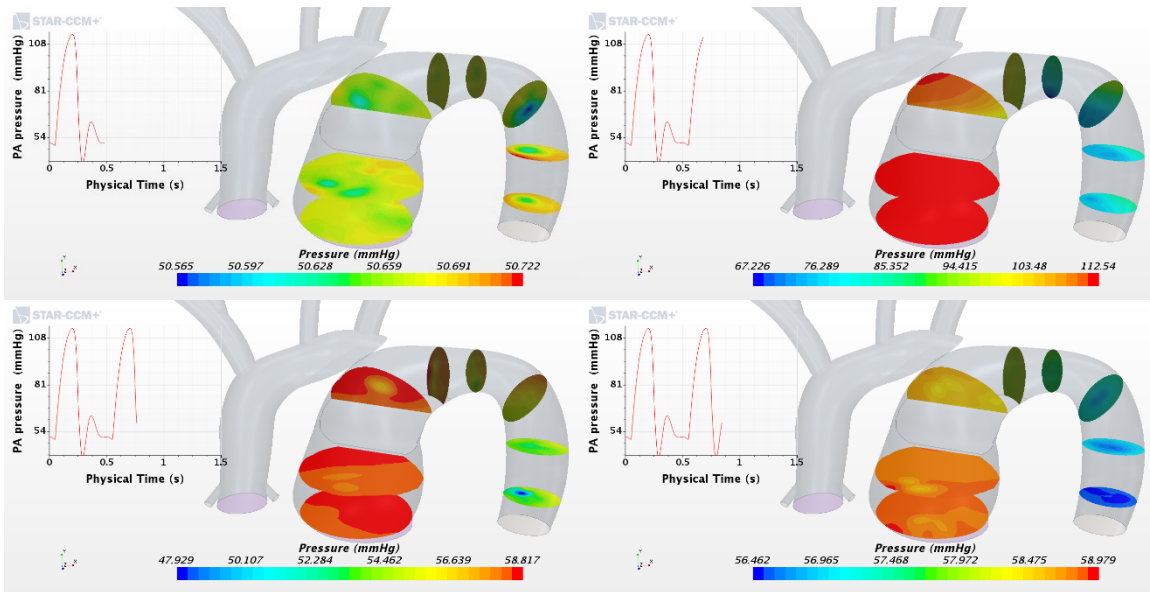




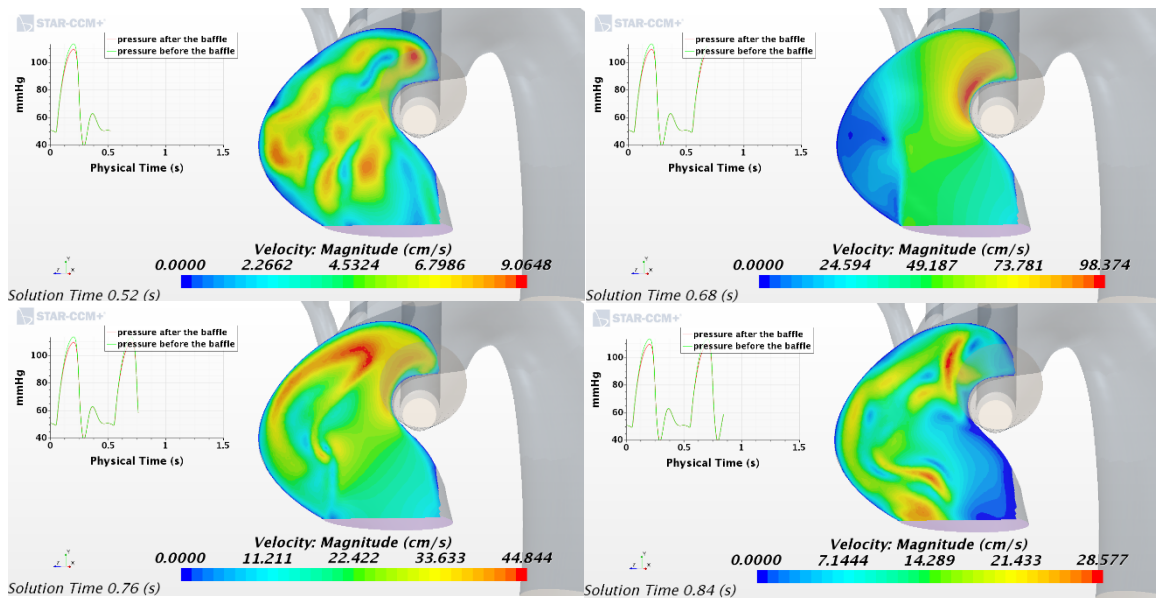


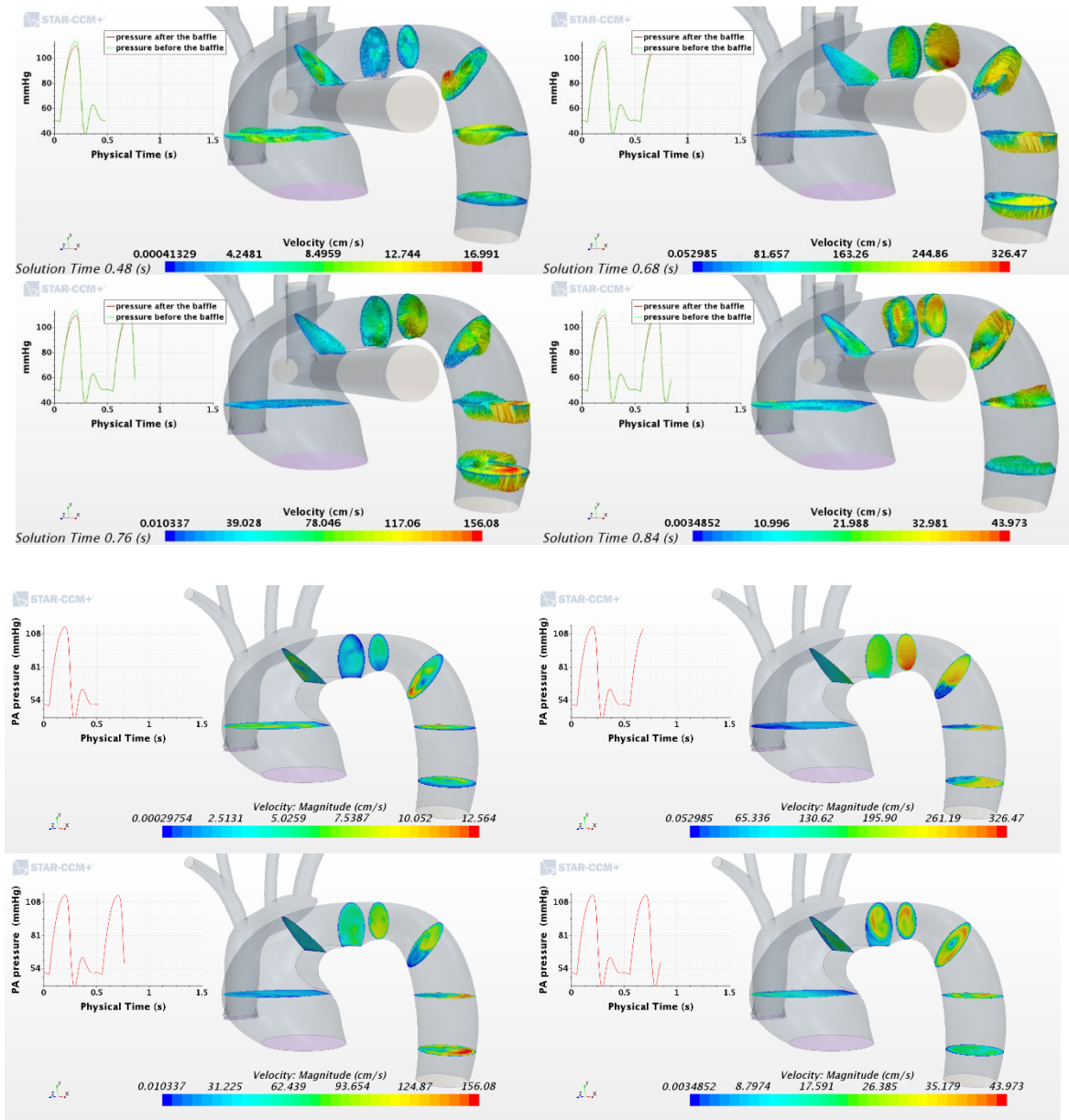
Case5

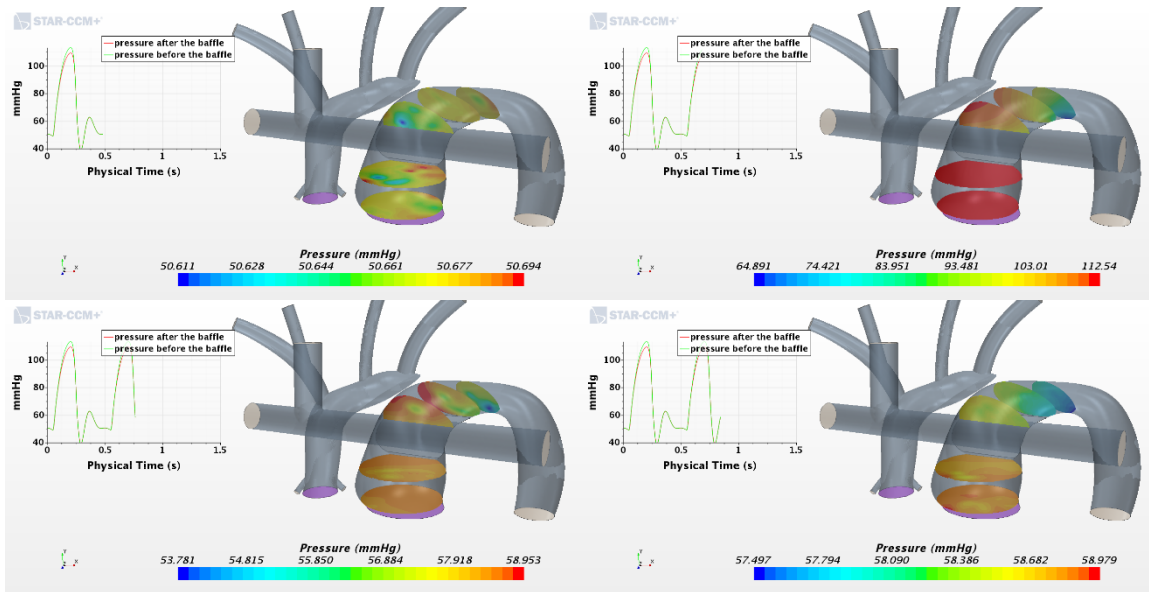




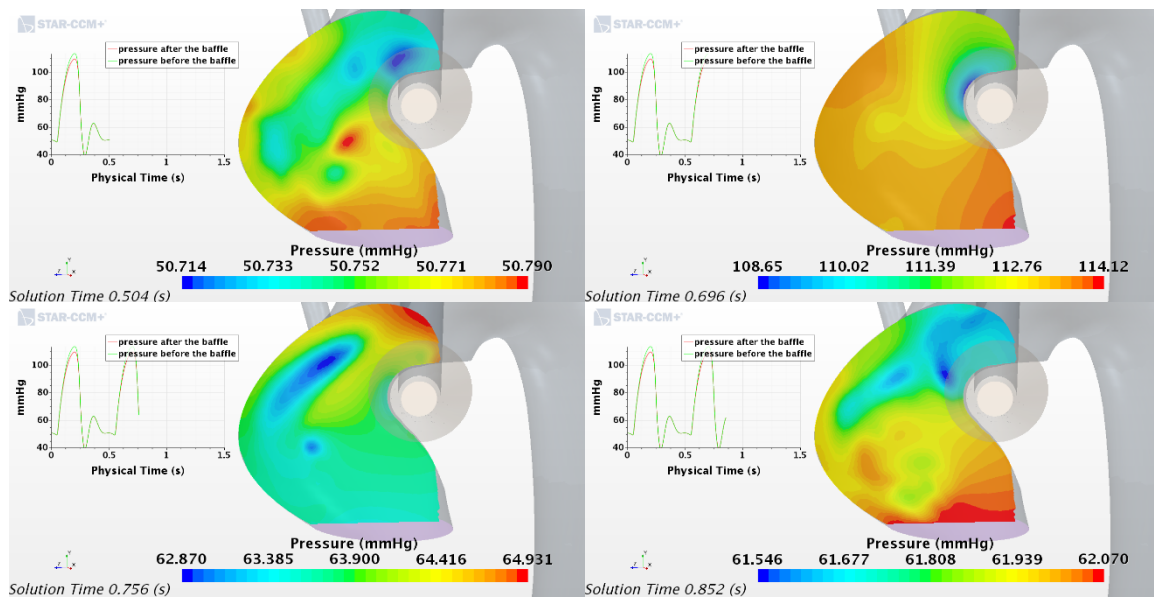
Case

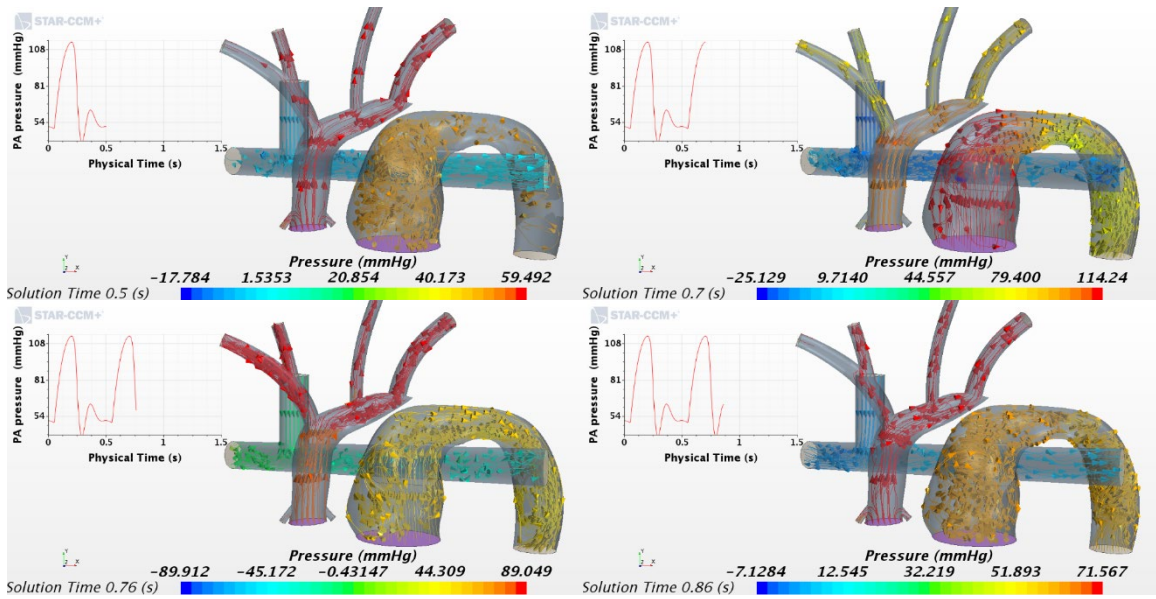




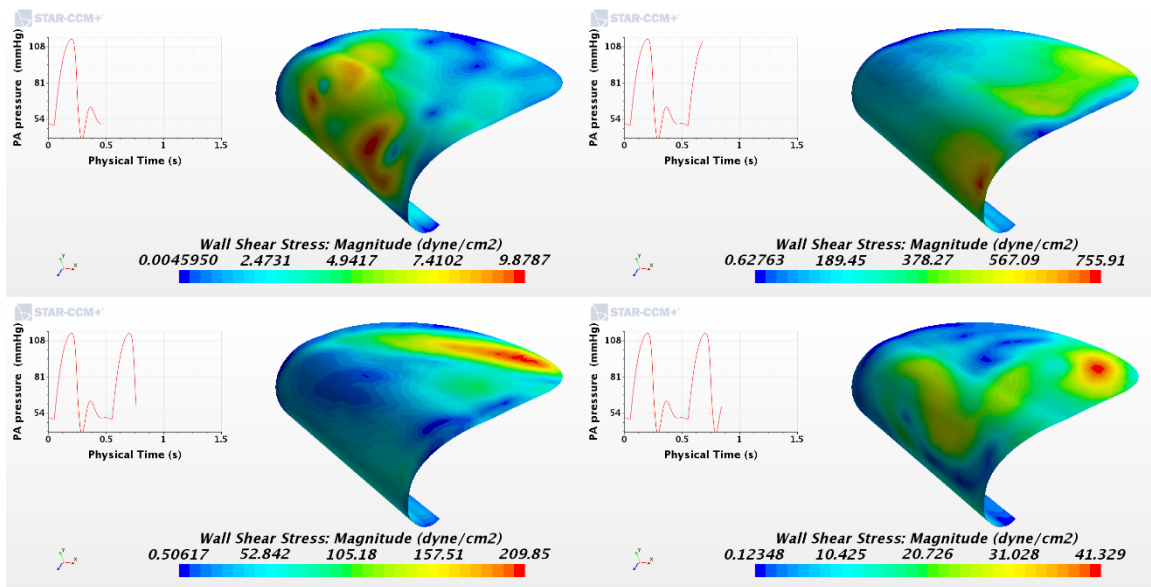


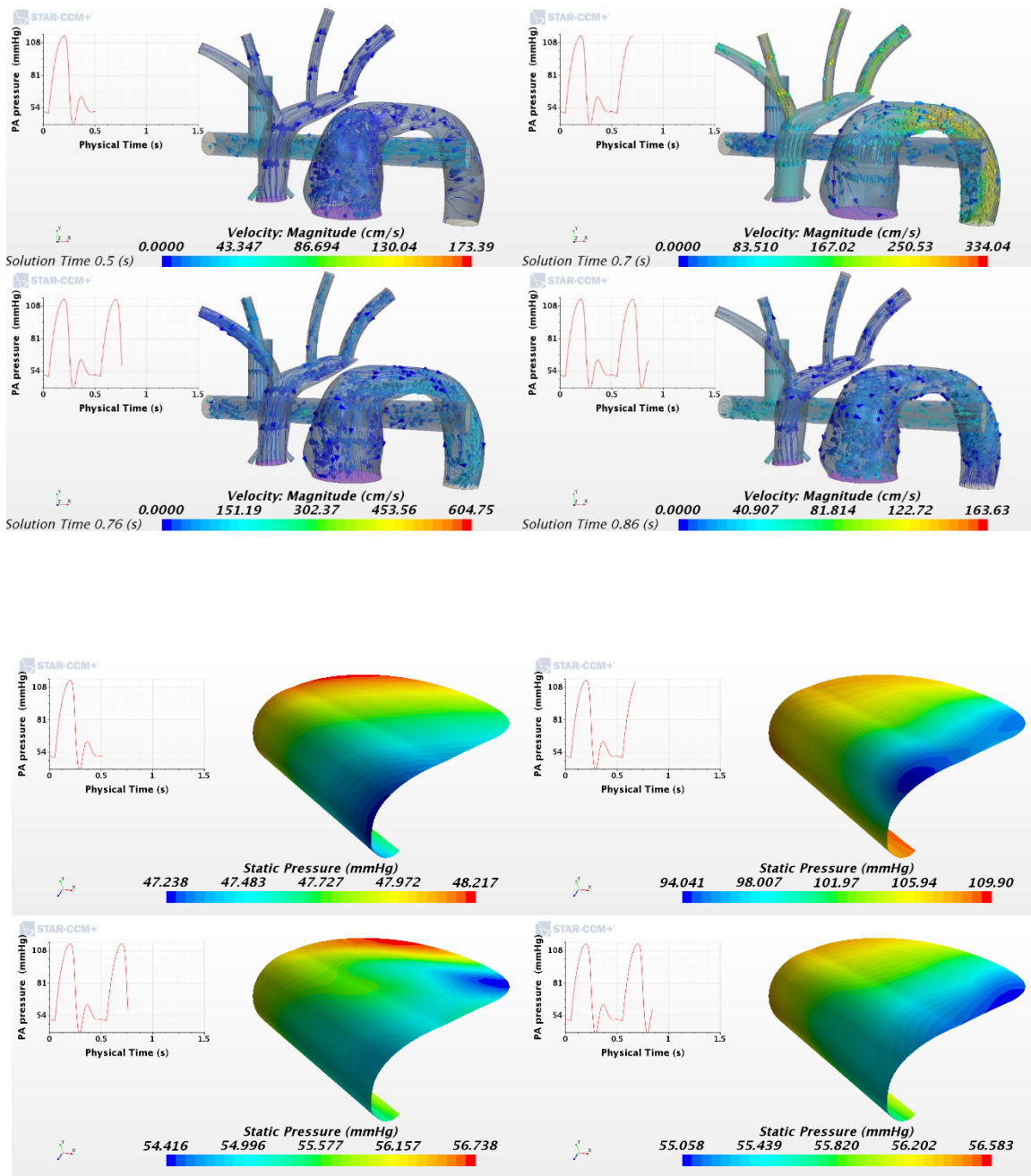
Case9

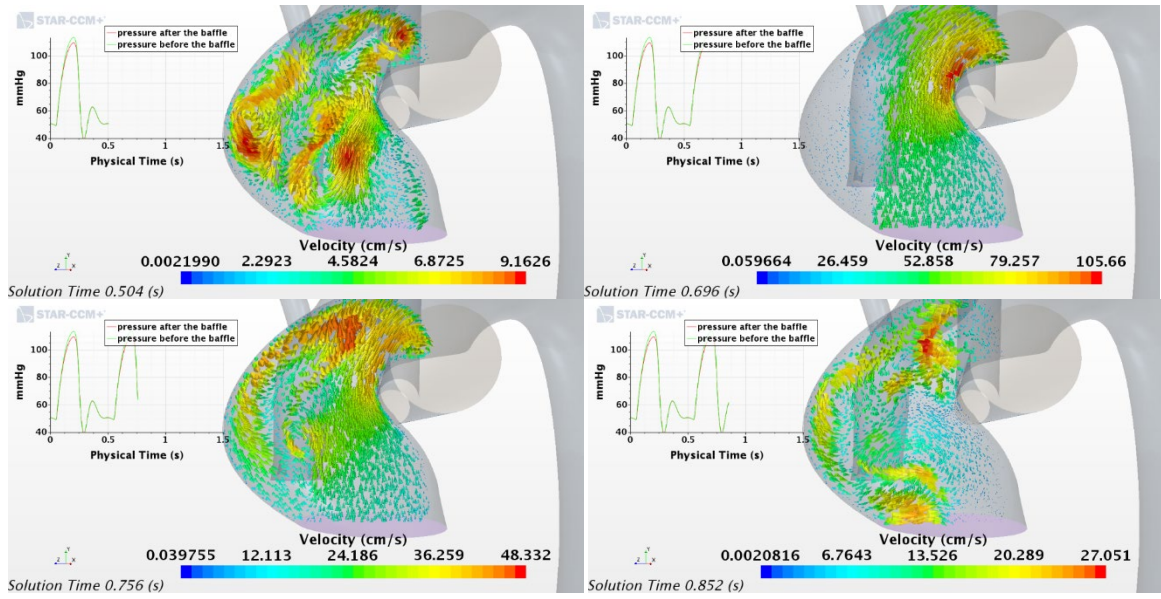




ase9

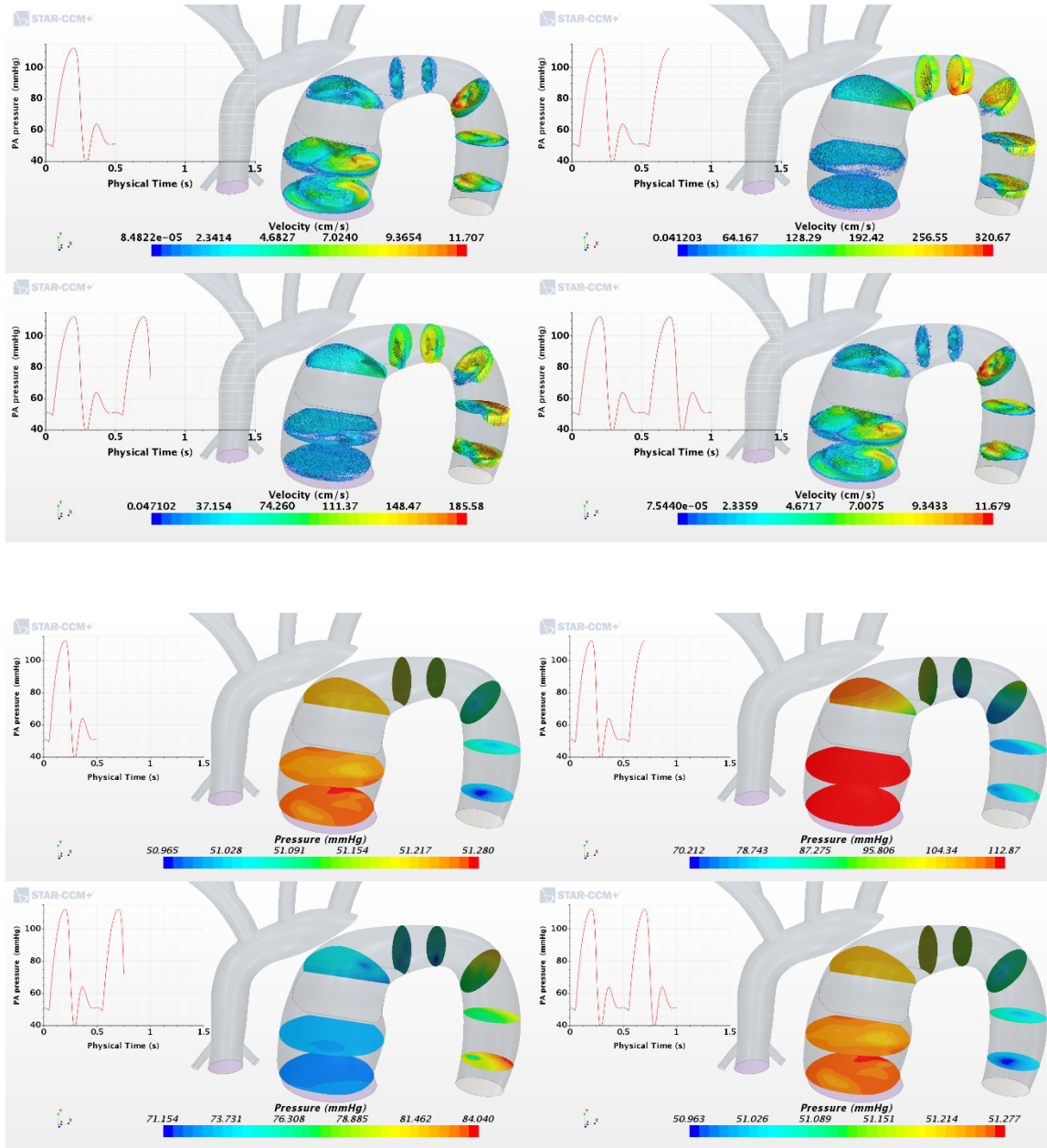


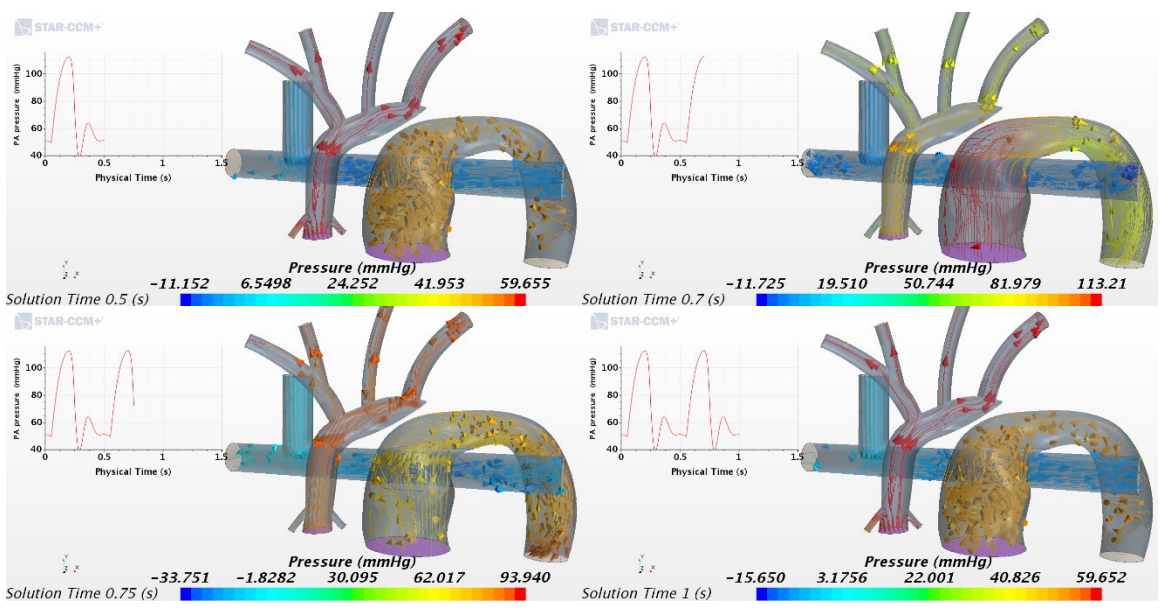
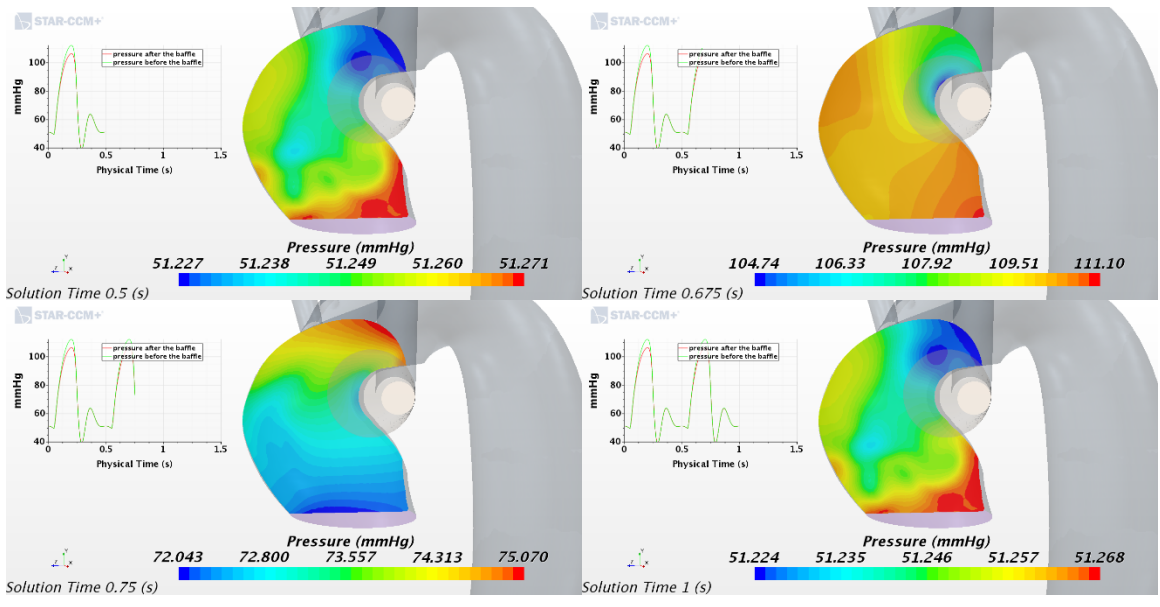


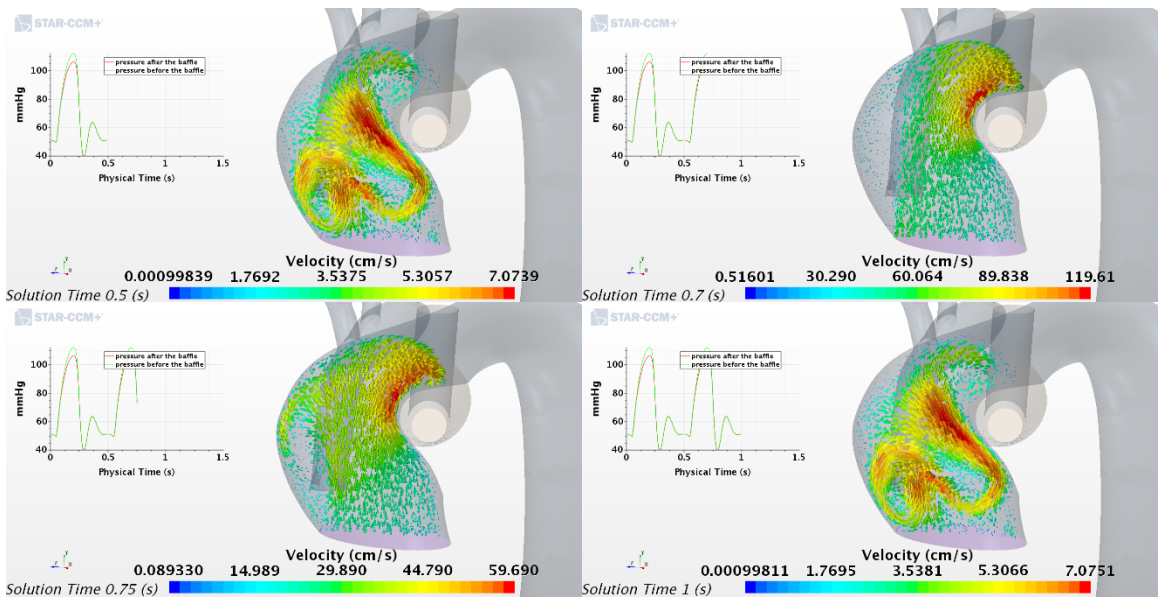
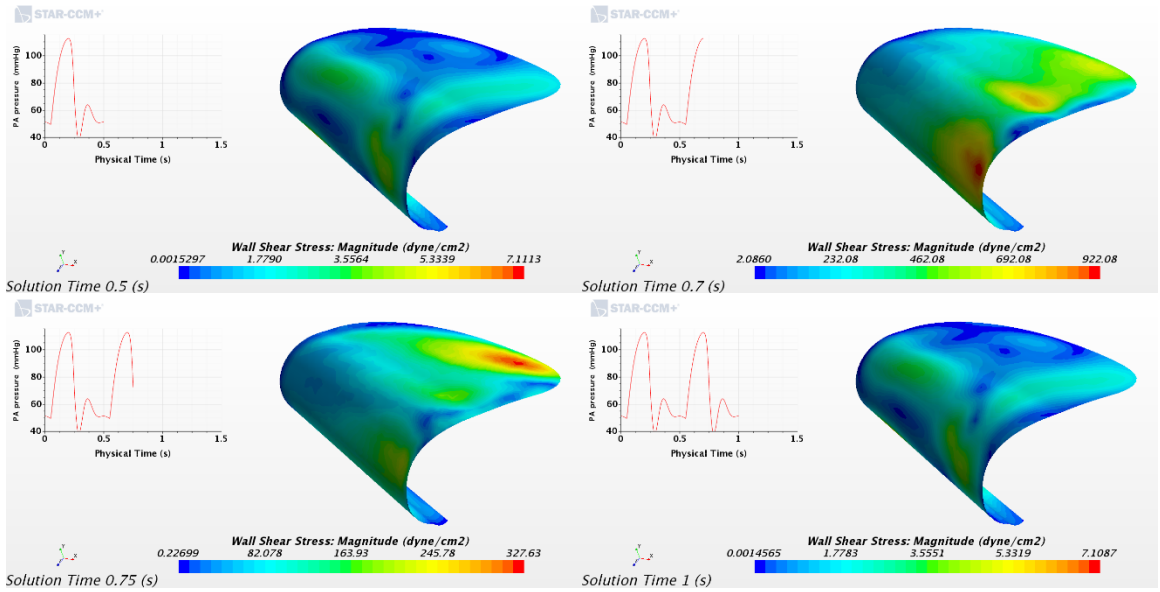


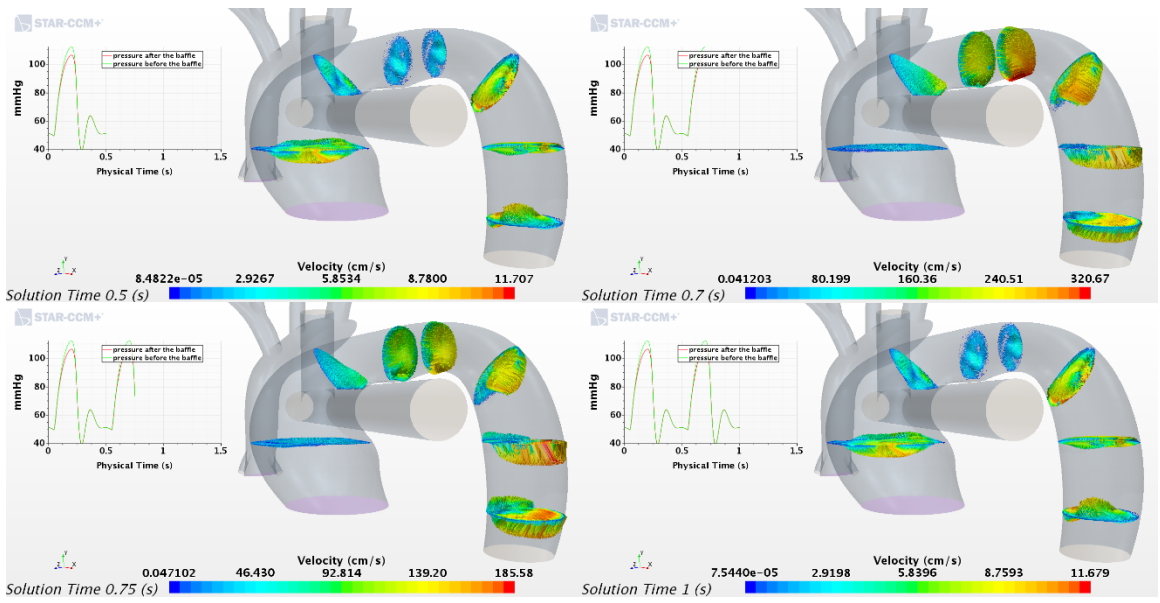
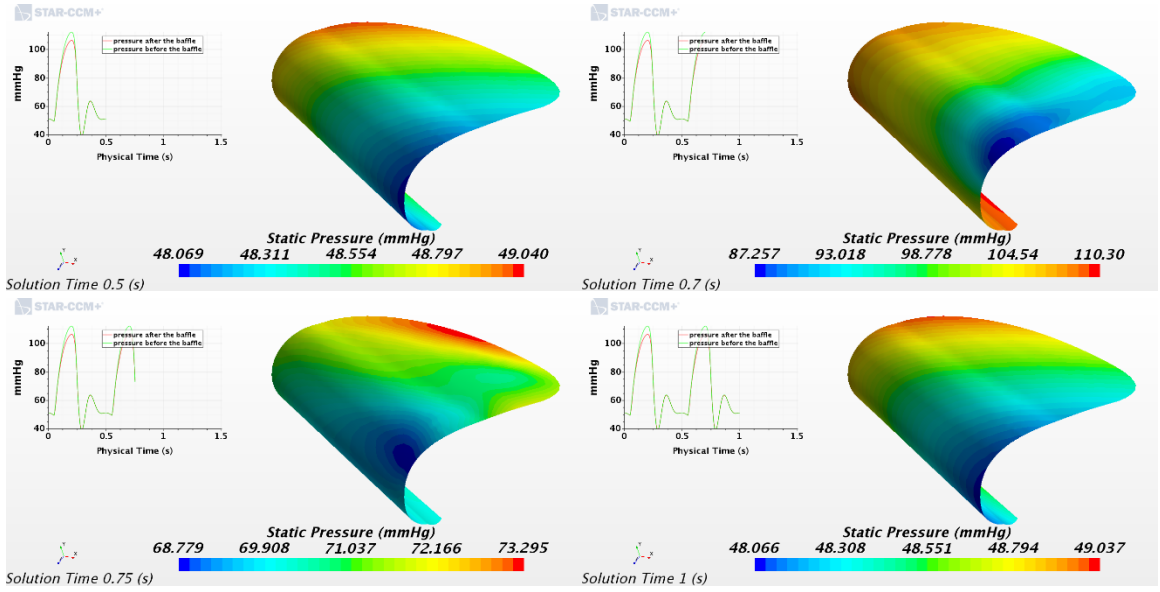
APPENDIX C: AREA OVER THE BAFFLE STUDY CFD SCENES

Case1

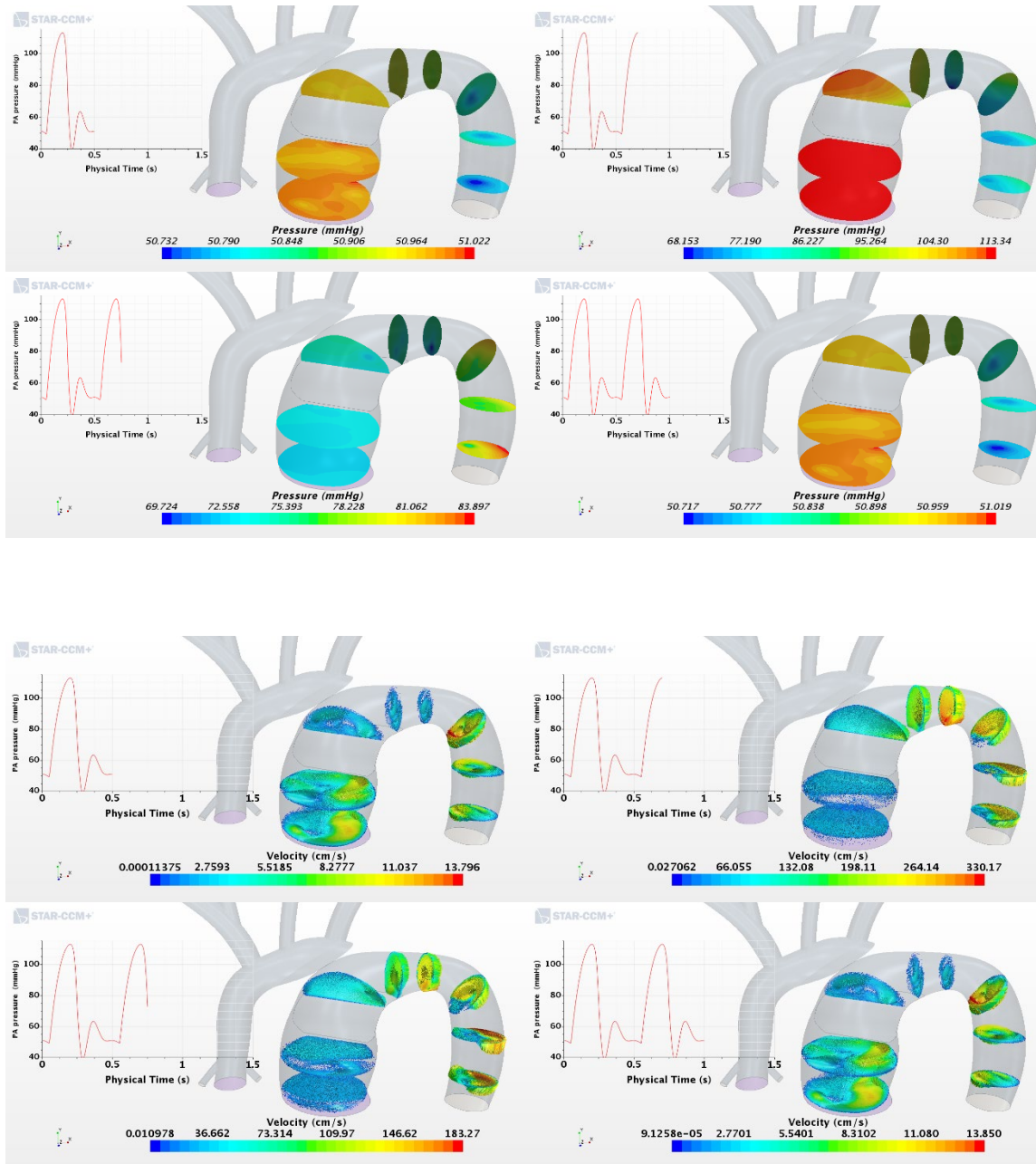


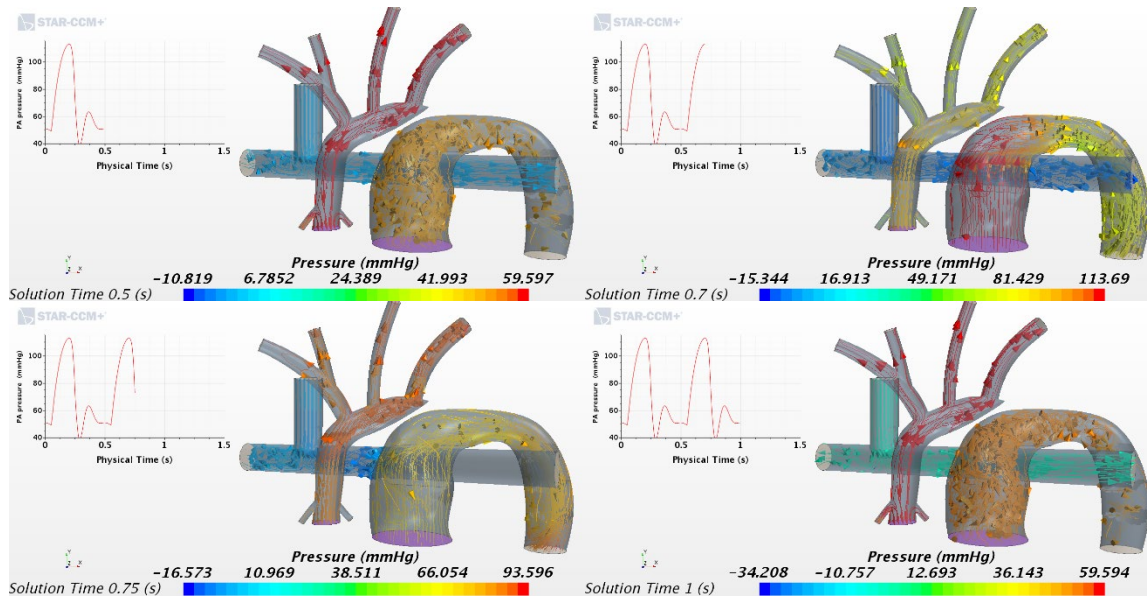
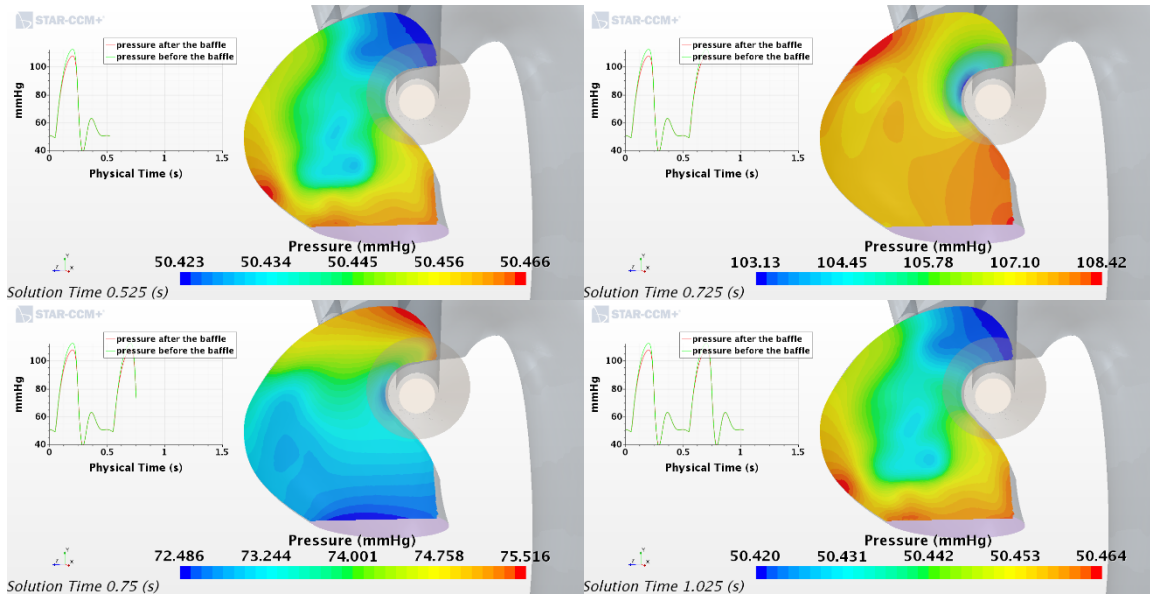


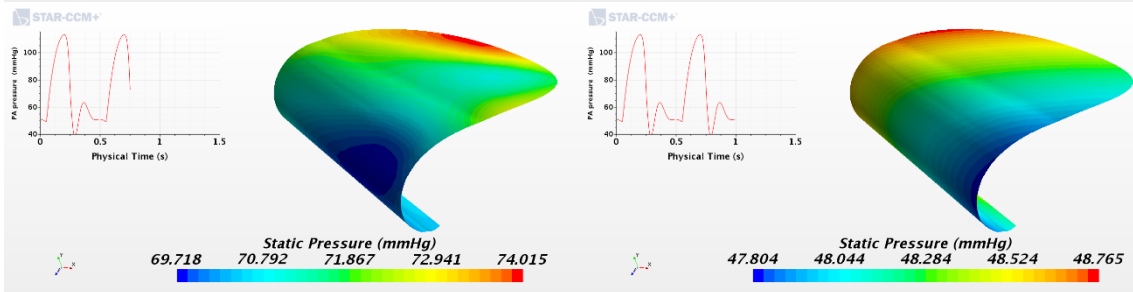
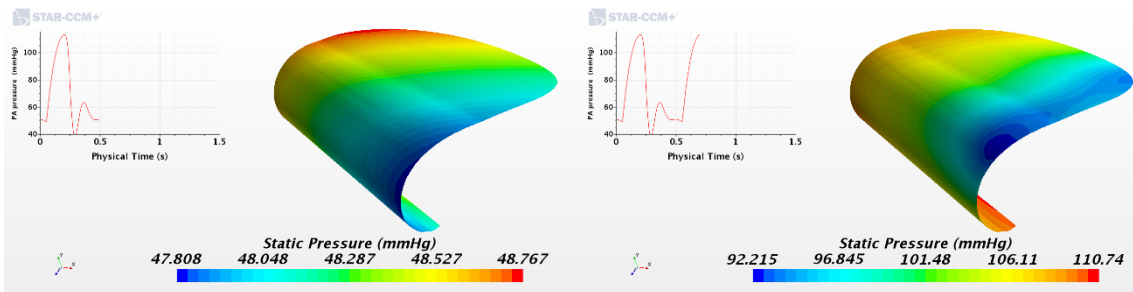
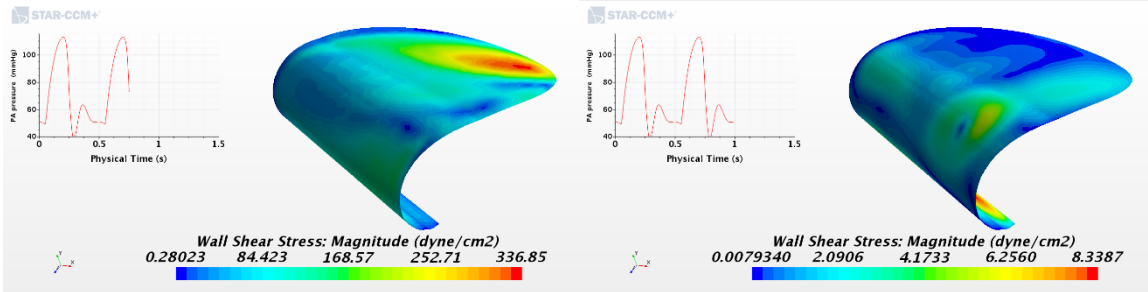
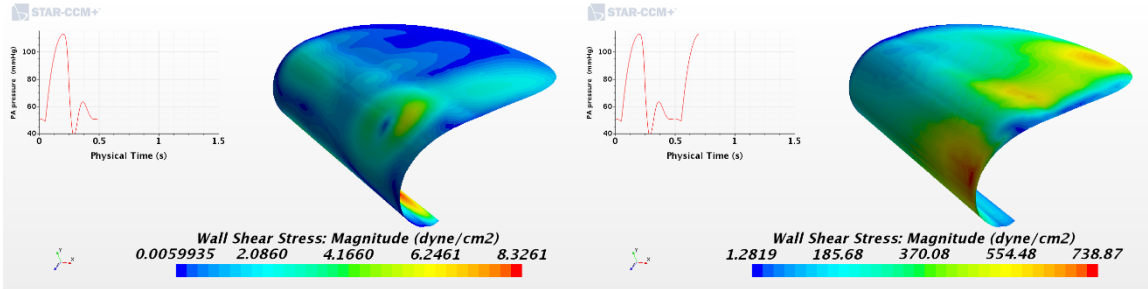


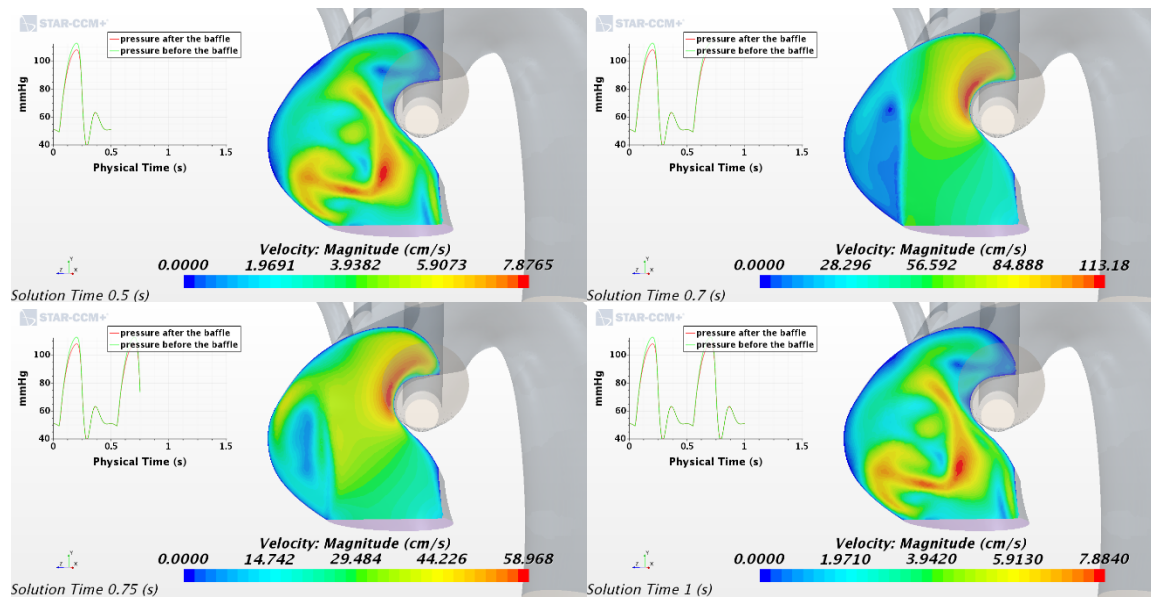
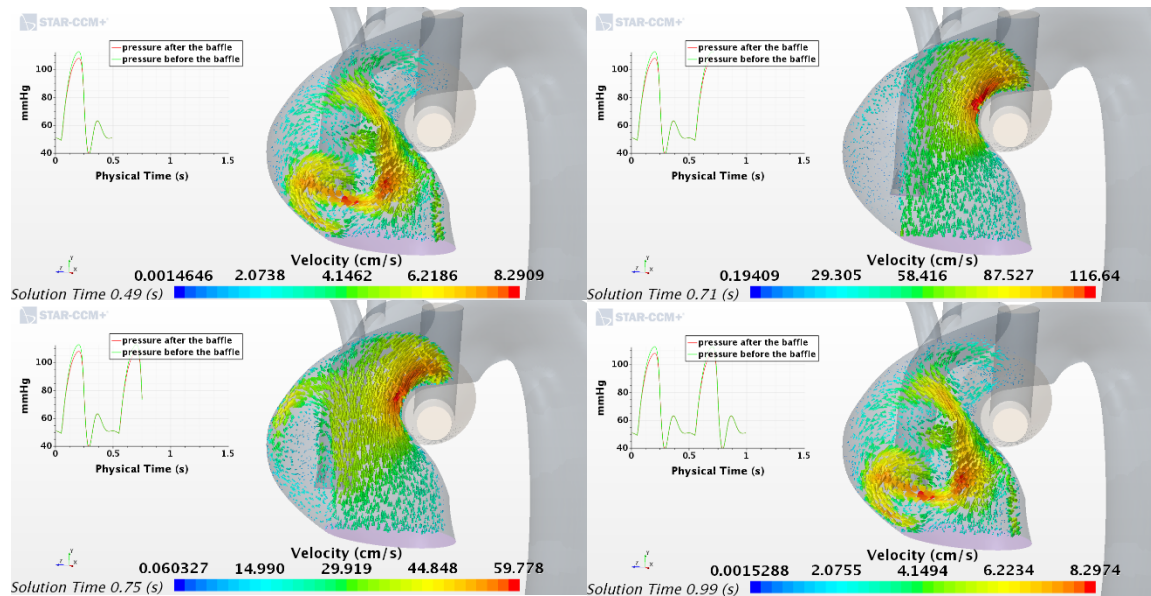


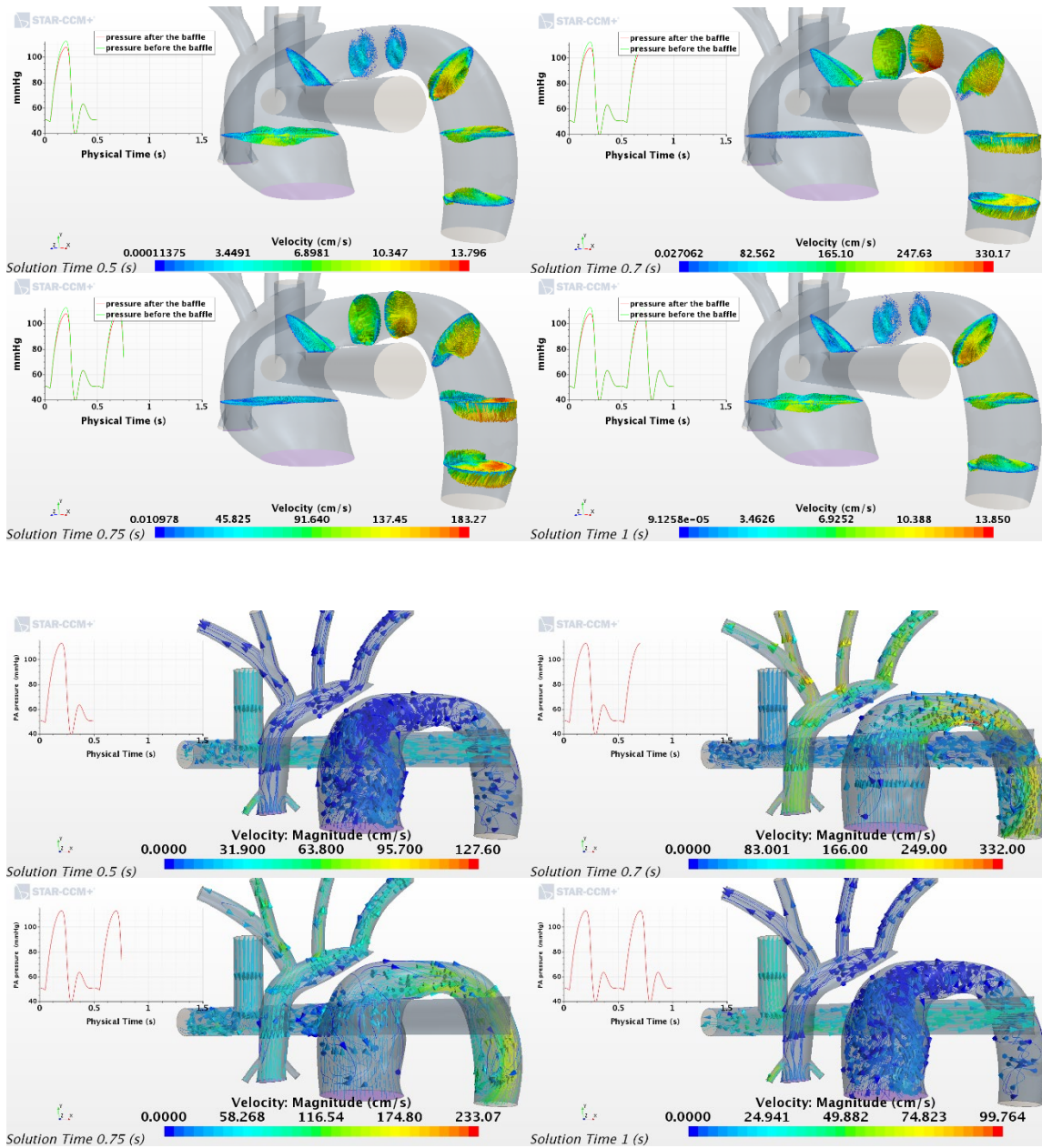
Cas2



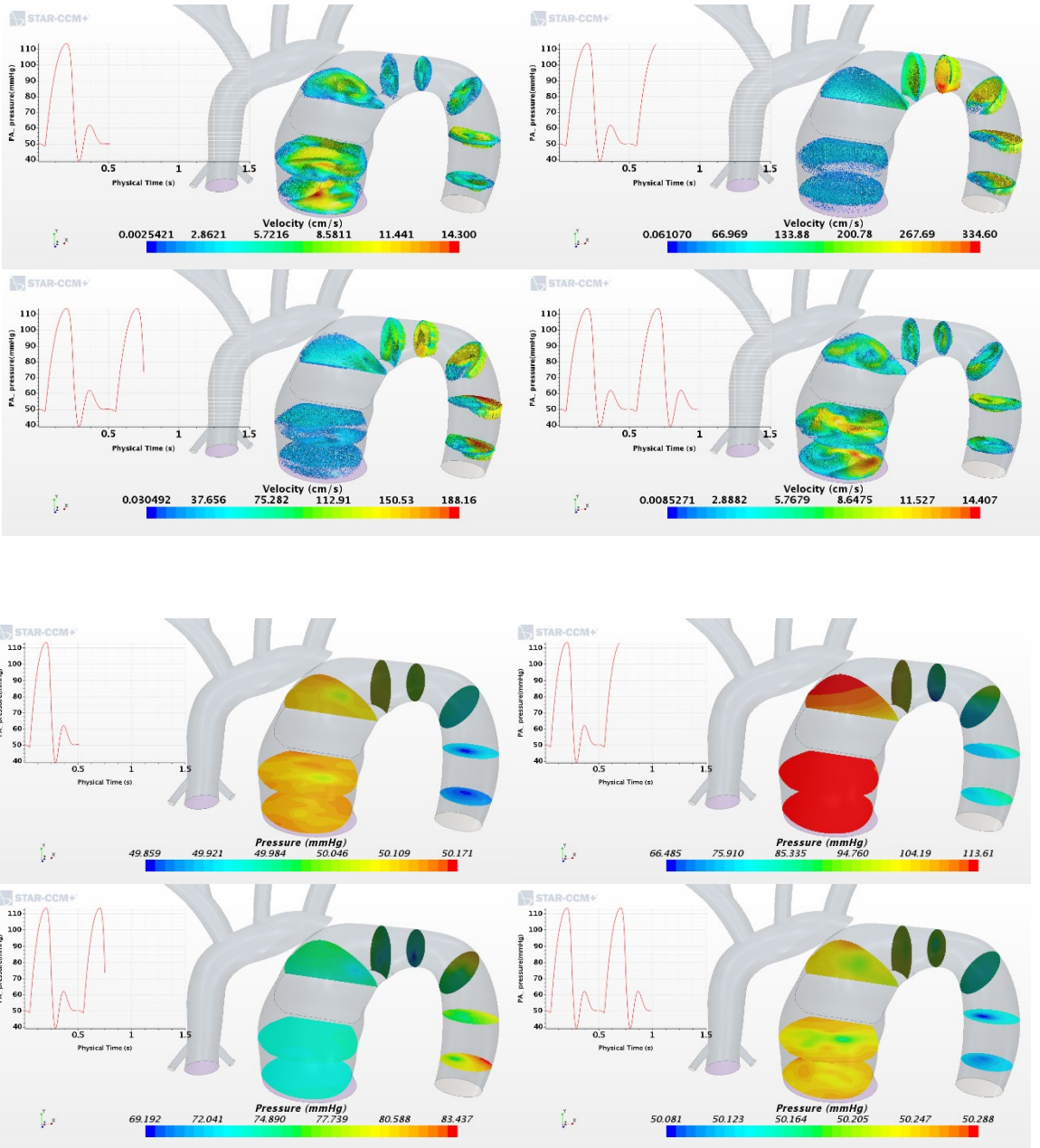


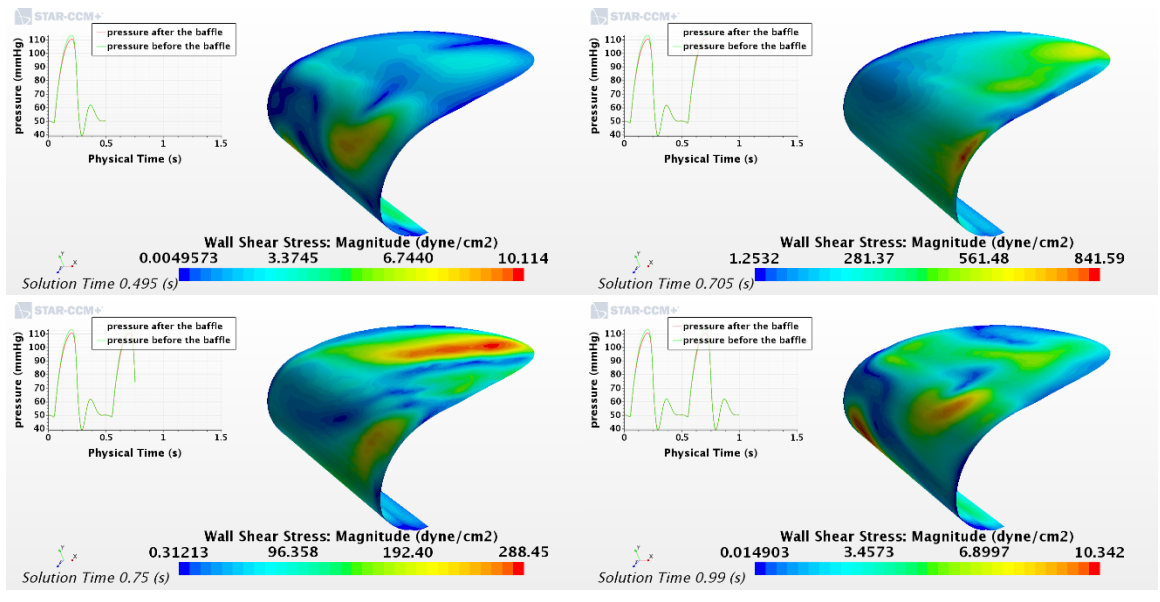
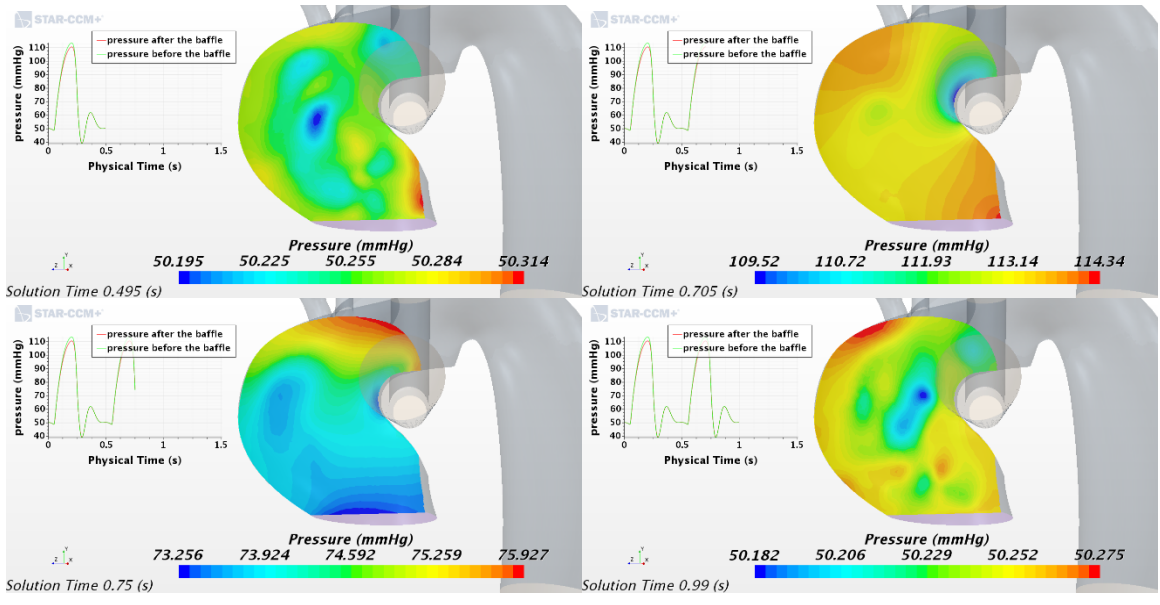


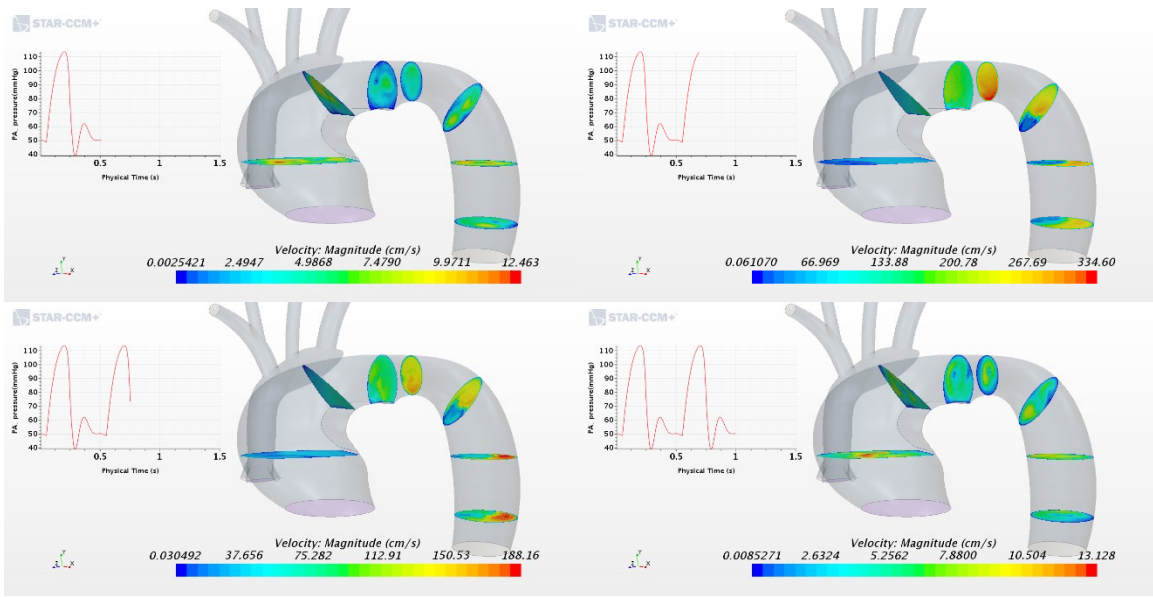
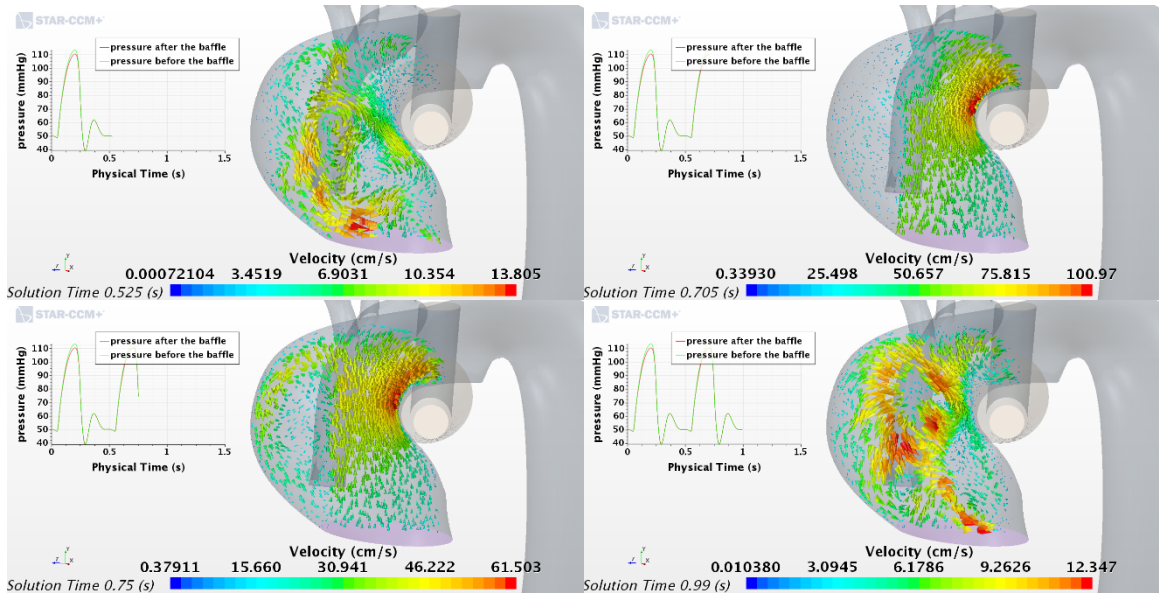


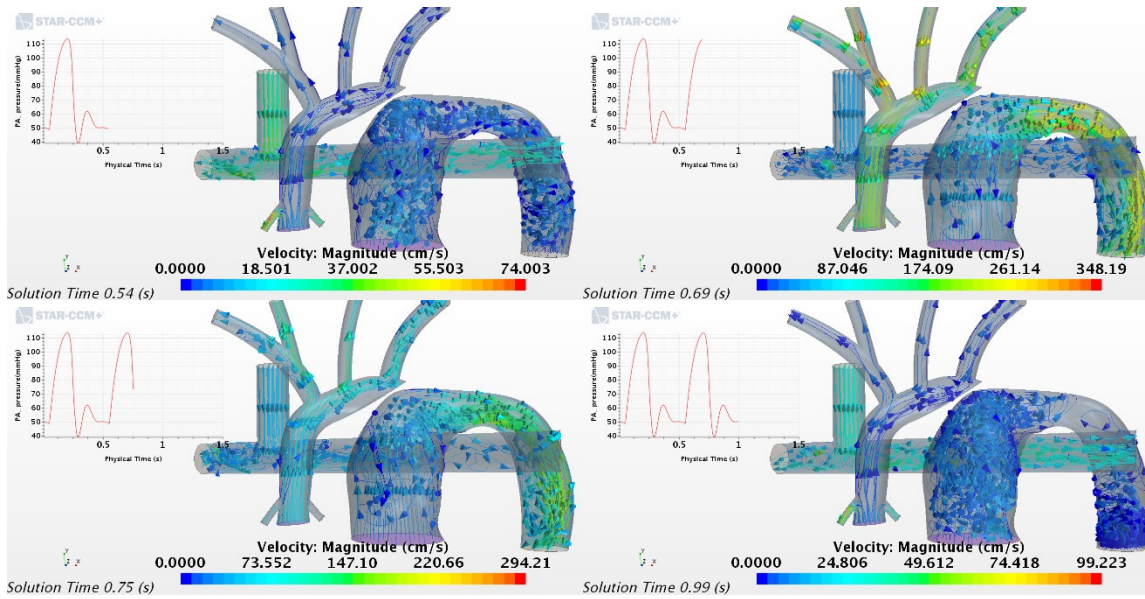


Case3

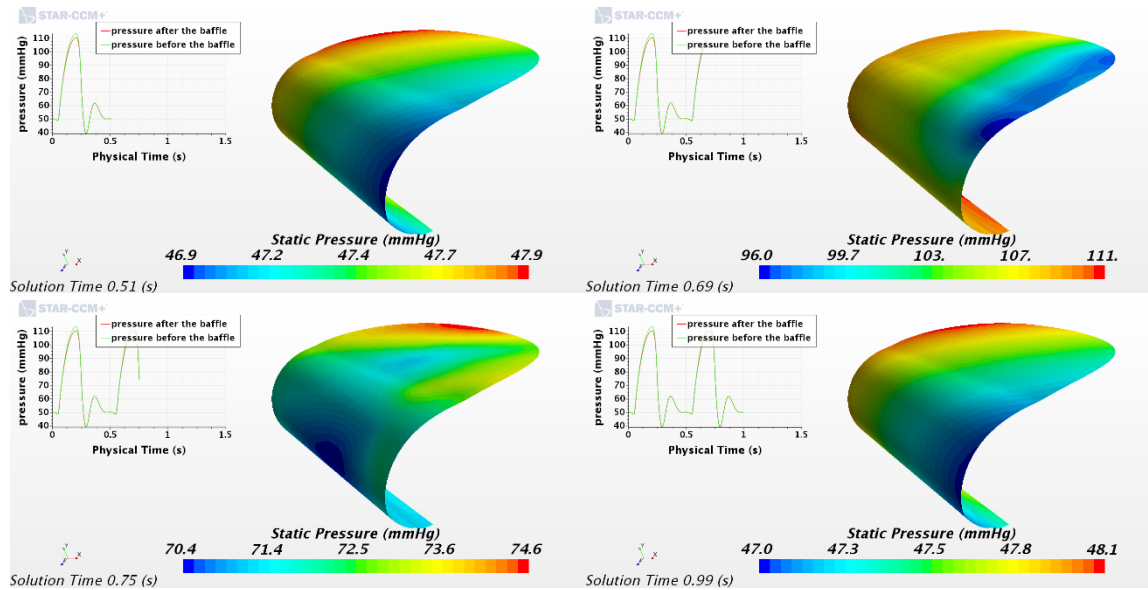




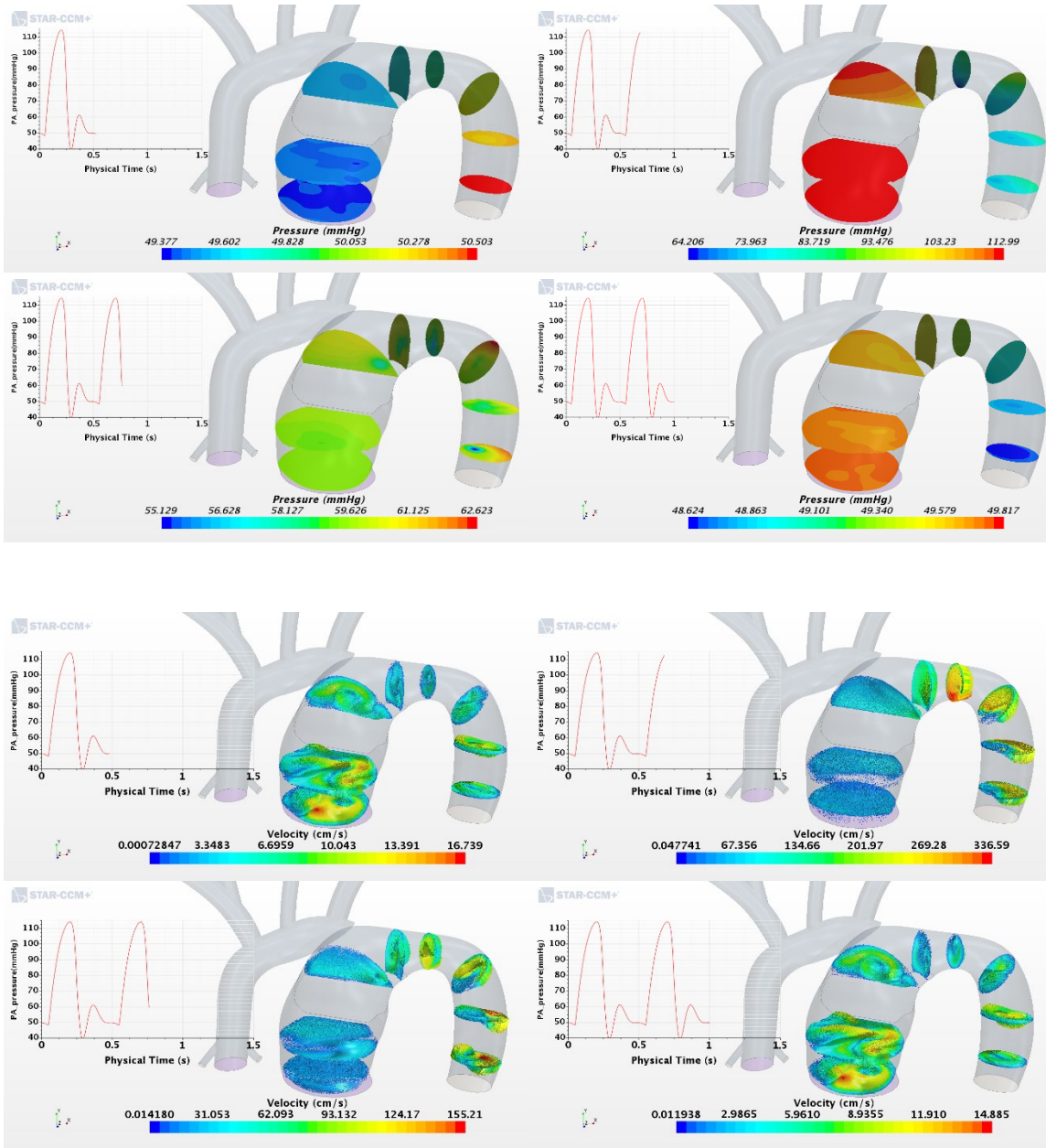


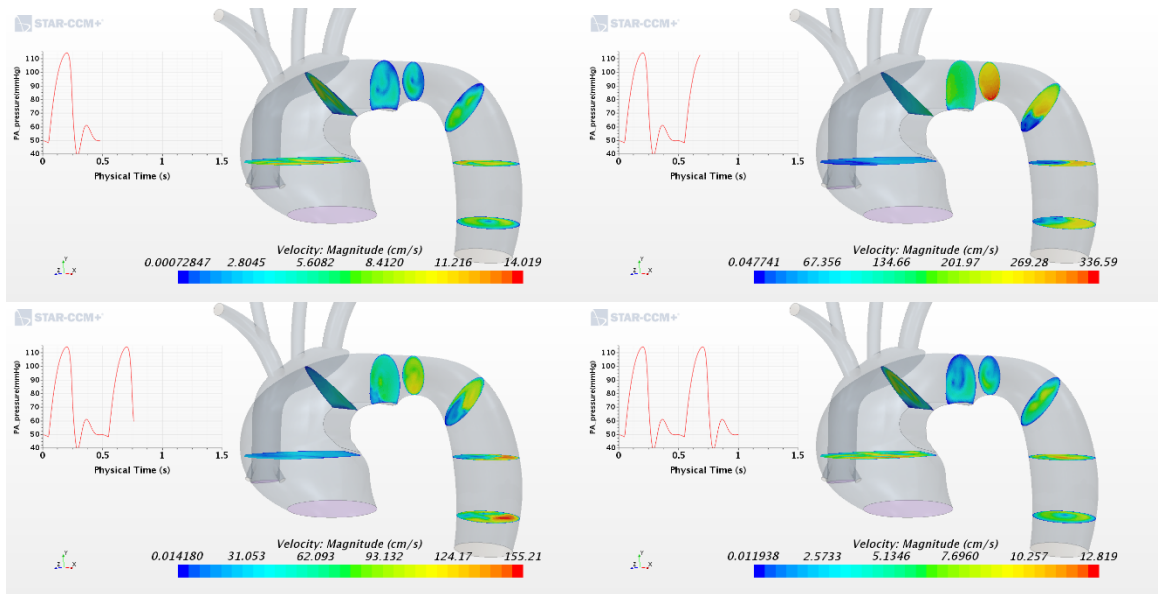
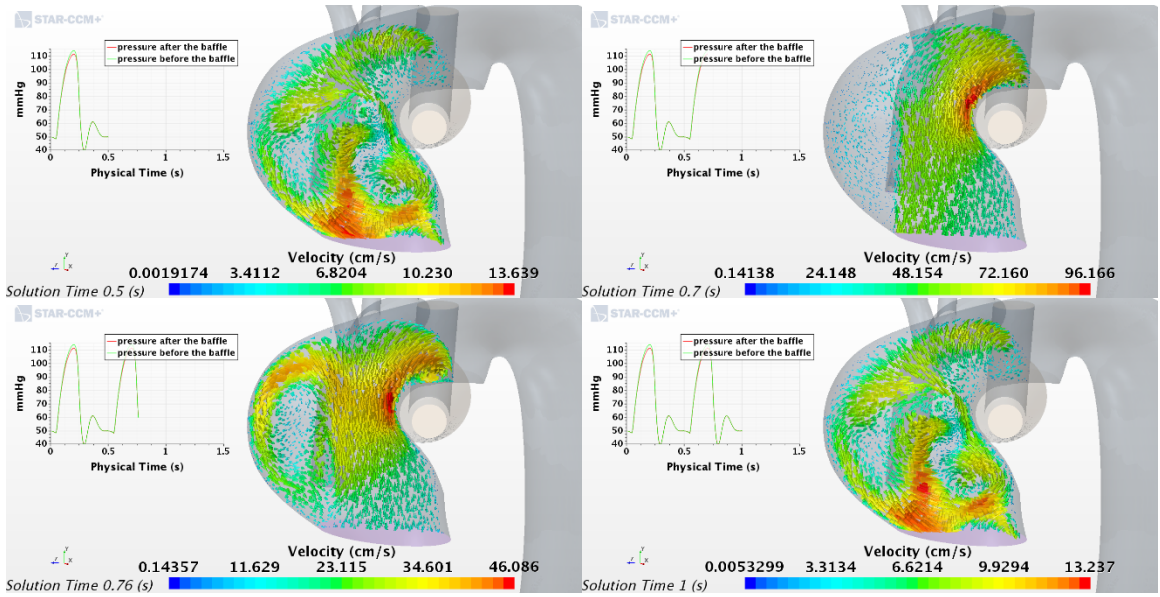


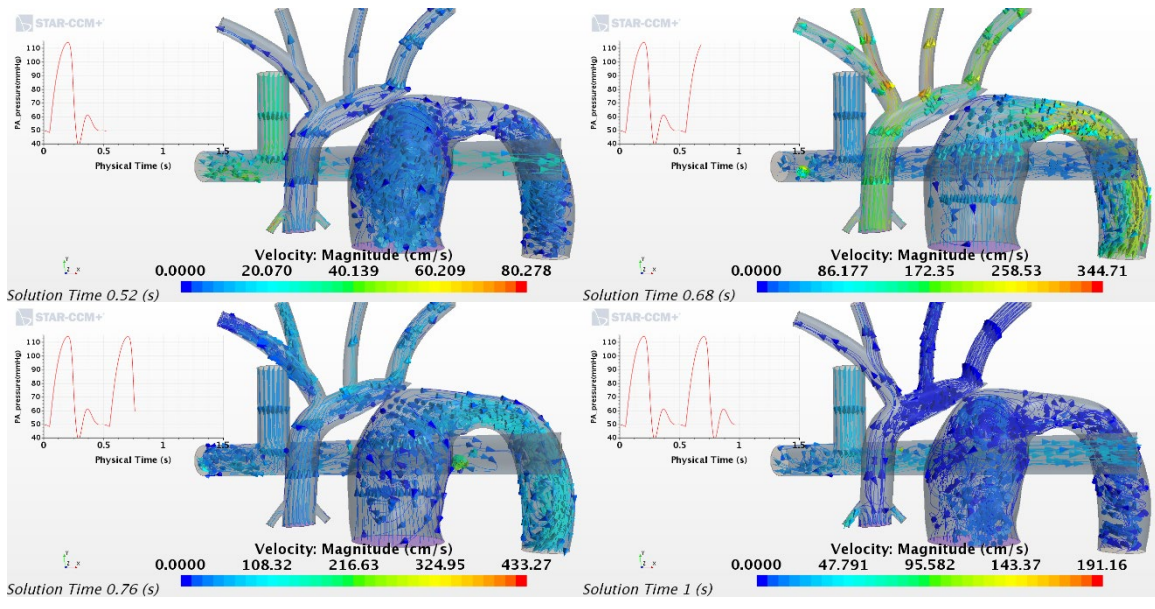
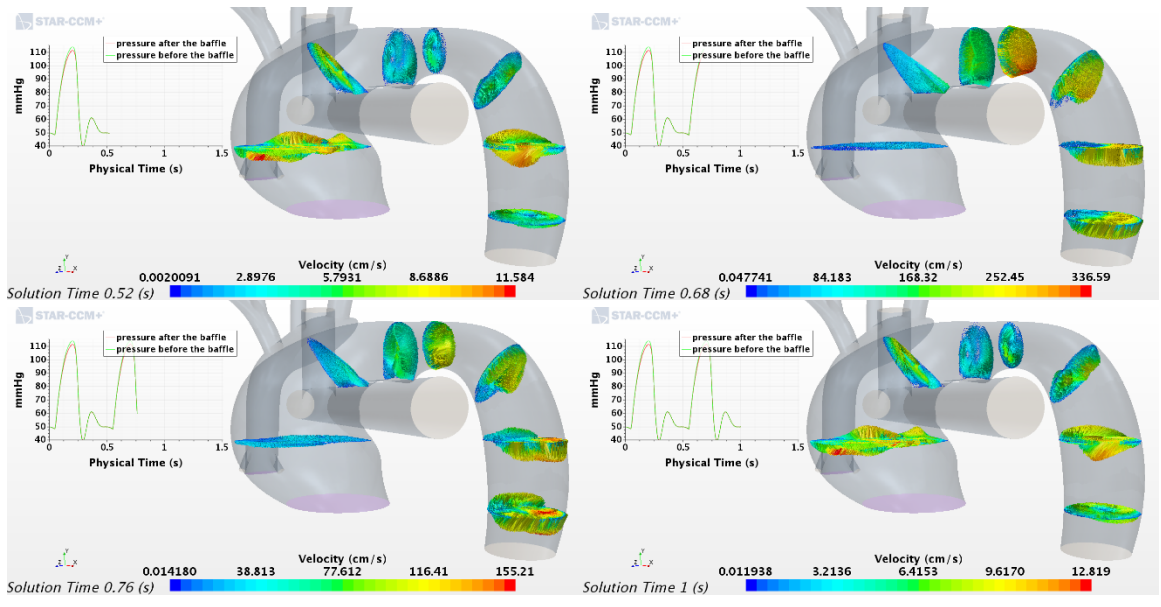
Case15



case4







LIST OF REFERENCES

- [1] N. C. Institute. Circulatory System. Available:<http://www.scientificpsychic.com/health/cardiovascular-system.gif>.
- [2] M. Yabrodi, C.W. Mastropietro, Hypoplastic left heart syndrome: from comfort care to long-term survival, *Pediatric research*, 81 (2017) 142.
- [3] D.S. Fruitman, Hypoplastic left heart syndrome: prognosis and management options, *Paediatrics & child health*, 5 (2000) 219-225.
- [4] C.D. Morris, J. Outcalt, V.D. Menashe, Hypoplastic left heart syndrome: natural history in a geographically defined population, *Pediatrics*, 85 (1990) 977-983.
- [5] A. Garson, J.T. Bricker, D.J. Fisher, S. Neish, *The science and practice of pediatric cardiology*, Williams & Wilkins Baltimore, 1998.
- [6] T.A. Glauser, L.B. Rorke, P.M. Weinberg, R.R. Clancy, Congenital brain anomalies associated with the hypoplastic left heart syndrome, *Pediatrics*, 85 (1990) 984-990.
- [7] J.K. Perloff, *The clinical recognition of congenital heart disease*, (1988).
- [8] W.D. Caplan, T.R. Cooper, J.A. Garcia-Prats, B.A. Brody, Diffusion of innovative approaches to managing hypoplastic left heart syndrome, *Archives of pediatrics & adolescent medicine*, 150 (1996) 487-490.
- [9] A.J. Razzouk, R.E. Chinnock, S.R. Gundry, J.K. Johnston, R.L. Larsen, M.F. Baum, N.F. Mulla, L.L. Bailey, Transplantation as a primary treatment for hypoplastic left heart syndrome: intermediate-term results, *The Annals of thoracic surgery*, 62 (1996) 1-8.
- [10] B. Rogers, M. Msall, G. Buck, N. Lyon, M. Norris, J.-M. Roland, R. Gingell, D. Cleveland, D. Pieroni, Neurodevelopmental outcome of infants with hypoplastic left heart syndrome, *The Journal of pediatrics*, 126 (1995) 496-498.
- [11] B. Furst, *Single-Ventricle Physiology*, in: *The Heart and Circulation*, Springer, 2014, pp. 203-210.
- [12] D.M. Cohen, H.D. Allen, New developments in the treatment of hypoplastic left heart syndrome, *Current opinion in cardiology*, 12 (1997) 44-50.
- [13] K. Bando, M.W. Turrentine, K. Sun, T.G. Sharp, R.L. Caldwell, R.K. Darragh, G.J. Ensing, T.M. Cordes, T. Flaspohler, J.W. Brown, Surgical management of hypoplastic left heart syndrome, *The Annals of thoracic surgery*, 62 (1996) 70-77.
- [14] A.J. Razzouk, R.E. Chinnock, S.R. Gundry, L.L. Bailey, Cardiac transplantation for infants with hypoplastic left heart syndrome, *Progress in Pediatric Cardiology*, 5 (1996) 37-47.
- [15] M.L. Jacobs, E.H. Blackstone, L.L. Bailey, T.C.H.S. Society, Intermediate survival in neonates with aortic atresia: a multi-institutional study, *The Journal of thoracic and cardiovascular surgery*, 116 (1998) 417-431.
- [16] H. Staff, *Learning About Hypoplastic Left Heart Syndrome in Newborns*, (2018).
- [17] M. Michael A. Bingler, *Hypoplastic Left Heart Syndrome Surgery: The Norwood Procedure*, in, 2018.
- [18] A. Blalock, H.B. Taussig, The surgical treatment of malformations of the heart: in which there is pulmonary stenosis or pulmonary atresia, *Journal of the American Medical Association*, 128 (1945) 189-202.
- [19] A. Moulton, J. Brenner, R. Ringel, A. Nordenberg, M. Berman, S. Ali, J. Burns, Classic versus modified Blalock-Taussig shunts in neonates and infants, *Circulation*, 72 (1985) II35-44.
- [20] D.J. Barron, M.D. Kilby, B. Davies, J.G. Wright, T.J. Jones, W.J. Brawn, Hypoplastic left heart syndrome, *The Lancet*, 374 (2009) 551-564.
- [21] S. Talwar, V.V. Nair, S.K. Choudhary, B. Airan, The Hemi-Fontan operation: A critical overview, *Annals of pediatric cardiology*, 7 (2014) 120.

- [22] W.I. Douglas, C.S. Goldberg, R.S. Mosca, I.H. Law, E.L. Bove, Hemi-Fontan procedure for hypoplastic left heart syndrome: outcome and suitability for Fontan, *The Annals of thoracic surgery*, 68 (1999) 1361-1367.
- [23] Treatment for Your Child's Hypoplastic Ventricle: Stage II, (2018).
- [24] F. Fontan, E. Baudet, Surgical repair of tricuspid atresia, *Thorax*, 26 (1971) 240-248.
- [25] Staged Reconstruction Heart Surgery.
- [26] N.D. Bridges, J. Mayer Jr, J.E. Lock, R.A. Jonas, F.L. Hanley, J.F. Keane, S.B. Perry, A.R. Castaneda, Effect of baffle fenestration on outcome of the modified Fontan operation, *Circulation*, 86 (1992) 1762-1769.
- [27] J.A. Feinstein, D.W. Benson, A.M. Dubin, M.S. Cohen, D.M. Maxey, W.T. Mahle, E. Pahl, J. Villafañe, A.B. Bhatt, L.F. Peng, Hypoplastic left heart syndrome: current considerations and expectations, *Journal of the American College of Cardiology*, 59 (2012) S1-S42.
- [28] C. W Mastropietro, J. A Clark, L. M Grimaldi, J. S Killinger, M. Richmond, The patient with a single cardiac ventricle, *Current Pediatric Reviews*, 8 (2012) 253-276.
- [29] E.L. Bove, F. Migliavacca, M.R. de Leval, R. Balossino, G. Pennati, T.R. Lloyd, S. Khambadkone, T.-Y. Hsia, G.J.T.J.o.t. Dubini, c. surgery, Use of mathematic modeling to compare and predict hemodynamic effects of the modified Blalock–Taussig and right ventricle–pulmonary artery shunts for hypoplastic left heart syndrome, 136 (2008) 312-320. e312.
- [30] J.H. Kern, C.J. Hayes, R.E. Michler, W.M. Gersony, J.M. Quaegebeur, Survival and risk factor analysis for the Norwood procedure for hypoplastic left heart syndrome, *The American journal of cardiology*, 80 (1997) 170-174.
- [31] T.R. Lloyd, Prognosis of the hypoplastic left heart syndrome, *Progress in Pediatric Cardiology*, 5 (1996) 57-64.
- [32] K.N. Pundi, J.N. Johnson, J.A. Dearani, K.N. Pundi, Z. Li, C.A. Hinck, S.H. Dahl, B.C. Cannon, P.W. O'Leary, D.J. Driscoll, 40-year follow-up after the Fontan operation: long-term outcomes of 1,052 patients, *Journal of the American College of Cardiology*, 66 (2015) 1700-1710.
- [33] A.F. Corno, C. Vergara, C. Subramanian, R.A. Johnson, T. Passerini, A. Veneziani, L. Formaggia, N. Alphonso, A. Quarteroni, J.C. Jarvis, Assisted Fontan procedure: animal and in vitro models and computational fluid dynamics study, *Interactive cardiovascular and thoracic surgery*, 10 (2010) 679-684.
- [34] K. Pekkan, D. Frakes, D. De Zelicourt, C.W. Lucas, W.J. Parks, A.P. Yoganathan, Coupling pediatric ventricle assist devices to the Fontan circulation: simulations with a lumped-parameter model, *ASAIO journal*, 51 (2005) 618-628.
- [35] M.D. Rodefeld, S.H. Frankel, G.A. Giridharan, Cavopulmonary assist:(em) powering the univentricular Fontan circulation, *Seminars in Thoracic and Cardiovascular Surgery: Pediatric Cardiac Surgery Annual*, 14 (2011) 45-54.
- [36] J. Valdovinos, E. Shkolyar, G.P. Carman, D.S. Levi, In Vitro Evaluation of an External Compression Device for Fontan Mechanical Assistance, *Artificial organs*, 38 (2014) 199-207.
- [37] E. Bove, M. De Leval, F. Migliavacca, R. Balossino, G. Dubini, Toward optimal hemodynamics: computer modeling of the Fontan circuit, *Pediatric cardiology*, 28 (2007) 477-481.
- [38] M. De Leval, G. Dubini, H. Jalali, R. Pietrabissa, Use of computational fluid dynamics in the design of surgical procedures: application to the study of competitive flows in cavopulmonary connections, *The Journal of Thoracic and Cardiovascular Surgery*, 111 (1996) 502-513.
- [39] T.-Y. Hsia, F. Migliavacca, S. Pittaccio, A. Radaelli, G. Dubini, G. Pennati, M. De Leval, Computational fluid dynamic study of flow optimization in realistic models of the total cavopulmonary connections, *Journal of Surgical Research*, 116 (2004) 305-313.
- [40] K. Itatani, K. Miyaji, T. Tomoyasu, Y. Nakahata, K. Ohara, S. Takamoto, M.J.T.A.o.t.s. Ishii, Optimal conduit size of the extracardiac Fontan operation based on energy loss and flow stagnation, 88 (2009) 565-573.
- [41] E. Kung, A. Baretta, C. Baker, G. Arbia, G. Biglino, C. Corsini, S. Schievano, I.E. Vignon-Clementel, G. Dubini, G.J.J.o.b. Pennati, Predictive modeling of the virtual Hemi-Fontan operation for second stage single ventricle palliation: two patient-specific cases, 46 (2013) 423-429.

- [42] M. Gewillig, The fontan circulation, *Heart*, 91 (2005) 839-846.
- [43] M. Gewillig, S.C. Brown, B. Eyskens, R. Heying, J. Ganame, W. Budts, A.L. Gerche, M.J.I.C. Gorenflo, T. Surgery, The Fontan circulation: who controls cardiac output?, 10 (2010) 428-433.
- [44] M. Gewillig, D.J. Goldberg, Failure of the fontan circulation, *Heart failure clinics*, 10 (2014) 105-116.
- [45] C.N. Stasik, C.S. Goldberg, E.L. Bove, E.J. Devaney, R.G. Ohye, Current outcomes and risk factors for the Norwood procedure, *The Journal of thoracic and cardiovascular surgery*, 131 (2006) 412-417.
- [46] E.L. Bove, Current status of staged reconstruction for hypoplastic left heart syndrome, *Pediatric cardiology*, 19 (1998) 308-315.
- [47] E.L. Bove, T.R. Lloyd, Staged reconstruction for hypoplastic left heart syndrome. Contemporary results, *Annals of surgery*, 224 (1996) 387.
- [48] S.M. Bradley, R.S. Mosca, H.A. Hennein, D.C. Crowley, T.J. Kulik, E.L. Bove, Bidirectional superior cavopulmonary connection in young infants, *Circulation*, 94 (1996) II5-11.
- [49] E.A. Bacha, S. Daves, J. Hardin, R.-i. Abdulla, J. Anderson, M. Kahana, P. Koenig, B.N. Mora, M. Gulecyuz, J.P. Starr, Single-ventricle palliation for high-risk neonates: the emergence of an alternative hybrid stage I strategy, *The Journal of thoracic and cardiovascular surgery*, 131 (2006) 163-171. e162.
- [50] M. Galantowicz, J.P. Cheatham, A. Phillips, C.L. Cua, T.M. Hoffman, S.L. Hill, R. Rodeman, Hybrid approach for hypoplastic left heart syndrome: intermediate results after the learning curve, *The Annals of thoracic surgery*, 85 (2008) 2063-2071.
- [51] C. Pizarro, C.D. Derby, J.M. Baffa, K.A. Murdison, W.A. Radtke, Improving the outcome of high-risk neonates with hypoplastic left heart syndrome: hybrid procedure or conventional surgical palliation?, *European Journal of Cardio-Thoracic Surgery*, 33 (2008) 613-618.
- [52] J.L. Gibbs, C. Wren, K. Watterson, S. Hunter, J. Hamilton, Stenting of the arterial duct combined with banding of the pulmonary arteries and atrial septectomy or septostomy: a new approach to palliation for the hypoplastic left heart syndrome, *Heart*, 69 (1993) 551-555.
- [53] M. Sarkar, V. Prabhu, Basics of cardiopulmonary bypass, *Indian journal of anaesthesia*, 61 (2017) 760.
- [54] M.O. Murphy, H. Bellsham-Revell, G.J. Morgan, T. Krasemann, E. Rosenthal, S.A. Qureshi, C. Salih, C.B. Austin, D.R. Anderson, Hybrid procedure for neonates with hypoplastic left heart syndrome at high-risk for norwood: midterm outcomes, *The Annals of thoracic surgery*, 100 (2015) 2286-2292.
- [55] N. Ota, M. Murata, Y. Tosaka, Y. Ide, M. Tachi, H. Ito, A. Sugimoto, K. Sakamoto, Is routine rapid-staged bilateral pulmonary artery banding before stage I Norwood a viable strategy?, *The Journal of thoracic and cardiovascular surgery*, 148 (2014) 1519-1525.
- [56] C.A. Pedra, S.F. Pedra, M.B. Jatene, The Brazilian hybrid approach for hypoplastic left heart syndrome, in: *Fetal and Hybrid Procedures in Congenital Heart Diseases*, Springer, 2016, pp. 229-241.
- [57] I. Michel-Behnke, H. Akintürk, D. Schranz, Fate of the stented arterial duct, *Circulation*, 102 (2000) E178-E178.
- [58] D. Schranz, A. Bauer, B. Reich, B. Steinbrenner, S. Recla, D. Schmidt, C. Apitz, J. Thul, K. Valeske, J. Bauer, Fifteen-year single center experience with the "Giessen Hybrid" approach for hypoplastic left heart and variants: current strategies and outcomes, *Pediatric cardiology*, 36 (2015) 365-373.
- [59] M. Galantowicz, J.P. Cheatham, A. Phillips, C.L. Cua, T.M. Hoffman, S.L. Hill, R.J.T.A.o.t.s. Rodeman, Hybrid approach for hypoplastic left heart syndrome: intermediate results after the learning curve, 85 (2008) 2063-2071.
- [60] S.C. Stoica, A.B. Philips, M. Egan, R. Rodeman, J. Chisolm, S. Hill, J.P. Cheatham, M.E. Galantowicz, The retrograde aortic arch in the hybrid approach to hypoplastic left heart syndrome, *The Annals of thoracic surgery*, 88 (2009) 1939-1947.

- [61] R.R. Davies, W. Radtke, M.A. Bhat, J.M. Baffa, E. Woodford, C. Pizarro, Hybrid palliation for critical systemic outflow obstruction: neither rapid stage 1 Norwood nor comprehensive stage 2 mitigate consequences of early risk factors, *The Journal of thoracic and cardiovascular surgery*, 149 (2015) 182-193.
- [62] R.A. Russell, N.S. Ghanayem, M.E. Mitchell, R.K. Woods, J.S. Tweddell, Bilateral pulmonary artery banding as rescue intervention in high-risk neonates, *The Annals of thoracic surgery*, 96 (2013) 885-890.
- [63] A. Young, T. Gourlay, S. McKee, M.H. Danton, Computational modelling of the hybrid procedure in hypoplastic left heart syndrome: a comparison of zero-dimensional and three-dimensional approach, *Medical engineering & physics*, 36 (2014) 1549-1553.
- [64] H. Akintuerk, I. Michel-Behnke, K. Valeske, M. Mueller, J. Thul, J. Bauer, K.-J. Hagel, J. Kreuder, P. Vogt, D. Schranz, Stenting of the arterial duct and banding of the pulmonary arteries: basis for combined Norwood stage I and II repair in hypoplastic left heart, *Circulation*, 105 (2002) 1099-1103.
- [65] M. Galantowicz, A.R. Yates, Improved outcomes with the comprehensive stage 2 procedure after an initial hybrid stage 1, *The Journal of thoracic and cardiovascular surgery*, 151 (2016) 424-429.
- [66] K. Baba, Y. Kotani, D. Chetan, R.R. Chaturvedi, K.-J. Lee, L.N. Benson, L. Grosse-Wortmann, G.S. Van Arsdell, C.A. Caldarone, O. Honjo, Hybrid versus Norwood strategies for single-ventricle palliation, *Circulation*, 126 (2012) S123-S131.
- [67] P.S. Venugopal, K.P. Luna, D.R. Anderson, C.B. Austin, E. Rosenthal, T. Krasemann, S.A. Qureshi, Hybrid procedure as an alternative to surgical palliation of high-risk infants with hypoplastic left heart syndrome and its variants, *The Journal of thoracic and cardiovascular surgery*, 139 (2010) 1211-1215.
- [68] A.N. Naguib, E. Dewhirst, P.D. Winch, J. Simsic, M. Galantowicz, J.D. Tobias, Pain Management After Comprehensive Stage 2 Repair for Hypoplastic Left Heart Syndrome, *Pediatric Cardiology*, 34 (2013) 52-58. 10.1007/s00246-012-0381-x.
- [69] M. Galantowicz, A.R.J.T.J.o.t. Yates, c. surgery, Improved outcomes with the comprehensive stage 2 procedure after an initial hybrid stage 1, 151 (2016) 424-429.
- [70] W.G. MEMBERS, E.J. Benjamin, M.J. Blaha, S.E. Chiuve, M. Cushman, S.R. Das, R. Deo, S.D. de Ferranti, J. Floyd, M.J.C. Fornage, Heart disease and stroke statistics—2017 update: a report from the American Heart Association, 135 (2017) e146.
- [71] Y. d'Udekem, M.Y. Xu, J.C. Galati, S. Lu, A.J. Iyengar, I.E. Konstantinov, G.R. Wheaton, J.M. Ramsay, L.E. Grigg, J.J.J.o.t.A.C.o.C. Millar, Predictors of survival after single-ventricle palliation: the impact of right ventricular dominance, 59 (2012) 1178-1185.
- [72] D.J. Barron, M.D. Kilby, B. Davies, J.G. Wright, T.J. Jones, W.J.J.T.L. Brawn, Hypoplastic left heart syndrome, 374 (2009) 551-564.
- [73] A. Ceballos, E. Divo, R. Argueta-Morales, C. Calderone, A. Kassab, W. DeCampli, A multi-scale CFD analysis of the hybrid Norwood palliative treatment for hypoplastic left heart syndrome: Effect of reverse Blalock-Taussing shunt diameter, *ASME 2013 International Mechanical Engineering Congress and Exposition*, (2013) V03BT03A045-V003BT003A045.
- [74] A. Ceballos, I.R. Argueta-Morales, E. Divo, R. Osorio, C.A. Caldarone, A.J. Kassab, W.M.J.T.A.o.t.s. DeCampli, Computational analysis of hybrid Norwood circulation with distal aortic arch obstruction and reverse Blalock-Taussig shunt, 94 (2012) 1540-1550.
- [75] U. Yörüker, H. Akintürk, Giessen Procedure as Comprehensive Stage II Palliation With Aortic Arch Reconstruction After Hybrid Bilateral Pulmonary Artery Banding and Ductal Stenting for Hypoplastic Left Heart Syndrome, *Seminars in Thoracic and Cardiovascular Surgery: Pediatric Cardiac Surgery Annual*, 21 (2018) 19-27.
- [76] W.M. DeCampli, C.E. Fleishman, D.G. Nykanen, Hybrid approach to the comprehensive stage II operation in a subset of single-ventricle variants, *The Journal of thoracic and cardiovascular surgery*, 149 (2015) 1095-1100.
- [77] D.A. de Zélicourt, C.M. Haggerty, K.S. Sundareswaran, B.S. Whited, J.R. Rossignac, K.R. Kanter, J.W. Gaynor, T.L. Spray, F. Sotiropoulos, M.A.J.T.J.o.t. Fogel, c. surgery, Individualized computer-based surgical planning to address pulmonary arteriovenous malformations in patients with a single ventricle with an interrupted inferior vena cava and azygous continuation, 141 (2011) 1170-1177.

- [78] A.L. Marsden, A.J. Bernstein, V.M. Reddy, S.C. Shadden, R.L. Spilker, F.P. Chan, C.A. Taylor, J.A.J.T.J.o.T. Feinstein, C. Surgery, Evaluation of a novel Y-shaped extracardiac Fontan baffle using computational fluid dynamics, 137 (2009) 394-403. e392.
- [79] A.L. Marsden, V.M. Reddy, S.C. Shadden, F.P. Chan, C.A. Taylor, J.A.J.C.H.D. Feinstein, A new multiparameter approach to computational simulation for Fontan assessment and redesign, 5 (2010) 104-117.
- [80] K. Pekkan, B. Whited, K. Kanter, S. Sharma, D. De Zelicourt, K. Sundareswaran, D. Frakes, J. Rossignac, A.P.J.M. Yoganathan, b. engineering, computing, Patient-specific surgical planning and hemodynamic computational fluid dynamics optimization through free-form haptic anatomy editing tool (SURGEM), 46 (2008) 1139-1152.
- [81] F. Migliavacca, G. Dubini, G. Pennati, R. Pietrabissa, R. Fumero, T.-Y. Hsia, M.R. de Leval, Computational model of the fluid dynamics in systemic-to-pulmonary shunts, Journal of biomechanics, 33 (2000) 549-557.
- [82] Y. Qian, J. Liu, K. Itatani, K. Miyaji, M. Umezu, Computational hemodynamic analysis in congenital heart disease: simulation of the Norwood procedure, Annals of biomedical engineering, 38 (2010) 2302-2313.
- [83] M.L. Elsayed, O. Mesalhy, J.P. Kizito, Q.H. Leland, L.C. Chow, Performance of a guided plate heat sink at high altitude, International Journal of Heat and Mass Transfer, 147 (2020) 118926.
- [84] M.L. Elsayed, O. Mesalhy, R.H. Mohammed, J.P. Kizito, Q.H. Leland, L.C. Chow, Enhancement of a heat sink performance using a partial shield and/or a guide plate, International Journal of Heat and Mass Transfer, 134 (2019) 948-958.
- [85] W. Schleicher, H. Ma, J. Riglin, Z. Kraybill, W. Wei, R. Klein, A. Oztekin, Characteristics of a micro-hydro turbine, Journal of Renewable and Sustainable Energy, 6 (2014) 013119.
- [86] C. Corsini, D. Cosentino, G. Pennati, G. Dubini, T.-Y. Hsia, F.J.J.o.b. Migliavacca, Multiscale models of the hybrid palliation for hypoplastic left heart syndrome, 44 (2011) 767-770.
- [87] T.-Y. Hsia, D. Cosentino, C. Corsini, G. Pennati, G. Dubini, F. Migliavacca, M.o.C.H.A. Investigators, Use of mathematical modeling to compare and predict hemodynamic effects between hybrid and surgical Norwood palliations for hypoplastic left heart syndrome, Circulation, 124 (2011) S204-S210.
- [88] R.O. Prather, J. Seligson, M. Ni, E. Divo, A. Kassab, W.J.C.j.o.p. DeCampli, pharmacology, Patient-Specific Multiscale Computational Fluid Dynamics Assessment Of Embolization Rates In The Hybrid Norwood: Effects of Size and Placement of the Reverse Blalock-Taussig Shunt, (2018).
- [89] F. Migliavacca, R. Balossino, G. Pennati, G. Dubini, T.-Y. Hsia, M.R. de Leval, E.L. Bove, Multiscale modelling in biofluidynamics: application to reconstructive paediatric cardiac surgery, Journal of biomechanics, 39 (2006) 1010-1020.
- [90] K. Lagana, R. Balossino, F. Migliavacca, G. Pennati, E.L. Bove, M.R. de Leval, G. Dubini, Multiscale modeling of the cardiovascular system: application to the study of pulmonary and coronary perfusions in the univentricular circulation, Journal of biomechanics, 38 (2005) 1129-1141.
- [91] S. Asada, M. Yamagishi, K. Itatani, Y. Maeda, S. Taniguchi, S. Fujita, H. Hongu, H. Yaku, Early outcomes and computational fluid dynamic analyses of chimney reconstruction in the Norwood procedure, Interactive cardiovascular and thoracic surgery, (2019).
- [92] F. Migliavacca, R. Yates, G. Pennati, G. Dubini, R. Fumero, M.R. de Leval, Calculating blood flow from Doppler measurements in the systemic-to-pulmonary artery shunt after the Norwood operation: a method based on computational fluid dynamics, Ultrasound in medicine & biology, 26 (2000) 209-219.
- [93] S.G. Raja, I. Atamanyuk, M. Kostolny, V. Tsang, In hypoplastic left heart patients is Sano shunt compared with modified Blalock–Taussig shunt associated with deleterious effects on ventricular performance?, Interactive cardiovascular and thoracic surgery, 10 (2010) 620-624.
- [94] K.O. Maher, C. Pizarro, S.S. Gidding, K. Januszewska, E. Malec, W.I. Norwood Jr, J.D. Murphy, Hemodynamic profile after the Norwood procedure with right ventricle to pulmonary artery conduit, Circulation, 108 (2003) 782-784.

- [95] J.W. Gaynor, W.T. Mahle, M.I. Cohen, R.F. Ittenbach, W.M. DeCampli, J.M. Steven, S.C. Nicolson, T.L. Spray, Risk factors for mortality after the Norwood procedure, *European journal of cardio-thoracic surgery*, 22 (2002) 82-89.
- [96] E. Malec, K. Januszewska, J. Kołcz, J. Pająk, Factors influencing early outcome of Norwood procedure for hypoplastic left heart syndrome, *European journal of cardio-thoracic surgery*, 18 (2000) 202-206.
- [97] J. Photiadis, A.E. Urban, N. Sinzobahamvya, C. Fink, E. Schindler, M. Schneider, A.M. Brecher, B. Asfour, Restrictive left atrial outflow adversely affects outcome after the modified Norwood procedure, *European journal of cardio-thoracic surgery*, 27 (2005) 962-967.
- [98] S. Sata, N. Sinzobahamvya, C. Arenz, P. Zartner, B. Asfour, V. Hraska, Restrictive atrial septum defect becomes a risk factor for Norwood palliation of hypoplastic left heart syndrome only when it is combined with mitral or aortic atresia, *The Thoracic and cardiovascular surgeon*, 63 (2015) 354-359.
- [99] J.S. Tweddell, L.A. Sleeper, R.G. Ohye, I.A. Williams, L. Mahony, C. Pizarro, V.L. Pemberton, P.C. Frommelt, S.M. Bradley, J.F. Cnota, Intermediate-term mortality and cardiac transplantation in infants with single-ventricle lesions: risk factors and their interaction with shunt type, *The Journal of thoracic and cardiovascular surgery*, 144 (2012) 152-159. e152.
- [100] V.L. Vida, E.A. Bacha, A. Larrazabal, K. Gauvreau, R. Thiagaragan, F. Fynn-Thompson, F.A. Pigula, J.E. Mayer Jr, J. Pedro, W. Tworetzky, Hypoplastic left heart syndrome with intact or highly restrictive atrial septum: surgical experience from a single center, *The Annals of thoracic surgery*, 84 (2007) 581-586.
- [101] D.A. Ashburn, B.W. McCrindle, C.I. Tchervenkov, M.L. Jacobs, G.K. Lofland, E.L. Bove, T.L. Spray, W.G. Williams, E.H. Blackstone, C.H.S. Society, Outcomes after the Norwood operation in neonates with critical aortic stenosis or aortic valve atresia, *The Journal of thoracic and cardiovascular surgery*, 125 (2003) 1070-1082.
- [102] T. Asakura, T. Karino, Flow patterns and spatial distribution of atherosclerotic lesions in human coronary arteries, *Circulation research*, 66 (1990) 1045-1066.
- [103] J. Cole, M. Gillan, S. Raghunathan, A CFD study of steady and pulsatile flows within an arterial bifurcation, 36th AIAA Aerospace Sciences Meeting and Exhibit, (2010) 790.
- [104] M.-H. Song, M. Sato, Y. Ueda, Three-dimensional simulation of the Blalock-Taussig shunt using computational fluid dynamics, *Surgery today*, 31 (2001) 688-694.
- [105] J.R.M. Sant'Anna, D.C. Pereira, R.A. Kalil, P.R. Prates, E. Horowitz, R.T. Sant'Anna, P.R. Prates, I.A. Nesralla, Computer dynamics to evaluate blood flow through the modified Blalock-Taussig shunt, *Brazilian Journal of Cardiovascular Surgery*, 18 (2003) 253-260.
- [106] Z. Małota, Z. Nawrat, P. Kostka, J. Mizerski, K. Nowinski, J. Waniewski, Physical and computer modelling of blood flow in a systemic-to-pulmonary shunt, *The International journal of artificial organs*, 27 (2004) 990-999.
- [107] F. Migliavacca, G. Pennati, G. Dubini, R. Fumero, R. Pietrabissa, G. Urcelay, E.L. Bove, T.-Y. Hsia, M.R. de Leval, Modeling of the Norwood circulation: effects of shunt size, vascular resistances, and heart rate, *American Journal of Physiology-Heart and Circulatory Physiology*, 280 (2001) H2076-H2086.
- [108] M.E. Moghadam, F. Migliavacca, I.E. Vignon-Clementel, T.-Y. Hsia, A.L. Marsden, Optimization of shunt placement for the Norwood surgery using multi-domain modeling, *Journal of biomechanical engineering*, 134 (2012) 051002.
- [109] T. Kitagawa, I. Katoh, Y. Fukumura, M. Yoshizumi, Y. Masuda, T. Hori, Achieving optimal pulmonary blood flow in the first-stage of palliation in early infancy for complex cardiac defects with hypoplastic left ventricles, *Cardiology in the Young*, 5 (1995) 21-27.
- [110] G. Pennati, G.B. Fiore, F. Migliavacca, K. Lagana, R. Fumero, G. Dubini, In vitro steady-flow analysis of systemic-to-pulmonary shunt haemodynamics, *Journal of biomechanics*, 34 (2001) 23-30.
- [111] W. Glenn, M. Browne, R. Whittmore, Circulatory bypass of the right side of the heart: cava-pulmonary artery shunt—indications and results (report of a collected series of 537 cases), in: *The heart and circulation in the newborn and infant*, Grune & Stratton, New York, 1966, pp. 345-357.

- [112] D.E. Schiavazzi, E.O. Kung, A.L. Marsden, C. Baker, G. Pennati, T.-Y. Hsia, A. Hlavacek, A.L. Dorfman, M.o.C.H.A.I.J.T.J.o. thoracic, c. surgery, Hemodynamic effects of left pulmonary artery stenosis after superior cavopulmonary connection: a patient-specific multiscale modeling study, 149 (2015) 689-696. e683.
- [113] M. Esmaily-Moghadam, T.-Y. Hsia, A.L. Marsden, M.o.C.H.A.I.J.T.J.o. thoracic, c. surgery, The assisted bidirectional Glenn: A novel surgical approach for first-stage single-ventricle heart palliation, 149 (2015) 699-705.
- [114] J. Zhou, M. Esmaily-Moghadam, T.A. Conover, T.-Y. Hsia, A.L. Marsden, R.S. Figliola, M.I.J.C. engineering, technology, In vitro assessment of the assisted bidirectional Glenn procedure for stage one single ventricle repair, 6 (2015) 256-267.
- [115] M. Esmaily-Moghadam, T.-Y. Hsia, A.L. Marsden, M.o.C.H.A. Investigators, The assisted bidirectional Glenn: A novel surgical approach for first-stage single-ventricle heart palliation, The Journal of thoracic and cardiovascular surgery, 149 (2015) 699-705.
- [116] E.L. Bove, M.R. de Leval, F. Migliavacca, G. Guadagni, G.J.T.J.o.T. Dubini, C. Surgery, Computational fluid dynamics in the evaluation of hemodynamic performance of cavopulmonary connections after the Norwood procedure for hypoplastic left heart syndrome, 126 (2003) 1040-1047.
- [117] J. Strony, A. Beaudoin, D. Brands, B.J.A.J.o.P.-H. Adelman, C. Physiology, Analysis of shear stress and hemodynamic factors in a model of coronary artery stenosis and thrombosis, 265 (1993) H1787-H1796.
- [118] P.A. Holme, U. Ørvim, M.J. Hamers, N.O. Solum, F.R. Brosstad, R.M. Barstad, K.S.J.A. Sakariassen, thrombosis,, v. biology, Shear-induced platelet activation and platelet microparticle formation at blood flow conditions as in arteries with a severe stenosis, 17 (1997) 646-653.
- [119] H. Baumgartner, K.J.A.o.t.N.Y.A.o.S. Sakariassen, Factors controlling thrombus formation on arterial lesions, 454 (1985) 162-177.
- [120] K.S. Sakariassen, R. Joss, R. Muggli, H. Kuhn, T.B. Tschopp, H. Sage, H.R.J.A. Baumgartner, Thrombosis,, V. Biology, Collagen type III induced ex vivo thrombogenesis in humans. Role of platelets and leukocytes in deposition of fibrin, 10 (1990) 276-284.
- [121] G. Troianowski, C.A. Taylor, J.A. Feinstein, I.E. Vignon-Clementel, Three-dimensional simulations in Glenn patients: clinically based boundary conditions, hemodynamic results and sensitivity to input data, Journal of biomechanical engineering, 133 (2011) 111006.
- [122] E. Kung, A. Baretta, C. Baker, G. Arbia, G. Biglino, C. Corsini, S. Schievano, I.E. Vignon-Clementel, G. Dubini, G. Pennati, Predictive modeling of the virtual Hemi-Fontan operation for second stage single ventricle palliation: two patient-specific cases, Journal of biomechanics, 46 (2013) 423-429.
- [123] K. Pekkan, L.P. Dasi, D. de Zélicourt, K.S. Sundareswaran, M.A. Fogel, K.R. Kanter, A.P. Yoganathan, Hemodynamic performance of stage-2 univentricular reconstruction: Glenn vs. hemi-Fontan templates, Annals of biomedical engineering, 37 (2009) 50-63.
- [124] A.K. Pridjian, A.M. Mendelsohn, F.M. Lupinetti, R.H. Beekman III, M. Dick II, G. Serwer, E.L. Bove, Usefulness of the bidirectional Glenn procedure as staged reconstruction for the functional single ventricle, The American journal of cardiology, 71 (1993) 959-962.
- [125] M. Gewillig, D.J.J.H.f.c. Goldberg, Failure of the Fontan circulation, 10 (2014) 105-116.
- [126] C.G. DeGroff, W. Orlando, J. Hertzberg, R. Shandas, L. Valdes-Cruz, Effect of reverse flow on the fluid dynamics of the Total Cavo-pulmonary Connection: a potential cause of progressive heart failure, Journal of the American College of Cardiology, 39 (2002) 407.
- [127] G. Guadagni, E.L. Bove, F. Migliavacca, G. Dubini, Effects of pulmonary afterload on the hemodynamics after the hemi-Fontan procedure, Medical engineering & physics, 23 (2001) 293-298.
- [128] F. Migliavacca, M.R. de Leval, G. Dubini, R. Pietrabissa, A computational pulsatile model of the bidirectional cavopulmonary anastomosis: the influence of pulmonary forward flow, Journal of biomechanical engineering, 118 (1996) 520-528.

- [129] J.-M. Van Haesdonck, L. Mertens, R. Sizaïre, G. Montas, B. Purnode, W. Daenen, M. Crochet, M. Gewillig, Comparison by computerized numeric modeling of energy losses in different Fontan connections, *Circulation*, 92 (1995) 322-326.
- [130] V. Alexi-Meskishvili, S. Ovroutski, P. Ewert, I. Dähnert, F. Berger, P.E. Lange, R.J.E.j.o.c.-t.s. Hetzer, Optimal conduit size for extracardiac Fontan operation, 18 (2000) 690-695.
- [131] M. Ni, Computational Fluid Dynamics Proof of Concept and Analysis of a Self-Powered Fontan Circulation, (2017).
- [132] Y. Delorme, K. Anupindi, A. Kerlo, D. Shetty, M. Rodefeld, J. Chen, S. Frankel, Large eddy simulation of powered Fontan hemodynamics, *Journal of biomechanics*, 46 (2013) 408-422.
- [133] S. Shimizu, T. Kawada, D. Une, M. Fukumitsu, M.J. Turner, A. Kamiya, T. Shishido, M. Sugimachi, Partial cavopulmonary assist from the inferior vena cava to the pulmonary artery improves hemodynamics in failing Fontan circulation: a theoretical analysis, *The Journal of Physiological Sciences*, 66 (2016) 249-255.
- [134] T. Mackling, T. Shah, V. Dimas, K. Guleserian, M. Sharma, J. Forbess, M. Ardura, J. Gross-Toalson, Y. Lee, J. Journeycake, Management of single-ventricle patients with Berlin Heart EXCOR Ventricular Assist Device: single-center experience, *Artificial organs*, 36 (2012) 555-559.
- [135] M.D. Rodefeld, J.H. Boyd, C.D. Myers, B.J. LaLone, A.J. Bezruczko, A.W. Potter, J.W. Brown, Cavopulmonary assist: circulatory support for the univentricular Fontan circulation, *The Annals of thoracic surgery*, 76 (2003) 1911-1916.
- [136] S. Tsuda, T. Sasaki, K. Maeda, R.K. Riemer, S.H. Reichenbach, O. Reinhartz, Recovery during mid-term mechanical support of fontan circulation in sheep, *Asaio Journal*, 55 (2009) 406-411.
- [137] A.L. Throckmorton, K.K. Ballman, C.D. Myers, K.N. Litwak, S.H. Frankel, M.D. Rodefeld, Mechanical cavopulmonary assist for the univentricular fontan circulation using a novel folding propeller blood pump, *Asaio Journal*, 53 (2007) 734-741.
- [138] R. John, F. Kamdar, K. Liao, M. Colvin-Adams, A. Boyle, L. Joyce, Improved survival and decreasing incidence of adverse events with the HeartMate II left ventricular assist device as bridge-to-transplant therapy, *The Annals of thoracic surgery*, 86 (2008) 1227-1235.
- [139] D.V. Amin, J.F. Antaki, P. Litwak, D. Thomas, Z.J. Wu, M. Watach, Induction of ventricular collapse by an axial flow blood pump, *ASAIO journal (American Society for Artificial Internal Organs: 1992)*, 44 (1998) M685-690.
- [140] R.K. Riemer, G. Amir, S.H. Reichenbach, O. Reinhartz, Mechanical support of total cavopulmonary connection with an axial flow pump, *The Journal of thoracic and cardiovascular surgery*, 130 (2005) 351-354.
- [141] M.E. Moghadam, Y. Bazilevs, T.-Y. Hsia, I.E. Vignon-Clementel, A.L.J.C.M. Marsden, A comparison of outlet boundary treatments for prevention of backflow divergence with relevance to blood flow simulations, 48 (2011) 277-291.
- [142] K.S. Sakariassen, P.A. Holme, U. Ørvim, R.M. Barstad, N.O. Solum, F.R.J.T.r. Brosstad, Shear-induced platelet activation and platelet microparticle formation in native human blood, 92 (1998) S33-S41.
- [143] J.A. Moore, B.K. Rutt, S.J. Karlik, K. Yin, C.R. Ethier, Computational blood flow modeling based on in vivo measurements, *Annals of biomedical engineering*, 27 (1999) 627-640.
- [144] C.A. Taylor, M.T. Draney, J.P. Ku, D. Parker, B.N. Steele, K. Wang, C.K. Zarins, Predictive medicine: Computational techniques in therapeutic decision-making, *Computer Aided Surgery: Official Journal of the International Society for Computer Aided Surgery (ISCAS)*, 4 (1999) 231-247.
- [145] M. Shojima, M. Oshima, K. Takagi, R. Torii, M. Hayakawa, K. Katada, A. Morita, T. Kirino, Magnitude and role of wall shear stress on cerebral aneurysm: computational fluid dynamic study of 20 middle cerebral artery aneurysms, *Stroke*, 35 (2004) 2500-2505.
- [146] F.P. Glor, Q. Long, A.D. Hughes, A.D. Augst, B. Ariff, S.A.M. Thom, P.R. Verdonck, X.Y. Xu, Reproducibility Study of Magnetic Resonance Image-Based Computational Fluid Dynamics Prediction of Carotid Bifurcation Flow, *Annals of Biomedical Engineering*, 31 (2003) 142-151. 10.1114/1.1537694.

- [147] J.B. Thomas, J.S. Milner, B.K. Rutt, D.A. Steinman, Reproducibility of Image-Based Computational Fluid Dynamics Models of the Human Carotid Bifurcation, *Annals of Biomedical Engineering*, 31 (2003) 132-141. 10.1114/1.1540102.
- [148] D. Dillon-Murphy, A. Noorani, D. Nordsletten, C.A. Figueroa, Multi-modality image-based computational analysis of haemodynamics in aortic dissection, *Biomechanics and modeling in mechanobiology*, 15 (2016) 857-876.
- [149] I.E. Vignon-Clementel, A.L. Marsden, J.A. Feinstein, A primer on computational simulation in congenital heart disease for the clinician, *Progress in Pediatric Cardiology*, 30 (2010) 3-13.
- [150] R. Balossino, G. Pennati, F. Migliavacca, L. Formaggia, A. Veneziani, M. Tuveri, G. Dubini, Computational models to predict stenosis growth in carotid arteries: Which is the role of boundary conditions?, *Computer methods in biomechanics and biomedical engineering*, 12 (2009) 113-123.
- [151] J.C. Greenfield Jr, D.L. Fry, Relationship between instantaneous aortic flow and the pressure gradient, *Circulation research*, 17 (1965) 340-348.
- [152] L. Formaggia, A. Quarteroni, A. Veneziani, *Cardiovascular Mathematics: Modeling and simulation of the circulatory system*, Springer Science & Business Media, 2010.
- [153] M. Mohagheghi, H. Zawati, T. Pinol, J. Gou, C. Xu, J. Kapat, Use of 1-D Finite Enthalpy Method for a High-Temperature Recuperator Made of Polymer Derived Ceramic Composite for a Supercritical Carbon Dioxide Power System, *The 5th International Symposium–Supercritical CO2 Power Cycles March*, (2016) 28-31.
- [154] F. Migliavacca, K. Laganà, G. Pennati, M.R. de Leval, E.L. Bove, G. Dubini, Global mathematical modelling of the Norwood circulation: a multiscale approach for the study of the pulmonary and coronary arterial perfusions, *Cardiol Young*, 14 (2004) 71-76.
- [155] H. Zawati, M. Elmore, J. Kapat, N. Nagaiah, Thermal Analysis and Pressure Loss Modeling for an Optimized Heat Exchanger Used in a Recuperated CO2 Power Cycle, *ASME Turbo Expo 2018: Turbomachinery Technical Conference and Exposition*, (2018).
- [156] O. Frank, The basic shape of the arterial pulse. First treatise: mathematical analysis, *Journal of molecular and cellular cardiology*, 22 (1990) 255-277.
- [157] N. Stergiopoulos, J.-J. Meister, N.J.A.J.o.P.-H. Westerhof, C. Physiology, Determinants of stroke volume and systolic and diastolic aortic pressure, 270 (1996) H2050-H2059.
- [158] A. Ferreira, S. Chen, M.A. Simaan, J.R. Boston, J.F. Antaki, A nonlinear state-space model of a combined cardiovascular system and a rotary pump, *Decision and Control, 2005 and 2005 European Control Conference. CDC-ECC'05. 44th IEEE Conference on*, (2005) 897-902.
- [159] E. Fallon, R. Feddersen, J. Kurtzleben, M.A. Lee, S. Rowchette-Crawley, A. Reader's, *DePARTment of LIBeRAL ARts, Course Booklet 2014-15*, 126 90.
- [160] S. Paeme, K.T. Moorhead, J.G. Chase, B. Lambermont, P. Kolh, V. D'orio, L. Pierard, M. Moonen, P. Lancellotti, P.C. Dauby, Mathematical multi-scale model of the cardiovascular system including mitral valve dynamics. Application to ischemic mitral insufficiency, *Biomedical engineering online*, 10 (2011) 86.
- [161] G. Pennati, F. Migliavacca, G. Dubini, R. Pietrabissa, M.R. de Leval, A mathematical model of circulation in the presence of the bidirectional cavopulmonary anastomosis in children with a univentricular heart, *Medical engineering & physics*, 19 (1997) 223-234.
- [162] M.L. Elsayed, O. Mesalhy, Studying the performance of solid/perforated pin-fin heat sinks using entropy generation minimization, *Heat and Mass Transfer*, 51 (2015) 691-702.
- [163] A. Quarteroni, S. Ragni, A. Veneziani, Coupling between lumped and distributed models for blood flow problems, *Computing and Visualization in Science*, 4 (2001) 111-124.
- [164] A. Quarteroni, A. Veneziani, Analysis of a geometrical multiscale model based on the coupling of ODE and PDE for blood flow simulations, *Multiscale Modeling & Simulation*, 1 (2003) 173-195.

- [165] M.E. Moghadam, I.E. Vignon-Clementel, R. Figliola, A.L. Marsden, M.o.C.H.A. Investigators, A modular numerical method for implicit 0D/3D coupling in cardiovascular finite element simulations, *Journal of Computational Physics*, 244 (2013) 63-79.
- [166] C. Wang, K. Pekkan, D. de Zélicourt, M. Horner, A. Parihar, A. Kulkarni, A.P. Yoganathan, Progress in the CFD Modeling of Flow Instabilities in Anatomical Total Cavopulmonary Connections, *Annals of Biomedical Engineering*, 35 (2007) 1840-1856. 10.1007/s10439-007-9356-0.
- [167] Viscosity of Blood, in, 2017.
- [168] B.C. Good, S. Deutsch, K.B. Manning, Hemodynamics in a pediatric ascending aorta using a viscoelastic pediatric blood model, *Annals of biomedical engineering*, 44 (2016) 1019-1035.
- [169] K. Pekkan, D. De Zélicourt, L. Ge, F. Sotiropoulos, D. Frakes, M.A. Fogel, A.P. Yoganathan, Physics-driven CFD modeling of complex anatomical cardiovascular flows—a TCPC case study, *Annals of biomedical engineering*, 33 (2005) 284-300.
- [170] C. DeGroff, B. Birnbaum, R. Shandas, W. Orlando, J. Hertzberg, Computational simulations of the total cavopulmonary connection: insights in optimizing numerical solutions, *Medical engineering & physics*, 27 (2005) 135-146.
- [171] M.L. Elsayed, O. Mesalhy, Effect of a Slotted Shield on Thermal and Hydraulic Performance of a Heat Sink, *Journal of Electronic Packaging*, 137 (2015) 011004.
- [172] D. Bluestein, L. Niu, R.T. Schoepfoerster, M.K. Dewanjee, Fluid mechanics of arterial stenosis: relationship to the development of mural thrombus, *Annals of biomedical engineering*, 25 (1997) 344.
- [173] L. Rouleau, M. Farcas, J.-C. Tardif, R. Mongrain, R.L. Leask, Endothelial cell morphologic response to asymmetric stenosis hemodynamics: effects of spatial wall shear stress gradients, *Journal of biomechanical engineering*, 132 (2010) 081013.
- [174] Z. Xu, N. Chen, M.M. Kamocka, E.D. Rosen, M. Alber, A multiscale model of thrombus development, *Journal of the Royal Society Interface*, 5 (2007) 705-722.
- [175] H. Meng, Z. Wang, Y. Hoi, L. Gao, E. Metaxa, D.D. Swartz, J. Kolega, Complex hemodynamics at the apex of an arterial bifurcation induces vascular remodeling resembling cerebral aneurysm initiation, *Stroke*, 38 (2007) 1924-1931.
- [176] A.J. Reininger, C.B. Reininger, U. Heinzmann, L.J. Wurzing, Residence time in niches of stagnant flow determines fibrin clot formation in an arterial branching model-detailed flow analysis and experimental results, *Thrombosis and haemostasis*, 73 (1995) 916-922.
- [177] M.J. Kunov, D. Steinman, C.R. Ethier, Particle volumetric residence time calculations in arterial geometries, *Journal of biomechanical engineering*, 118 (1996) 158-164.
- [178] G.-Y. Suh, A.S. Les, A.S. Tenforde, S.C. Shadden, R.L. Spilker, J.J. Yeung, C.P. Cheng, R.J. Herfkens, R.L. Dalman, C.A. Taylor, Quantification of particle residence time in abdominal aortic aneurysms using magnetic resonance imaging and computational fluid dynamics, *Annals of biomedical engineering*, 39 (2011) 864-883.
- [179] D. Sengupta, A.M. Kahn, J.C. Burns, S. Sankaran, S.C. Shadden, A.L. Marsden, Image-based modeling of hemodynamics in coronary artery aneurysms caused by Kawasaki disease, *Biomechanics and modeling in mechanobiology*, 11 (2012) 915-932.
- [180] A.L. Marsden, A.J. Bernstein, V.M. Reddy, S.C. Shadden, R.L. Spilker, F.P. Chan, C.A. Taylor, J.A. Feinstein, Evaluation of a novel Y-shaped extracardiac Fontan baffle using computational fluid dynamics, *The Journal of Thoracic and Cardiovascular Surgery*, 137 (2009) 394-403. e392.
- [181] C. Long, M.C. Hsu, Y. Bazilevs, J. Feinstein, A. Marsden, Fluid–structure interaction simulations of the Fontan procedure using variable wall properties, *International journal for numerical methods in biomedical engineering*, 28 (2012) 513-527.